

AFIT/DS/ENG/96-12

MICROELECTROMECHANICAL ISOLATION
OF ACOUSTIC WAVE RESONATORS

DISSERTATION

James R. Reid, Jr., Captain, USAF

AFIT/DS/ENG/96-12

19970214 028

Approved for public release; distribution unlimited

DTIC QUALITY INSPECTED 1

The views expressed in this dissertation are those of the author and do not reflect the official policy or position of the Department of Defense or the U. S. Government.

AFIT/DS/ENG/96-12

MICROELECTROMECHANICAL ISOLATION OF ACOUSTIC WAVE
RESONATORS

DISSERTATION

Presented to the Faculty of the Graduate School of Engineering
of the Air Force Institute of Technology
Air University in Partial Fulfillment of the
Requirements for the Degree of
Doctor of Philosophy

James R. Reid, Jr., B.S.E.E., M.S.E.E.
Captain, USAF

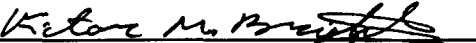
December 1996

Approved for public release; distribution unlimited

MICROELECTROMECHANICAL ISOLATION OF ACOUSTIC WAVE RESONATORS

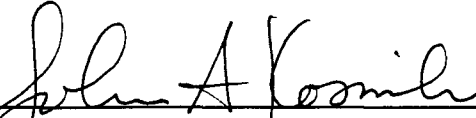
James R. Reid, Jr., B.S.E.E., M.S.E.E.
Captain, USAF

Approved:




Victor M. Bright, PhD (Chairman)
AFIT Department of Electrical and Computer Engineering

25 Nov 96
Date



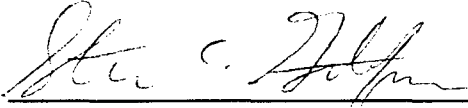
John A. Kosinski, PhD
US Army CECOM

25 Nov 96
Date



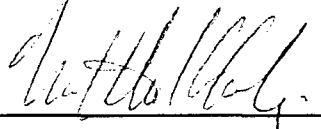
Milton E. Franke, PhD
AFIT Department of Aeronautics and Astronautics

25 Nov 96
Date



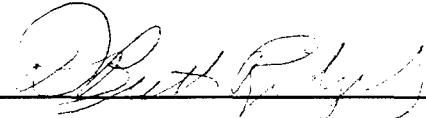
Steven C. Gustafson, PhD
University of Dayton, Department of Electro-Optics

25 Nov 96
Date



Matthew Kabrisky
AFIT Department of Electrical and Computer Engineering


25 Nov 96
Date



Brett D. Ridgely, PhD (Dean's Representative)
AFIT Department of Aeronautics and Astronautics

25 Nov 96
Date

Accepted:



Robert A. Calico, Jr.
Dean, Graduate School of Engineering

Acknowledgements

This dissertation would not have been possible without the assistance, advice, and patience of a great number of people and I would like to thank each one of them personally. Special thanks goes to the sponsor Dr. John Kosinski for the original idea that resulted in this research. Throughout my studies Dr. Kosinski has provided invaluable assistance and support. Under Dr. Kosinski's direction, the work was funded by Army Missile Command. This financial support provided for lab supplies and publication expenses related to this research. Dr. Kosinski also provided encouragement throughout, and helped get everything started by providing research materials and contacts that would not have otherwise been available. I would also like to thank Dr. Jim Stewart for providing the finite element analysis tools and his personal expertise. Much of this work would not have been possible without his contributions. Thanks also goes to SAWTEK, Inc. SAWTEK provided both the 1 GHz STW resonators and technical support that made this research happen. Particularly, I would like to thank Dave Jordan for helping me with the configuration and testing of the oscillators. His help saved many weeks of work.

During the course of this research, my advisor, Dr. Victor Bright, has provided suggestions and allowed me to explore a wide range of ideas. Many of these ideas have led to the design and fabrication of exciting new MEMS systems that wouldn't have been created had it not been for Dr. Bright's encouragement. I would also like to thank the other MEMS students: Maj. Dave Burns, Capt. Jeff Butler, Maj. John Comtois, Maj. Bill Cowan, Capt. George Dalton, and Capt. Darren Sene, who made many of the long nights in the lab almost enjoyable. Many of the accomplishments of this research are due to the open and stimulating environment created by the MEMS group.

Charlie Powers deserves a special thanks for making everything happen. Particularly pushing orders through the procurement system in time to get MUMPS die fabricated. I would also like to thank the lab technicians, Bill Trop and Chris O'Brien.

Special thanks goes to the members of my research committee: Dr. Steven Gustafson, Dr. Milton Franke, Dr. Brett Ridgely, and Dr. Matt Kabrisky. Particular thanks goes to Dr. Kabrisky for his never ending passion for knowledge. His drive and energy were often an inspiration during my years at AFIT.

Most importantly, I would like to thank my family. Throughout this research and throughout my life, my parents, Bob and Penny Reid, and my sister, Trisha Reid, have always been there providing me support and encouragement. And last but certainly not least I would like to thank Dr. Corike Toxopeus for sticking with me despite the long hours I have spent in the lab over the last year.

James R. Reid, Jr.

Table of Contents

	Page
Acknowledgements	iii
List of Figures	ix
List of Tables	xix
Abstract	xx
 I. Introduction	 1-1
1.1 Problem Statement	1-1
1.2 Research Accomplishments	1-3
1.3 Organization of this Dissertation	1-5
 II. Acceleration Sensitivity in Surface Acoustic Wave and Surface Transverse Wave Oscillators	 2-1
2.1 Surface Acoustic Waves	2-2
2.2 SAW Resonators	2-4
2.2.1 SAW Reflectors	2-4
2.2.2 One and Two Port SAW Resonators	2-5
2.3 Surface Transverse Wave Devices	2-7
2.4 SAW/STW Fixed-Frequency Oscillators	2-9
2.5 Acceleration Sensitivity in SAW/STW Based Oscillators . . .	2-10
2.5.1 Acceleration Induced Frequency Shifts	2-11
2.5.2 Effect of Acceleration on the Oscillator	2-11
2.5.3 The Cause of Acceleration Sensitivity	2-15
2.6 Current Techniques for Reducing Crystal Acceleration Sensi- tivity	2-18
2.6.1 State of the Art Oscillators	2-19
2.7 Summary	2-20

	Page
III. Fundamentals of Vibration Isolation	3-1
3.1 Analysis of an Undamped, One Degree of Freedom Mass-Spring System	3-2
3.2 The Effect of Damping on a Mass-Spring System	3-5
3.3 Active Vibration Isolation	3-10
IV. Microelectromechanical Systems	4-1
4.1 Micromachining Processes	4-1
4.1.1 Bulk Micromachining	4-1
4.1.2 Surface Micromachining	4-10
4.1.3 Microforming	4-14
4.1.4 The LIGA process	4-15
4.1.5 Electroplating with Photosensitive Polyimide	4-16
4.2 Microelectromechanical Components, Actuators, and Systems	4-17
4.2.1 Simple Structures	4-19
4.2.2 Movable Components and Structures	4-21
4.2.3 Actuators	4-31
4.2.4 Systems	4-44
4.3 Summary	4-52
V. Design	5-1
5.1 System Design	5-2
5.2 Finite Element Analysis	5-4
5.2.1 Calculation of STW Mode Shape	5-5
5.2.2 Calculation of Biasing State	5-7
5.2.3 Calculation of the Acceleration Sensitivity	5-8
5.2.4 Numerical Results	5-11
5.3 Mass-Spring Model	5-15
5.3.1 Calculation of Model Parameters	5-16

	Page
5.3.2 Model Results	5-18
5.4 Final System Design	5-19
5.4.1 Expected Vibration Sensitivity of the Modified Design	5-19
5.5 Summary	5-22
VI. Device Fabrication Process	6-1
6.1 Process Overview	6-1
6.2 Mask Fabrication	6-3
6.3 Oxidation	6-5
6.4 Back Side Patterning	6-7
6.5 Back Side Etch	6-8
6.6 Front Side Patterning	6-9
6.7 Metalization	6-11
6.8 Release Etch	6-13
6.9 Bonding	6-13
6.10 Summary	6-14
VII. Experimental Results	7-1
7.1 Mounting the Oscillator	7-1
7.2 Test Set Up	7-7
7.3 Vibration Sensitivity Measurements	7-8
7.3.1 Baseline Measurement	7-8
7.3.2 Oscillator 1	7-8
7.3.3 Oscillator 2	7-10
7.3.4 Oscillator 3	7-11
7.4 Discussion	7-12
7.5 Summary	7-16

	Page
VIII. Conclusions and Recommendations	8-1
8.1 Summary	8-1
8.2 Conclusions and Significance	8-2
8.3 Further Research	8-4
8.3.1 Design of the Isolation System	8-4
8.3.2 Low Mass Rigid Structures	8-5
8.3.3 Isolation of Packaged Resonators and Oscillators . .	8-5
8.3.4 Active Mounting	8-6
8.3.5 Modifications to the Fabrication Process	8-6
Appendix A. CMOS-MEMS Release Process	A-1
Appendix B. MUMPs Release Process	B-1
Appendix C. Mask Fabrication	C-1
Appendix D. Standard Piranha Clean	D-1
Appendix E. Oxidation	E-1
Appendix F. Back Side Patterning	F-1
Appendix G. KOH Etch Process	G-1
Appendix H. Front Side Patterning	H-1
Appendix I. Metalization	I-1
Appendix J. Commonly Used Acronyms	J-1
Appendix K. Submitted and Published Papers Related to This Research .	K-1
Bibliography	BIB-1
Vita	VITA-1

List of Figures

Figure		Page
2.1.	Rayleigh type waves at the surface of an elastic material.	2-2
2.2.	An inter-digital transducer on top of a piezoelectric substrate.	2-3
2.3.	Schematic of a SAW reflective grating.	2-5
2.4.	One and two port SAW resonators and their equivalent circuit models. (a) One port resonator (b) Two port resonator.	2-6
2.5.	Frequency response of a two port SAW resonator [27].	2-7
2.6.	General design of a SAW/STW oscillator circuit.	2-9
2.7.	Frequency response of a SAW oscillator vibrated at constant frequency of f_v	2-14
2.8.	The random vibration envelope of a typical aircraft [1].	2-15
2.9.	The effect of the random vibration defined by the envelope shown in Fig. 2.8 on an oscillator with an acceleration sensitivity of $10^{-9}/g$ [1].	2-16
2.10.	Equivalent circuit for modeling changes in the transimpedance of the oscillator loop excluding the SAW resonator [2].	2-16
2.11.	An all quartz package mounted to a stiffener to reduce acceleration sensitivity [53].	2-20
2.12.	A commercially fabricated crystal based oscillator with low acceleration sensitivity [23].	2-21
3.1.	A vibration isolation system is used to separate a vibration source from an object that requires a reduced vibration.	3-1
3.2.	A mass connected to a vibrating foundation via an isolation system. The mass is free to move in any of 3 spatial dimensions, and can also rotate about any of the 3 spatial axes. This results in a system with six degrees of freedom.	3-2
3.3.	A mass, M_0 connected to a vibration foundation by a spring, k . The vibration of the foundation is represented by a time dependent motion, $v_f(t)$. The motion of the foundation results in a motion of the mass, $v_m(t)$. All motion is limited to a single axis as shown.	3-3

Figure		Page
3.4.	Magnitude and phase of the absolute transmissability of a foundation vibration to the mass. The absolute transmissability is defined as $T_a = v_m/v_f$. Note that the phase change shows that the motion of the mass trails that of the foundation by 180 degrees for values of $\omega > \omega_0$	3-5
3.5.	A mass-spring system with a damper added in parallel to the spring.	3-5
3.6.	Absolute transmissability of a damped mass-spring system for several values of C_m . All of the curves have $C_r = 0$	3-9
3.7.	Absolute transmissability of a damped mass-spring system for several values of C_r . All of the curves have $C_m = 0$	3-9
3.8.	A one degree of freedom mass-spring system with both passive and active damping.	3-10
4.1.	Etching profile of an isotropic etchant. The etch proceeds equally in all directions resulting in an undercutting of the masking material that is directly proportional to the etch time.	4-3
4.2.	Miller indices for the cubic crystal planes.	4-3
4.3.	Etching profile of an anisotropic etch with EDP or KOH. (a) On a {100} oriented silicon wafer. (b) On a {110} oriented silicon wafer. .	4-5
4.4.	(a) SEM micrograph of pyramidal pits etched into {100} oriented silicon wafer using EDP [4]. (b) Anisotropic etching can be used to undercut a thin oxide layer on the surface of a wafer resulting in a released structure. The structures shown in (b) were designed by the author and fabricated using a commercial foundry. The devices were then released by etching in EDP at AFIT.	4-6
4.5.	Structures fabricated in quartz using the MITE process [88]. (a) The ion tracks are formed normal to the quartz surface resulting in vertical etch planes. (b) The ion tracks are at a 45 degree angle to the surface resulting in tilted etch planes.	4-7

Figure		Page
4.6.	Sacrificial micromachining process for the fabrication of a cantilever beam. (a) Deposit a silicon nitride (Si_3N_4) passivation layer on a silicon substrate. (b) Deposit and pattern the sacrificial silicon oxide (SiO_2) layer. (c) Deposit and pattern the structural polysilicon layer. (d) Release the cantilever beam by removing the sacrificial layer in a HF etch.	4-10
4.7.	SEM micrographs showing structures fabricated by the author using a commercial surface micromachining process, MUMPs. The micrographs show arrays of force testers, (a), and several suspended platforms, (b). As can be seen, the lateral dimensions of the structures are much greater than the vertical dimensions.	4-12
4.8.	Bending of released cantilever beams due to residual stress [4].	4-12
4.9.	MUMPs ⁷ layer thicknesses.	4-14
4.10.	The LIGA process.	4-16
4.11.	Devices fabricated at AFIT using the thin LIGA process offered by MCNC. The devices are 30 μm thick nickel. The fingers, (a), have an equal width and separation of 5 μm . The AFIT logo, (b), also has 5 μm thick arms.	4-17
4.12.	SEM micrograph of a copper gear fabricated by electroplating into a polyimide mold [73]. The gear is 300 μm across and 45 μm tall. . . .	4-18
4.13.	Fabrication with photosensitive polyimide and electroplating.	4-18
4.14.	Fabrication of a cantilever in a bulk micromachining process. (a) A thin film such as SiO_2 is deposited and patterned. (b) The cantilever is released using an anisotropic etchant such as EDP or TMAH.	4-19
4.15.	Cantilevers fabricated using MUMPs. The cantilevers in (b) were stuck to the surface when the die was dried.	4-20
4.16.	A micromechanical spring fabricated using MUMPs.	4-21
4.17.	Several IR pixels fabricated at AFIT using the CMOS-MEMS process.	4-22
4.18.	Sliders that allow linear motion of a plate are fabricated in surface micromachining processes using two releasable polysilicon layers. The basic design is shown in the schematic view, (a), while a fabricated slider is also shown, (b).	4-23

Figure		Page
4.19.	SEM micrograph of a pin joint fabricated using MUMPs.	4-23
4.20.	The basic substrate hinge consists of a staple and a pivot arm. (a) Schematic of a substrate hinge. (b) SEM micrograph showing a substrate hinge fabricated using MUMPs.	4-24
4.21.	The floating substrate hinge is a modification of the substrate hinge that allows the staple to be held in place by either a slider or a pin-joint instead of anchors. The floating substrate hinge allows the fabrication of movable flip-up structures.	4-25
4.22.	(a) A flip-up mirror fabricated by the author using all three types of micro-hinges. (b) Close up of the scissors hinge connecting the two plates.	4-25
4.23.	A plate that has been flipped up off of the substrate.	4-26
4.24.	A flip-up helper.	4-27
4.25.	Close up view of a self engaging locking mechanism fabricated by the author. (a) In the original design, the end of the lock was contoured making it difficult to flip-up the plate. (b) Redesigning the plate removes the contours making it east to flip-up the plate.	4-28
4.26.	A Fresnel lens is raised 100 μm above the substrate using several flip-up plates connected by micro-hinges.	4-29
4.27.	A Fresnel lens is raised 100 μm above the surface of the substrate. The elevated lens can then be moved so that it is over another device that is fabricated on the surface of the substrate. The device shown here has been slid over a gold mirror.	4-30
4.28.	A mirror is flipped up and locked into a position normal to the substrate. The mirror is free to rotate 360 degrees around the pin joint while remaining normal to the substrate.	4-30
4.29.	Parallel plate actuators can be used to fabricate either a piston actuator (a), or a torsional actuator (b). The arrows indicate motion of the suspended plate when a voltage is applied to the electrodes.	4-32
4.30.	Comb resonators fabricated by the author using MUMPs (a), and LIGA (b).	4-33

Figure		Page
4.31.	Basic design of the lateral thermal actuator. Typical dimensions are: $t = 2.0 \mu\text{m}$, $w_h = 2.5 \mu\text{m}$, $w_c = 15 \mu\text{m}$, $l_f = 40 \mu\text{m}$, $l_c = 200 \mu\text{m}$, $s = 2.5 \mu\text{m}$. The $4 \mu\text{m}$ square dimples prevent stiction to the substrate. This actuator provides deflections of $16 \mu\text{m}$ at 3 V and 3.5 mA	4-34
4.32.	A lateral thermal actuator fabricated using MUMPs.	4-35
4.33.	A force, F , is applied to a beam that is rigidly supported on one end. The force is applied a distance, a , from the supported end of the beam. As a result, the beam deflects a distance, d , at the tip.	4-36
4.34.	Schematic of the force tester, the thickness, t , is uniform. Typical values are $w = 2.0 \mu\text{m}$, $a = 60 \mu\text{m}$, $l = 240 \mu\text{m}$, and $t = 2.0 \mu\text{m}$	4-37
4.35.	Scanning electron micrograph of a released force tester next to a thermal actuator. The force tester shown here has values $w = 2.0 \mu\text{m}$, $a = 25 \mu\text{m}$, $l = 125 \mu\text{m}$, and $t = 2.0 \mu\text{m}$. The actuator has parameters $t = 2.0 \mu\text{m}$, $w_h = 2.0 \mu\text{m}$, $w_c = 14 \mu\text{m}$, $l_f = 50 \mu\text{m}$, $l_c = 150 \mu\text{m}$, $s = 4.0 \mu\text{m}$	4-37
4.36.	Electrical power versus the delivered force. The actuators have parameters: $t = 2.0 \mu\text{m}$, $w_c = 14 \mu\text{m}$, $l_f = 30 \mu\text{m}$, $l_c = 170 \mu\text{m}$, $s = 2.0 \mu\text{m}$	4-39
4.37.	Maximum delivered force versus hot arm width. The actuators have parameters: $t = 2.0 \mu\text{m}$, $w_c = 14 \mu\text{m}$, $l_f = 30 \mu\text{m}$, $l_c = 170 \mu\text{m}$, $s = 2.0 \mu\text{m}$	4-39
4.38.	Maximum delivered force versus cold arm length. The actuators have parameters: $t = 2.0 \mu\text{m}$, $w_h = 2.0 \mu\text{m}$, $w_c = 14 \mu\text{m}$, $l_f = 30 \mu\text{m}$, and $s = 2.0 \mu\text{m}$	4-40
4.39.	Maximum delivered force versus arm separation. The actuators have parameters: $t = 2.0 \mu\text{m}$, $w_h = 2.0 \mu\text{m}$, $w_c = 14 \mu\text{m}$, $l_f = 50 \mu\text{m}$, and $l_c = 150 \mu\text{m}$	4-40
4.40.	Maximum delivered force versus flexure length. The actuators have parameters: $w_h = 2.0 \mu\text{m}$, $w_c = 14 \mu\text{m}$, $l_c + l_f = 50 \mu\text{m}$, and $s = 2.0 \mu\text{m}$	4-41
4.41.	Scanning electron micrograph of an array of six $210 \mu\text{m}$ long thermal actuators connected with a compliant yoke. The yoke combines the forces of the actuators and converts their arcing motions into a linear motion of the yoke. Actuators are wired in parallel. The array shown here is connected to a force tester.	4-42

Figure		Page
4.42.	Maximum delivered force versus number of actuators in an array. The actuators have parameters: $t = 2.0 \mu\text{m}$, $w_h = 2.0 \mu\text{m}$, $w_c = 14 \mu\text{m}$, $l_f = 50 \mu\text{m}$, $l_c = 160 \mu\text{m}$, and $s = 2.0 \mu\text{m}$. The linear projection is based on the force of an individual array multiplied by the number of actuators.	4-42
4.43.	The optimized actuator array shown here has 10 actuators that are each $230 \mu\text{m}$ long. The yoke design is similar to one developed by Comtois [4].	4-43
4.44.	Scanning electron micrograph of the scanning micromirror. The gold mirror surface is a square with $75 \mu\text{m}$ sides. The tether is $15 \mu\text{m}$ wide.	4-45
4.45.	Three of the assembled scanning micromirrors.	4-46
4.46.	Triangle formed by the mirror, substrate, and tether. C_1 is the length of the tether, C_2 is the length from the base of the mirror to the tether lock, and $L(v)$ is the length from the base of the mirror to the actuator array.	4-47
4.47.	A corner cube reflector fabricated using the scanning micromirror. . .	4-48
4.48.	The assembled lateral scanning mirror. The thermal actuators are $210 \mu\text{m}$ long. The gold coated mirror surface is $57 \mu\text{m}$ high by $108 \mu\text{m}$ wide.	4-50
4.49.	Teeth etched into the edge of the support plate interface with the motor drive.	4-51
4.50.	A flip rotating micromirror. The mirror surface is $100 \mu\text{m}$ square. The support plate has a radius of $110 \mu\text{m}$	4-52
5.1.	Illustration of the vibration isolation system with a STW resonator mounted on the isolated platform.	5-4
5.2.	Diagram of the top of the isolation system. Metal bonding pads are located on the top of the support rim and platform. Wires are patterned along the support arms to connect the bonding pads from the platform to the bonding pads on the support rim.	5-5
5.3.	Coordinate system for calculation of the STW mode shape and finite element analysis of the isolation platform.	5-6

Figure		Page
5.4.	The required computation time grows exponentially with the number of terms in the Floquet series.	5-7
5.5.	One quarter model finite element mesh.	5-8
5.6.	A 1 g acceleration is applied in the x_2 direction. After the calculating the deformations, the one quarter model is mirrored about two axes to generate a complete model.	5-9
5.7.	Convergence of the calculated acceleration sensitivity with respect to the number of sub-regions, m_1 , m_2 , m_3 . The percentage change is relative to the acceleration sensitivity calculated with the maximum value of sub-regions in the direction that is being evaluated.	5-10
5.8.	Model parameters for the silicon isolation system. Not shown, the system is of a uniform thickness, t	5-11
5.9.	The effect of support location on acceleration sensitivity. Data are presented for three different silicon thickness values.	5-12
5.10.	The effect of platform and support thickness on acceleration sensitivity.	5-12
5.11.	The effect of platform overhang on acceleration sensitivity. Note, inset = 0.8 mm.	5-13
5.12.	The effect of support width on acceleration sensitivity.	5-14
5.13.	The effect of support length on acceleration sensitivity.	5-14
5.14.	Model parameters of the single degree of freedom, damped, mass-spring system. M_0 is the mass of the isolated platform and the resonator, k_{sys} is the spring constant resulting from the support arms, and C is the viscous damping coefficient with two components, C_m and C_r as defined in Chapter III.	5-15
5.15.	The platform is suspended by the springs a distance, d , above the substrate.	5-17
5.16.	Schematic view of the modified resonator design.	5-19
5.17.	The modified design of the isolation system. The cut away views on the right and the bottom run along the dotted lines of the top view. .	5-20
5.18.	Expected absolute transmissability of the micromachined vibration isolation system for several different plate separation values, d	5-21

Figure		Page
5.19.	Expected vibration sensitivity of the STW resonator mounted on the vibration isolation platform for several values of plate separation, d . .	5-22
6.1.	Overview of the fabrication process.	6-2
6.2.	The pattern used for the back side oxide mask is shown here.	6-4
6.3.	The pattern used for the front side oxide mask. Dark regions remain protected while light regions are etched.	6-4
6.4.	The pattern used for the metal mask. The dark areas represent the regions where metal is deposited on the wafers. The bond pads on the support rim are $250\text{ }\mu\text{m}$ by $500\text{ }\mu\text{m}$ while the bond pads on the platform are $200\text{ }\mu\text{m}$ by $500\text{ }\mu\text{m}$. The wires are $30\text{ }\mu\text{m}$ wide.	6-5
6.5.	Profile of the oxide etch. The etch depth of $2.4\text{ }\mu\text{m}$ corresponds with the oxide thickness as expected.	6-8
6.6.	Profile of the wafer after a 15 minute etch in KOH. Hillocks that formed during the etch are visible on the bottom of the etched surface. The formation of the hillocks did not noticeably effect the etch.	6-9
6.7.	Photograph of a wafer following the KOH etch. The rough appearance of the etched regions is due to the formation of hillocks on the etched surface.	6-10
6.8.	The device wafer is attached to the handle wafer using positive photoresist as an adhesive layer. The device wafer overhangs the edge of the handle wafer by 2-3 mm to facilitate the alignment of the front side oxide mask.	6-10
6.9.	Profile of the wafers following the metalization. The metal layer is approximately $2700\text{ }\text{\AA}$ while the oxide is approximately $9000\text{ }\text{\AA}$	6-12
6.10.	A photograph of the fabricated isolation system with a STW resonator bonded on the platform.	6-14
7.1.	The isolated resonator is mounted on the end of the oscillator. One side of the isolator overhangs the edge of the oscillator substrate by approximately 1 mm. (a) The top view shows the position of the isolator, and the bonding, while (b) a side view shows how the overhang was secured with epoxy.	7-1

Figure		Page
7.2.	The signal loss across two support arms shorted together with a bonding wire showed 36.7 dB of loss.	7-3
7.3.	The wires on the support arms were bypassed by directly bonding from the oscillator circuit to the STW resonator.	7-4
7.4.	Impedance matching of the STW resonator to the oscillator circuit. (a) Looking into the STW resonator. (b) Looking into the oscillator circuit.	7-4
7.5.	Magnitude and phase of the oscillator loop.	7-5
7.6.	The output spectrum of the oscillator. The center frequency is at 1.0001042 GHz, and the noise close to the carrier is over 70 dB below the peak at the center frequency. The plot has a frequency span of 100 kHz.	7-5
7.7.	To provide a larger gap and decrease the damping, a spacer was placed in between the isolation platform and the substrate. The spacer is simply the support rim of an isolation platform with the isolation platform removed.	7-6
7.8.	Vibration of the oscillator results in vibration induced sidebands in the frequency spectrum. Here a 1 g vibration at a frequency, $f_v = 2250$ Hz is applied to the oscillator. The vibration is normal to the surface of the resonator. The plot has a span of 6 kHz.	7-7
7.9.	Measured vibration sensitivity of the baseline oscillator.	7-9
7.10.	Measured vibration sensitivity of oscillator 1. The vibration sensitivity of the baseline oscillator is shown for comparison.	7-9
7.11.	Measured vibration sensitivity of oscillator 2.	7-10
7.12.	Measured vibration sensitivity of oscillator 3.	7-11
7.13.	Predicted vibration sensitivity for an isolated resonator with the isolation platform separated from the oscillator substrate by 25 μm compared with the measured vibration sensitivity of oscillator 1. The measured values, x's and o's, were measured with a vibration with a 0.5 g magnitude.	7-12

Figure		Page
7.14.	Predicted vibration sensitivity for an isolated resonator with the isolation platform separated from the oscillator substrate by 20.5 μm compared with the measured vibration sensitivity of oscillator 1. The measured values, x's and o's, were measured using vibrations of 0.5 g magnitude.	7-13
7.15.	Predicted vibration sensitivity compared with measured vibration sensitivity. The two solid curves are the predicted sensitivity for isolation platforms separated from the oscillator substrate by 20.5 μm and 25 μm . The o's show the vibration sensitivity of the oscillator to a 3 g vibration, while the x's show the measured sensitivity to a 1 g vibration.	7-14
7.16.	Measured vibration sensitivity of oscillator 2 compared with the predicted vibration sensitivity. Predicted curves for 25 μm and 36 μm separations are presented. Measured values were taken with 1 g, o's, and 3 g, x's, vibrations.	7-15
7.17.	Measured vibration sensitivity of oscillator 3 compared with the predicted vibration sensitivity. The predicted curve is for an isolator with 450 μm between the oscillator substrate and the isolation platform. Measured data was taken using vibrations of 1 g magnitude.	7-15
A.1.	EDP etching setup.	A-2

List of Tables

Table		Page
2.1.	SAW Parameters of Selected Piezoelectric Substrates [24].	2-3
3.1.	Types of Damping and the resulting damping force, F_D [58].	3-6
4.1.	Properties of Anisotropic Silicon Etchants.	4-4
4.2.	Structural and Sacrificial Layers Used in Surface Micromachining. . .	4-13
4.3.	Desired Actuator Criteria	4-31
5.1.	Maximum Displacement Resulting from a 1 g Simple Harmonic Vibra- tion of Frequency, f	5-2
5.2.	Calculated Mass-Spring Model Parameters for the Final Isolation Sys- tem Design	5-21
6.1.	Fabrication Process Requirements	6-1
8.1.	Additional MEMS Devices Fabricated During This Research.	8-2

Abstract

Microelectromechanical systems (MEMS) is a rapidly expanding field of research into the design and fabrication of actuated mechanical systems on the order of a few micrometers to a few millimeters. MEMS potentially offers new methods to solve a variety of engineering problems. A large variety of MEMS systems including flip-up platforms, scanning micromirrors, and rotating micromirrors are developed to demonstrate the types of MEMS that can be fabricated. The potential of MEMS for reducing the vibration sensitivity of surface acoustic wave and surface transverse wave resonators is then evaluated. A micromachined vibration isolation system is designed and modeled. A fabrication process utilizing two sided anisotropic etching of {110} silicon wafers is developed. The process utilizes standard microelectronic fabrication equipment to batch fabricate the isolation systems. The fabricated systems are only 1 cm \times 1 cm \times 1 mm. Several oscillators are fabricated using commercially fabricated STW resonators mounted on the isolation systems. The resonators are driven by their standard oscillator circuit. Incorporating the isolation system into the oscillator does not result in an appreciable increase the size or the weight of the oscillator. Testing of the oscillators shows that the isolators successfully function as passive vibration isolation systems.

MICROELECTROMECHANICAL ISOLATION OF ACOUSTIC WAVE RESONATORS

I. Introduction

Microelectromechanical systems (MEMS) is a rapidly developing field. MEMS is the study of mechanical systems on the order of micrometers to millimeters with individual components having dimensions on the order of a few micrometers. The mechanical systems are actuated by a variety of mechanisms typically relying on electromagnetic forces. The field borrows much from the microelectronics industry, including both processing equipment and techniques. More recently, new fabrication techniques, unique to MEMS have been developed. Initially, MEMS devices were primarily novelty items such as microgears or cantilevers. However, advances in the field have led to several commercial applications including pressure sensors, accelerometers, ink jet nozzles, and projection displays. The research in this dissertation evaluates potential applications of MEMS for use in an entirely new area. This chapter presents the purpose of this research, a summary of what has been done, and an overview of this document.

1.1 Problem Statement

Vibration of surface acoustic wave (SAW) and surface transverse wave (STW) resonator based oscillators results in a variation of oscillator output frequency. In operational environments, these vibration induced frequency shifts are the primary source of noise close to the carrier frequency [1]. This noise limits system performance in many applications including the ability of Doppler radar to detect slow moving targets. With rigid printed circuit board designs and solid state electronic components, the SAW/STW resonator has become the primary source of frequency variation in SAW/STW resonator based oscillators [2]. The vibration applies a time dependent acceleration on the resonator. As a result of the acceleration, the resonator mount applies body forces to the resonator which result in the deformation of the resonator [3]. This deformation is responsible for variations in the

dimensions and effective material constants of the piezoelectric crystal resulting in a change in resonator transimpedance, and thus a change in the oscillator output frequency [2, 3].

Reducing the sensitivity of the oscillator to vibration can be done by either reducing the magnitude of the vibration or controlling the resonator deformation such that a minimum frequency shift is achieved. The magnitude of the vibration can be reduced through the use of a mechanical vibration isolation system. Control of the resonator deformation requires careful design of the resonator mounting system. While research has been progressing for several decades, the need for a process for fabricating small, low cost, low vibration sensitivity SAW/STW resonators exists [2]. *The research in this dissertation looks at the application of MEMS to reducing the vibration sensitivity of the SAW/STW resonator. This research covers the design, fabrication, and testing of a vibration isolation system for the SAW/STW resonator.* This research was supported by the Army Missile Command through Army Research Lab in order to evaluate if MEMS can provide a viable system for use in missile seeker systems. In particular, it is desired to fabricate a low cost system that does not significantly increase the size or weight of fixed frequency and voltage controlled oscillators. This research is the first attempt to design and fabricate a micromachined vibration isolation system for SAW/STW resonators. Therefore, this dissertation aims to answer several fundamental questions:

- 1) Can a micromachined system be built around SAW/STW resonators?
- 2) Can a micromachined system be reliably manufactured in large quantities at low cost?
- 3) Can a micromachined isolation system successfully reduce the vibration sensitivity of SAW/STW resonators?
- 4) Can a micromachined system be incorporated with existing oscillators without significantly increasing the size or weight of the oscillator?
- 5) What areas should future research focus on in the design of a micromachined vibration isolation system?

These questions are answered with the design, fabrication, and testing of a micromachined vibration isolation system. The isolation system is designed around a commercially avail-

able 1 GHz STW resonator. A process for fabricating the system was developed. The process provides the batch fabrication of isolation systems allowing the cost of the devices to be spread over a large number of fabricated units. Several STW resonators mounted on the fabricated micromachined vibration isolation systems were mounted to existing oscillator circuits. The fabricated systems clearly show that a micromachined vibration isolation system can be cheaply fabricated. Further, the isolation system does not significantly increase the size or the weight of the oscillator. The isolated resonators exhibit vibration sensitivity curves consistent with the isolation provided by a passive vibration isolation system. This research shows the potential of micromechanical systems for reducing vibration sensitivity. Areas for future research are discussed in the last chapter of this dissertation.

1.2 Research Accomplishments

A large amount of research was done both in the development of a micromechanical vibration isolation system, and in more general studies of the types of devices that can be fabricated using a commercial foundry MEMS process. Utilizing the multi-user MEMS processes (MUMPS), the author designed and fabricated a variety of MEMS. This work included the characterization, optimization, and application of a lateral thermal actuator that was originally designed by Comtois [4]. The following is a list of some of the significant results of the author's research using MUMPS:

- Extensive measurements were taken of the force generated by lateral thermal actuators with respect to the actuator design parameters. These studies showed that minor variations in the design parameters can more than double the force delivered by the actuator without a significant reduction in the actuator deflection.
- An optimized thermal actuator and array were implemented, and test cells to fully characterize the new designs were fabricated.
- Complex flip-up structures using micro-hinges were designed and fabricated. The structures include mirrors, lenses, and gratings at various angles to the substrate. Flip-up platforms were designed to allow devices to be suspended parallel to the

substrate at a distance from a few microns to over 100 microns above the substrate. Further, flip-up systems capable of moving either rotationally or laterally were developed.

- A new class of flip-up components that directly couples the motion of thermal actuator arrays to flip-up mirrors was created. Two separate designs were developed including a scanning micromirror that modulates the angle between the mirror and substrate according to an applied control voltage, and a second design that flips up into a position normal to the substrate and allows the actuators to rotate the mirror around a pin joint according to an applied control voltage.
- Rotating flip-up micromirrors driven by a thermal actuator based micromotor were developed. The mirrors rotate through 360 degrees around a pin joint. Both large mirrors capable of being electrically rotated through 180 degrees and smaller mirrors capable of being electrically rotated through 360 degrees were designed and fabricated.
- Many of these results were included in scholarly publications [5]-[9].

The main focus of this research, however, was on the design, fabrication, and testing of a micromachined isolation system for SAW/STW resonators. The research presented here demonstrates that such a system is possible and shows the potential of this type of system for reducing the vibration sensitivity of SAW/STW resonator based oscillators. The primary accomplishments of this work are:

- Modeling of the basic isolation platform using finite element analysis. Code developed by Stewart [10], was used to predict the acceleration sensitivity of the isolated resonators. This analysis provided a better understanding of the function of the isolation system, and illustrates some of the advantages and disadvantages of the MEMS approach.
- Modeling of the basic isolation system as a damped mass-spring system. The model successfully predicts the resonance frequency of the system and the general shape of the vibration sensitivity curve of the isolated STW resonators that were tested.

- A fabrication process utilizing two sided etching of {110} silicon wafers was created. The process provides a method for the batch fabrication of the isolation platforms, therefore allowing overhead costs to be shared across a large number of devices. The process requires only common microelectronic processing equipment and can thus be performed in most semiconductor processing facilities.
- The fabrication process was used to fabricate over 100 isolation platforms. Over 20 STW resonators were successfully mounted on the isolation platforms. This is the first time that such a system has been fabricated for the purpose of providing vibration isolation for SAW/STW resonators.
- Isolated resonators were connected to 4 proprietary oscillators provided by SAWTEK, Inc. The oscillators required only minor modifications for the STW resonators to be mounted. This illustrates that micromachined isolation systems can be used with existing technologies, thus keeping the cost of incorporating a micromachined isolation system low. All four oscillators were successfully operated, and vibration sensitivity measurements were taken from three of the oscillators.
- Early results of this research have been published [11], and more recent results have been submitted for publication [12].

1.3 Organization of this Dissertation

This dissertation is organized into eight chapters. Following this chapter, background is provided for the major areas that this research draws on. Namely, Chapter II provides a discussion of surface acoustic wave and surface transverse wave oscillators and provides a basic analysis of acceleration sensitivity. Chapter III discusses vibration isolation, and Chapter IV provides a discussion of microelectromechanical systems. Chapter IV also includes discussion of the major MEMS fabrication processes, and presents many of the devices that were fabricated by the author during the course of this research. Following the background the document presents the design, fabrication, and testing of the vibration isolation system. Chapter V presents the system design and modeling. Chapter VI details the fabrication process that was developed. Chapter VII gives the test set up and exper-

imental results. Finally, the document concludes with a summary and recommendations for future research.

Several terms used throughout this dissertation have similar but distinct meanings. These terms, acceleration sensitivity, vibration sensitivity, oscillator, oscillator circuit, and resonator are defined here for clarity. Acceleration sensitivity is the sensitivity of the oscillator to an acceleration. The acceleration can be either steady state such as gravity, or time dependent such as a vibration. Vibration sensitivity, however, is the sensitivity of the oscillator to vibration only. The oscillator is defined as a complete fixed frequency or voltage controlled oscillator including all circuitry and the crystal resonator. The electronic drive circuitry of the oscillator is referred to as the oscillator circuit, while the crystal resonator is referred to as the resonator.

II. Acceleration Sensitivity in Surface Acoustic Wave and Surface Transverse Wave Oscillators

The mathematical framework for surface elastic waves dates back to Lord Rayleigh in the 19th century [13]. However, it was not until the introduction of the inter-digital transducer (IDT) in the 1960's that Rayleigh type surface acoustic wave (SAW) devices became practical for use in electronic circuits [14]. Due to their high quality factor and small size, SAW devices quickly found applications as oscillators in a variety of military equipment such as Doppler radars and radio systems [15, 16]. Since their initial uses in military systems, SAW devices have become popular for a large number of other applications [17]. In particular, SAW devices have been used as resonators and filters in a variety of circuits. Notable among these is their use as stable fixed frequency and voltage controlled oscillators.

Since initially being demonstrated in 1976 [18], the surface transverse wave (STW) has been widely studied. Surface transverse wave devices offer several primary advantages over SAW devices including: decreased surface sensitivity, increased power handling ability, higher frequency operation than SAW resonators with the same dimensions, and lower device phase noise. Unfortunately, difficulties with fabricating STW oscillators with sufficiently high Q values have limited their use in commercial applications [19, 20].

Recently, both SAW and STW resonators have been designed with high long term frequency stability, low phase noise levels, and low temperature sensitivity [16], [20]-[22]. However, the resonators are sensitive to accelerations caused by mechanical vibrations that are introduced by mobile platforms such as tanks, planes, or missiles. Research has proceeded for several years into determining the cause of acceleration sensitivity and providing a solution. Significant improvements have been made enabling the design of devices with acceleration sensitivities on the order of $10^{-10}/g$ (where $1g$ is the acceleration due to gravity, or 9.8 m/s^2) [22, 23]. However, current requirements call for devices with acceleration sensitivities on the order of $10^{-12}/g$ [15]. Further, the cost, size, and limited reproducibility of many designs limit their use in applications such as missiles where a large number of devices are required and space is limited.

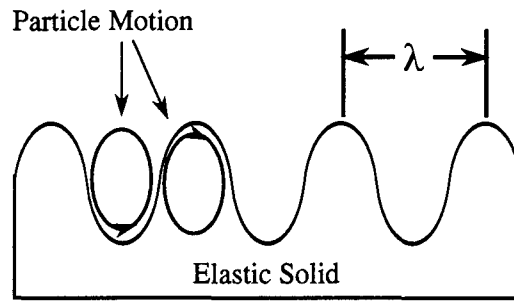


Figure 2.1. Rayleigh type waves at the surface of an elastic material.

2.1 Surface Acoustic Waves

Surface elastic waves were originally studied by Lord Rayleigh in conjunction with his studies of earthquakes. He theorized and showed mathematically that waves could propagate along the free surface of an elastic solid [13]. The existence of these waves in earthquakes was later verified. As seen in Fig. 2.1, the wave is created by an elliptical motion of the particles at the surface of the solid. The motion of the particles is greater in the direction normal to the surface of the solid than it is in the direction parallel to the surface. The depth of the wave into the solid is on the order of the wavelength, λ . In crystals, the motion of the wave is more complex than that described here. However, by choosing specific crystal cuts it is possible to get a wave as shown.

Although the existence of SAWs was known for several decades, it was not until 1965, with the introduction of the IDT [14], that SAW devices could be easily fabricated and incorporated with electrical systems. The basic IDT, shown in Fig. 2.2, consists of a series of intertwined metal fingers deposited on the surface of a piezoelectric material such as quartz. Placing an electrical potential between the fingers causes stresses in the piezoelectric material. By driving the metal fingers with a periodic electric potential, a SAW is launched on the crystal. The frequency of the SAW wave is determined by the input signal, however, maximum power coupling occurs when the IDT fingers are spaced by a distance of $\lambda_0/2$ from center to center, where λ_0 is the wavelength of the SAW.

The amount of energy that is coupled into the substrate depends on several factors. These include design factors such as the finger spacing and width, and material factors such as the crystal type and cut. For material properties, the primary measure of electrical

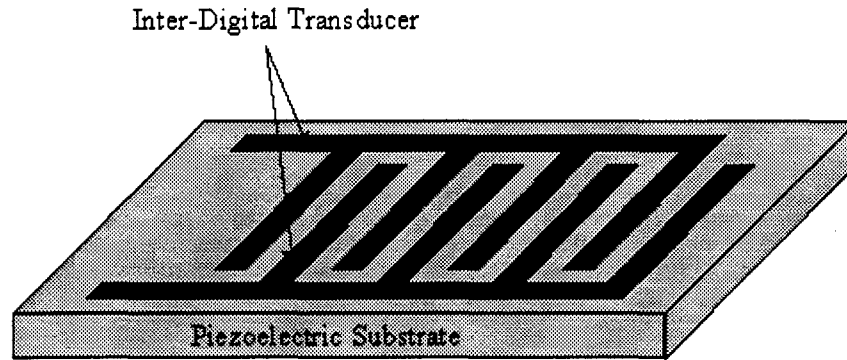


Figure 2.2. An inter-digital transducer on top of a piezoelectric substrate.

Table 2.1. SAW Parameters of Selected Piezoelectric Substrates [24].

Material	Crystal Cut	SAW Axis	Velocity v (m/s)	K^2 (%)	Temperature Coefficient of Delay (ppm/°C)	Applications
Quartz	ST	X	3158	0.11	0	Oscillators, filters
LiNbO ₃	Y	Z	3488	4.5	+94	Wideband filters
LiNbO ₃	128°	X	3992	5.3	+75	Wideband filters
Bi ₂ GeO ₂₀	<110>	<001>	1681	1.4	+120	Long delay lines
LiTaO ₃	Y	Z	3230	0.72	+35	Oscillators
*GaAs	<001>	(110)	<2841	<0.06	≈-49	Semiconductor Integrated Circuits

*Most useful cut for SAW with maximum K^2 on GaAs.

to mechanical coupling is the electromechanical coupling coefficient, K^2 . This is defined as [24]

$$K^2 = \frac{e^2}{c\epsilon} \quad (2.1)$$

where e is the piezoelectric coefficient, c is the elastic constant, and ϵ is the dielectric permittivity of the material. Table 2.1 provides information on several piezoelectric substrates commonly used for SAW devices. Despite its relatively low electromechanical coupling coefficient, quartz is the most widely used material for SAW devices. This is due to several factors including wide availability of quartz, its low cost, and its low thermal coefficient of delay at room temperature for certain cuts.

2.2 SAW Resonators

A resonator is formed by placing a transducer in between two reflectors. A traveling wave launched by the transducer is reflected back upon itself by the reflectors. For certain waves, the reflected components add coherently with the original wave resulting in a standing wave. This occurs only for waves having a wavelength that is a divisor of the cavity length. Waves with longer or shorter wavelengths will not add coherently and rapidly dissipate.

2.2.1 SAW Reflectors. The fabrication of a SAW resonator begins with the design of an acoustic wave reflector. When a SAW encounters an abrupt junction in the surface, part of the wave is reflected. Therefore, by using either a metal strip on top of the substrate or a slit cut into the substrate the SAW can be partially reflected. It is also possible to combine both a slit and a metal strip to form a reflective element.

At the edge of the reflective element, part of the wave is reflected back in the direction it originated from, part of the wave is reflected into the bulk of the substrate, and part of the wave is transmitted past the reflective element. The reflectivity of the element is specified as r . This value is dependent upon the substrate and metal material properties, as well as the metal strip thickness and SAW wavelength [25]. The value of $|r|$ is typically small with $|r| \approx 0.01$. The energy reflected into the bulk is negligible [26]. The transmission, t , accounts for the remaining energy of the wave such that $|r|^2 + |t|^2 = 1$.

Since the reflected energy is so low, it is necessary to use an array of reflectors to reflect the majority of the wave. Typically, the array is formed by an array of metal strips as seen in Fig. 2.3. As can be seen, the spacing between the individual strips is $\lambda_0/2$. With this spacing, reflected waves of frequency $f_0 = v/\lambda_0$ add coherently, while waves that are not at f_0 are not completely in phase and thus are reduced in magnitude. The total amount of the wave energy that is reflected at the resonant frequency, f_0 , has been derived as $R \approx \tanh^2(N|r|)$, where r is the reflectivity of an individual reflector and N is the number of reflectors [25]. For $N|r| \gg 1$, R approaches unity. The reflective grating can then be approximated as a mirror reflecting the wave at a distance, L_p , from the leading edge of the reflector grating. This value is important in determining the effective cavity

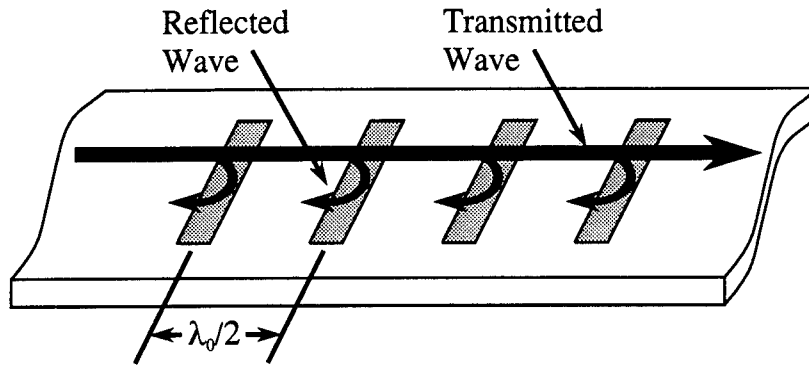


Figure 2.3. Schematic of a SAW reflective grating.

length of a resonator. L_p can be approximated as [25]

$$L_p = \frac{\lambda}{|r|} \quad (2.2)$$

2.2.2 One and Two Port SAW Resonators. One port SAW resonators are created by placing a single IDT in between two reflective gratings such that the gratings are normal to the SAW launched by the IDT. A two port SAW resonator is formed by replacing the single IDT with two IDT's in a delay line configuration. Figure 2.4 shows schematic diagrams of both types of resonators with their equivalent RLC circuit representations. The equivalent RLC circuit models are accurate in the region near the resonant frequency [26]. The parameters R , C , and L are primarily functions of the reflective grating design and material properties, while the transducer capacitances C_t , C_{it} , and C_{ot} are functions of the IDT designs. Datta provides a discussion of the calculation of the values of the equivalent circuits [25].

Two port resonators are inherently easier to use in circuit applications because the series resonant arm is not shunted by the transducer capacitance [25]. Since two port resonators are typically used for oscillator applications, the remaining discussion will focus solely on two port resonators.

The size of a SAW resonator depends upon the frequency of the device. With 2 reflective gratings typically having 200 to 400 reflective elements spaced $\lambda_0/2$, the device must be approximately 400λ long. As an example, consider a 350 MHz SAW device

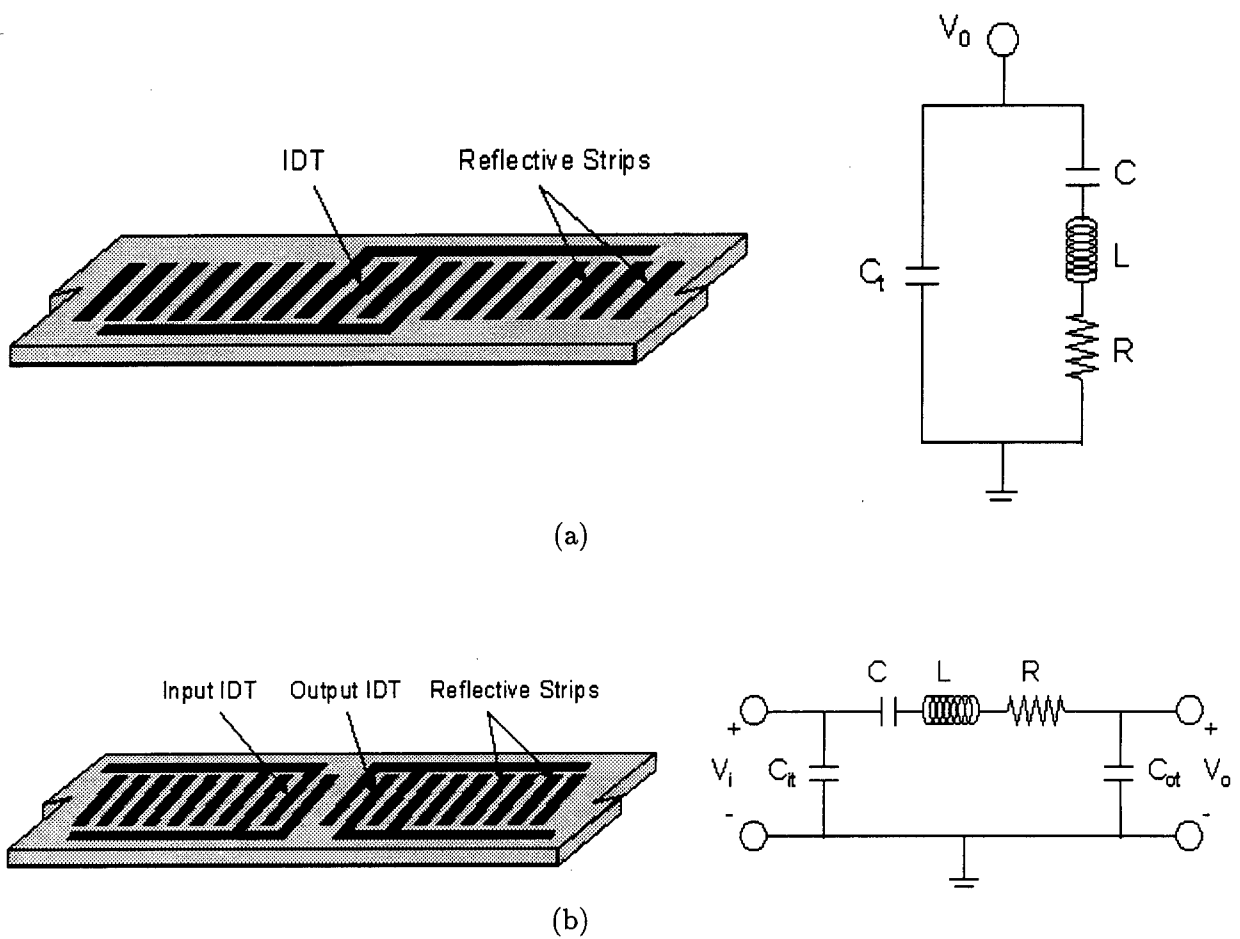


Figure 2.4. One and two port SAW resonators and their equivalent circuit models.
 (a) One port resonator (b) Two port resonator.

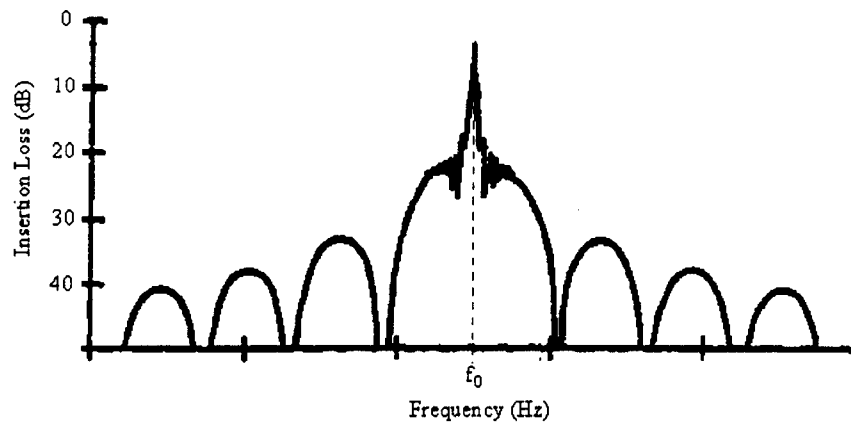


Figure 2.5. Frequency response of a two port SAW resonator [27].

on an ST-cut quartz substrate. The wave travels with a velocity, $v = 3158$ m/s. The wavelength is then computed as $\lambda_0 = v/f_0 = 9.02 \mu\text{m}$. Therefore, the device must be approximately 400λ or 3.6 mm in length. Note, higher frequency devices are shorter, while lower frequency devices are longer. Practical SAW resonators are limited to a frequency range from around 50 MHz up to approximately 1 GHz. The lower frequency devices are limited by the cost incurred due to the large size. The higher frequency devices are limited by the resolution of the IDT fingers and the attenuation of the wave due to viscous damping. For SAW devices, viscous damping causes the maximum Q to decrease with the square of the frequency [25, 26].

The performance of a SAW resonator is characterized by the input and output impedance, the insertion loss, the center frequency of the device, and the Q value. Figure 2.5 shows the expected response of a two port SAW resonator. Typical SAW devices have insertion losses of 8 to 10 dB. The center frequency for SAW devices is generally from 50 MHz to 1 GHz. In comparison to solid state RLC-resonator circuits SAW devices offer very high Q values. Typically unloaded SAW Q values are on the order of 10^3 to 10^5 .

2.3 Surface Transverse Wave Devices

In 1977, Yen, *et al.*, demonstrated that a shear horizontal (SH) bulk wave could be launched using an IDT [28]. The shear horizontal bulk wave is an acoustic wave that propagates at a shallow angle into the substrate. The wave deforms the crystal in a

direction normal to the direction of propagation, but parallel to the surface. These waves, generally referred to as surface skimming bulk waves (SSBW), generated a large deal of interest because they propagate approximately 1.6 times faster than a SAW. Unfortunately, the majority of energy is transmitted into the bulk, and is thus lost.

Several researchers suggested that a corrugated surface or a metal grating could be used to trap the wave near the surface of the substrate [18], [29]-[31]. The confined wave propagates parallel to the surface of the substrate, and thus the wave energy can be transmitted to another IDT without a high loss. In 1987, Bagwell and Bray successfully demonstrated this with the fabrication of a 1.7 GHz shear horizontal wave resonator having an unloaded Q of 5600 [19]. This type of wave is generally referred to as a surface transverse wave (STW), or a guided Bleustein-Gulyaev wave.

Surface transverse wave devices offer several advantages over SAW devices [32]. First, STWs propagate approximately 60% faster than Rayleigh type waves. This means that STW devices with the same dimensions as SAW devices operate at higher frequencies. Second, STW devices exhibit at least 2 orders of magnitude higher radio frequency power handling capabilities [32]. This is believed to be due to the fact that crystal strain from a STW occurs near but not at the crystal surface [32]. Third, STW devices have lower residual $1/f$ phase noise. Fourth, since the STW causes strain below the surface, the effects of surface contamination are reduced. It is believed that this may lead to decreased aging effects. Finally, STW devices offer higher intrinsic Q values than SAW devices [32].

Surface transverse wave resonators have not been used as widely as SAW resonators due primarily to the difficulty in fabricating quality resonators. The primary difficulty lies in the fact that the performance of STW devices is dependent not only on the device geometry, but also on how well the STW is trapped to the surface [33]. Recently, however, several resonators have been developed using surface transverse waves [20, 28, 34, 35]. Further, resonators with center frequencies in the 2-3 GHz have been fabricated [33, 36]. Surface transverse wave resonators typically have insertion losses of approximately 6-8 dB [20], while Q values are on the order of 10^3 to 10^4 [19]. Acceleration sensitivity of the resonators varies with several factors, but Almar and Cavin have reported on 1 GHz STW oscillators with acceleration sensitivities around 2 to 3×10^{-10} per g [22, 35].

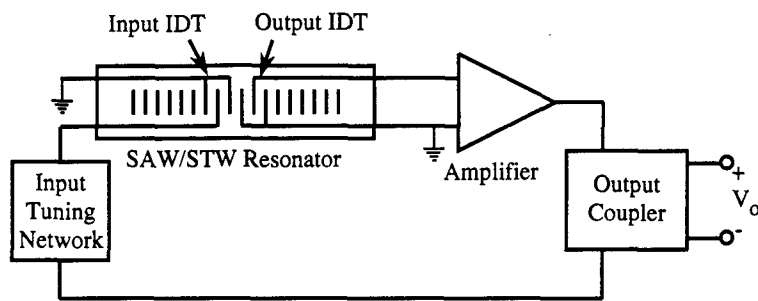


Figure 2.6. General design of a SAW/STW oscillator circuit.

2.4 SAW/STW Fixed-Frequency Oscillators

Figure 2.6 shows a simplified circuit for a SAW/STW based oscillator. The circuit begins with a SAW/STW resonator. The output signal of the resonator is amplified, coupled to the output, phase matched with a tuning circuit, and then connected to drive the input of the resonator. Design details for SAW/STW oscillators can be found in references [21, 37].

There are two primary concerns in the design of the oscillator circuit. First, the loop of the circuit should provide a 2-4 dB net power gain. Therefore, the amplifier must provide enough gain to overcome the insertion loss of the SAW/STW resonator and an additional 2-4 dB of gain. This allows the functioning oscillator to settle into a state where the net loop gain is exactly 1 so that the output level remains constant. The additional gain ensures that the oscillator can operate over a range of environmental conditions. Second, the net loop phase delay must be $2\pi n$, where n is an integer value. Any variation in the phase of the resonator or the tuning circuit will result in a change in the output frequency of the oscillator.

The construction of an oscillator circuit can be done using commercially available parts. A low noise amplifier with adjustable gain up to 20 dB and a 20 dB isolated coupler can be directly purchased from several electronic supply companies. A tuning circuit for phase matching can be constructed with standard LC components. Variable capacitors and inductors are used to allow the device to be tuned as needed. Using voltage controlled components allows the network to be tuned electronically, and also allows the design of voltage controlled oscillators.

The performance of the crystal based oscillator is affected by a variety of sources. Long term effects such as aging and radiation lead to a change in the center frequency over time. Shock, acceleration, vibration, and temperature lead to a short term variation of the center frequency of the resonator. In a non-laboratory environment, vibration induced acceleration effects are the primary source of oscillator noise [38].

2.5 Acceleration Sensitivity in SAW/STW Based Oscillators

Applications such as Doppler radars and communications devices require precision fixed frequency oscillators [15, 16, 39]. Variations in the oscillator frequency can undermine the performance of these systems. Unfortunately, mobile platforms such as automobiles, planes, missiles, and satellites, are constantly vibrating. These vibrations induce a time dependent acceleration on the oscillator circuit.

It has been known for several decades that accelerations can cause variations in the center frequency of fixed-frequency oscillators [40]. Advances in solid state electronics have left the crystal resonator as the primary source of acceleration induced frequency variation in crystal based oscillator circuits. After a decade of work, it is still difficult to design reproducible quartz based resonators with good acceleration sensitivity (less than $10^{-10}/g$) [2, 40].

This section provides a background on the problem of acceleration sensitivity in quartz based resonators. Detailed derivations of the causes of acceleration sensitivity are very mathematically intense and are not needed for the research described in this dissertation. Therefore, they are not included in this document. Mathematical analysis of acceleration sensitivity is initially discussed by Baumhauer and Tiersten [41], while further analysis has been provided in a number of papers [3], [42]-[46]. In the following discussion, the problem of acceleration sensitivity is first evaluated with respect to frequency variation in the crystal based oscillator and then with respect to variations caused by the crystal resonator. This is followed by the derivation necessary for determining the acceleration sensitivity, $\bar{\Gamma}$, from experimental data. The majority of the information in this discussion summarizes the analysis presented in papers by Filler [39], Kosinski [2, 47, 48], and Vig [1, 38].

2.5.1 Acceleration Induced Frequency Shifts. Experimental studies have shown that the acceleration induced frequency shift in a crystal controlled, fixed frequency oscillator is proportional to both the magnitude of the acceleration and the direction of the acceleration relative to the crystal coordinate system [49]. It was subsequently shown that the acceleration sensitivity of quartz resonators is a vector quantity [50]. The change in frequency due to acceleration can be described by the vector equation

$$\delta f = f_0(\vec{\Gamma} \cdot \vec{a}) \quad (2.3)$$

where δf is the frequency shift, f_0 is the center frequency of the resonator, $\vec{\Gamma}$ is the acceleration sensitivity vector of the crystal resonator, and \vec{a} is the applied external acceleration [2]. For commonly experienced accelerations, $|\vec{\Gamma}|$ is independent of $|\vec{a}|$ [39]. By defining a three dimensional coordinate system with axes i , j , and k , the quantity $\vec{\Gamma} \cdot \vec{a}$ can be transformed into the scalar equation

$$\vec{\Gamma} \cdot \vec{a} = \Gamma_i a_i + \Gamma_j a_j + \Gamma_k a_k \quad (2.4)$$

Each component is independent, and therefore the problem of acceleration sensitivity can be examined with respect to each axis independently (i.e. the problem is linearly separable). Also, if \vec{a} is normal to $\vec{\Gamma}$ the frequency shift is zero.

From Eq. 2.3 it can be seen that the frequency shift can be decreased by reducing either $|\vec{\Gamma}|$ or $|\vec{a}|$. In terms of designing the oscillator, $|\vec{a}|$ can not be changed, and therefore an understanding of $|\vec{\Gamma}|$ is necessary. However, mechanical isolators have been used to reduce the magnitude of vibration induced accelerations. Much of the work detailed in this dissertation focuses on the design, fabrication, and testing of mechanical isolation systems.

2.5.2 Effect of Acceleration on the Oscillator. The effect of acceleration on the oscillator is dependent upon the type of acceleration which is dependent upon the source. Common causes of oscillator acceleration are gravity, motion, and vibration.

A steady state acceleration results in a frequency shift according to Eq. 2.3. As long as the acceleration does not change, the frequency of the oscillator will remain stable.

Changing the angle between the oscillator and the acceleration results in a change in the center frequency of the oscillator. This can be observed using the effect of gravity on an oscillator. At rest, gravity results in a normal acceleration applied to the oscillator. As the oscillator is rotated through 360° the center frequency of the oscillator changes. This is caused because the gravity continually applies a $1g$ acceleration in one direction. As the oscillator is rotated, the direction of the acceleration vector relative to $\vec{\Gamma}$ changes. When the oscillator has been rotated 180° , the effect is a change in the applied acceleration by $2g$. Therefore, the test is often referred to as a "2g tipover".

A vibration of the oscillator at a single frequency, f_v , results in the application of a sinusoidal acceleration to the oscillator at the same frequency. To determine the effect of a single frequency vibration consider the acceleration

$$\vec{a} = \vec{A} \cos(2\pi f_v t) \quad (2.5)$$

where \vec{A} is the peak acceleration vector, f_v is the frequency of vibration, and t is the time. The perturbed frequency of the oscillator is defined as

$$f(\vec{a}) = f_0 + \delta f \quad (2.6)$$

Combining Eqs. 2.3, 2.5, and 2.6 yields

$$f(\vec{a}) = f_0 \left(1 + (\vec{\Gamma} \cdot \vec{A}) \cos(2\pi f_v t) \right) \quad (2.7)$$

Then, by defining $\Delta f = \max(\delta f)$ to be the maximum frequency shift, or

$$\Delta f = f_0 (\vec{\Gamma} \cdot \vec{A}) \quad (2.8)$$

and substituting this into Eq. 2.7 results in

$$f(\vec{a}) = f_0 + \Delta f \cos(2\pi f_v t) \quad (2.9)$$

The output voltage of the oscillator is defined as

$$V(t) = V_0 \cos(\phi(t)) \quad (2.10)$$

where the phase $\phi(t)$ is derived from the frequency as

$$\phi(t) = 2\pi \int_{t_0}^t f(x) dx \quad (2.11)$$

Solving for $\phi(t)$ using Eqs. 2.9 and 2.11 yields

$$\phi(t) = 2\pi f_0 t + \left(\frac{\Delta f}{f_v} \right) \sin(2\pi f_v t) \quad (2.12)$$

This is substituted into Eq. 2.10 to get

$$V(t) = V_0 \cos \left(2\pi f_0 t + \left(\frac{\Delta f}{f_v} \right) \sin(2\pi f_v t) \right) \quad (2.13)$$

This is a frequency-modulated signal that can be expanded into an infinite series of Bessel functions resulting in [51]

$$\begin{aligned} V(t) = & V_0 [J_0(\beta) \cos(2\pi f_0 t) \\ & + J_1(\beta) \cos(2\pi(f_0 + f_v)t) \\ & + J_1(\beta) \cos(2\pi(f_0 - f_v)t) \\ & + J_2(\beta) \cos(2\pi(f_0 + 2f_v)t) \\ & + J_2(\beta) \cos(2\pi(f_0 - 2f_v)t) + \dots] \end{aligned} \quad (2.14)$$

where $\beta = \Delta f/f_v$ is the modulation index. The frequency spectrum that is generated by Eq. 2.14 is shown in Fig. 2.7. Note that the first term of Eq. 2.14 is a sinusoidal wave at the carrier frequency, while the remaining terms represent vibration induced sidebands. The ratio of the power in the n th sideband to the power in the carrier, \mathcal{L}_v^n , is given by

$$\mathcal{L}_v^n(dBc) = 20 \log(J_n(\beta)/J_0(\beta)) \quad (2.15)$$

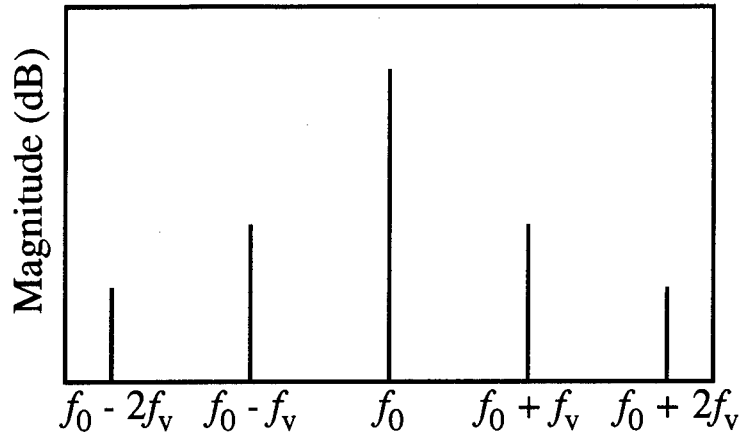


Figure 2.7. Frequency response of a SAW oscillator vibrated at constant frequency of f_v .

where dBc refers to decibels relative to the carrier and v refers to the vibration.

For values of $\beta < 0.1$ the following approximations can be made

$$\begin{aligned} J_0(\beta) &= 1 \\ J_1(\beta) &= \frac{\beta}{2} \\ J_{n \geq 2}(\beta) &= 0 \end{aligned} \tag{2.16}$$

Using these approximations and substituting for β , Eq. 2.15 becomes

$$\mathcal{L}_v^1 = 20 \log(\Delta f / 2f_v) \tag{2.17}$$

Using Eqs. 2.8 and 2.17 the acceleration sensitivity can then be solved as

$$\vec{\Gamma} \cdot \vec{A} = \frac{2f_v}{f_0} 10^{(\mathcal{L}_v^1(\text{dBc})/20)} \tag{2.18}$$

where \vec{A} , f_v , f_0 , and \mathcal{L}_v^1 are all measurable quantities. Recall, however, that the acceleration sensitivity is linearly separable into three scalar quantities. Therefore, by vibrating the device in a direction along only one axis, i , Eq. 2.18 reduces to

$$\Gamma_i = \frac{2f_v}{A_i f_0} 10^{(\mathcal{L}_i^1(\text{dBc})/20)} \tag{2.19}$$

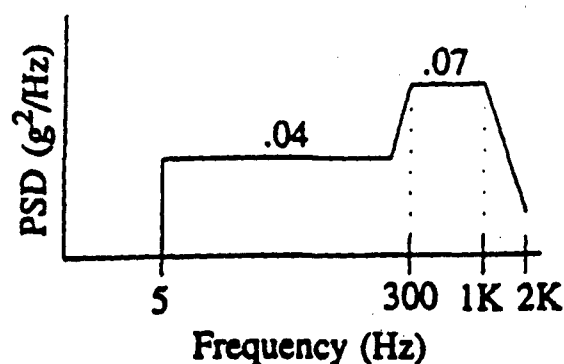


Figure 2.8. The random vibration envelope of a typical aircraft [1].

The assumption that $\beta < 0.1$ will generally hold for devices with a low acceleration sensitivity.

In a non-laboratory environment, the vibration applied to the oscillator is not a single sinusoidal vibration but is instead a random collection of motions. This random vibration is typically considered by evaluating the energy of the vibrations in the frequency domain. The vibration envelope of a typical aircraft is shown in Fig 2.8. It is clear that vibrations over a range of frequencies are applied to the oscillator. The effect of random vibration is evaluated by looking at the frequency spectrum of the oscillator phase noise. For a small modulation index, the oscillator phase noise is given by

$$\mathcal{L}(f) = 20 \log \left(\frac{\vec{\Gamma} \cdot \vec{A} f_0}{2f} \right) \quad (2.20)$$

where $|\vec{A}| = [2(PSD)]^{1/2}$ and PSD is the power spectral density of the vibration [1]. A random vibration defined by the aircraft envelope shown in Fig 2.8 applied to an oscillator with $|\vec{\Gamma}| = 10^{-9}/g$ results in a degradation of the oscillator phase noise as seen in Fig. 2.9.

2.5.3 The Cause of Acceleration Sensitivity. Acceleration can modify the performance of the crystal oscillator by affecting either the performance of the resonator or the performance of the electronic drive circuit of the oscillator. As reported by Kosinski [2], the changes in the loop circuit transimpedance can be modeled as seen in Fig. 2.10, where

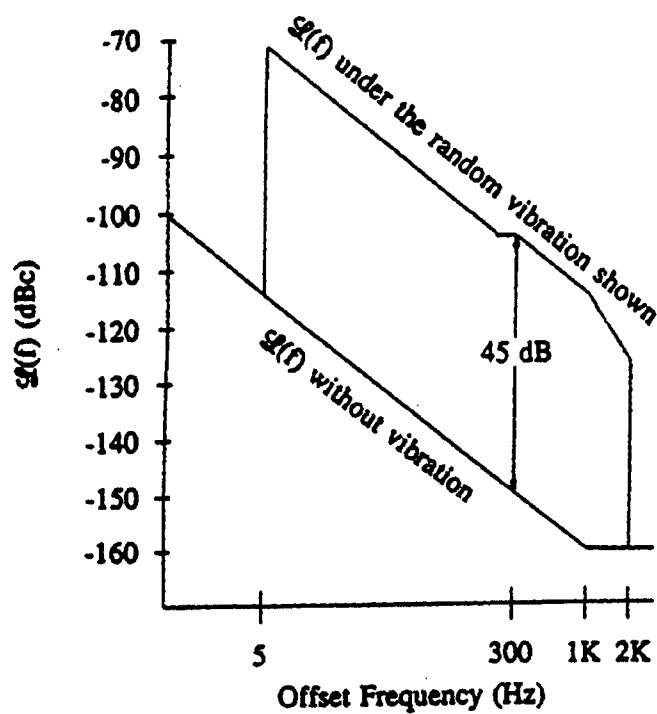


Figure 2.9. The effect of the random vibration defined by the envelope shown in Fig. 2.8 on an oscillator with an acceleration sensitivity of $10^{-9}/g$ [1].

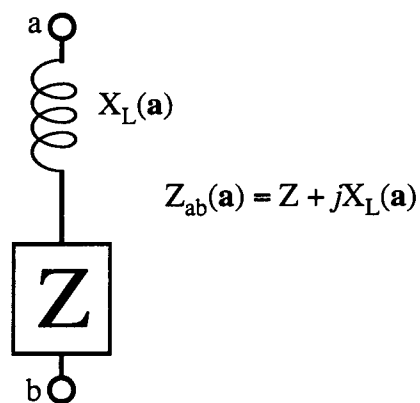


Figure 2.10. Equivalent circuit for modeling changes in the transimpedance of the oscillator loop excluding the SAW resonator [2].

X_L is a variable reactance due to vibration induced changes in the loop oscillator electronic components and Z is the transimpedance of an ideal amplifier. Acceleration induced phase perturbations are primarily due to shifts in loop components and lead contacts. Through the use of rigid circuit construction and elimination of motion sensitive components, loop perturbations can be minimized. Therefore, the primary cause of oscillator acceleration sensitivity is the crystal resonator.

Ideally, an oscillator should operate at the center frequency of the resonator. However, it is not possible to construct a phase matching tuning network that perfectly matches the phase delay of an arbitrary resonator, leading to a $2\pi n$ loop phase delay. As such, the typical crystal controlled oscillator operates near but not at the center frequency of the crystal resonator [47]. Then, the acceleration induced shift in the oscillator frequency is not caused by a shift in the center frequency of the resonator, but instead, is due to a change in the transimpedance of the crystal resonator [2]. More precisely, vibration induced shifts in the phase delay of the resonator cause the net loop phase shift of the oscillator to stray from $2\pi n$. Therefore, the frequency of the oscillator circuit must change for the loop to again be in phase with the crystal resonator. It has been shown that in a series-resonance oscillator, a phase shift of $\delta\phi$ results in a change of the output frequency of [1]

$$\delta f = - \left(\frac{\delta\phi}{2Q_L} \right) f \quad (2.21)$$

Then for an applied acceleration, a_i , resulting in a phase shift, $\delta\phi(a_i) = \phi(\vec{a}) - \phi(\vec{a} = 0)$, the acceleration sensitivity can be calculated as [2]

$$|\vec{\Gamma}| = - \frac{\phi(\vec{a}) - \phi(\vec{a} = 0)}{2|a|Q_L} \quad (2.22)$$

where $\phi(\vec{a})$ is the phase of the resonator transimpedance under an applied acceleration, \vec{a} , $\phi(\vec{a} = 0)$ is the unperturbed phase of the resonator transimpedance, and Q_L is the loaded Q of the resonator at the operating point of the oscillator circuit [47]. It can be seen from Eq. 2.22 that $|\vec{\Gamma}|$ is reduced by both decreasing the acceleration induced phase perturbations and maximizing the loaded Q of the crystal resonator.

Changes in the resonator transimpedance are caused by deformations of the resonator due to applied forces generated when the resonator is accelerated [2, 3]. Deformation of the crystal has two primary effects. First, the dimensions of the crystal are changed. Second, the material properties in the deformed crystal are different from that of the non-deformed crystal. Modifying the dimensions of the crystal has a "linear" effect on the frequency, while modifications to the material properties have a "nonlinear" effect. To reduce the acceleration sensitivity, it is then necessary to reduce the deformation of the crystal, or reduce the effect of the deformation on the resonator. It is important to note that the resonator is not sensitive to an applied acceleration, but is sensitive to the deformation caused by body forces applied due to the acceleration.

2.6 *Current Techniques for Reducing Crystal Acceleration Sensitivity*

Research has been progressing for several decades into minimizing resonator acceleration sensitivity [2, 52]. However, it is only recently that significant progress has been made [2]. The primary techniques for reducing acceleration sensitivity rely on modifying the mode shape of the acoustic wave and the deformation of the resonator such that the two interact to produce the minimum frequency shift. Utilizing these techniques, it is now possible to reliably fabricate both SAW [23, 53] and STW [22] resonators with acceleration sensitivities on the order of 2 to $5 \times 10^{-10}/g$.

Early research showed that the mounting of a resonator had a significant effect on the resonator acceleration sensitivity [40]. The cause of this has been determined to be the interaction of the crystal deformation with the mode shape of the acoustic wave. For many surface and bulk acoustic wave resonators, it is possible to calculate the distribution of motion in the crystal due to the acoustic wave [40]. The vibrational motion for a specific mode of vibration can be referred to as the mode shape of the crystal. The acceleration induced frequency shift in a crystal can be written as [40]

$$\frac{\delta f}{f} = \int (\text{mode shape}) \times (\text{stress pattern}) \quad (2.23)$$

where the stress pattern is the pattern of stress and strain on the crystal from the mounting supports. Therefore, it is possible to reduce the acceleration sensitivity of the crystal by either modifying the mode shape of the resonator [40, 54], or by adjusting the mounting supports [2]. A device with a perfectly symmetrical mode shape (mathematically described by an even function) combined with a perfectly symmetrical mount (which causes the stress pattern to be described by an odd function) should therefore have no acceleration sensitivity [2].

Electronically altering the mode shape has been successfully used to reduce the acceleration sensitivity of certain SAW and BAW resonators [40, 54]. Ballato reports that a 20 fold or greater improvement in $|\vec{\Gamma}|$ is possible through electronic mode shaping. However, this is not sufficient to reduce the sensitivity down to desired levels on the order of $10^{-12}/g$. Mode shaping has also been performed utilizing mass loading to induce the proper stress/strain distributions [23]. Unfortunately, these methods can not be applied to all SAW crystals [2].

By fixing the lateral dimensions of the crystal to a certain ratio, specific stresses can be cancelled out. This technique, referred to as aspect-ratio compensation, can be used to significantly reduce the acceleration sensitivity of SAW resonators to acceleration in the normal direction [43]-[46]. For a resonator that is approximately twice as long as it is wide, or an aspect ratio of 2, it should be possible to reduce the normal acceleration sensitivity, Γ_{normal} , of the device to under $10^{-10}/g$ [55].

2.6.1 State of the Art Oscillators.

Raytheon all quartz package SAW oscillators. Raytheon fabricates oscillators with low acceleration sensitivities based around an all quartz package (AQP) mounted to a thick alumina or ceramic stiffener [21, 23, 53, 56]. The general design of the device is shown in Fig. 2.11. The stiffener provides a rigid support to reduce deformations of the crystal. The AQP also utilizes a special glass frit mounting system to further reduce acceleration sensitivity [53]. Andres reports minimum acceleration sensitivities, Γ_i , as low as 3 or $4 \times 10^{-10}/g$ [23] while typical values are on the order of $10^{-9}/g$ for vibrations in

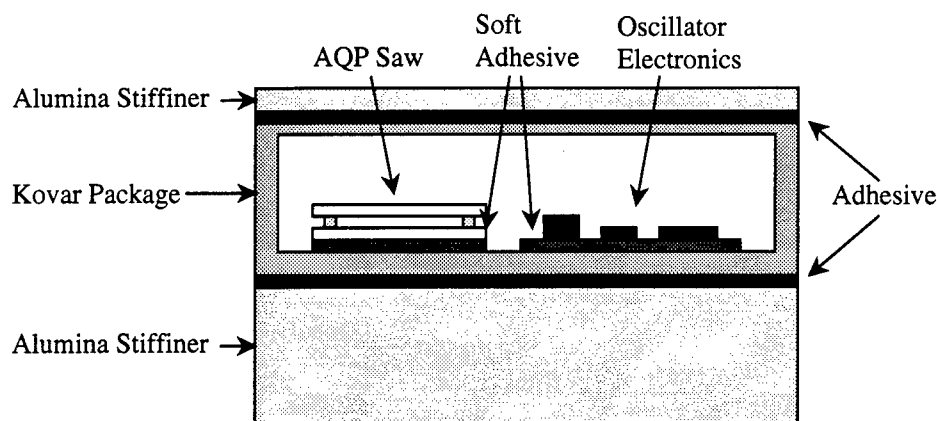


Figure 2.11. An all quartz package mounted to a stiffener to reduce acceleration sensitivity [53].

the range of 50 Hz to 7 kHz [23]. Unfortunately, the overall package shown in Fig. 2.12 is large, measuring over 2 inches square and over 1 inch high, and does not fit into all desired systems [23]. The majority of the size is in the alumina stiffener that serves as a rigid support. For applications requiring a smaller system, the alumina support can be removed. However, the performance of the system is degraded when the rigid support is removed.

SAWTEK STW oscillators. SAWTEK produces STW based oscillators with similarly low acceleration sensitivities [22]. The devices consist of STW resonators mounted in hermetically sealed surface mount packages (SMPs). These packages may serve as a rigid mount decreasing the oscillator acceleration sensitivity. Reported acceleration sensitivities range from 1 to $6 \times 10^{-10}/g$ over frequencies from 500 Hz to 2000 Hz. The entire oscillator is mounted in a standard 14-pin dual inline package (DIP).

2.7 Summary

SAW/STW resonators are typically manufactured on high quality quartz. These resonators can be made with high Q, low insertion loss, good phase noise performance, good long term stability and good temperature stability. Therefore, they are often used in stable fixed frequency oscillators. However, the crystal resonators are sensitive to accelerations

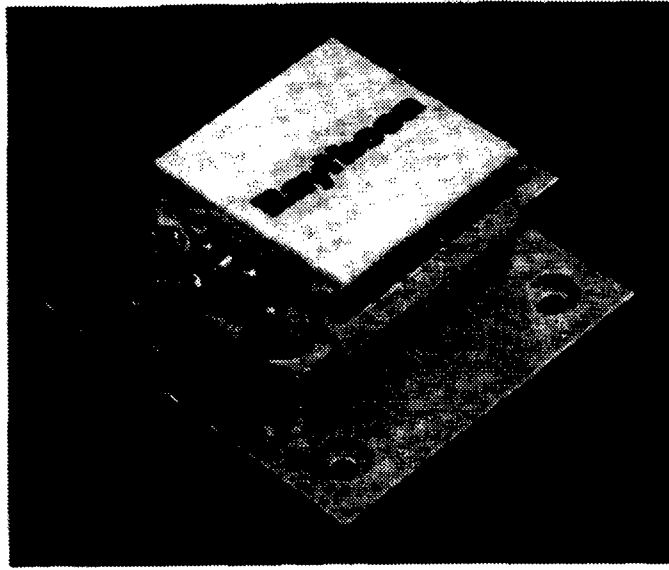


Figure 2.12. A commercially fabricated crystal based oscillator with low acceleration sensitivity [23].

induced by vibrations from mobile platforms. These vibrations limit the performance of communications and radar systems that utilize the oscillators. It is necessary to provide some method of minimizing the acceleration sensitivity of the resonators.

It has been shown that the primary source of frequency shifts in SAW/STW oscillators is a change in the transimpedance of the resonator due to acceleration induced deformation of the crystal. In order to reduce the frequency shift of the oscillator, it is necessary to reduce the acceleration sensitivity, $\vec{\Gamma}$, reduce the acceleration, or mount the resonator such that the applied acceleration is in a direction of minimum acceleration sensitivity. Reducing the acceleration can be done externally with vibration isolation. Reducing the acceleration sensitivity can be done by controlling the body forces applied to the resonator such that resonator deformation interacts with the acoustic wave mode shape in a manner that results in the minimum frequency shift. Mounting the resonator can be done on an application basis.

III. Fundamentals of Vibration Isolation

Vibration isolation refers to a method for reducing the vibration transmitted from a vibration source to an object. The study of vibration isolation is not new, and a large body of literature exists on the topic [57, 58]. The basic design of a vibration isolation system is shown in Fig. 3.1. As shown, the isolation system rests between a vibration source and an object that needs to be isolated. A SAW/STW resonator can be considered to be a mass connected to a vibrating foundation by a series of springs as shown in Fig. 3.2. When the foundation is vibrated, the vibration is transmitted through the vibration isolation system to the resonator. The resonator is free to move in any of the three spatial dimensions, and can also rotate about any of the three spatial axes, resulting in a system with six degrees of freedom. In order to simplify the analysis presented here, it is assumed that the system is constrained to move in only one spatial axis. This assumption is not always valid, however, the purpose of this chapter is simply to provide an understanding of the basic concepts of vibration isolation. Therefore, a system with only one degree of freedom is used.

Two primary classes of vibration isolation systems exist: passive, and active. Passive systems rely on a low mechanical resonance. As ω of the vibration increases above the mechanical resonance of the isolation system, the magnitude of the vibration transmitted to the isolated object decreases. As will be shown, for vibration frequencies that are greater than the resonance frequency multiplied by $\sqrt{2}$, the vibration passed to the object is less than the vibration of the foundation. Passive systems can be as simple as a spring, and require no active control system or power supply. Active systems aim to reduce, or even

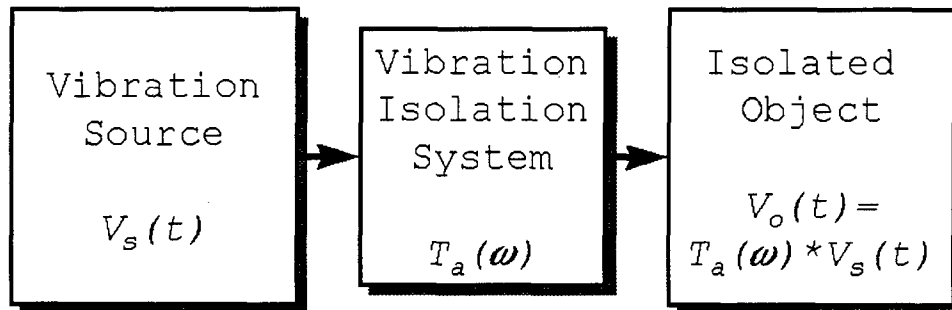


Figure 3.1. A vibration isolation system is used to separate a vibration source from an object that requires a reduced vibration.

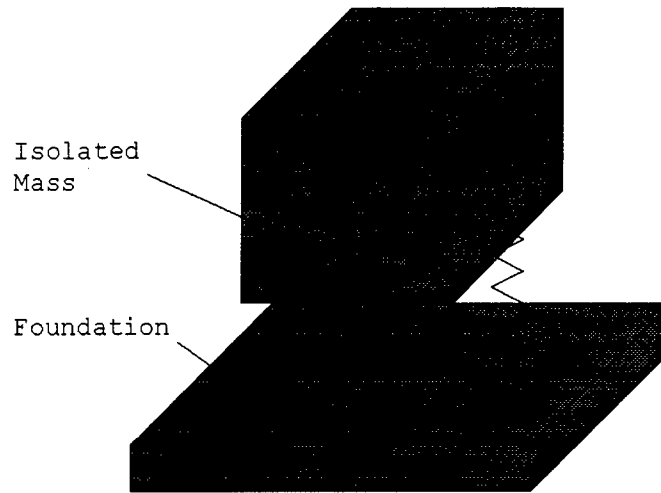


Figure 3.2. A mass connected to a vibrating foundation via an isolation system. The mass is free to move in any of 3 spatial dimensions, and can also rotate about any of the 3 spatial axes. This results in a system with six degrees of freedom.

eliminate the vibration by generating a force or motion to counter the force applied by the vibration. Active systems are inherently more complex, but potentially offer better isolation.

The following sections provide an analysis of passive spring systems. In the next section, the response of a mass connected by a spring to a vibrating foundation is evaluated. The following section considers the addition of a damping element into the system. Finally, a brief discussion of active systems is provided.

3.1 Analysis of an Undamped, One Degree of Freedom Mass-Spring System

A one degree of freedom mass-spring system is shown in Fig. 3.3. The system consists of a mass, M_0 , supported by a spring with stiffness, k . Vibration of the foundation is represented by a time varying motion of the platform, $v_f(t)$. For brevity, the time dependence of the function is omitted except where required for clarity. This motion results in a deflection of the supporting spring

$$x = v_f - v_m \quad (3.1)$$

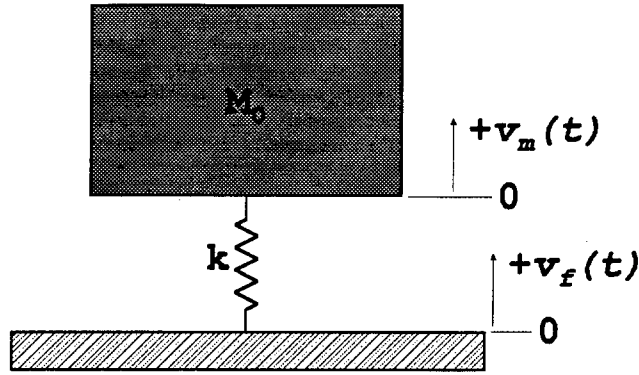


Figure 3.3. A mass, M_0 connected to a vibration foundation by a spring, k . The vibration of the foundation is represented by a time dependent motion, $v_f(t)$. The motion of the foundation results in a motion of the mass, $v_m(t)$. All motion is limited to a single axis as shown.

where v_f and v_m are the position of the foundation and the mass, respectively. When deflected, the spring exerts a force,

$$f = kx \quad (3.2)$$

on the mass resulting in an acceleration

$$M_0 \ddot{v}_m = kx \quad (3.3)$$

where $\ddot{v}_m = (d^2/dt^2)v_m(t)$. The equation of motion for the mass is then written as

$$M_0 \ddot{v}_m - k(v_f - v_m) = 0 \quad (3.4)$$

Substituting a harmonic vibration of the foundation

$$v_f(t) = A \sin(\omega t) \quad (3.5)$$

into Eq. 3.4 and rearranging results in

$$M_0 \ddot{v}_m + kv_m = kA \sin(\omega t) \quad (3.6)$$

The solution of Eq. 3.6 is assumed to be of the form

$$v_m = B \sin(\omega t) \quad (3.7)$$

$$\dot{v}_m = \omega B \cos(\omega t) \quad (3.8)$$

$$\ddot{v}_m = -\omega^2 B \sin(\omega t) \quad (3.9)$$

This is substituted into Eq. 3.6 resulting in

$$-M_0 \omega^2 B \sin(\omega t) + k B \sin(\omega t) = k A \sin(\omega t) \quad (3.10)$$

The absolute transmissability through the vibration isolation system, from the foundation to the mass is then solved as

$$\begin{aligned} T_a &= \frac{v_m}{v_f} \\ &= \left(1 - \left(\frac{M_0}{k}\right) \omega^2\right)^{-1} \end{aligned} \quad (3.11)$$

Resonance of the system occurs at $\omega_0 = \sqrt{\frac{k}{M_0}}$ (rad/s). Substituting this into Eq. 3.11 results in

$$T_a = \left(1 - \left(\frac{\omega}{\omega_0}\right)^2\right)^{-1} \quad (3.12)$$

Figure 3.4 shows a plot of the absolute transmissability for the system. At low frequencies ($\omega \ll \omega_0$), $|T_a| \approx 1$. Therefore, vibration is passed to the mass without a change in amplitude. As ω approaches ω_0 , $|T_a|$ increases rapidly, reaching infinity at resonance ($\omega = \omega_0$). In reality, the system loses energy through a variety of mechanisms including friction and losses in the spring. These losses damp the system and are described in the next section. As ω increases above ω_0 , $|T_a|$ rapidly decreases. When $\omega = \sqrt{2}\omega_0$ the absolute transmissability is equal to 1. As ω increases above $\sqrt{2}\omega_0$, the absolute transmissability decreases below one. In this region, the vibration of the mass is smaller than that of the foundation. Therefore, the mass is isolated from vibrations of these frequencies. The mass moves in phase with the foundation at frequencies below resonance, however, at resonance a jump occurs in the phase difference. Above resonance, the motion of the mass lags behind that of the foundation by 180° . Again, the discontinuity in the

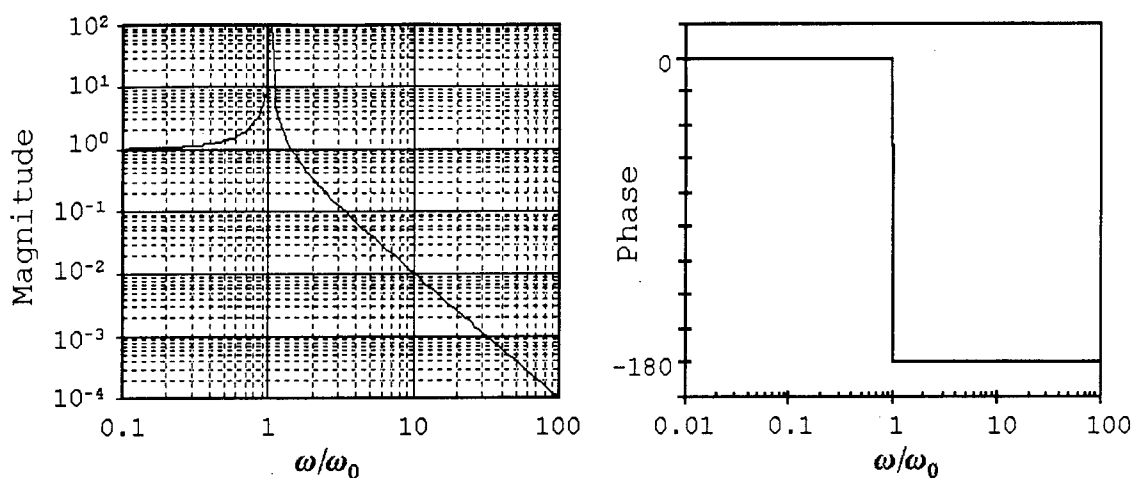


Figure 3.4. Magnitude and phase of the absolute transmissibility of a foundation vibration to the mass. The absolute transmissibility is defined as $T_a = v_m/v_f$. Note that the phase change shows that the motion of the mass trails that of the foundation by 180 degrees for values of $\omega > \omega_0$.

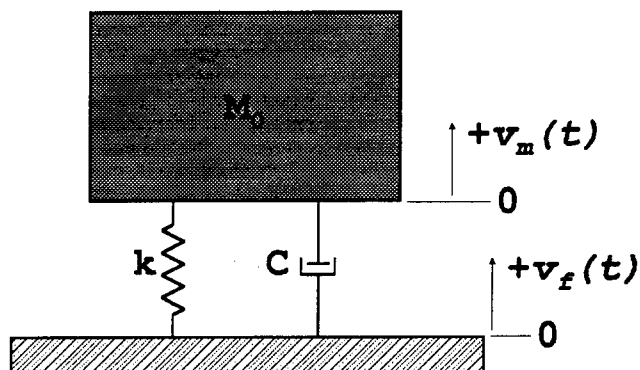


Figure 3.5. A mass-spring system with a damper added in parallel to the spring.

phase is not possible in a real system. Damping results in a more gradual change in the phase as discussed in the next section.

3.2 The Effect of Damping on a Mass-Spring System

The loss of energy due to friction, viscous air flow, and resistance in the spring damp the motion of the mass. The effect of such loss is incorporated into the model through the use of a damper as shown in Fig 3.5. The damping element results in a resistive force, F_D .

Table 3.1. Types of Damping and the resulting damping force, F_D [58].

Type of Damping	Damping force, F_D	Damping Coefficient
Viscous	$-C\dot{x}$	C
Coulomb	$-F_f \text{sgn}(\dot{x})$	F_f
Quadratic	$-C_2 \dot{x}^2 \text{sgn}(\dot{x})$	C_2
Velocity	$-C_n \dot{x} ^n \text{sgn}(\dot{x})$	C_n
Histeretic	$-\frac{h}{\omega} \dot{x}$	h

This force is included into Eq. 3.2 as

$$f = kx + F_D \quad (3.13)$$

The damping force is resistive to either the motion of the mass, as in the case of friction and viscous air flow, or the relative motion of the foundation and the mass as in the case of resistive losses in the spring. The damping force can then be represented as

$$F_D = F_m + F_r \quad (3.14)$$

where F_m is the force resistive to the motion of the mass, and F_r is the force resistive to the relative motion. The values of F_m and F_r are dependent upon the type of damping that exists. Table 3.1 shows several types of damping and the resulting equations for calculating the damping force. Viscous damping is the most commonly experienced and the absolute transmissability of a viscously damped system is described below.

A resistive force always opposes the motion of the object. Therefore the force resistive to the motion of the mass is calculated as

$$F_m = -C_m \dot{v}_m \quad (3.15)$$

where C_m is the viscous damping coefficient for the mass motion. The force resistive to relative motion is then

$$F_r = -C_r (\dot{v}_m - \dot{v}_f) \quad (3.16)$$

where C_r is the damping coefficient of the relative motion. Combining the two damping forces with the force from the spring then results in the force applied to the mass

$$f = kx - (C_m + C_r)\dot{v}_m + C_r\dot{v}_f \quad (3.17)$$

As before, this results in an acceleration

$$M_0\ddot{v}_m = kx - (C_m + C_r)\dot{v}_m + C_r\dot{v}_f \quad (3.18)$$

The equation of motion for the system is then

$$M_0\ddot{v}_m - k(v_f - v_m) + (C_m + C_r)\dot{v}_m - C_r\dot{v}_f = 0 \quad (3.19)$$

Substituting the harmonic vibration of Eq. 3.5 into Eq. 3.19 and rearranging results in

$$M_0\ddot{v}_m - C'\dot{v}_m + kv_m = -C_r\omega A \cos(\omega t) + kA \sin(\omega t) \quad (3.20)$$

$$= A\sqrt{k^2 + (C_r\omega)^2} \sin(\omega t + \epsilon_1) \quad (3.21)$$

where

$$\epsilon_1 = -\tan^{-1} \left(\frac{C_r\omega}{k} \right) \quad (3.22)$$

and

$$C' = C_m + C_r \quad (3.23)$$

The solution is assumed to be of the form

$$v_m = B \sin(\omega t - \phi) \quad (3.24)$$

$$\dot{v}_m = \omega B \cos(\omega t - \phi) \quad (3.25)$$

$$\ddot{v}_m = -\omega^2 B \sin(\omega t - \phi) \quad (3.26)$$

where ϕ is the phase change between the motion of the mass and the motion of the foundation. Substituting this into Eq. 3.21 results in

$$B\sqrt{(k - M_0\omega^2)^2 + (C'\omega)^2} \sin(\omega t - \phi + \epsilon_2) = A\sqrt{k^2 + (C_r\omega)^2} \sin(\omega t + \epsilon_1) \quad (3.27)$$

where

$$\epsilon_2 = -\tan^{-1} \left(\frac{C'\omega}{k - M_0\omega^2} \right) \quad (3.28)$$

For the two sides of Eq. 3.27 to be equal, it is necessary that the sinusoids have the same phase, or $\phi = \epsilon_2 - \epsilon_1$. Therefore the change in phase between the motion of the mass and the foundation is

$$\phi = \tan^{-1} \left(\frac{C_r\omega}{k} \right) - \tan^{-1} \left(\frac{C'\omega}{k - M_0\omega^2} \right) \quad (3.29)$$

The magnitude of the absolute transmissibility through the vibration isolation system, from the foundation to the mass is then solved as

$$|T_a| = \sqrt{\frac{k^2 + (C_r\omega)^2}{(k - M_0\omega^2)^2 + (C'\omega)^2}} \quad (3.30)$$

which can be rearranged as

$$|T_a| = \sqrt{\frac{1 + \left(\frac{C_r\omega}{k}\right)^2}{\left(1 - \left(\frac{\omega}{\omega_0}\right)^2\right)^2 + \left(\frac{C'\omega}{k}\right)^2}} \quad (3.31)$$

Figure 3.6 shows the effect of damping relative to the motion of the mass, while Fig. 3.7 shows the effect of damping relative to the relative motion. Evaluation of both plots and Eq. 3.31 leads to several conclusions. Increasing damping relative to the motion of the mass results in a decreasing motion of the mass in all cases. The effect of C_m is primarily near resonance. As ω increases, the curves for all values of C_m converge. Increasing C_r also decreases the absolute transmissibility in the region near resonance, but the effect of C_r is also seen at higher frequencies. As C_r increases, the motion of the mass becomes more tightly coupled to the motion of the foundation. Therefore, as C_r is increased, the motion of the mass approaches the motion of the platform, and for $C_r = \infty$, the motion

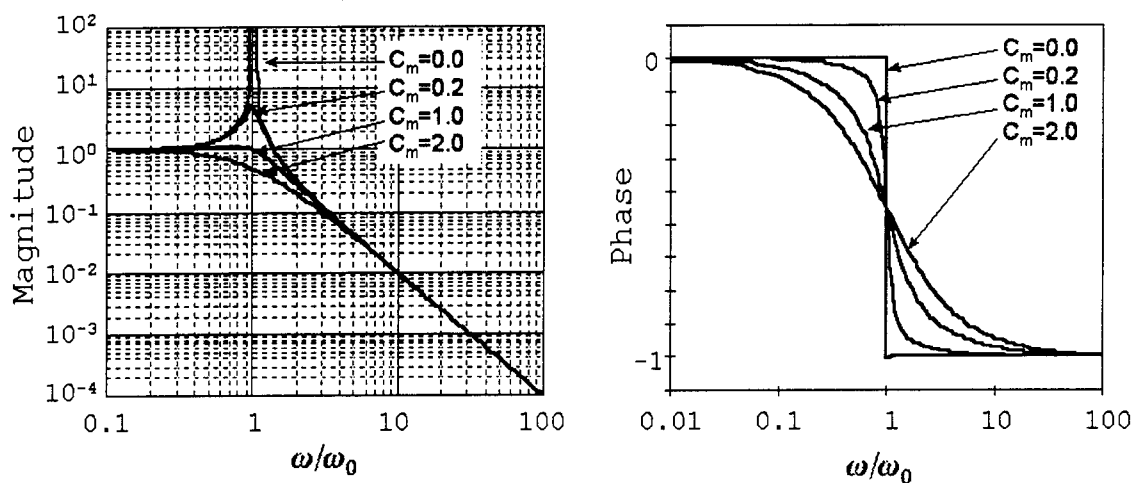


Figure 3.6. Absolute transmissability of a damped mass-spring system for several values of C_m . All of the curves have $C_r = 0$.

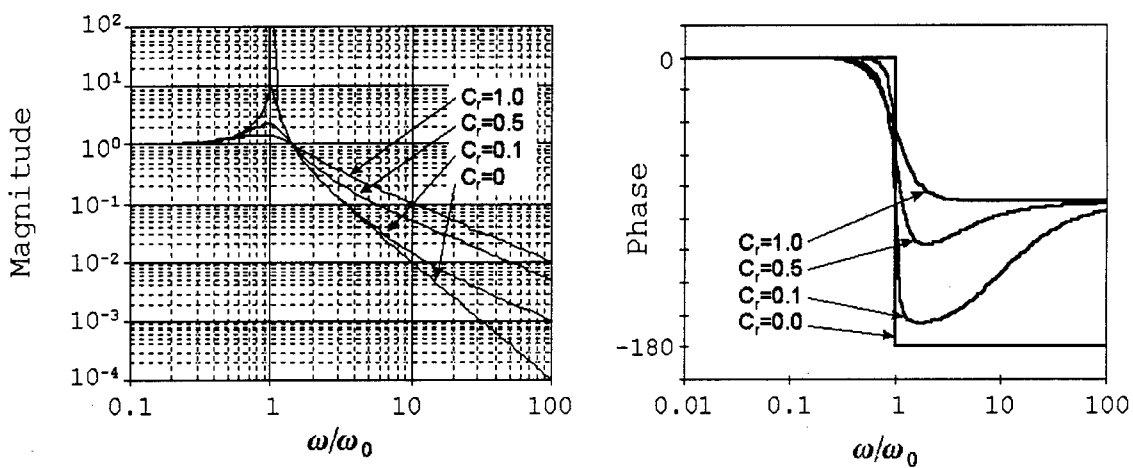


Figure 3.7. Absolute transmissability of a damped mass-spring system for several values of C_r . All of the curves have $C_m = 0$.

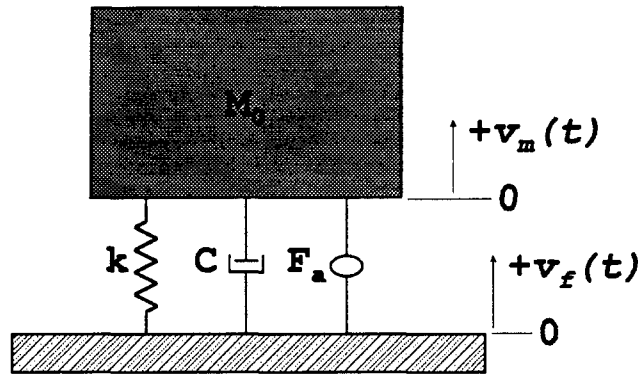


Figure 3.8. A one degree of freedom mass-spring system with both passive and active damping.

of the mass will equal that of the foundation for all frequencies resulting in $T_a = 1$. It is then clear that a high value of C_m is desirable while a low value of C_r is desirable.

The magnitude of T_a at resonance is an important value for most systems. From Eq. 3.31 the absolute transmissability at resonance is calculated as

$$|T_a(\omega = \omega_0)| = \sqrt{\left(\frac{k}{C'\omega_0}\right)^2 + \left(\frac{C_r}{C'}\right)^2} \quad (3.32)$$

For systems with $C_m \gg C_r$, this simplifies to

$$|T_a(\omega = \omega_0)| = \frac{k}{C'\omega_0} \quad (3.33)$$

Note that this magnitude is primarily dependent on the ratio of the spring constant and the damping coefficient, C' . It is then clear that the shape of the absolute transmissability curve is determined by the ratio of the damping forces and the spring force.

3.3 Active Vibration Isolation

The basic design of a one degree of freedom vibration isolation system with an active control mechanism is shown in Fig. 3.8. As can be seen, the system is the same as a passively damped system with the addition of an active control element. The active force

is incorporated into the system as

$$f = kx + F_D + F_a \quad (3.34)$$

where F_a is the force applied by the active damper. It is possible to simultaneously optimize the active and passive damping mechanisms to minimize the absolute transmissability of the system [59]. The active damping relies on the performance of an actuator capable of providing sufficient force and displacement to damp the vibration, and sensors to measure the acceleration of both the foundation and the mass.

IV. Microelectromechanical Systems

The field of microelectromechanical systems (MEMS) was originally conceived in a talk given by physicist Richard Feynman on December 26, 1959 [60]. In this talk Feynman discusses the possibility that miniscule systems and robots will eventually be fabricated. Since his talk, a large deal of MEMS research has occurred and several commercial applications now exist [62, 63]. Research is currently evaluating MEMS for a wide variety of applications ranging from accelerometers [64, 65], gyroscopes [66], and pressure sensors [67, 68], to adaptive optics [69], and neural probes [70, 71].

The following sections provide a background on the basic processes used in the fabrication of MEMS and a variety of example devices that can be fabricated with these processes. The three primary MEMS processes, bulk micromachining, surface micromachining, and microforming are discussed in the next section. Following this, a variety of devices that were fabricated by the author as part of the research for this dissertation are presented. The devices illustrate simple structures such as cantilevers and bridges; more complex movable structures such as micro-hinges, sliders, and pin joints; electrostatic and thermal actuators; and finally, systems that are fabricated using these basic components.

4.1 Micromachining Processes

A large variety of micromachining processes exist, however, the primary ones can be grouped into three categories: bulk micromachining, surface micromachining, and microforming. Bulk micromachining utilizes patterning of a bulk material, typically silicon, to form structures. Surface micromachining uses standard microelectronic techniques to deposit thin films on top of a substrate. By patterning the thin films, and selectively removing undesired films MEMS are formed. Microforming selectively deposits material to form a device. Processes such as LIGA and deep UV patterning rely on electroplating to deposit material into a mold [72, 73], while other processes grow the desired structures [74].

4.1.1 Bulk Micromachining. Bulk micromachining, as the name implies, uses processing of the bulk material to form micro-structures. A typical process uses a combination of deposition and photolithographic steps borrowed from microelectronic fabrica-

tion, selective etching of the bulk material, and wafer bonding. Microelectronic fabrication deposition techniques are used to add thin films to the surface of a wafer. The films can be metal, polycrystalline silicon (polysilicon), silicon oxide, silicon nitride, or various polymers. The layers can be patterned individually to allow the design of different structures [4, 75]. These processes are directly borrowed from microelectronic fabrication, and are also used in surface micromachining. Further discussion of the deposition and masking processes is provided in Section 4.1.2. Etching selectively removes undesired material from the bulk wafer, while wafer bonding provides a method to add more bulk material and combine etched devices. Combinations of these methods allow the formation of a variety of devices, including suspended structures, microbridges, cantilevers, and diaphragms [4], [75]-[80].

Etching. Bulk etching is typically performed using a liquid, or "wet", etchant. Using techniques borrowed from microelectronic fabrication, a protective coating is deposited and patterned onto one or both sides of the wafer. The type of masking material used is dependent upon the etchant with silicon oxide and silicon nitride being the most commonly used materials. The thickness of the protective coating depends on the desired etch time and the selectivity of the etchant for the bulk material with respect to the masking material. After the etch mask is patterned, the wafer is submerged into the etchant and the exposed bulk material is etched. The manner in which the bulk material is removed depends upon the type of etchant used. The simplest type of etch removes the bulk material at an equal rate in all directions. This type of etch is referred to as isotropic. It does not allow much control over which material is removed and which material remains. This is particularly a problem because the etch undercuts the masking material as seen in Fig. 4.1. The problem of material being removed from under the mask is generally referred to as undercutting of the mask. Undercutting of the masking material can be used to form suspended structures such as cantilevers and bridges. However, isotropic etching also makes it difficult to define the shape of the remaining bulk material. Due to the problems in controlling the etch, wet isotropic etching is seldom used as a bulk etchant except in conjunction with an etch stop method such as in electrochemical or dopant dependent etching. Both of these methods are discussed later in this section.

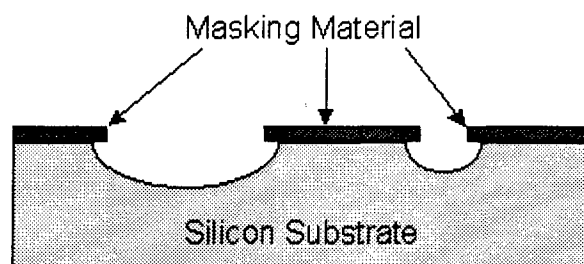


Figure 4.1. Etching profile of an isotropic etchant. The etch proceeds equally in all directions resulting in an undercutting of the masking material that is directly proportional to the etch time.

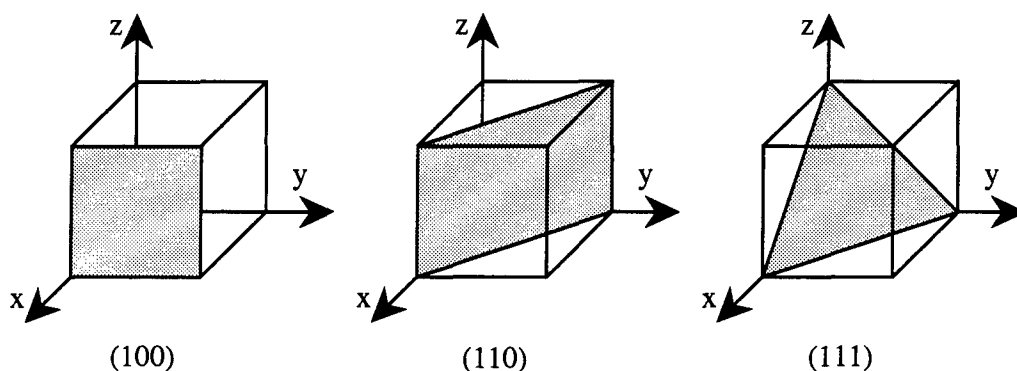


Figure 4.2. Miller indices for the cubic crystal planes.

Fortunately, it has been known since the late 1950's that certain chemicals, such as ethylene diamine pyrocatechol (EDP) and potassium hydroxide (KOH) etch crystalline silicon at different rates along the various crystal planes [76]. To aid in the discussion, the crystal planes are specified using Miller's indices [81, 82]. Figure 4.2 shows the Miller indices for a material with a cubic crystal lattice such as silicon. Etching silicon in a solution of 750 ml of ethylene diamine, 120 grams of pyrocatechol, and 100 ml of water proceeds 35 times faster in the $\langle 100 \rangle$ direction than it does in the $\langle 111 \rangle$ direction, while for a solution of 44 grams of KOH diluted in 100 ml of water the ratio is 400 to 1 for the same directions [76]. The etch rate varies with the temperature of the solution. For the EDP solution above, at a temperature of 115°C the etch rate in the $\langle 100 \rangle$ direction is $0.75 \mu\text{m}$ per minute, while for the KOH solution at 85°C the etch rate is $1.4 \mu\text{m}$ per minute in the same direction [76]. During the etch, the $\{111\}$ planes effectively act as etch

Table 4.1. Properties of Anisotropic Silicon Etchants.

Etchant	Typical Solution	<111>/<100> Selectivity	<100> etch rate ($\mu\text{m}/\text{minute}$)
Potassium Hydroxide (KOH) [76]	50 grams KOH 100 ml DIW	400	1.0 at 50°C
Ethylene Diamine Pyrocatechol (EDP) [76]	750 ml Ethylene diamine 120 grams Pyrocatechol 240 ml DIW	35	0.75 at 115°C
Tetramethyl Ammonium (TMAH) [83, 84]	22 grams TMAH 100 ml DIW	25	0.6 at 80°C

stops, while the etch proceeds in the <100> direction. The reasons for the varying etch rates are not completely understood, however, enough is known to allow the fabrication of useful devices.

As with isotropic etchants, the masking material is dependent upon the etchant with the primary masking materials again being silicon oxide and silicon nitride. Table 4.1 lists several of the most commonly used anisotropic silicon etchants and some of their key attributes. Originally, KOH and EDP were primarily used for anisotropic etching of silicon. Unfortunately, both KOH and EDP also etch aluminum. Recently, tetramethyl ammonium hydroxide (TMAH) has been studied as an anisotropic silicon etchant [83, 84, 85]. TMAH exhibits extremely high selectivity for silicon over silicon oxide (up to 1000:1 [83]), and it has been shown that the etch rate of aluminum in TMAH can be reduced by dissolving silicon into the solution [83]. Because of the high oxide and aluminum selectivity, TMAH etching is compatible with the fabrication of CMOS devices [85]. Finally, TMAH is also used as a positive photo-resist developer, and therefore is readily available in semiconductor grade solutions. Unfortunately, the <111> to <100> selectivity is not as high as that of KOH. Therefore, it is still necessary to choose an etchant depending upon the structure that is being fabricated. For example, to fabricate deep vertical wall grooves in {110} silicon wafers, the high selectivity of KOH is required [86, 87].

Due to the anisotropic nature of the etch, the surface orientation of the wafer determines the etch profile. Figure 4.3 shows the etch profiles for silicon wafers with {100} and

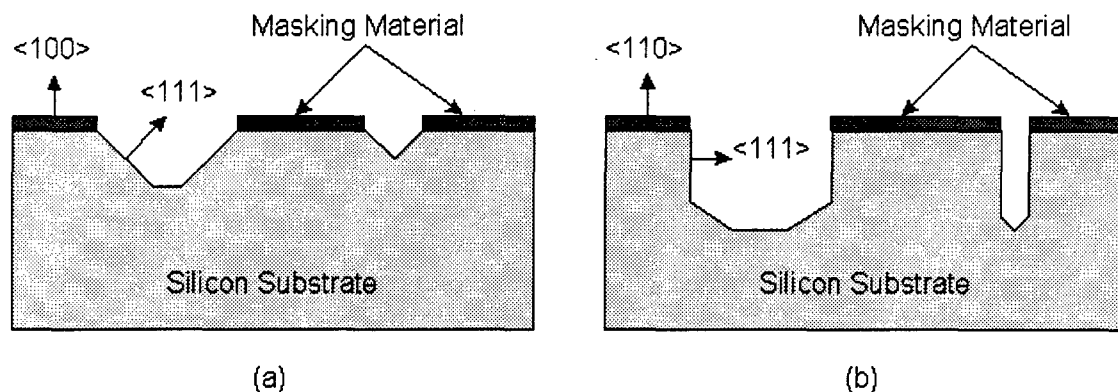
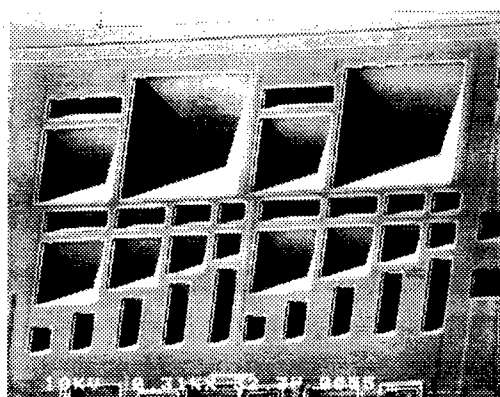


Figure 4.3. Etching profile of an anisotropic etch with EDP or KOH. (a) On a {100} oriented silicon wafer. (b) On a {110} oriented silicon wafer.

{110} crystal plane surfaces. As shown in Fig. 4.3, the etch progresses in all directions, however, it proceeds significantly slower in the {111} directions causing the formation of defined etch planes. The {111} planes are at a 54.74° angle with the {100} planes. This allows a precise specification of the bulk material that is to be removed [76]. Typically, metal oxide semiconductor (MOS) fabrication is done using {100} oriented wafers. Opening a square cut aligned with the {110} wafer flat into the mask, and then etching the wafer in an anisotropic etchant yields inverted pyramidal pits that are etched into the wafer. The sides of the pits are defined by the {111} planes projecting down into the wafer. Combining anisotropic etching with surface layers, various devices such as cantilevers, microbridges, and diaphragms can be fabricated [4, 75, 76]. The anisotropic nature of the etch makes it easy to control which regions are supposed to be undercut and which regions are not. Figure 4.4 shows inverted pyramidal pits and a released structure formed by using anisotropic etching to undercut an oxide layer deposited on the surface of a {100} silicon wafer.

Anisotropic etching allows substantial control over the etching process, however, it is limited to etching along the crystal planes of the bulk material. Recently, researchers have developed a method called Micromachining by Ion Track Etching (MITE) to etch bulk materials along arbitrary planes [88, 89]. The process begins by applying a masking layer on a bulk wafer. The wafer is bombarded with high energy heavy ions causing the formation of linear ion tracks in the material. The etch mask is then patterned and the



(a)



(b)

Figure 4.4. (a) SEM micrograph of pyramidal pits etched into {100} oriented silicon wafer using EDP [4]. (b) Anisotropic etching can be used to undercut a thin oxide layer on the surface of a wafer resulting in a released structure. The structures shown in (b) were designed by the author and fabricated using a commercial foundry. The devices were then released by etching in EDP at AFIT.

bulk material is etched. The ion tracks result in the formation of artificial etch planes. This method allows the definition of arbitrary planes coming down from the surface allowing the fabrication of a variety of structures such as those shown in Fig 4.5 fabricated from a quartz wafer. The process, however is limited to linear planes, and the formation of the ion trails results in damage to the structural material. It is unlikely that the process is compatible with the fabrication of active semiconductor devices. Therefore, other etch stop methods are also used. Primarily, dopant and electrochemical methods are used to provide for more flexible etch control.

Many etchant solutions, including EDP and KOH, exhibit sensitivity to the doping type and concentration of the bulk material [90]. In particular, the rate with which EDP etches silicon drops to almost zero with high enough boron doping concentrations ($> 7 \times 10^{20}/\text{cm}^3$). This type of etch stop can be used in conjunction with masking to limit undercutting of the mask [91]. Dopant dependent etch stops also offer new methods for the fabrication of thin structures consisting of the highly doped material. This has been used in devices such as neural probes [92] and thin diaphragms [93]. Dopant controlled etching

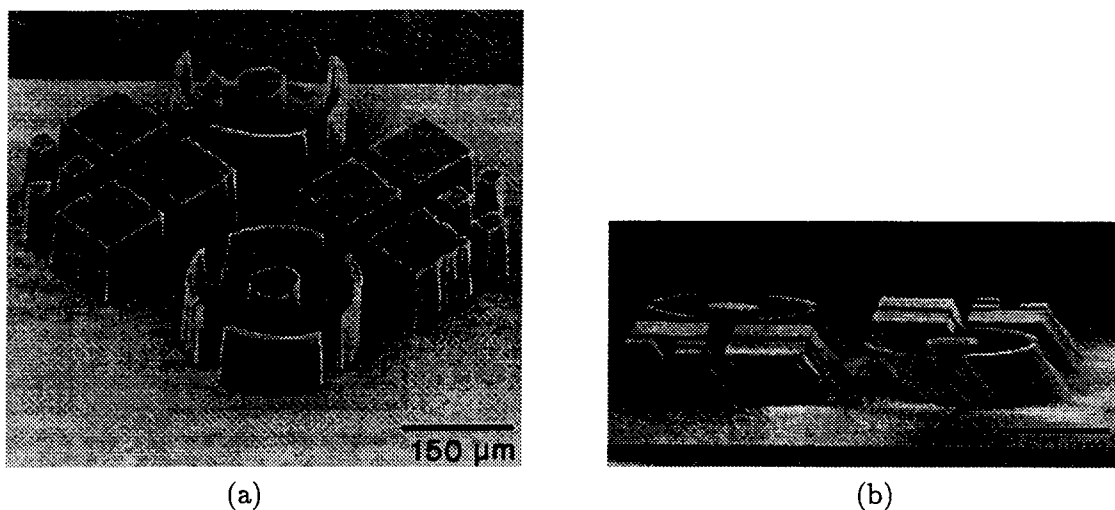


Figure 4.5. Structures fabricated in quartz using the MITE process [88]. (a) The ion tracks are formed normal to the quartz surface resulting in vertical etch planes. (b) The ion tracks are at a 45 degree angle to the surface resulting in tilted etch planes.

allows precise control over the material that is to be removed. However, it is limited by the fact that only regions highly doped with boron survive the etch.

Electrochemical etch stop methods also exist, and have been developed to provide an alternative method for controlling material removed during bulk etching [76, 90]. Several types of electrochemical etch stops have been experimented with. The two primary types are summarized here.

The first method uses hydrofluoric acid (HF) diluted in water [76]. The ratio of HF to water is dependent upon the desired etch rate. Typically, the HF will be diluted on the order of 10:1 HF:H₂O. The HF etches silicon oxide but does not etch the silicon. An anode is attached to a silicon wafer, while a cathode is placed in the solution. Running current through the material causes oxidation at the surface of the wafer resulting in the formation of silicon oxide. The silicon oxide at the wafer surface reacts with the HF and is removed. The etch rate is dependent on a number of conditions, including the dopant level of the wafer, and the current density. Removing the current flow stops the etching.

A more recent method consists of forming a pn-junction in the wafer [76, 90]. The n-doped region is connected to an anode and the cathode is placed into the solution, thus

reverse biasing the pn-junction. Typically, the solutions used are anisotropic etchants such as KOH or EDP. The etchant etches through the wafer until the junction is reached. At this point, the current flowing from the anode to the cathode increases sharply. After a short time the current decreases to nearly zero, and the etch stops [90]. The process that stops the etch is not fully understood. However, it is believed that when the p-doped region has been removed, current flows directly from the n-doped material into the etchant solution forming a thin oxide on the surface of the wafer, and thus stopping the etch [90]. This method has the advantage of not requiring the high doping levels necessary for dopant controlled etch stops.

Finally, a variety of "dry" etching methods are now being explored. The dry etching is done in a gaseous or a plasma environment. Two primary methods are now being used. Plasma etching has been used to etch vertical holes into silicon substrates [94]. Kovacs reported the fabrication of 8-14 μm diameter holes from 50 to 100 μm deep. Unfortunately, the minimum diameter of the hole was dependent on the depth of the etch. Recently, xenon difluoride (XeF_2) has shown promise as an isotropic silicon etchant. XeF_2 exhibits an extremely high selectivity for silicon oxide, aluminum, and photo-resist while isotropically etching silicon [95, 96].

Wafer Bonding. Wafer bonding is the process of fusing together two silicon wafers without the use of adhesives. This is done by forming a molecular bond between the wafers [90]. The general process is to begin with two mirror polished wafers. The polished sides are cleaned and placed together. The wafers are then placed into an oven where heat and pressure are applied forming a permanent bond between the wafers. A detailed description of silicon wafer bonding mechanisms can be found in reference [90].

As an example, consider the bonding of two silicon wafers. Initially, the wafers are polished to a mirror smooth surface and cleaned of any contaminants. Next, the polished sides are placed into contact. At this point, Van der Waals forces hold the two wafers together. It is thus difficult to separate the wafers, but it can be done. Heating the wafers up to 200°C leads to the formation of hydroxyl bonds. Above 200°C Si-O-Si bonds begin to form, and above 400°C strong covalent Si-Si bonds begin to form [90]. Several MEMS

devices have been fabricated using wafer bonding in conjunction with bulk etching such as resonant structures [67], and microphones [97].

The CMOS-MEMS Process. The Metal Oxide Semiconductor Implementation Service (MOSIS) is currently offering a standard CMOS compatible MEMS process [91]. This process allows the fabrication of suspended structures on a standard CMOS die. The process is provided through the Orbit foundry in conjunction with a standard CMOS run. Following fabrication, the wafers are diced and the individual die are returned to the user. In order to form suspended structures, the die are etched in EDP or TMAH.

The process begins by laying the devices out using a program called MAGIC. MAGIC allows the designer to specify how the individual layers are patterned during fabrication. With the Orbit process there are several diffusion layers, two polysilicon layers, two metal layers, and a variety of glass (SiO_2) layers. For the fabrication of MEMS devices, two new layers are added to the MAGIC layout. The first, OPEN, specifies an area where the bare silicon is to be exposed. The second, PSTOP, specifies a high concentration p-type (boron) diffusion. After the design is laid out, it is converted into a standard format and sent electronically to MOSIS for fabrication.

As mentioned, the CMOS-MEMS dice are fabricated in conjunction with standard CMOS dice. Therefore, no additional processing steps are added. Instead, the OPEN layer in MAGIC is converted into a series of previously defined glass cuts. When all of the glass cuts are combined by the OPEN layer, the bare silicon is exposed. The PSTOP layer is just a standard diffusion that has been renamed for the MEMS process. In effect, the CMOS process is not compromised for the fabrication of MEMS devices. This results in limitations on the types of MEMS devices that can be fabricated. Currently, only suspended structures such as cantilever beams, or suspended platforms can be built. These devices are composed of glass that can encase up to two polysilicon and two metal layers [91]. After the chips are returned to the user, they are etched using EDP or TMAH. The EDP etch process used at AFIT to release the devices is described in Appendix A.

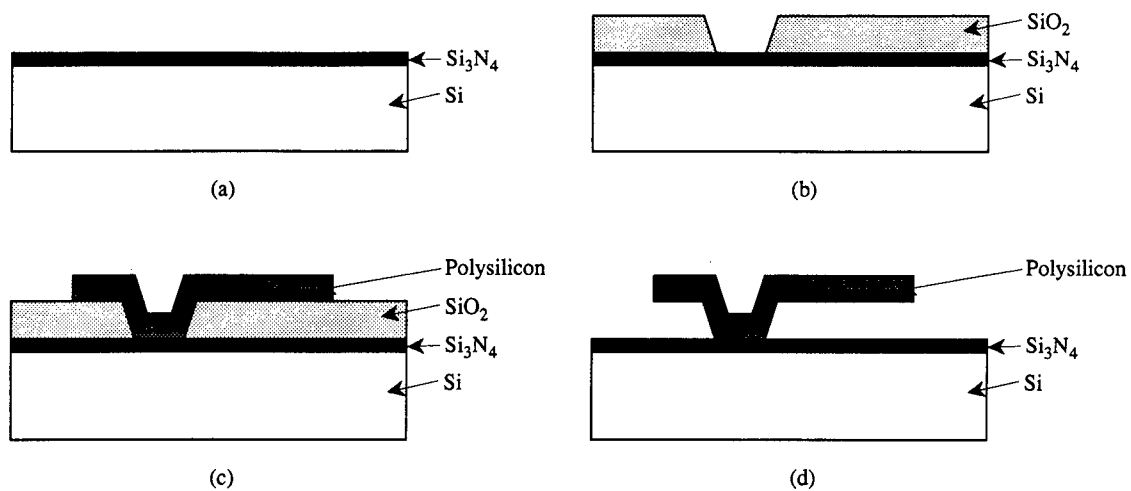


Figure 4.6. Sacrificial micromachining process for the fabrication of a cantilever beam. (a) Deposit a silicon nitride (Si_3N_4) passivation layer on a silicon substrate. (b) Deposit and pattern the sacrificial silicon oxide (SiO_2) layer. (c) Deposit and pattern the structural polysilicon layer. (d) Release the cantilever beam by removing the sacrificial layer in a HF etch.

4.1.2 Surface Micromachining. Surface micromachining utilizes materials deposited onto the surface of a wafer for the fabrication of devices. The processes used to deposit and pattern the materials are borrowed from microelectronic fabrication. These deposition and etching processes have been refined for the fabrication of integrated circuits, and thus allow precise control over the dimensions of the fabricated structures. Widely available processes such as the multi-user MEMS process (MUMPs) allow the fabrication of devices with feature sizes as small as two microns [98]. However, microelectronic processing commonly allows submicron feature sizes.

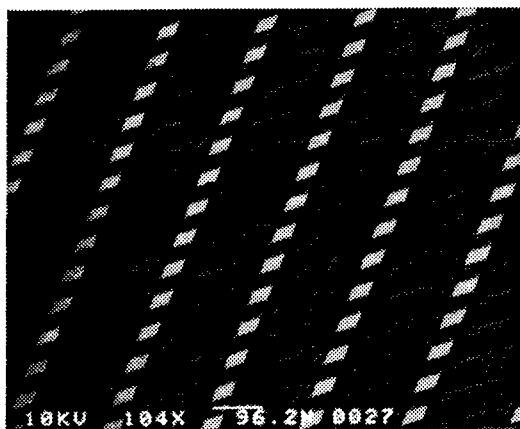
The general surface, or sacrificial layer, micromachining process begins with the deposition of an isolation layer on a bulk wafer. The isolation layer is commonly silicon nitride, while the wafer is silicon. Following the isolation layer, alternating sacrificial and structural layers are deposited and patterned. Finally, the sacrificial layers are removed with a wet isotropic etch. This process is illustrated in Fig. 4.6 for the fabrication of a cantilever beam using one structural and one sacrificial layer.

As mentioned, the structural and sacrificial layers are deposited using processes from microelectronic fabrication. The processes for depositing materials include atmospheric

pressure chemical vapor deposition (APCVD), plasma enhanced chemical vapor deposition (PECVD), low pressure chemical vapor deposition (LPCVD), RF-sputtering, and evaporation. However, LPCVD is the most commonly used method for depositing silicon nitride and polysilicon [90].

Patterning of materials is performed using several different methods. For metals, patterning is typically done using a lift off process. The lift off process begins with the deposition of a photo-resist. The photo-resist is exposed to high intensity ultraviolet light through a photo-mask. The photo-resist is then developed leaving behind an image corresponding to the photo-mask. Following this, the metal is deposited over the entire wafer on top of the photo-resist layer. The photo-resist is then removed by immersing the wafer in an organic solvent such as acetone. During this process, any metal deposited on the photo-resist is removed with the photo-resist, while metal deposited on the exposed wafer surface is left behind. For patterning thicker materials such as polysilicon or silicon oxide, a photo-resist mask is used in combination with an etch. For these processes, the material is initially deposited to cover the entire wafer. This is followed by the deposition of a photo-resist. The photo-resist is exposed and developed. The undesired material is then removed in either a wet or dry etch. A wet etch is performed by immersing the wafer in a liquid isotropic etchant while dry etching is performed in a plasma environment. The most commonly used dry etching process is reactive ion etching (RIE) due to the straight-walled cuts generated [90, 99]. These processes are capable of forming devices with minimum feature sizes of a few micrometers or less. However, the processes are essentially planar with individual layers generally on the order of a few micrometers thick, as seen in Fig. 4.7. Surface micromachining offers the ability to batch fabricate a large number of devices as is clear from Fig. 4.7a.

A further difficulty encountered in micromachining is residual stresses in the deposited layers. Materials such as polysilicon are in a state of compression after deposition with LPCVD, APCVD, or PECVD [90]. The amount of stress is dependent upon the parameters of the deposition [90]. Internal stresses in the materials cause the devices to buckle or bend as shown in Fig. 4.8. However, at temperatures around 1100°C the polysilicon recrystallizes, thus reducing the internal stress [90]. Therefore, a high temperature



(a)



(b)

Figure 4.7. SEM micrographs showing structures fabricated by the author using a commercial surface micromachining process, MUMPs. The micrographs show arrays of force testers, (a), and several suspended platforms, (b). As can be seen, the lateral dimensions of the structures are much greater than the vertical dimensions.

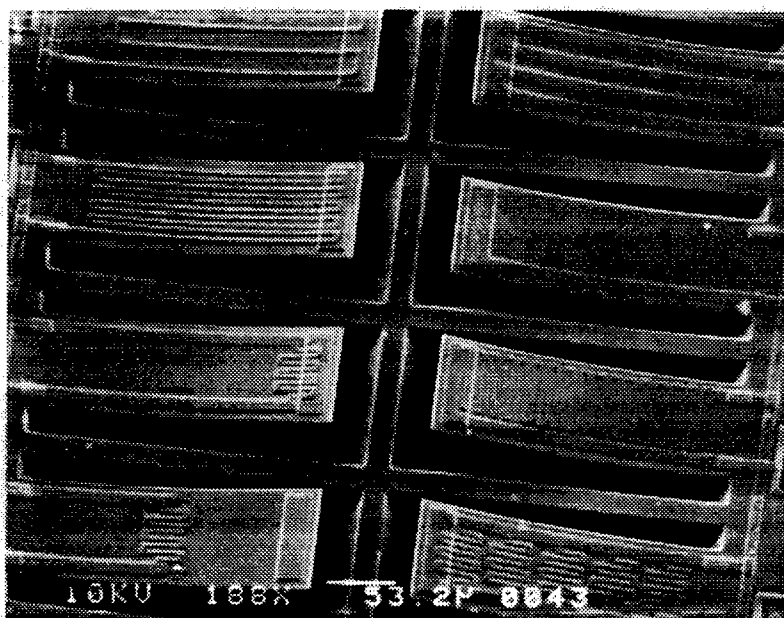


Figure 4.8. Bending of released cantilever beams due to residual stress [4].

Table 4.2. Structural and Sacrificial Layers Used in Surface Micromachining.

Structural Layer	Sacrificial layer
Polysilicon	SiO ₂ , Phosphosilicate glass (PSG)
Si ₃ N ₄	SiO ₂ , PSG
SiO ₂	Polysilicon
Polyimide	Al
Ni	Polyimide

anneal is often used to alleviate the stress. Unfortunately at temperatures this high, the dopants in the bulk wafer diffuse, washing out the sharp doping gradients needed for the fabrication of microelectronic devices.

The structural material used for fabricating devices is generally chosen for specific material properties such as reflectivity or Young's modulus, while the sacrificial layer is chosen so that a highly selective etchant can be used. Table 4.2 lists several structural materials and their corresponding sacrificial layers. Polysilicon is the most commonly used structural material in conjunction with silicon oxide as the most commonly used sacrificial layer. Using this combination allows hydrofluoric acid to be used as the etchant of the oxide due to high etch selectivity. As can be seen in Table 4.2, the same materials can be used as either a structural or sacrificial layer depending on the process. However, this causes problems with integrating MEMS devices with microelectronic devices. Often the micromachining sacrificial layer, such as Al, polysilicon, or silicon oxide, is necessary in the fabrication of microelectronic devices, and etching to remove the sacrificial layer destroys the microelectronic devices.

The Multi-User MEMS Process. The Microelectronic Corporation of North Carolina (MCNC) currently offers a process for fabricating surface micromachined devices. This process, the multi-user MEMS process (MUMPs) is a surface micromachining process aimed specifically at the fabrication of MEMS devices. MUMPs uses polysilicon as the structural material and phosphosilicate glass (PSG) as the sacrificial layer. There are three polysilicon layers. The first, Poly0, is a thin layer that is directly connected to a silicon nitride isolation layer. A thin metal layer is deposited on top of the final polysilicon layer.




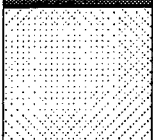



	Film	Thickness (nm)	Stress (MPa)
	Metal	531.8	21 (Tensile)
	Poly2	1470.6	11.1 (Compressive)
	Oxide2	528.1	NA
	Poly1	2010.0	8.0 (Compressive)
	Oxide1	2040.0	NA
	Poly0	488.0	NA
	Nitride	604.9	41.0 (Tensile)
Silicon Substrate			

Figure 4.9. MUMPs7 layer thicknesses.

The structural polysilicon layers are deposited using LPCVD. Following deposition of the second and third polysilicon layers, the wafers are annealed at 1050°C for one hour to relieve stress. Patterning of the polysilicon, and PSG layers is done with RIE, while the metal is patterned using a lift-off process. After the deposition of all the layers, the wafers are diced, and the individual die are sent to the users. Figure 4.9 shows the thickness and stress of the layers from MUMPs7. These numbers are typical for the MUMPs process.

After the die are returned, the polysilicon structures are released at AFIT using the process described in Appendix B. As a consequence of the release etch, it is necessary to put etch holes in devices larger the 50 μm square to allow the etchant to fully undercut the structure. Utilizing this standard process, a large variety of devices can be fabricated as shown in later sections.

4.1.3 Microforming. Recently, several new fabrication methods have been developed specifically for micromachining. These processes can be considered to be surface micromachining processes because they produce devices on the surface of a bulk wafer.

However, unlike sacrificial layer processing, instead of depositing a film over the entire wafer and then etching the film to remove undesired material, microforming methods selectively deposit material only where desired. Processes such as electron-beam induced fabrication have been developed to grow material in a selective location on a wafer without using a mask or mold [74]. However, these methods have not been widely used due to slow deposition rates and the cost of the specialized equipment that is required. More widely available processes have been developed. These processes utilize electroplating to deposit a metal inside a prefabricated mold. One process fabricates a plastic mold using x-ray resist and synchrotron radiation, while in a second process, photosensitive polyimide is used to form a mold. As these two processes are more widely available, they are discussed below in further detail.

4.1.4 The LIGA process. The LIGA process was initially developed in Germany, and LIGA is a German acronym for lithography, electroplating, and molding. Over the past 10 years, the process has undergone significant refinement and modification. As such, a number of process varieties have been developed. However, the defining characteristic of the process remains the use of synchrotron x-rays to expose a resist and form a mold.

The LIGA process begins by coating a substrate with a metallic seed layer followed by a thick x-ray resist such as polymethylacrylate (PMMA). The x-ray resist is then exposed to synchrotron x-rays through a special x-ray mask. Developing the resist forms a plastic template of the desired structure. Next, metal is deposited into the mold using electroplating. The remaining resist is removed with a highly selective etchant leaving behind metal structures. These structures can either be the final device, or a mold for the mass fabrication of devices. This process is illustrated in Fig. 4.10. With the addition of a sacrificial layer, this process can be easily adapted for the fabrication of movable parts [72, 100, 101].

Recently, MCNC in conjunction with the University of Wisconsin began offering a LIGA process [100]. The MCNC-LIGA process starts with a sacrificial layer of 1 μm thick oxide, followed by 500 nm of titanium for a seed layer. PMMA is then deposited as an x-ray resist and exposed with synchrotron radiation. The PMMA is developed and nickel

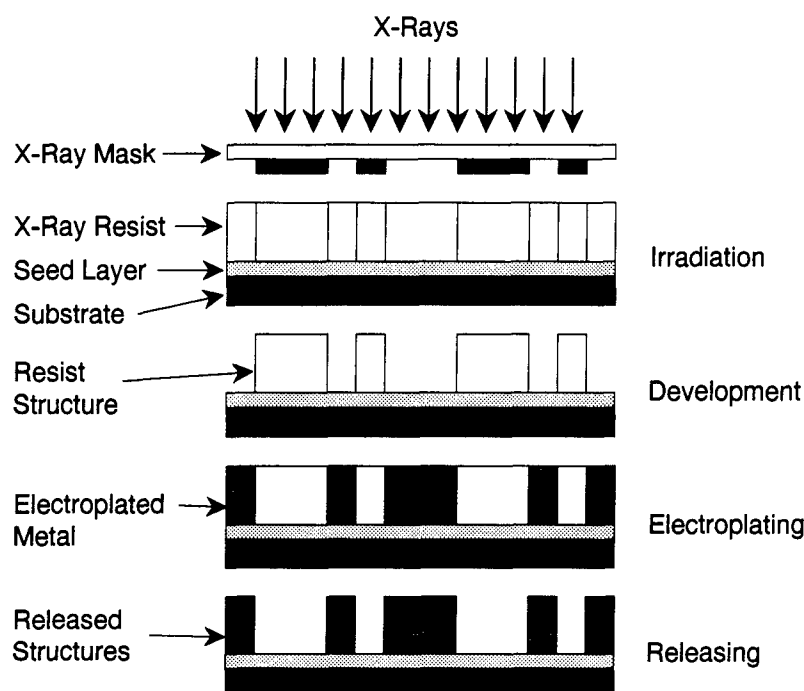


Figure 4.10. The LIGA process.

is electroplated to form the devices. MCNC offers two separate processes. One provides devices that are $30\text{ }\mu\text{m}$ tall, while the second provides devices that are $150\text{ }\mu\text{m}$ tall. For both processes, the minimum line and spacing sizes are set at $5\text{ }\mu\text{m}$. Figure 4.11 shows several devices fabricated by the author using the thin LIGA process offered by MCNC.

While the MCNC process provides devices up to $150\text{ }\mu\text{m}$ tall, Rogner, *et al.*, report that devices up to $500\text{ }\mu\text{m}$ tall can be fabricated with minimum feature sizes as low as $2\text{ }\mu\text{m}$ [72]. The ratio of the height of a device to the minimum width is called the aspect ratio. Currently, the LIGA process is the only process capable of providing devices with aspect ratios greater than 100. However, the process is limited by the need for a source of synchrotron x-rays and the expense of fabricating x-ray masks.

4.1.5 Electroplating with Photosensitive Polyimide. In the past several years, Frazier, *et al.*, have demonstrated a process using photosensitive polyimide as a mold for electroplating [73, 102, 103]. The method used is very similar to the LIGA process except x-ray resist exposed with synchrotron x-rays is replaced with photosensitive polyimide

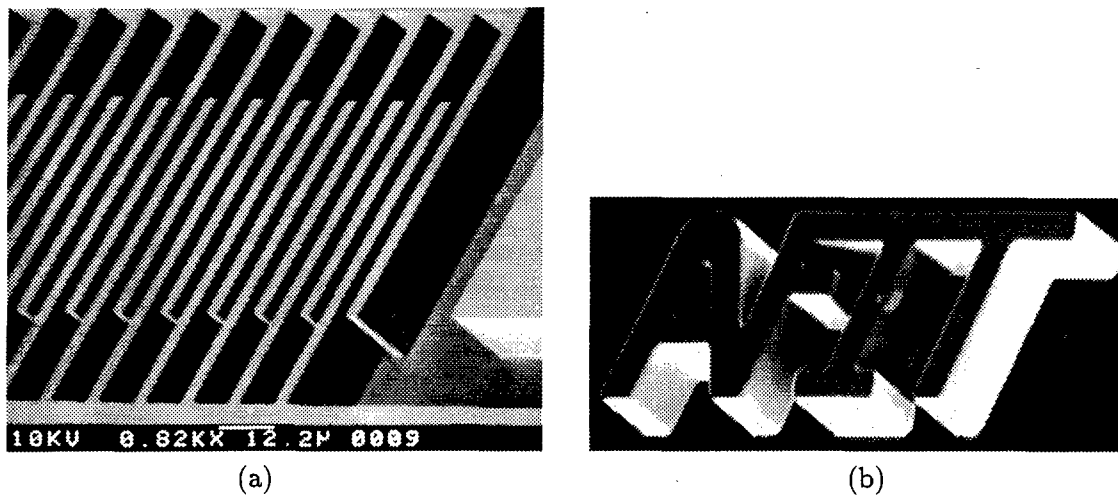


Figure 4.11. Devices fabricated at AFIT using the thin LIGA process offered by MCNC. The devices are 30 μm thick nickel. The fingers, (a), have an equal width and separation of 5 μm . The AFIT logo, (b), also has 5 μm thick arms.

exposed with ultraviolet light. This allows the use of common integrated circuit fabrication equipment in a clean room environment. However, the polyimide is typically only 1 to 50 μm thick, and the definition of side walls is not as precise [104]. Still, devices with aspect ratios greater than 1 can be fabricated as seen in Fig. 4.12.

The process begins with the deposition of a metallic seed layer followed by a coating of polyimide. The polyimide is then exposed using an ultraviolet mask aligner. Next, the polyimide is developed and the metal is electroplated to form the devices. Figure 4.13 illustrates the general process. Frazier, *et al.*, have reported several expansions to the process including the use of the seed layer as a sacrificial layer and the fabrication of devices utilizing multiple metal layers [73].

4.2 Microelectromechanical Components, Actuators, and Systems

The majority of the components presented in this section were fabricated by the author as a part of this dissertation research. Many of the components were originally designed by other researchers, however, the systems presented were developed by the author. All of the devices were fabricated using either the CMOS-MEMS process described in Section 4.1.1, the MUMPs described in Section 4.1.2, or the MCNC LIGA process described

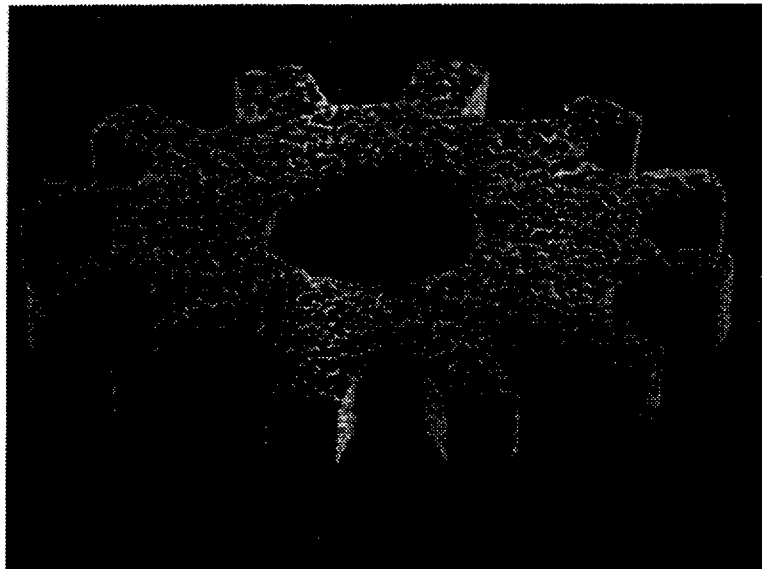


Figure 4.12. SEM micrograph of a copper gear fabricated by electroplating into a polyimide mold [73]. The gear is $300\ \mu\text{m}$ across and $45\ \mu\text{m}$ tall.

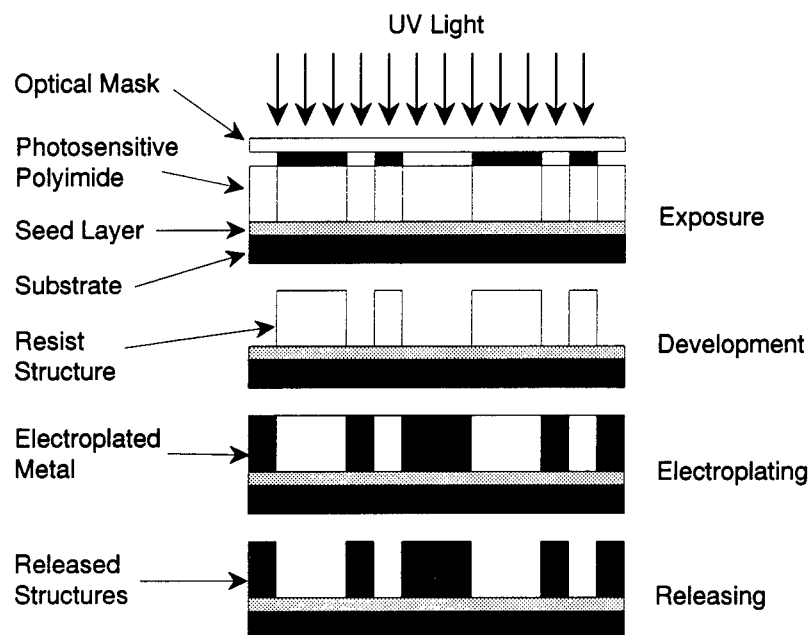


Figure 4.13. Fabrication with photosensitive polyimide and electroplating.

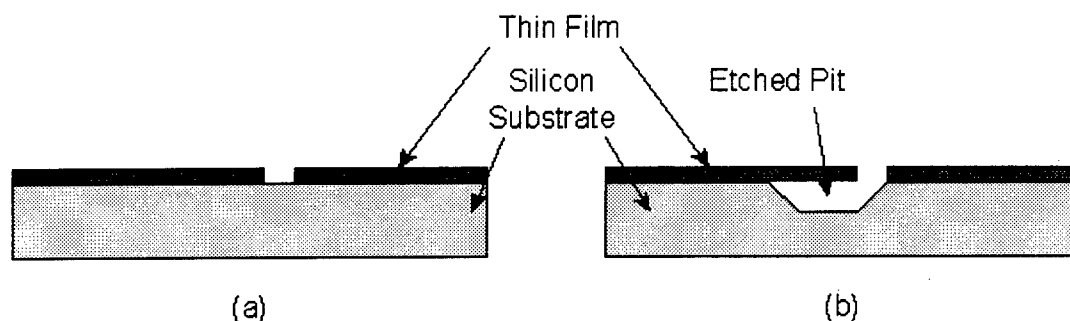


Figure 4.14. Fabrication of a cantilever in a bulk micromachining process. (a) A thin film such as SiO_2 is deposited and patterned. (b) The cantilever is released using an anisotropic etchant such as EDP or TMAH.

in Section 4.1.4. A large variety of devices and systems have been fabricated during the course of this research. This section provides an overview of the primary devices that were designed and fabricated.

The devices are presented in order of their complexity. Initially, simple structures, such as cantilevers, bridges, and springs are presented. This is followed by structures utilizing more complex, moving components such as sliders, rotating pin joints, and micro-hinges. Next, several actuators are presented, including lateral and vertical electrostatic and thermal actuators. Finally, systems utilizing both structures and actuators are presented.

4.2.1 Simple Structures.

Cantilevers and Bridges. The simplest MEM structures are cantilevers and bridges. A cantilever is a beam connected to the substrate at one end, while a bridge is a beam connected to the substrate at both ends. With a bulk micromachining process, a cantilever is formed by patterning a thin film such as silicon oxide on the surface of a wafer and then etching away the bulk material under the pattern using an anisotropic etchant such as TMAH or EDP. This process is shown in Fig. 4.14. Fabricating bridges in a bulk process is similar. However, the sides of the bridge can not run along the $\{110\}$ planes. If the bridge does run along these planes, the anisotropic etch will not undercut the thin film but will instead form two separate inverted pyramidal pits.

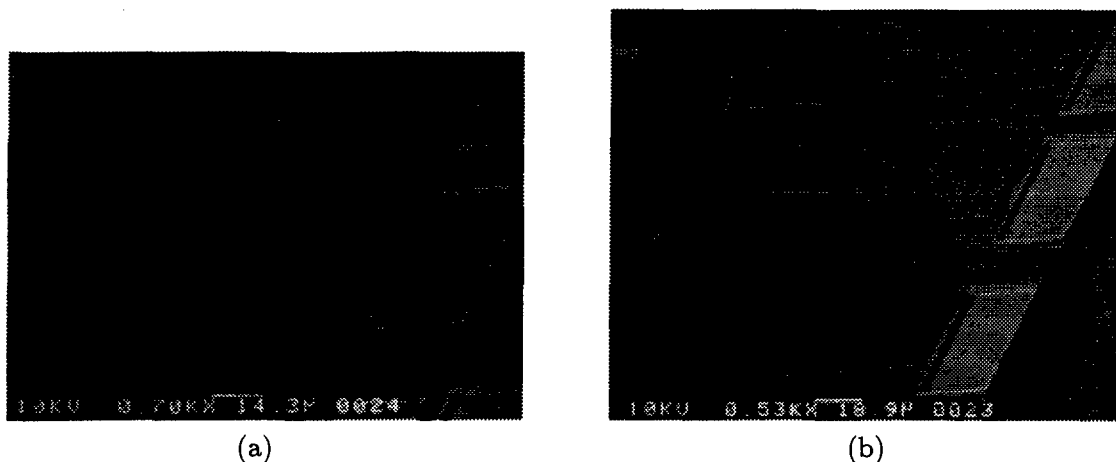


Figure 4.15. Cantilevers fabricated using MUMPs. The cantilevers in (b) were stuck to the surface when the die was dried.

In a surface micromachining process, arbitrary bridges and cantilevers can be fabricated. Initially, the sacrificial layer is deposited. Holes are cut into the sacrificial layer to form anchors. Next, the structural layer is deposited, and finally, the sacrificial layer is removed in a highly selective etch. Figure 4.15 shows several cantilevers that were fabricated using MUMPs. The primary difficulty in fabricating bridges and cantilevers in a surface micromachining process is stiction. After releasing a structure in a wet etch, and rinsing the device in deionized water, it is necessary to dry the device. During the drying process, the surface tension of the evaporating water pulls the released device towards the substrate. If the cantilever is pulled into contact with the substrate it forms a bond and remains stuck as shown in Fig. 4.15b. To reduce the effect of stiction, the designer has two primary options. The first is to use a final rinse in a liquid with a lower surface tension than water such as methyl or isopropyl alcohol. The second is to use small bumps in the structural layers called dimples. The dimples project below the cantilever and thus make contact with the substrate before the flat cantilever surface. Since the area of the dimples is significantly smaller, the bond with the substrate is weaker.

Springs. Micromechanical springs can also be formed in both bulk and surface micromachining processes. The fabrication of the spring is the same as that of a cantilever except that the pattern used is a winding spring instead of a rectangular

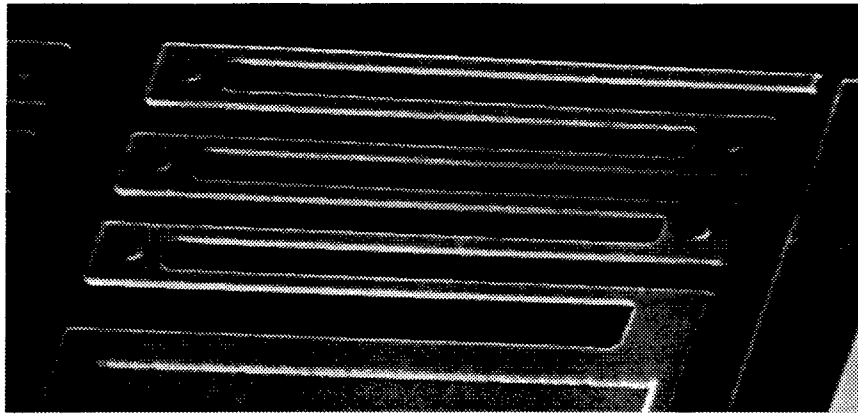


Figure 4.16. A micromechanical spring fabricated using MUMPs.

cantilever. Fig. 4.16 shows a spring fabricated using MUMPs. An example of a bulk micromachined spring shaped as an AFIT logo was shown previously in Fig. 4.4b.

IR Pixels. One of the first devices fabricated using the CMOS-MEMS process was an infra-red (IR) pixel. The pixel is formed by patterning a polysilicon resistor in between two oxide layers onto the surface of a {100} wafer and then etching away the bulk silicon from under the resistor. Several IR pixels fabricated by the author are shown in Fig. 4.17. The advantage of this type of structure is that the resistor is thermally isolated from the bulk of the wafer. Therefore, when current is driven through the resistor and the resistor heats up, the heat is not dispersed into the bulk material. Instead, the heat is emitted as IR radiation. If enough current is applied to the resistor, the isolated platform generates enough thermal energy to emit light in the visible spectrum. These devices show one of the advantages that bulk micromachining can provide. In this case, thermal isolation is provided allowing the pixel to more efficiently emit IR radiation, however, with other devices, the advantage is the electrical isolation provided [85].

4.2.2 Movable Components and Structures. Using the simple structures discussed above, a large variety of devices can be fabricated. However, with surface micromachined designs, the above components are limited to the design of planar fixed position structures. In order to overcome these limitations, a variety of movable components can be fabricated. The primary components of movable systems are sliders to allow linear motion, pin joints to

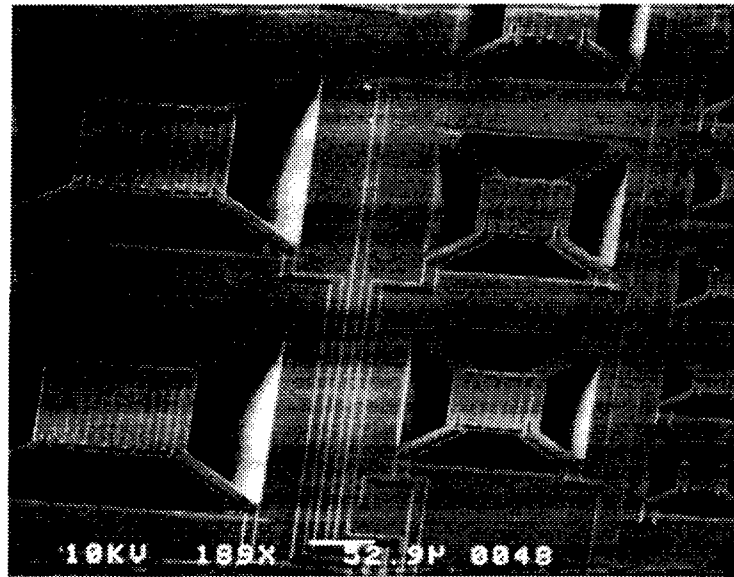


Figure 4.17. Several IR pixels fabricated at AFIT using the CMOS-MEMS process.

allow rotation, and micro-hinges to allow flip-up structures. Combining these components allows the design of a large variety of micromechanical systems. Several examples of flip-up devices that utilize sliders, pin joints and micro-hinges are also included in the following discussion.

Sliders. A micromechanical slider is shown in Fig. 4.18. The slider consists of two pieces; a releasable plate, and a guide. The releasable plate is formed from the first releasable polysilicon layer in the MUMPs process. The plate is not anchored to the substrate, and is therefore free to move. The guide is formed using the second releasable polysilicon layer. One side of the guide projects over the edge of the releasable plate while the other side is anchored to the substrate. By placing guides on opposing sides of the plate, the movement of the plate is restricted to the direction defined by the guides.

Pin Joints. The construction of a pin joint is similar to that of a slider, except that the guide is now circular as shown in Fig. 4.19. The center of the guide is anchored while the outside edge projects over the plate. A circular hole is cut into the center of the plate in conjunction with the circular anchor of the pin joint.

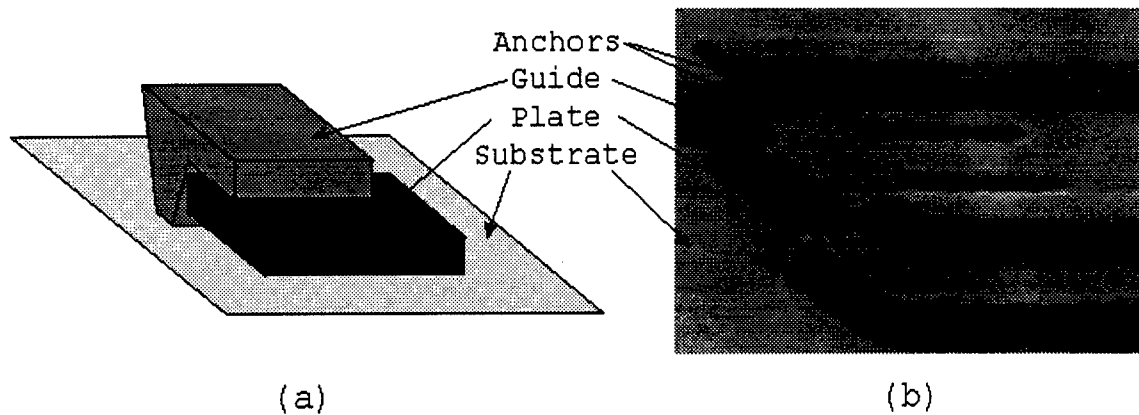


Figure 4.18. Sliders that allow linear motion of a plate are fabricated in surface micromachining processes using two releasable polysilicon layers. The basic design is shown in the schematic view, (a), while a fabricated slider is also shown, (b).

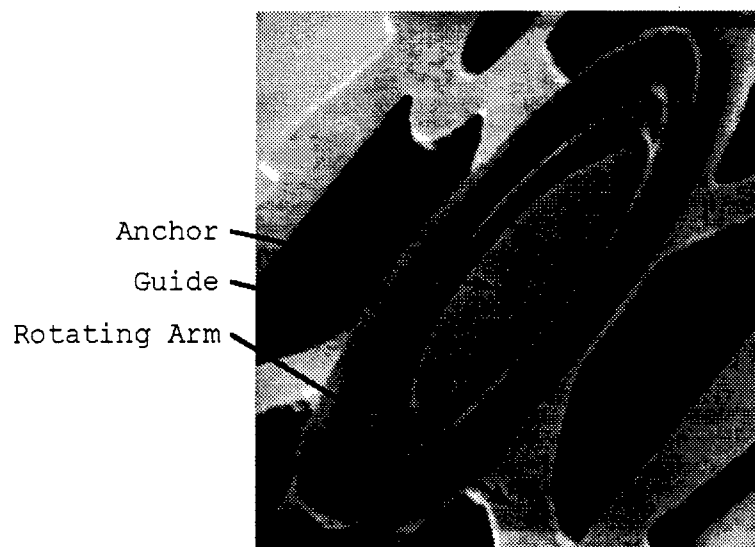


Figure 4.19. SEM micrograph of a pin joint fabricated using MUMPs.

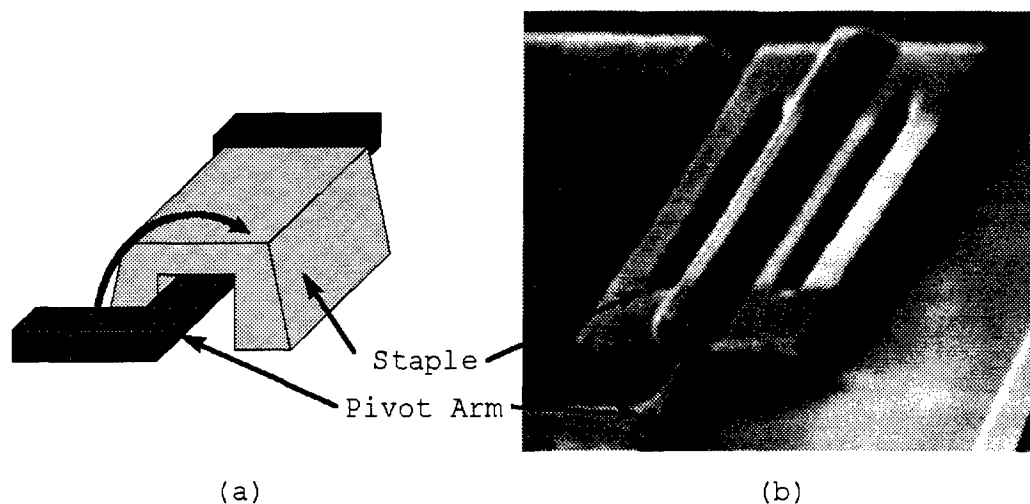


Figure 4.20. The basic substrate hinge consists of a staple and a pivot arm. (a) Schematic of a substrate hinge. (b) SEM micrograph showing a substrate hinge fabricated using MUMPs.

Micro-Hinges. Three basic types of micro-hinges exist; the substrate hinge, the floating substrate hinge, and the scissors hinge. The substrate hinge and the scissors hinge were originally designed and fabricated by Pister, *et al.* [105, 106], while the floating substrate hinge is a modification of the substrate hinge. All three hinge designs require two releasable polysilicon layers for their fabrication.

The basic substrate hinge is shown in Fig. 4.20. The hinge consists of two components, a pivot arm and a staple. The pivot arm is simply a long, narrow, thin arm fabricated from the lower releasable polysilicon layer. The structure that is going to be flipped up off of the substrate is connected at the ends of the pivot arm. The staple is fabricated from the upper releasable polysilicon layer, and forms a bridge over the pivot arm. The staple is not connected to the pivot arm, and allows the rotation of the pivot arm as seen in Fig 4.20.

A floating substrate hinge is fabricated by replacing the anchors of the substrate hinge with connections to the lower polysilicon layer as shown in Fig. 4.21. The pivot arm is still not connected to the staple, but the staple is now floating which allows the hinge to move. The staple is mounted to the substrate by either connecting it to a pin joint or a slider.

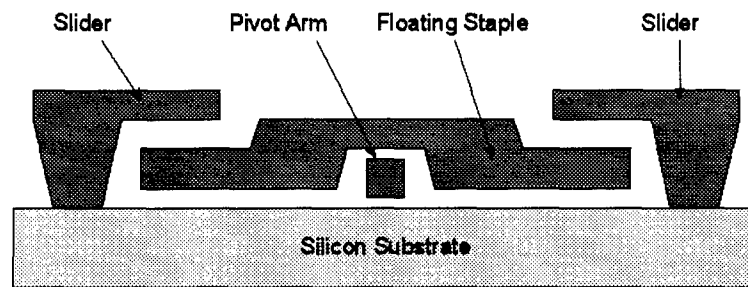


Figure 4.21. The floating substrate hinge is a modification of the substrate hinge that allows the staple to be held in place by either a slider or a pin-joint instead of anchors. The floating substrate hinge allows the fabrication of movable flip-up structures.

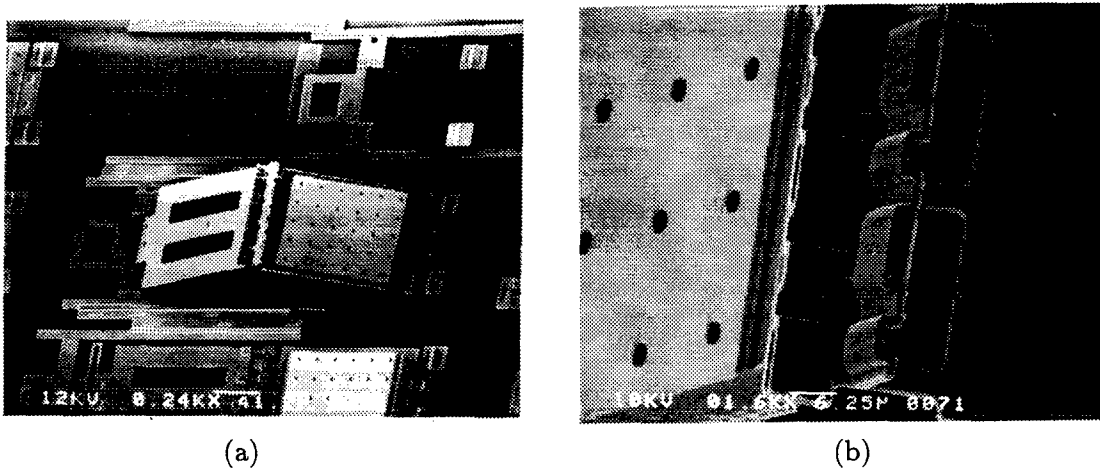


Figure 4.22. (a) A flip-up mirror fabricated by the author using all three types of micro-hinges. (b) Close up of the scissors hinge connecting the two plates.

Scissors hinges are fabricated by interlocking fingers of both polysilicon layers. Scissors hinges allow two plates to be connected together while still allowing them to pivot. A flip-up mirror that utilizes all three types of hinges shown in Fig. 4.22a, while Fig. 4.22b shows a close up of the scissors hinge. This device was the first complete system successfully fabricated by the author using MUMPs.

Flip-Up Components. Utilizing substrate hinges, it is possible to build a large variety of flip-up components such as plates, mirrors, gratings, and lenses [9, 8]. An example of a flip-up plate is shown in Fig. 4.23. The plate can be patterned as desired to serve the appropriate function. After the devices are released, the plates are flipped up

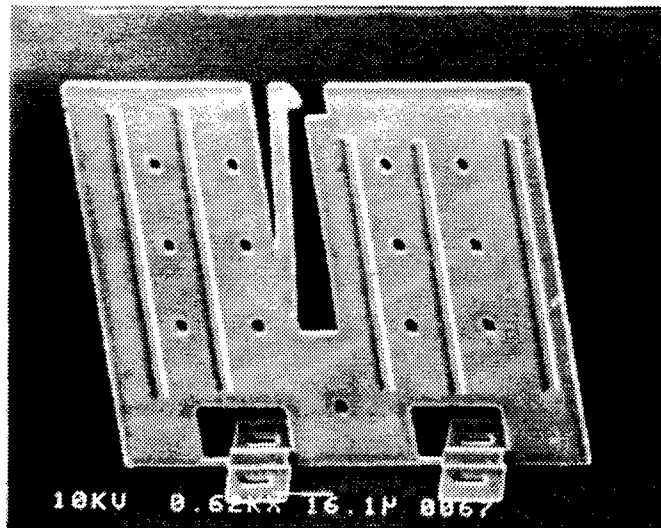


Figure 4.23. A plate that has been flipped up off of the substrate.

off of the substrate using microprobes. Unfortunately it is often difficult to get the probe under the plate. Therefore, it becomes necessary to employ a micromachined device to aid in lifting the plate. Figure 4.24 shows the device that is typically used at AFIT. This device was originally designed by Sene as part of his Masters degree thesis research [107]. The devices shown in Fig. 4.24 are part of a test cell designed by the author to study the performance of self engaging locks that will be described later. The flip helper consists of a micro-jack and a sliding push up mechanism. The jack is a narrow cantilever formed from the lower releasable polysilicon layer. The micro-jack runs from an anchor, under an arm connected to the flip-up plate, and ends with a fat end that can be pushed with a microprobe. By pushing on the end of the jack, the cantilever bows pushing up on the arm connected to the plate and lifting the plate off of the substrate. The push up mechanism is connected to the flip-up plate by a scissors hinge. By sliding the push up mechanism towards the plate hinges, the arm of the helper pushes the plate up off of the substrate.

For most applications, it is desirable to fix the plate in a specific position. In order to do this, a locking mechanism is required. Several different locking mechanisms exist. Many designs utilize a second flip-up plate. The second plate is at a 90 degree angle with the first plate. The lock works by initially flipping the first plate into the desired position. Next, the second plate is flipped up. A notch in the second plate engages with the first

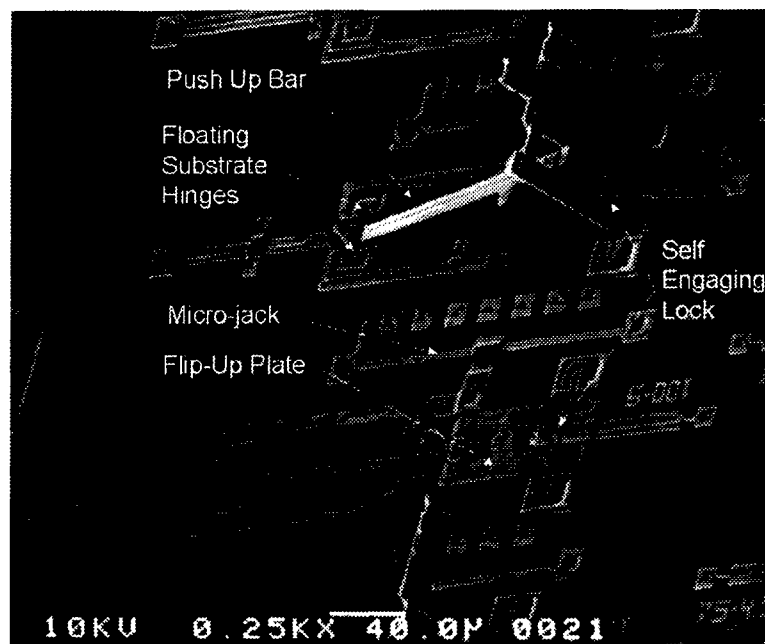


Figure 4.24. A flip-up helper.

plate, and the plates are both locked into position. The problem with this design is that both plates must be flipped up into position, therefore requiring that a person use a probe station to lift both plates.

Self engaging locking mechanisms have also been designed. The locking mechanism uses a keyhole type design. In the base of the flip-up plate, a hole with a narrow base and wide top is cut. Using the upper polysilicon layer, a lock arm is fabricated. The locking arm extends from over the top of the keyhole out over the pivot arm of the micro-hinges to an anchor. The width of the locking arm is larger than the width of the narrow hole, but thinner than the width of the wider hole. Near the end of the locking arm projecting over the keyhole, grooves are cut to match the width of the narrow hole. When the flip-up plate is rotated off of the substrate, it pushes upward on the arm and the tip of the arm extends through the hole. At a certain angle, determined by the location of the grooves on the locking arm, the grooves engage with the locking mechanism, and the plate is locked into position. Figure 4.25 shows two different locks that have been engaged. Figure 4.25a is an older design. The contouring at the end of the arm leads to problems with getting the lock engaged. However, as shown in Fig. 4.25b by redesigning the lock it is possible

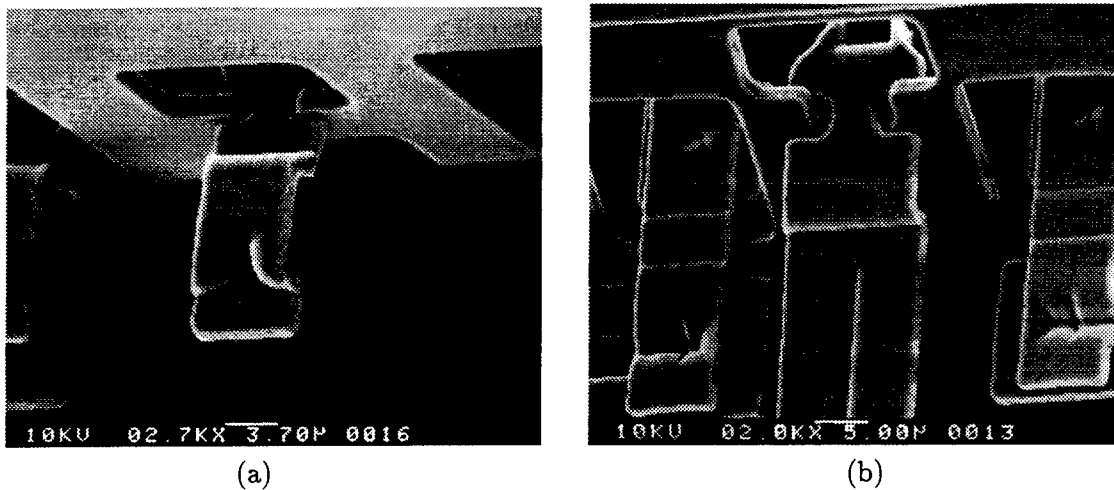


Figure 4.25. Close up view of a self engaging locking mechanism fabricated by the author. (a) In the original design, the end of the lock was contoured making it difficult to flip-up the plate. (b) Redesigning the plate removes the contours making it easy to flip-up the plate.

to remove the contours. The primary advantage of the self engaging lock is that it is only necessary to flip-up one plate. This becomes important in the design of electrically assembling structures. By anchoring the lock to a floating plate instead of the substrate, this type of lock can be easily implemented for floating structures.

Flip-Up Platforms. In the development of MEMS optical systems, it is often desirable for components to be positioned above the substrate by a significant distance. The author, therefore, designed flip-up platforms utilizing all three types of micro-hinges combined with several polysilicon plates. The platforms can be used to support components such as mirrors, lenses, and gratings. Figure 4.26 shows an example of an elevated platform with a Fresnel lens designed into the suspended plate. The lens is suspended $100\text{ }\mu\text{m}$ above and parallel to the substrate. The angle between the suspend platform and the substrate can be defined arbitrarily by sloping the top of the two supporting plates. This type of platform can potentially be used for interfacing semiconductor lasers to components on the substrate, or interfacing optical fibers.

Moving Flip-Up Devices. It is also possible to fabricate flip-up structures that can be moved. This is done by replacing the standard substrate hinges with floating

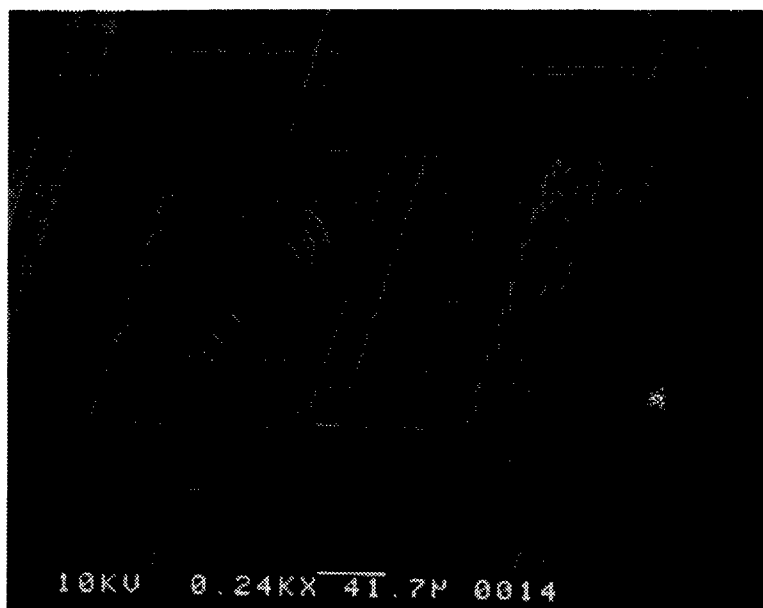


Figure 4.26. A Fresnel lens is raised 100 μm above the substrate using several flip-up plates connected by micro-hinges.

substrate hinges. Several advantages can be realized with moving structures. First, by moving a structure, it is no longer subjected to contouring caused by the design of lower layers. It is now possible to lift a structure and move it to a portion where lower layers have been fabricated completely independently. Second, rotating devices can be made for use in beam steering or other applications. And third, movable devices can be repositioned to align a system for better performance.

One example of a flip-up structure designed by the author is shown in Fig. 4.27. The structure is an elevated platform similar to that described in the last section. A lens is elevated 100 μm above the substrate. The base of the side plates are connected to floating substrate hinges connected to sliders. The entire structure can now be slid over a structure such as a mirror as shown in Fig. 4.27. Another device designed by the author is the rotating flip-up mirror shown in Fig. 4.28. The mirror flips up and is locked in a position normal to the substrate using self engaging locks. The mirror is connected to the substrate via floating substrate hinges mounted to a pin joint. When flipped up, the mirror is held normal to the substrate by self-engaging locks. After the mirror is locked into position, it can be rotated around the pin joint through 360 degrees.

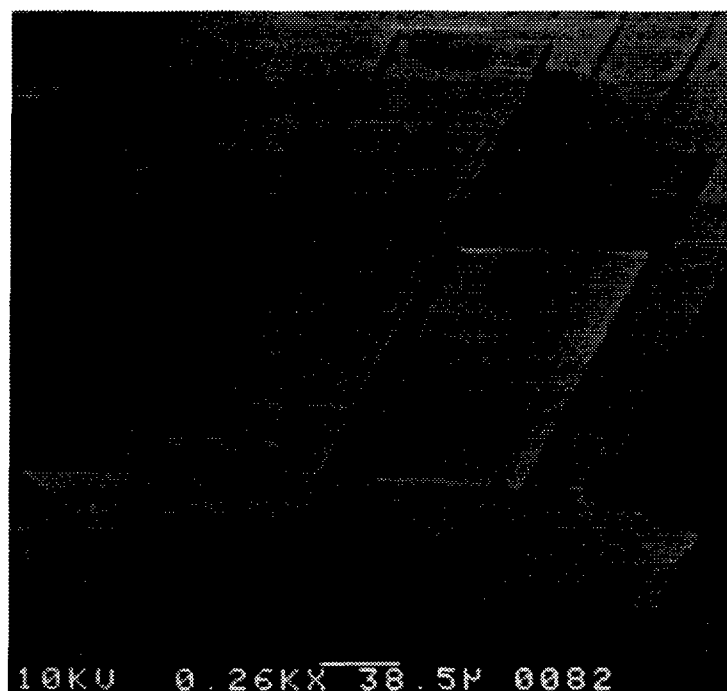


Figure 4.27. A Fresnel lens is raised 100 μm above the surface of the substrate. The elevated lens can then be moved so that it is over another device that is fabricated on the surface of the substrate. The device shown here has been slid over a gold mirror.

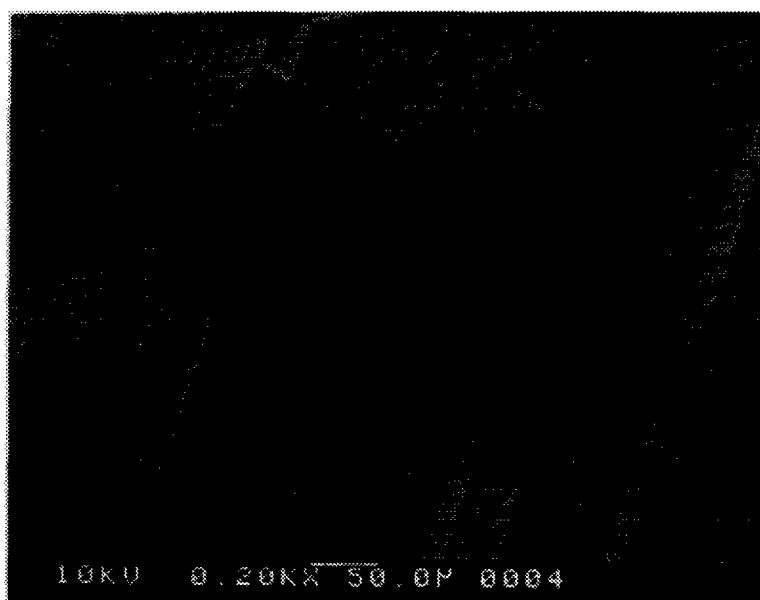


Figure 4.28. A mirror is flipped up and locked into a position normal to the substrate. The mirror is free to rotate 360 degrees around the pin joint while remaining normal to the substrate.

Table 4.3. Desired Actuator Criteria

Criteria	Reason
High Force	Necessary to drive large components and overcome the friction of moving components
Large Deflection	Actuator must deliver sufficient deflection for the problem
Low Electric Power Consumption	CMOS compatibility is desired for large scale MEMS applications, and integration with integrated CMOS control logic
Small Footprint	Allows the fabrication of more actuators on a die
High Frequency Operation	Many applications require high frequency modulation of the mechanical devices

4.2.3 Actuators. So far, all of the devices described have simply been micromechanical structures. In order to provide motion to these structures, a variety of actuators are needed. Much of the recent work in MEMS has been in the design of various types of actuators. The primary modes of actuation are electrostatic, thermal, and magnetic. All of the work done here at AFIT, has utilized electrostatic and thermal actuators.

Determining the proper type of actuator to use for a given application depends on a number of criteria. Table 4.3 lists the primary criteria. For actuators of the same size, electrostatic actuators typically generate less deflection and force than thermal actuators. This is primarily a problem when the actuator is required to deliver a static force, and as a result, electrostatic actuators are generally used in resonant systems allowing them to deliver a larger deflection. To produce larger forces, the electrostatic actuators must be increased in size. Unfortunately, thermal actuators generally require more electrical power than electrostatic actuators. Further, thermal actuators operate at lower frequencies than corresponding electrostatic actuators.

The following discussion covers several of the actuators used at AFIT. First, the two primary electrostatic actuators are presented. Next, three types of thermal actuators are discussed. This includes an extensive discussion of the design and performance of a lateral thermal actuator originally developed by Comtois [4]. This actuator is the primary actuator used at AFIT, and extensive tests were performed by the author to optimize the actuator design and characterize its performance.

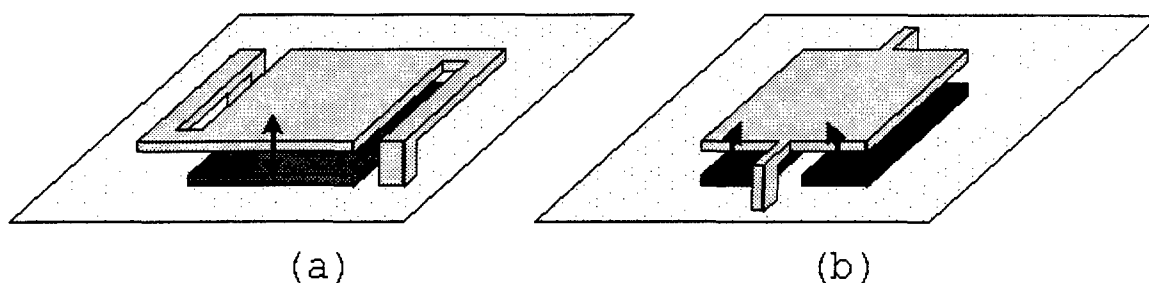


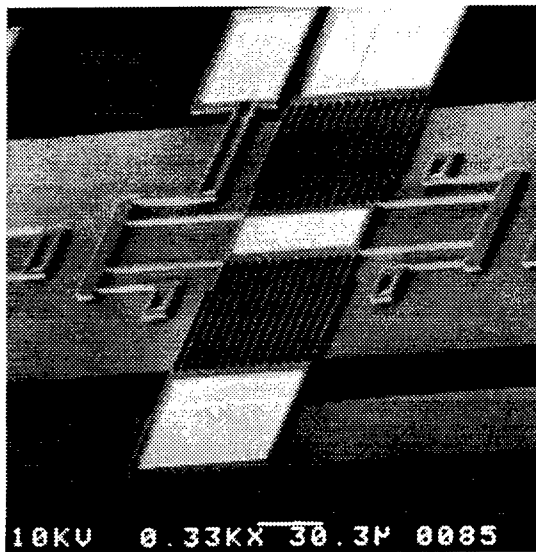
Figure 4.29. Parallel plate actuators can be used to fabricate either a piston actuator (a), or a torsional actuator (b). The arrows indicate motion of the suspended plate when a voltage is applied to the electrodes.

Parallel Plate Actuators. Applying a voltage potential across two plates results in an attractive force, F . The force can be calculated as [108]

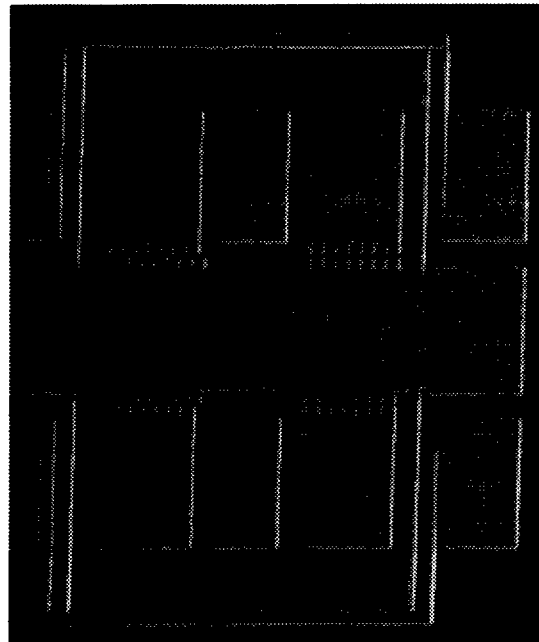
$$F = \frac{\epsilon_0 A V^2}{2d^2} \quad (4.1)$$

where ϵ_0 is the permittivity of air, A is the area of the plates, V is the applied voltage, and d is the distance between the two plates. For devices fabricated in a surface micromachining process, parallel plate actuators can be used in two primary types of designs as shown in Fig. 4.29. The piston type actuator is capable of moving in a single direction normal to the surface of the substrate, while the torsional axis allows a suspended plate to rotate about a beam. Mirrors based on both torsional rotation and piston motion have been fabricated at AFIT [4, 69, 109]. Piston mirrors were originally studied for aberration correction [69], while torsional mirrors have been used elsewhere for display applications [63, 110].

The motion of a parallel plate actuator is limited by the distance separating the suspended plate from the substrate. For the MUMPs process, this distance can be up to $4.75 \mu\text{m}$, however, the voltage required to move the device is directly proportional to the distance separating the plates. Therefore, the designer faces a trade off between the maximum motion of the actuator and the required voltage. A second problem with parallel plate actuators is that the force is inversely proportional to the square of the plate separation, d . Therefore, as the voltage is increased, the force increases, which pulls the plates closer together further increasing the force. The actuators become unstable after the gap has decreased by over one third of the total distance separating the plates [111].



(a)



(b)

Figure 4.30. Comb resonators fabricated by the author using MUMPs (a), and LIGA (b).

Typically this results in the actuator slamming down to the substrate, and the plates coming in contact. A final limitation of the parallel plate actuators is that the motion is normal to the substrate and no good method exists for coupling this motion with other components.

Comb Resonators. In order to use coulomb forces in a lateral resonator, it is necessary to find a method to couple power without the large surface area of two parallel plates. The conventional solution is to use intertwined fingers as shown in Fig. 4.30. The fingers of the electrodes appear like the teeth of a comb, and therefore the device is referred to as a comb resonator. The resonator has three elements, two electrodes and one platform. Typically, one electrode is used to drive the system and the other is used to sense the motion. Therefore, in many applications, only one electrode is used. Applying a potential between the electrode and the platform results in an attractive force. Unfortunately, the force is relatively small, and thus to achieve large displacements, it is necessary to either apply a large voltage or to operate the device in a resonant mode by applying an AC drive

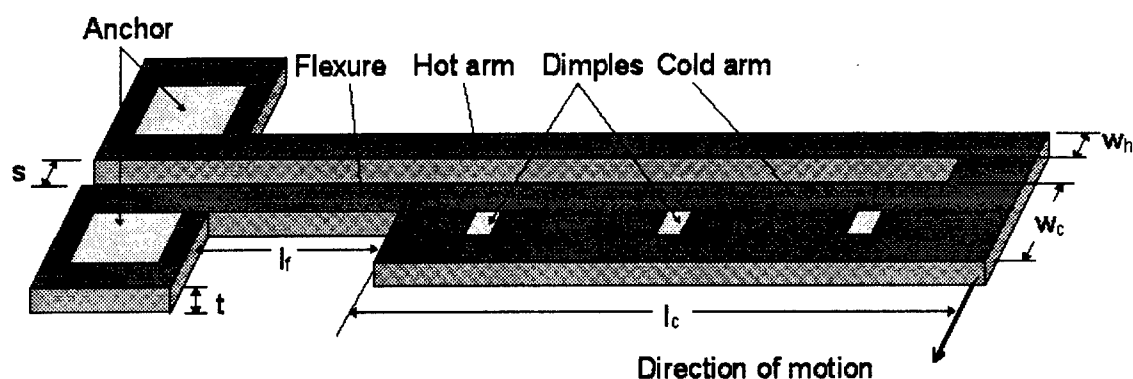


Figure 4.31. Basic design of the lateral thermal actuator. Typical dimensions are: $t = 2.0 \mu\text{m}$, $w_h = 2.5 \mu\text{m}$, $w_c = 15 \mu\text{m}$, $l_f = 40 \mu\text{m}$, $l_c = 200 \mu\text{m}$, $s = 2.5 \mu\text{m}$. The $4 \mu\text{m}$ square dimples prevent stiction to the substrate. This actuator provides deflections of $16 \mu\text{m}$ at 3 V and 3.5 mA.

signal to the drive electrode. Due to the large voltages, small static deflections, and low force generated, comb resonators have not been widely used at AFIT.

Bimorphs. A bimorph actuator is created by fabricating a cantilever utilizing two thin films, one on top of the other. The materials are chosen so that they have differing coefficients of thermal expansion. Therefore, when the materials are heated, one material expands more than the other and the actuator moves either up or down. This same principle can also be applied to stacks of thin films to generate multi-morph actuators.

The first actuators fabricated at AFIT utilized thermal heating of multi-morph layers to generate motion [75]. Read fabricated a large variety of multi-morph actuators and in his thesis he discusses their design, testing, and performance [75].

Lateral Thermal Actuators. Lateral thermal actuators are the primary actuators developed and used at AFIT. These actuators offer high force ($>5 \mu\text{N}$), large deflection ($>15 \mu\text{m}$), and CMOS compatible voltage and current levels. The actuators can be fabricated in either of the two releasable MUMPs layers or a combination of both. They were originally fabricated using MUMPs by Comtois and Phipps [112].

The basic design of the actuators is shown in Fig. 4.31. A fabricated actuator is shown in Fig. 4.32. Applying a voltage across the two anchors results in a current through the

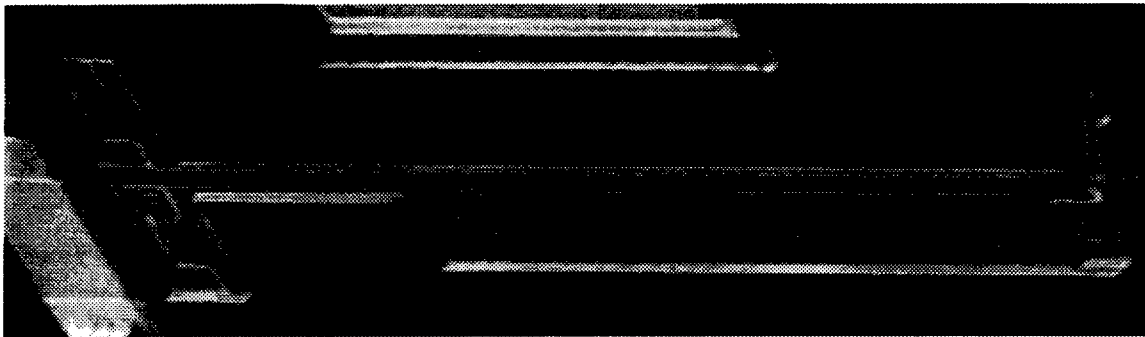


Figure 4.32. A lateral thermal actuator fabricated using MUMPs.

actuator. The higher electrical and thermal resistances of the hot arm cause it to heat up more than the cold arm. This results in a larger thermal expansion of the hot arm causing the tip of the actuator to deflect in an arcing motion in the direction shown in Fig. 4.31. Due to the simple design of the actuator, it can be fabricated in any MEMS process with a releasable current carrying layer. However, the relatively high resistivity of polysilicon allows the MUMPs based actuators to operate at voltages and currents compatible with standard integrated circuit electronics. For example, a $220\text{ }\mu\text{m}$ long, $2\text{ }\mu\text{m}$ thick actuator with a $2.5\text{ }\mu\text{m}$ wide hot arm produced a force of $4.4\text{ }\mu\text{N}$ at an input power of 10.8 mW (2.94 V , 3.68 mA) easily delivered by standard CMOS circuitry. This actuator can deflect up to $16\text{ }\mu\text{m}$ at the tip when unloaded.

The lateral thermal actuators operate in two primary modes. The first, or forward mode, is that described above. However, when a large current is applied to the actuators, the hot arm begins to glow and the polysilicon of the hot arm reforms. When the current is stopped, the device cools, and the actuator moves back into a negative deflection position. Driving the actuator with current causes the actuator to move from the new negative rest position back towards the initial zero deflection position. Typically, the actuators provide more deflection and force in the back bent mode of operation. Therefore, the actuators are typically designed to operate in the back bent mode.

Due to the simple and reliable design of the actuators, the high force delivered, the large deflections, and the small size required for individual actuators, these lateral thermal actuators are the primary actuators used at AFIT. Therefore, a large effort has

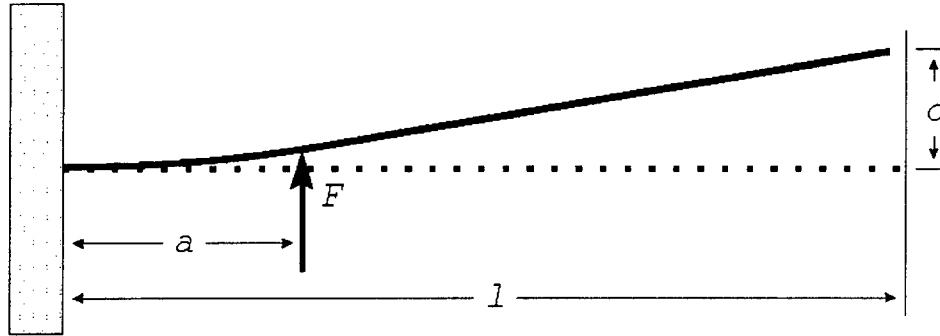


Figure 4.33. A force, F , is applied to a beam that is rigidly supported on one end. The force is applied a distance, a , from the supported end of the beam. As a result, the beam deflects a distance, d , at the tip.

gone into characterizing the performance of these actuators. Comtois and Phipps originally studied the deflection of the actuators with respect to the applied current [4, 112, 113]. The actuators are capable of producing deflections from 10-20 μm depending upon the design parameters used. In general, longer actuators provide more deflection. Prior force measurements of the devices were made by Comtois and showed the devices were capable of delivering several μN of force [4]. As a part of this dissertation research, extensive studies of the force produced by the thermal actuators were performed. The study was done using a new force tester designed by the author. The force is measured by using the actuator to apply a force to a flexible beam as shown in Fig. 4.33. The force that is applied to the beam can then be calculated from the observed deflection of the tip of the beam as [114]

$$F = \frac{Etw^3}{2(3a^2l - a^3)} \times d \quad (4.2)$$

where E is the effective Young's modulus of polysilicon, w is the width of the force tester beam, and a , d , and l are as defined in Figs. 4.33 and 4.34. Figure 4.34 shows the layout of the force tester, while Fig. 4.35 shows a fabricated force tester with a thermal actuator next to it.

Several arrays of force tester/actuator pairs were fabricated. Each array varied one or more parameters. Devices were fabricated with varying thickness, flexure length, cold arm length, hot arm width, and arm separation. Five copies of each individual tester/actuator pair were included. Measurements were taken by placing the released MUMPs die on a

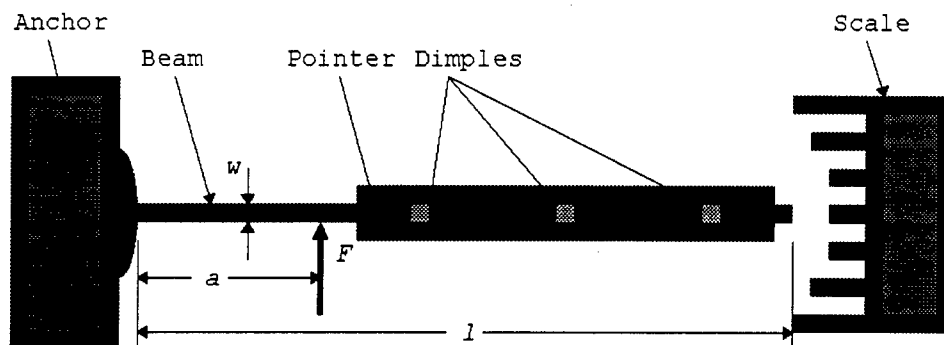


Figure 4.34. Schematic of the force tester, the thickness, t , is uniform. Typical values are $w = 2.0 \mu\text{m}$, $a = 60 \mu\text{m}$, $l = 240 \mu\text{m}$, and $t = 2.0 \mu\text{m}$.

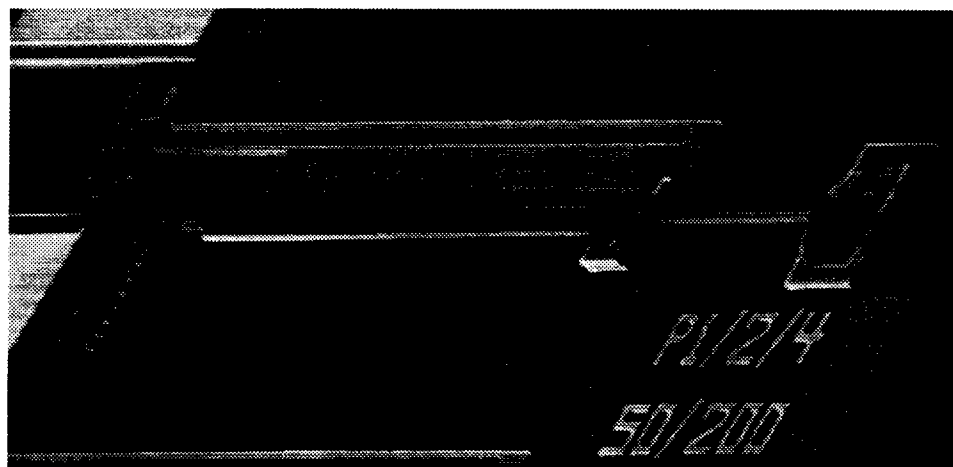


Figure 4.35. Scanning electron micrograph of a released force tester next to a thermal actuator. The force tester shown here has values $w = 2.0 \mu\text{m}$, $a = 25 \mu\text{m}$, $l = 125 \mu\text{m}$, and $t = 2.0 \mu\text{m}$. The actuator has parameters $t = 2.0 \mu\text{m}$, $w_h = 2.0 \mu\text{m}$, $w_c = 14 \mu\text{m}$, $l_f = 50 \mu\text{m}$, $l_c = 150 \mu\text{m}$, $s = 4.0 \mu\text{m}$.

probe station. Probes were used to place a differential voltage on the actuator anchors. The deflection of the force tester tip was observed, and the applied voltage adjusted until the tip was displaced by a multiple of $2.0\ \mu\text{m}$. The voltage and current were then recorded. Voltage measurements were made with a Fluke 77/bn digital multi-meter in parallel with the probes. Current measurements were taken with a Fluke 8600a digital multi-meter in series with one of the probes. Values were recorded for all deflections that are multiples of $2.0\ \mu\text{m}$ that the actuator could repeatably achieve. The maximum deflection of the force tester tip was also observed. Values of delivered force versus applied electric power were consistent for similar actuators. However, the maximum displacement showed more variance. Measurements were taken from three copies of each tester/actuator pair and the results averaged.

Using Eq. 4.2, the force required to deflect the tester was calculated. For a typical force tester with $E = 162\ \text{GPa}$, $w = 1.93\ \mu\text{m}$, $t = 2.0\ \mu\text{m}$, $a = 60\ \mu\text{m}$, and $l = 240\ \mu\text{m}$ a tip deflection of $6.0\ \mu\text{m}$ requires that $2.9\ \mu\text{N}$ be applied. The width, w , has a design parameter of $2.0\ \mu\text{m}$, however, during fabrication the polysilicon is over-etched resulting in a value that is below the design value. The actual value is determined by observing the devices under a scanning electron microscope. For all calculations, the corrected value is used, however, for general discussion the design values are reported. Figure 4.36 shows the electric power required to generate force for actuators of several thickness values, while Figs. 4.37-4.40 show the maximum force generated by actuators while individual parameters were varied.

The measured values provide several conclusions about the design of the actuators. First, the hot arm design width should be slightly larger than the actuator thickness. This is seen in Fig. 4.37 where the maximum delivered force rises rapidly until the hot arm width is over 1.25 times the thickness. It is also clear from Fig. 4.39 that increasing the arm separation results in improved force. However, increasing the separation also reduces the maximum deflection [112]. The typical separation used is then $2.5\ \mu\text{m}$. Flexure length appears to play a minor role in the overall delivered force, however, a flexure that is approximately one third of the cold arm length is desirable. Increasing the thickness results in improved force, but requires significantly more power. The $2.0\ \mu\text{m}$ thick polysilicon

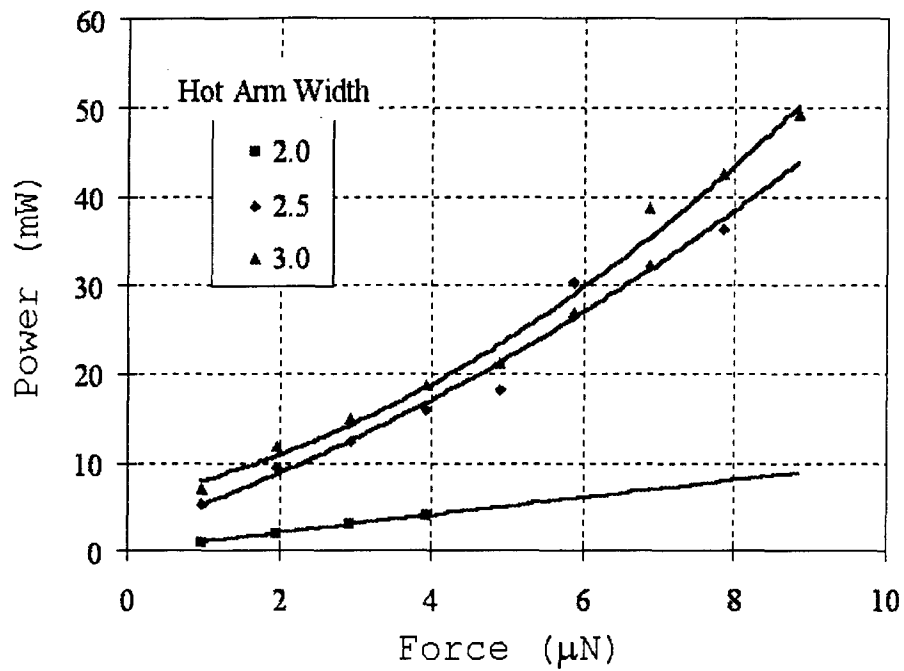


Figure 4.36. Electrical power versus the delivered force. The actuators have parameters: $t = 2.0 \mu\text{m}$, $w_c = 14 \mu\text{m}$, $l_f = 30 \mu\text{m}$, $l_c = 170 \mu\text{m}$, $s = 2.0 \mu\text{m}$.

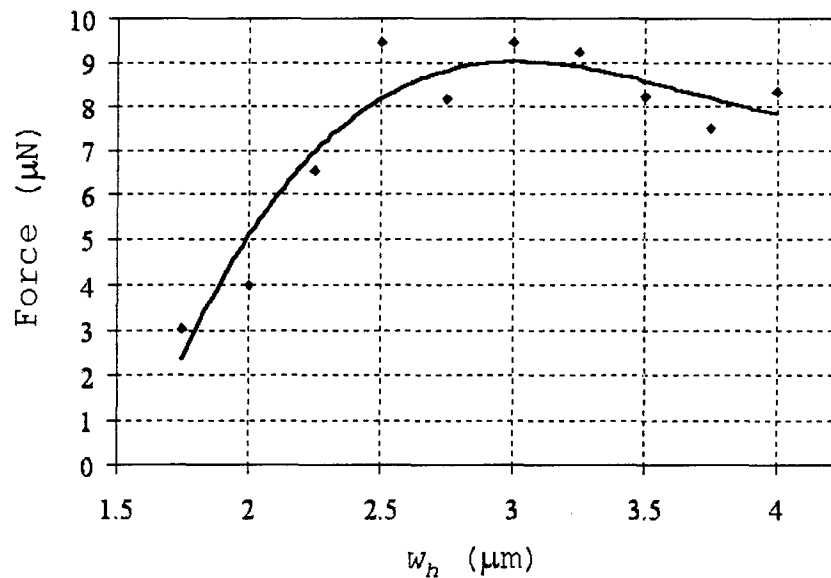


Figure 4.37. Maximum delivered force versus hot arm width. The actuators have parameters: $t = 2.0 \mu\text{m}$, $w_c = 14 \mu\text{m}$, $l_f = 30 \mu\text{m}$, $l_c = 170 \mu\text{m}$, $s = 2.0 \mu\text{m}$.

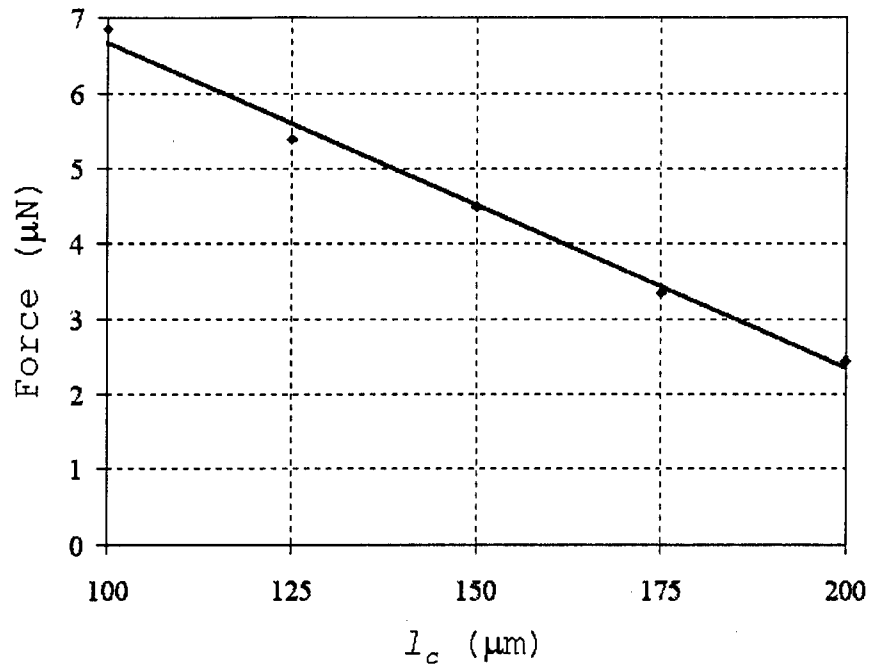


Figure 4.38. Maximum delivered force versus cold arm length. The actuators have parameters: $t = 2.0 \mu\text{m}$, $w_h = 2.0 \mu\text{m}$, $w_c = 14 \mu\text{m}$, $l_f = 30 \mu\text{m}$, and $s = 2.0 \mu\text{m}$.

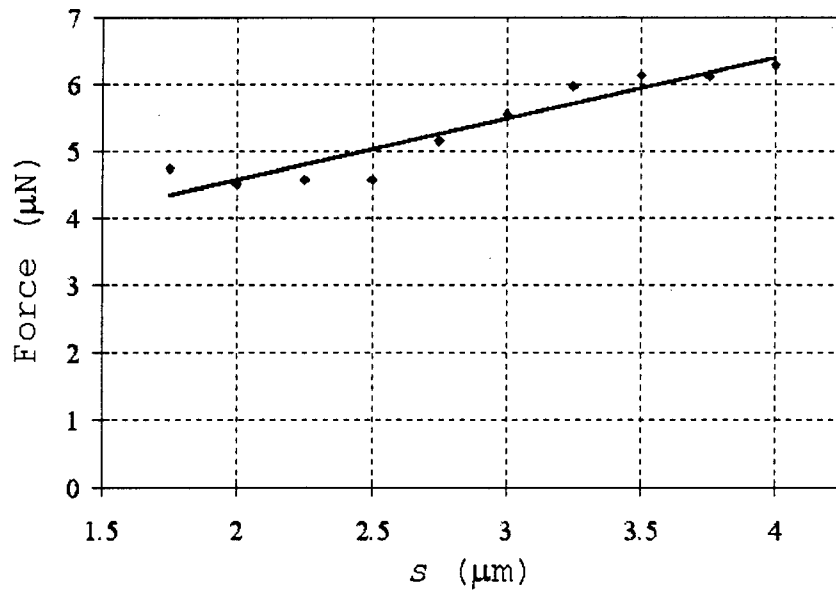


Figure 4.39. Maximum delivered force versus arm separation. The actuators have parameters: $t = 2.0 \mu\text{m}$, $w_h = 2.0 \mu\text{m}$, $w_c = 14 \mu\text{m}$, $l_f = 50 \mu\text{m}$, and $l_c = 150 \mu\text{m}$.

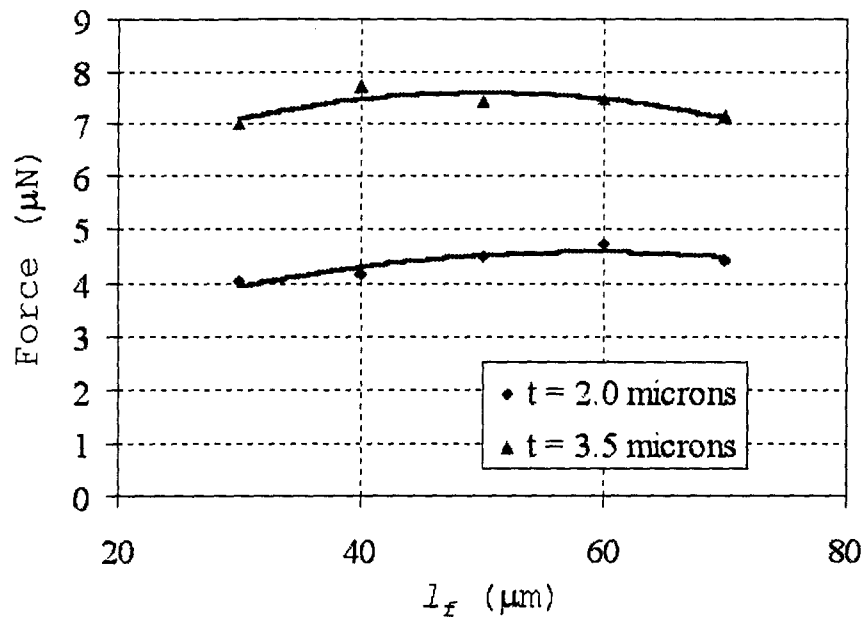


Figure 4.40. Maximum delivered force versus flexure length. The actuators have parameters: $w_h = 2.0 \mu\text{m}$, $w_c = 14 \mu\text{m}$, $l_c + l_f = 50 \mu\text{m}$, and $s = 2.0 \mu\text{m}$.

layer is ideal for the actuators since it results in CMOS compatible drive voltages and currents. Finally, increasing the length of the cold arm is shown to result in a decrease in the delivered force. Actuators with dimensions $t = 2.0 \mu\text{m}$, $w_h = 2.5 \mu\text{m}$, $w_c = 16 \mu\text{m}$, $l_f = 45 \mu\text{m}$, $l_c = 180 \mu\text{m}$, and $s = 2.5 \mu\text{m}$ provide a good balance between deflection, force, and electrical power.

Arrays of Lateral Thermal Actuators. Individual thermal actuators suffer from two primary limitations. First, the force delivered by an individual actuator is often insufficient to drive complex systems, and second, the actuators move in an arcing motion, while a linear motion is generally preferred. Both problems are solved by combining the force and motion of multiple actuators using a compliant yoke as seen in Fig. 4.41. The yoke combines the motion of the actuators into a linear deflection. It is critical that the yoke allow the actuators to freely move in a direction normal to the desired actuation while coupling their motion in the desired direction. Measurements of the force generated by actuator arrays with 2 to 20 actuators were taken using the force testers described in the previous section. Figure 4.42 shows the measured performance. Note that the coupled

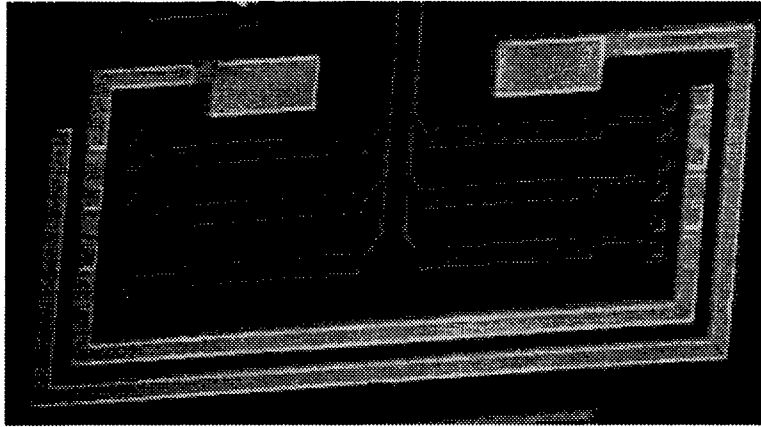


Figure 4.41. Scanning electron micrograph of an array of six $210\ \mu\text{m}$ long thermal actuators connected with a compliant yoke. The yoke combines the forces of the actuators and converts their arcing motions into a linear motion of the yoke. Actuators are wired in parallel. The array shown here is connected to a force tester.

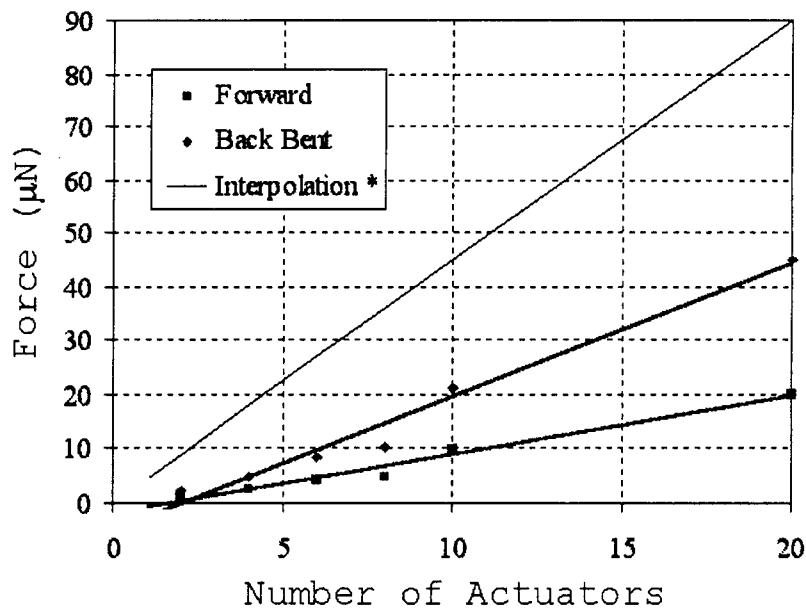


Figure 4.42. Maximum delivered force versus number of actuators in an array. The actuators have parameters: $t = 2.0\ \mu\text{m}$, $w_h = 2.0\ \mu\text{m}$, $w_c = 14\ \mu\text{m}$, $l_f = 50\ \mu\text{m}$, $l_c = 160\ \mu\text{m}$, and $s = 2.0\ \mu\text{m}$. The linear projection is based on the force of an individual array multiplied by the number of actuators.

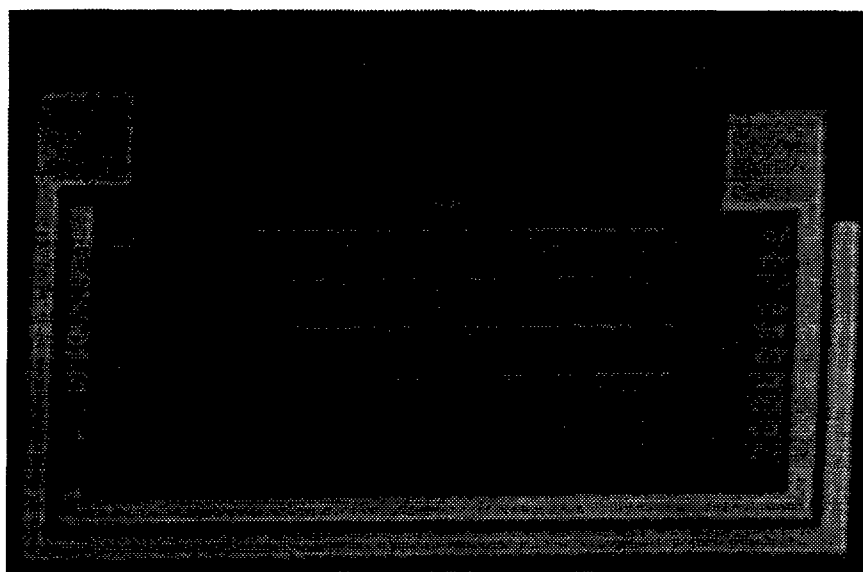


Figure 4.43. The optimized actuator array shown here has 10 actuators that are each $230\text{ }\mu\text{m}$ long. The yoke design is similar to one developed by Comtois [4].

force is approximately linear with respect to the number of actuators in the array, however, the measured force is well below the maximum force determined by multiplying out the maximum force of an individual actuator. The primary cause of the discrepancy is the yoke design. The yoke design used in the array from which the force measurements were taken was an older design resulting in lower performance. A newer yoke design has been fabricated and is shown in the next section.

Optimized Actuator Design and Characterization. Combining the information learned from deflection testing by Comtois and Phipps [112] with the force testing performed in this dissertation, a new optimized actuator has been designed. This actuator should provide both good deflection ($> 10\text{ }\mu\text{m}$) and good force ($> 5\text{ }\mu\text{N}$). Further, a modified yoke design based on the yoke of Comtois [4] has been designed. Test cells to measure the force, deflection, and back bending characteristics of the new design were fabricated on MUMPs14. Measurements have not yet been taken, but should be available shortly. The optimized actuators have dimensions: $t = 2.0\text{ }\mu\text{m}$, $w_h = 2.5\text{ }\mu\text{m}$, $w_c = 16\text{ }\mu\text{m}$, $l_f = 50\text{ }\mu\text{m}$, $l_c = 180\text{ }\mu\text{m}$, and $s = 2.5\text{ }\mu\text{m}$. The new actuator array is shown in Fig. 4.43.

Vertical Thermal Actuators. The basic principal of the lateral thermal actuators can be modified to allow a vertical thermal actuator to be fabricated. The design was originally fabricated by Phipps [113] and has since been modified. The basic design requires the fabrication of a cold arm and a hot arm at different elevations above the substrate. If the hot arm is lower than the cold arm, then when the resistor is heated, the actuator will move up, and if the hot arm is higher than the cold arm, the actuator will move down. However, as with the lateral thermal actuators, the device can be back bent, and the actuators can be used in either mode of operation. Vertical actuators have been fabricated to lift flip-up structures a few microns off of the substrate allowing probes to get under the plate, or allowing a linear micro-motor to be engaged and lift the plate into position [4].

4.2.4 Systems. Utilizing many of the components that have been described in the previous sections, complex MEMS can be designed and fabricated. Directly coupling the lateral thermal actuators with flip-up components led to the creation of several systems by the author. The first systems discussed are flip-up micromirrors that can be positioned using the thermal actuators. The first design allows the angle between the mirror and the substrate to be modulated, while the second design allows the mirror to be rotated about a pin joint. These directly coupled designs offer simplicity, and one to one position versus voltage responses, however, the motion of the mirrors is limited by the maximum deflection of the actuators. Therefore, several flip-up rotating micromirrors that are driven using a micromotor were also designed and fabricated by the author. The mirrors are locked into a position normal to the substrate and are free to rotate 360 degrees about a pin joint. A micromotor, based on the original design by Comtois [4], has been coupled to several of the mirrors. In most of the designs the motor is capable of driving the mirror through over 180 degrees, however in some of the designs, the motor can drive the mirror through 360 degrees.

Scanning Micromirror. The scanning micromirror design consists of three parts; an actuator array, a self-locking tether, and a flip-up mirror. The actuator array uses six thermal actuators connected with a single yoke. The actuators used in the array

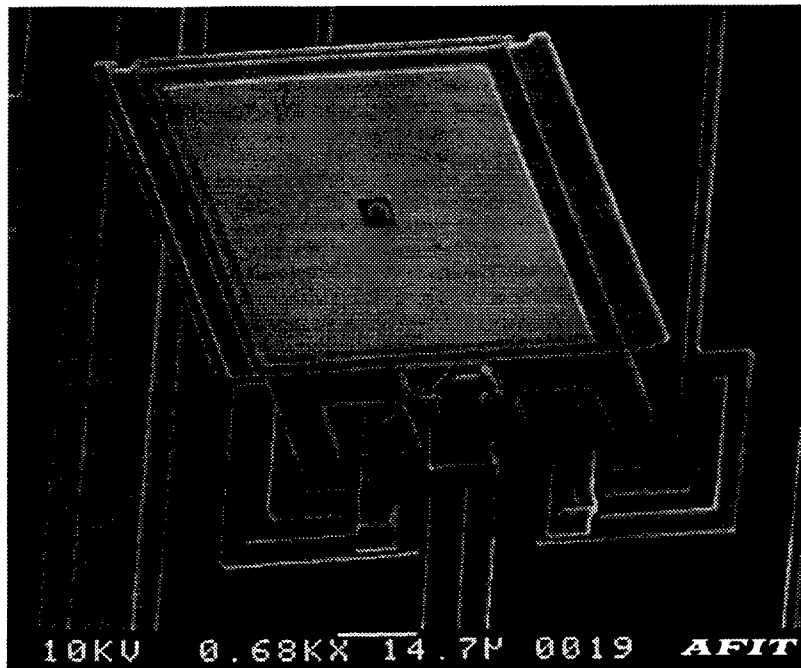


Figure 4.44. Scanning electron micrograph of the scanning micromirror. The gold mirror surface is a square with $75\ \mu\text{m}$ sides. The tether is $15\ \mu\text{m}$ wide.

are all identical and have the parameters: $t = 2.0\ \mu\text{m}$, $w_h = 2.5\ \mu\text{m}$, $w_c = 14\ \mu\text{m}$, $l_f = 50\ \mu\text{m}$, $l_c = 160\ \mu\text{m}$, and $s = 2.5\ \mu\text{m}$. The array operates in both the forward and back bent modes, however, the design of the yoke is such that the array performs better in the forward mode.

The self-locking tether is fabricated from the $1.5\ \mu\text{m}$ thick layer of polysilicon. It is $15\ \mu\text{m}$ wide and $100\ \mu\text{m}$ long. The tether is connected to the actuator yoke by a $3\ \mu\text{m}$ wide, $15\ \mu\text{m}$ long flexure. At the other end of the tether, a self engaging locking mechanism is used. When the mirror plate is lifted off of the substrate, the grooves in the tether fall into the small hole in the base of the mirror plate. Figure 4.44 shows the flipped up micromirror. The engaged tether lock is shown at the bottom of the mirror.

The mirror is fabricated using a combination of both layers of polysilicon, and a gold coating on the top layer of polysilicon to provide better reflection. Both polysilicon layers together provide a stiffer mirror which decreases any deflections caused by the internal stress in the polysilicon. The gold coated mirror surface is a square with $75\ \mu\text{m}$ sides. An etch hole is cut in the center of the mirror to ensure that the mirror is completely released

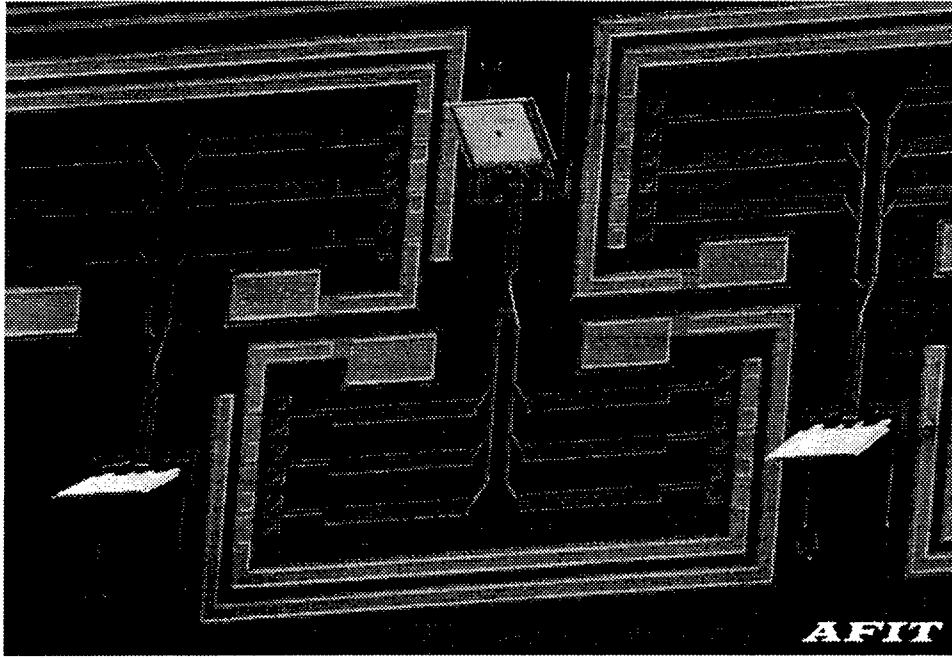


Figure 4.45. Three of the assembled scanning micromirrors.

during the oxide etch. The mirror is connected to the substrate using two substrate hinges. Several of the devices that have been fabricated and assembled are shown in Fig. 4.45. The entire layout of the scanning mirror including the actuator array has a footprint of $653 \mu\text{m}$ by $583 \mu\text{m}$.

The mirror functions by rotating around the pivot arm of the substrate hinges. The exact angle between the plate and the substrate cannot be calculated due to uncertainty in the position of the base of the mirror, the shape of the tether from the actuators to the mirror, and the position of the tether in the lock. However, by assuming that the mirror base rotates around the center point of the hinge staple and the tether is a linear bar of fixed length, C_1 , between a fixed point on the mirror and a moving point connected to the end of the actuators, the angle between the mirror and the substrate can be approximated using the law of cosines. Figure 4.46 shows the triangle formed by the mirror, the substrate, and the tether. Using this triangle, the angle, θ , is calculated as

$$\theta = \cos^{-1} \left(\frac{C_2^2 - C_1^2 + L^2(v)}{2C_2L(v)} \right) \quad (4.3)$$

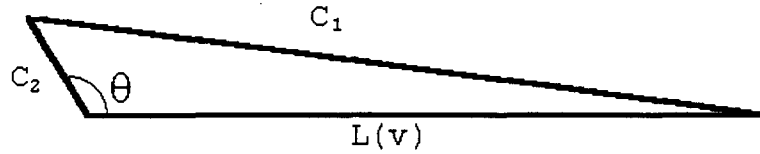


Figure 4.46. Triangle formed by the mirror, substrate, and tether. C_1 is the length of the tether, C_2 is the length from the base of the mirror to the tether lock, and $L(v)$ is the length from the base of the mirror to the actuator array.

where C_2 is the length from the mirror base to the tether lock and $L(v)$ is the distance between the mirror base and point where the actuators are connected to the tether. The mirror designed here has values of $C_1 = 109\mu\text{m}$, $C_2 = 16\mu\text{m}$, and $L(v) = 99\mu\text{m} + x(v)$ where $x(v)$ is the deflection of the actuator array. Substituting these values into Eq. 4.3 yields

$$\theta = \cos^{-1} \left(\frac{x^2(v) + 198x(v) - 1824}{3168 + 32x(v)} \right) \quad (4.4)$$

In the static position, $x(0) = 0$, the mirror rests at an angle, $\theta = 125.1^\circ$. The actuator array should be capable of deflections up to $10\mu\text{m}$ which results in an angle, $\theta = 85.8^\circ$. The change in the angle is then $\delta\theta = 29.3^\circ$.

After the mirror was fabricated, the performance of the mirror was measured by observing the motion of mirror under the microscope. The motion of the top of the mirror was observed, and this motion was then used to calculate the deflection of the mirror. The measured change in the angle between the mirror and the substrate was $\delta\theta = 15.7^\circ$. This was achieved at a power of 138.7 mW (5.82 V and 23.83 mA). This value is significantly below the expected value of $\delta\theta = 29.3^\circ$. The primary cause of the decreased deflection is the design of the actuator array yoke. Note, however, that the measurement is not exact, and the author used a conservative value for the deflection. An improved fan mirror was fabricated on the MUMPs14 fabrication run. The new mirror utilizes only two of the optimized thermal actuators and deflects approximately $15\text{-}20^\circ$, while requiring only 53.1 mW (5.9 V and 9.0 mA), which should be compatible with CMOS drive circuitry.

This mirror design offers a variety of potential applications. Currently, the design is being incorporated into a corner cube communications device as shown in Fig. 4.47. The design uses the scanning micromirror to modulate one side of the corner cube. When this

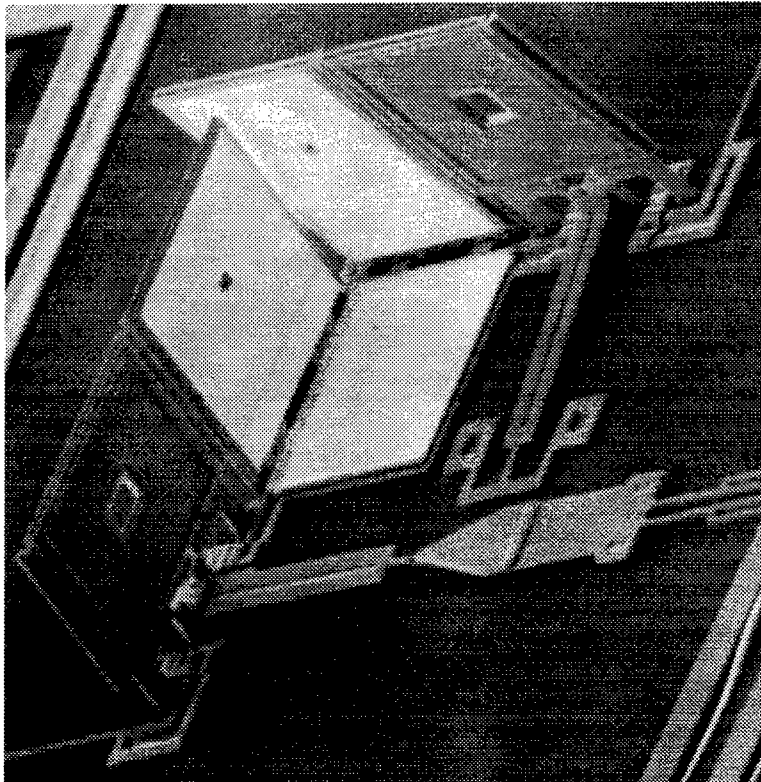


Figure 4.47. A corner cube reflector fabricated using the scanning micromirror.

side is normal to the other two sides, the three mirrors form a corner. In this configuration, any incoming light is reflected in the direction it originated from. When the side is not normal to the other two, the incoming beam is reflected at a different angle. The corner cube shown here rests at an angle past normal. By driving the actuator array, the mirror is pushed up into a normal position. The mirror used is driven by an array of six actuators, and requires 176.4 mW (6.39 V and 27.6 mA) to be driven several degrees past normal. Note that in future designs, the number of actuators should be reduced, significantly reducing the required power. Pister, *et al.*, presented a polysilicon corner cube in an earlier paper [115], however, they used electrostatic modulation of the lower mirror, and not thermal actuation.

Lateral Scanning Mirror Design. Direct coupling of thermal actuator arrays has also been used to fabricate a lateral scanning mirror. As with the original scanning mirror design, this mirror consists of three components, a flip-up mirror, a tether, and an actuator array. The actuator array uses six identical thermal actuators with the parameters: $t = 2.0 \mu\text{m}$, $w_h = 2.0 \mu\text{m}$, $w_c = 14 \mu\text{m}$, $l_c = 50 \mu\text{m}$, $l_c = 160 \mu\text{m}$, and $s = 2.0 \mu\text{m}$. The yoke is formed out of the $1.5 \mu\text{m}$ polysilicon layer. The mirror, shown in Fig. 4.48, is formed from both layers of polysilicon and a gold coating for the reflective surface. The gold coated mirror surface is $57 \mu\text{m}$ by $108 \mu\text{m}$. The mirror is mounted to the substrate with three floating substrate hinges. When the mirror is lifted into position, two locks engage to hold the mirror normal to the substrate. The hinged mirror is connected to the substrate via a rotating pin joint that allows the mirror to swivel. A $2 \mu\text{m}$ wide tether is fabricated from the $2.0 \mu\text{m}$ thick polysilicon layer, and is directly connected to the actuator array.

As the tether is moved by the actuators, the device rotates around the pin joint. The exact center of the rotation depends upon the fabrication tolerances, however, the change in the mirror's angle can be approximated as

$$\phi = \tan^{-1} \left(\frac{x(v)}{C_1} \right) \quad (4.5)$$

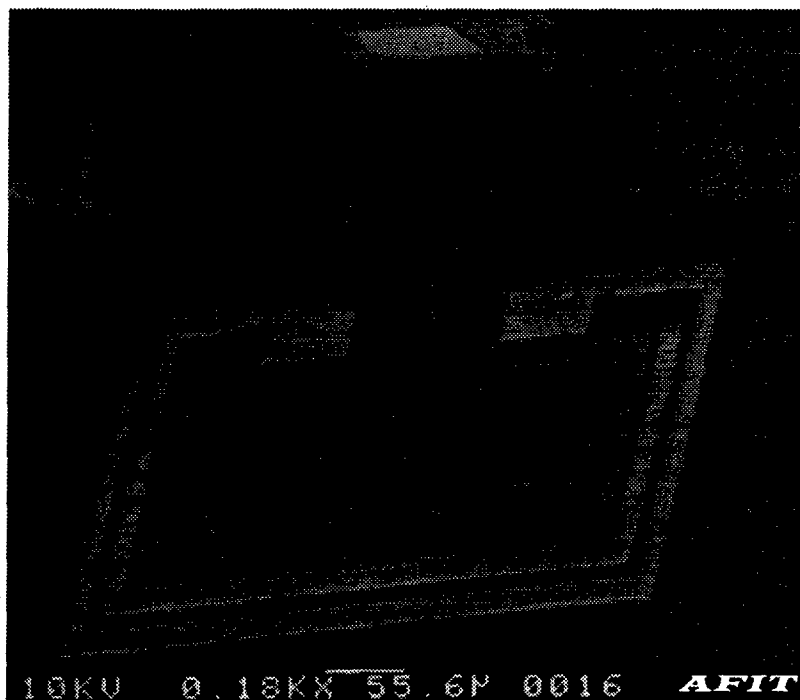


Figure 4.48. The assembled lateral scanning mirror. The thermal actuators are $210\ \mu\text{m}$ long. The gold coated mirror surface is $57\ \mu\text{m}$ high by $108\ \mu\text{m}$ wide.

where C_1 is the distance from the center of the pin joint to the point where the tether is connected and $x(v)$ is the deflection the actuator array. The mirror design here has a value $C_1 = 30\ \mu\text{m}$. For a maximum actuator deflection of $10\ \mu\text{m}$, the deflection of the mirror is $\phi = 18.4^\circ$.

The lateral scanning micromirror was also fabricated and operated, however, several problems were observed. First, the mirror tends to stick as it is rotated by the actuator. Lower drive voltages result in no deflection, then as the voltage is increased the mirror will jump to another position. Second, the lateral scanning mirror uses an older actuator and yoke design that delivers significantly less force. The maximum deflection of $\phi \approx 5$ was achieved at $90.0\ \text{mW}$ ($4.61\ \text{V}$ and $19.52\ \text{mA}$). Due to the problems above, this value is well below the expected value of $\phi = 18.4^\circ$. However, the problems with the mirror can be readily fixed with the use of the optimized actuator array, the redesign of the pin joint, and the use of dimples to reduce friction between the mirror and the substrate.

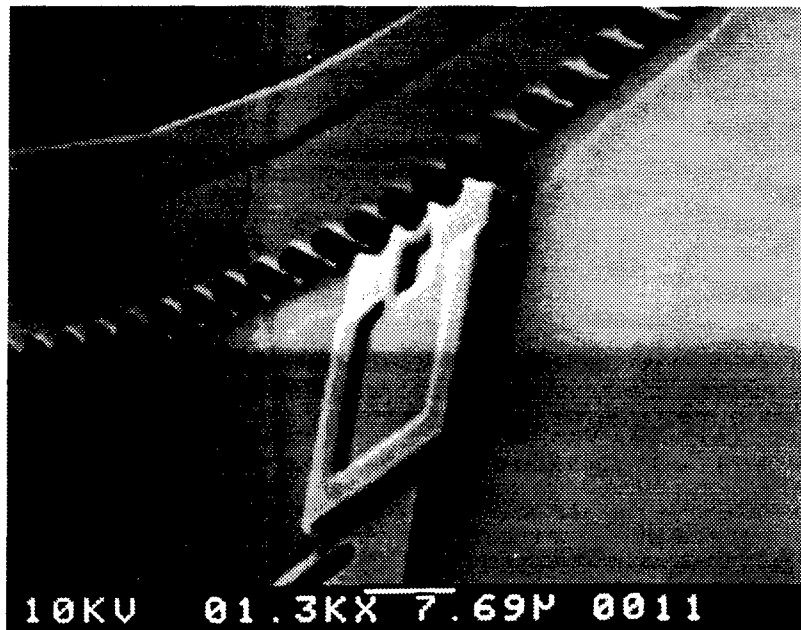


Figure 4.49. Teeth etched into the edge of the support plate interface with the motor drive.

Flip-Up Rotating Micromirrors. The author has designed and fabricated several flip-up rotating micromirrors. These mirrors can be used for directing a laser parallel to the substrate surface. Several designs have also replaced the mirror with Fresnel lenses or gratings. The first flip-up rotating micromirror fabricated at AFIT was shown previously in Fig. 4.28. This mirror consists of a $214\ \mu\text{m} \times 210\ \mu\text{m}$, $3.5\ \mu\text{m}$ thick polysilicon plate, coated with a $0.5\ \mu\text{m}$ thick layer of gold. The mirror is connected to the substrate by 3 floating substrate hinges. Using microprobes, the mirror is lifted off of the substrate and up into a self engaging lock. The lock holds the mirror normal to the substrate. The floating substrate hinges are connected to a $200\ \mu\text{m}$ diameter circular, $2.0\ \mu\text{m}$ thick polysilicon support plate. This plate is mounted to the substrate via a pin joint. The flipped up mirror was shown earlier in Fig. 4.28. Teeth are designed into the outer rim of the plate as shown in Fig 4.49. The teeth allow the mirror to engage with a micromotor designed by Comtois [4]. The motor is capable of bidirectionally driving the mirror through a range of 180 degrees. On this initial design, the motor did not work due to the use of an unoptimized actuator array. However, several newer designs have been fabricated using the optimized actuator arrays.

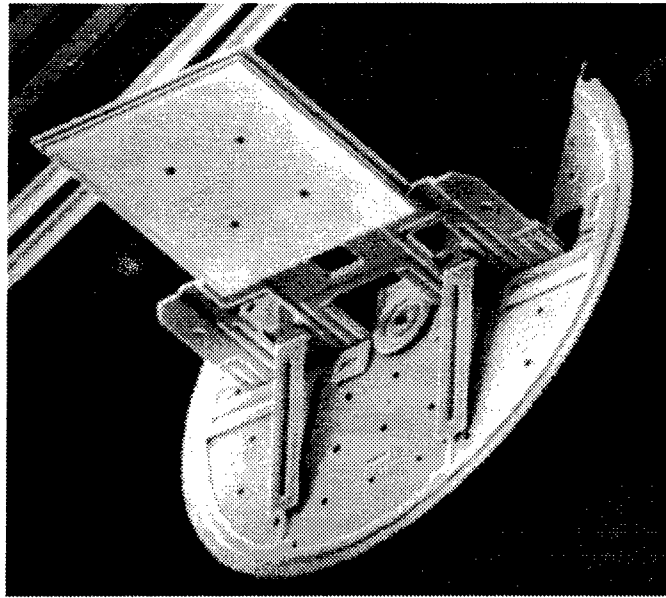


Figure 4.50. A flip rotating micromirror. The mirror surface is $100\ \mu\text{m}$ square. The support plate has a radius of $110\ \mu\text{m}$.

The mirror shown in Fig. 4.50 is one example of a working flip-up rotating micromirror fabricated by the author. The motor used with this mirror has a 10 actuator array. The array requires a maximum power of 214.5 mW (5.5 V and 39.0 mA). Designs capable of a full 360° of rotation have also been fabricated by the author.

4.3 Summary

Micromachining is a rapidly developing field. Currently it is possible to fabricate devices through a number of methods. Bulk micromachining relies on etching the bulk material to form structures, while surface micromachining deposits materials onto a wafer. Utilizing these processes, a large variety of devices can be designed and fabricated. Typically, bulk micromachined devices are larger structure with minimum feature sizes on the order of five to ten microns, while surface micromachined components are smaller planar structures with minimum feature sizes on the order of a couple of microns. The primary processes available at AFIT are the CMOS-MEMS process offered by MOSIS, MUMPs offered by MCNC, and in house bulk micromachining.

The author has demonstrated a large variety of MEMS utilizing the commercial foundry processes. Simple structures including cantilevers, bridges, and IR-pixels show the basic process capabilities. Moving components were fabricated through MUMPs utilizing micro-hinges, sliders, and pin joints. A variety of actuators were also presented. The primary actuator used at AFIT is the lateral thermal actuator. The author did extensive studies evaluating the force of this actuator with respect to the actuator design parameters. These studies were combined with previous studies by other researchers at AFIT to optimize the design of the actuators. Test cells designed to fully characterize this actuator were fabricated by the author on MUMPs14.

Complex systems were designed by the author utilizing the basic components. These systems include flip-up platforms for positioning optical components at arbitrary distances above the substrate. Scanning and lateral scanning micromirrors were fabricated using flip-up mirrors directly coupled to thermal actuators. These designs provide mirrors that have one to one deflection versus control voltage characteristics. Finally, flip-up rotating micromirrors were designed and fabricated. The author developed several designs including some capable of being driven through a full 360°.

V. Design

In Chapter II, it was shown that the output frequency of a SAW/STW resonator based oscillator varies when the oscillator is vibrated. The primary cause of the variation has been determined to be the SAW/STW resonator [2]. It has also been shown that the frequency shift results from changes in the resonator transimpedance caused by deformation of the resonator resulting from body forces applied to the resonator due to the vibration [3]. Two options exist to reduce the sensitivity of the resonator to the acceleration: reduce the applied vibration using a vibration isolation system, or control the deformation of the resonator in such a way that a minimum frequency shift occurs. Reducing the applied vibration has the advantage that it can be generically applied to any resonator. However, passive vibration isolation systems often result in an increased vibration of the resonator for vibrations having frequencies near or below the mechanical resonance of the isolator. Therefore, to reduce the vibration sensitivity of the resonator, both methods should be used.

A simple harmonic vibration can be represented by a sinusoidal acceleration as

$$v(t) = A \sin(2\pi ft) \quad (\text{m/s}^2) \quad (5.1)$$

where $f = \omega/2\pi$ is the frequency of the vibration and A is the amplitude of the vibration. The resulting motion is determined by integrating the vibration as

$$m(t) = \int \int v(t) dt^2 = -\frac{A}{(2\pi f)^2} \sin(2\pi ft) \quad (\text{m}) \quad (5.2)$$

The maximum displacement of the vibrating object is then

$$\text{Disp} = \frac{2A}{(2\pi f)^2} \quad (\text{m}) \quad (5.3)$$

For a vibration with a 1 g amplitude, $\text{Disp} \approx 500/f^2$ (mm). Table 5.1 shows the displacement resulting from 1 g vibrations of several frequencies. A vibration with an amplitude under five g results in a total displacement less than 100 μm when the frequency of the vibration is greater than 200 Hz. In Chapter IV, a number of MEM devices and systems

Table 5.1. Maximum Displacement Resulting from a 1 g Simple Harmonic Vibration of Frequency, f .

Frequency (Hz)	Motion (μm)
1	5×10^5
10	5×10^3
50	2×10^2
100	50
200	12.5
500	2
1000	0.5

capable of moving over 100 μm were presented, and therefore it is reasonable to expect that a micromachined system can be fabricated.

Chapter III mentions that both passive and active vibration isolation systems can be fabricated. However, passive systems offer several advantages. The design of a passive system is simpler. Further, passive systems do not require any power for operation, a trait that is highly desirable in applications where power is limited. Finally, active control must be built in conjunction with a passive system requiring that the passive system first be characterized. Therefore, the design and fabrication of a passive system is the logical choice for this research.

This chapter provides the design and modeling of a passive vibration isolation system. Initially a basic design is presented. Finite element analysis tools developed by Stewart are used to predict the acceleration sensitivity of the system. Next, the design is modeled as a damped mass-spring system, and the absolute transmissability is calculated. Finally, the model is revised to improve the vibration isolation.

5.1 System Design

It is necessary to consider the fabrication process that will be used in designing MEMS. This is a result of the nature of the micromachining processes. For instance, surface micromachining results in thin planar structures with very precise dimensions, while bulk micromachining offers larger three dimensional structures that typically have

coarser dimensions. Further, the processing steps must be compatible with the devices being manufactured. Therefore, attributes such as the size of the system and limitations on processing such as exposed aluminum must be considered in the system design. The system designed here isolates a quartz resonator that is approximately 2 mm wide by 4 mm long by 0.5 mm thick. The IDT and reflective gratings on the resonator are formed from a thin aluminum layer. The thickness of the electrodes is important in the performance of STW resonators, and therefore, the aluminum must not be damaged during fabrication.

Four main processes are available at AFIT: CMOS-MEMS, LIGA-MUMPs, MUMPs, and in house bulk micromachining. The CMOS-MEMS process is limited to thin film structures released by bulk etching. Further, the process is relatively expensive. The LIGA-MUMPs was run only once during the course of this research and the devices were returned over four months behind schedule. Further, the LIGA-MUMPs process only provides five die per fabrication site. The MUMPs process is inexpensive, has a rapid turn around, and delivers 15 die per fabrication site, however, MUMPs offers only planar surface micromachined processing. The MUMPs die are released with an etch in hydrofluoric acid which would damage both the quartz substrate and the aluminum fingers of the resonator. Therefore, it would be necessary to release the MUMPs die and then bond the resonator, a process that would be very difficult. It is also difficult to fabricate structures with dimensions over 500 μm using MUMPs without the devices sticking to the substrate during the release process. This leaves only in house bulk micromachining for fabricating the devices for this research. In house bulk micromachining allows the fabrication of large structures fabricated from silicon wafers. The minimum dimensions are not as precise as those provide by MUMPs or CMOS-MEMS, but are on the order of 5-10 μm . Therefore, an isolation system that can be fabricated from bulk silicon is designed.

The basic design of the isolation platform is seen in Fig. 5.1. The system consists of a platform for the resonator connected by four support arms to a support rim. The entire structure has a uniform thickness. The platform and the resonator act as a mass supported by the four support arms which act as springs. When the base is vibrated, the vibration is transmitted via the support arms to the platform and the resonator. As the frequency of the vibration increases above the mechanical resonance frequency of the

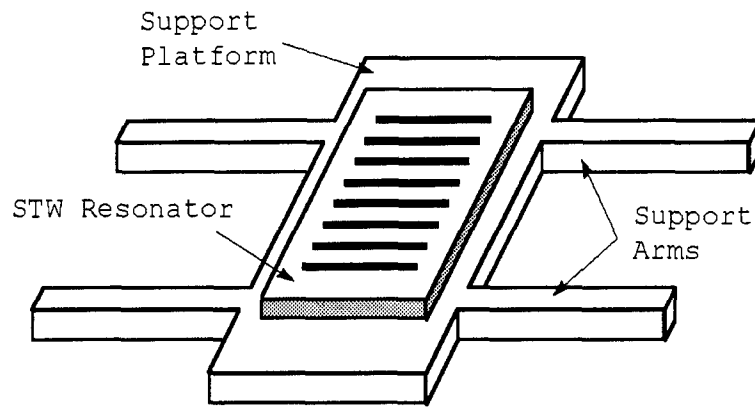


Figure 5.1. Illustration of the vibration isolation system with a STW resonator mounted on the isolated platform.

mass-spring system, the magnitude of the platform vibration is reduced below that of the base as described in Chapter III. The rigidity of the platform, the location of the support arms, and the mounting of the resonator on the platform determine the shape of the body forces applied to the resonator.

The top of the platform is large enough to mount the resonator and provide four metal bonding pads. Metal wires are patterned along the surface of the supports connecting the bonding pads on the platform to bonding pads located on the support rim. A schematic view of the top of the isolation system showing the metal bonding pads and wires is shown in Fig. 5.2. Fabricating wires from the platform to the support rim is done to allow the STW resonators to be mounted and bonded before the devices are fully released. When bonding the resonators to the oscillator circuit, it is only necessary to bond to the support rim, and therefore, damage to the narrow support arms is prevented.

5.2 Finite Element Analysis

Utilizing code developed by Stewart at Army Research Laboratory (ARL) [10, 116], an analysis of the acceleration sensitivity of the isolated resonators with respect to the various platform parameters was performed. The finite element analysis is not exact [117], however, it is sufficiently accurate to allow the design parameters of the isolation system to be evaluated and optimized [116, 117]. The analysis of the isolation system begins by

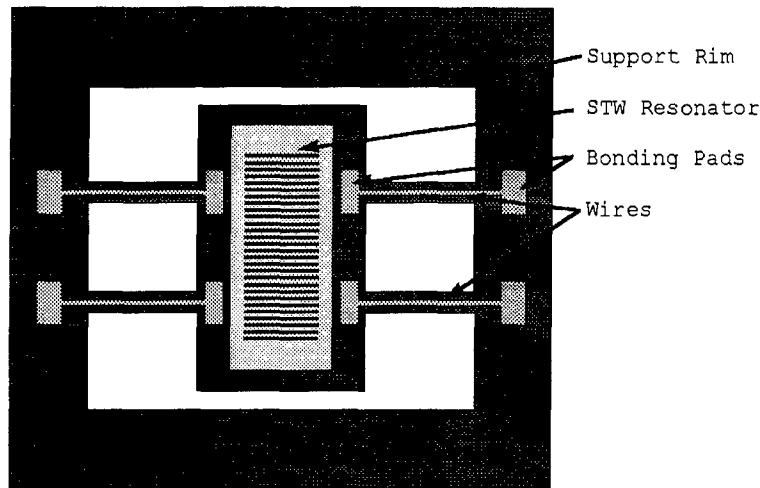


Figure 5.2. Diagram of the top of the isolation system. Metal bonding pads are located on the top of the support rim and platform. Wires are patterned along the support arms to connect the bonding pads from the platform to the bonding pads on the support rim.

calculating the STW mode shape. Next, a finite element mesh of the resonator mounted on the isolation system is created. Utilizing finite element analysis, the code calculates the deformation of the isolation system resulting from an applied acceleration. Finally, the code utilizes Tiersten's perturbation integral to calculate the frequency shift of the resonator [42]. Note that the code was not designed or modified for this dissertation. The creation of the model and the analysis are new and were performed by the author using time on a Cray C-90 provided by the Army Corps of Engineers, Vicksburg Center (pk.wes.army.mil).

5.2.1 Calculation of STW Mode Shape. The general coordinate system used to calculate the STW mode shape is shown in Fig. 5.3. In the code, the STW mode shape is represented as a finite Floquet series [10, 11]

$$u_1 = \sum_{n=-N}^{+N} A_n e^{i\alpha_n x_2} e^{i\beta_n x_3} e^{i\omega t} \quad (5.4)$$

where

$$\beta_n = \beta + \frac{2\pi n}{\Lambda} \quad (5.5)$$

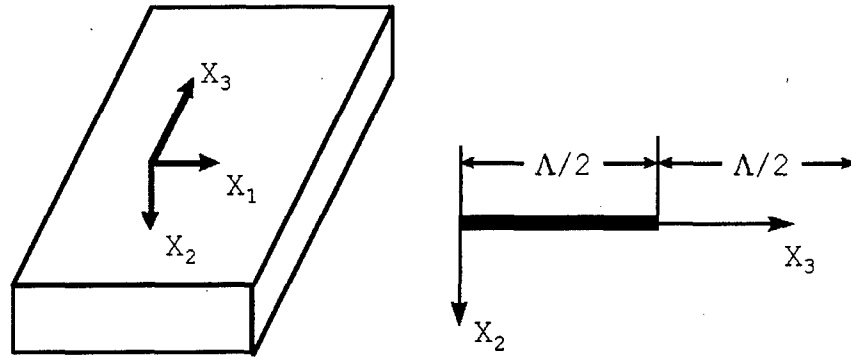


Figure 5.3. Coordinate system for calculation of the STW mode shape and finite element analysis of the isolation platform.

is the n^{th} space harmonic propagation constant, with β the Floquet wave propagation constant, α_n the (complex) propagation constant into the substrate, Λ the grating period, ω the angular frequency, and A_n the amplitude of the n^{th} space harmonic. The resulting solution is dependent upon a number of factors including the material properties of the substrate, the density of the electrodes, the dimensions of the electrodes, and the spacing of the electrodes. However, for this research the design of the resonator is not considered for reducing the acceleration sensitivity and therefore, all values that affect the STW mode shape of the unsupported resonator remain fixed.

The value N is specified by the user and results in $2N + 1$ terms in the Floquet series. A solution of the STW mode shape and corresponding output frequency is obtained iteratively by the code. The accuracy of the solution varies with N . A perfect solution requires $N = \infty$ which is not practical since the computation time required increases with the number of terms in the Floquet series. Therefore, the smallest number resulting in a reasonably converged solution is desired. An acceptable value of N is determined by measuring the convergence of the calculated output frequency of the STW resonator and convergence of the calculated acceleration sensitivity of the system. For the analysis, a STW resonator with a length of 3.99 mm, a width of 1.85 mm, and a thickness of 0.51 mm is used. The IDT and reflective gratings were aluminum with a thickness of 412 Å. The fingers were space 2.54 μm center to center. These dimensions were used for all of the finite element calculations in this chapter. The difference between both the calculated output frequency and the calculated acceleration sensitivity using 3 terms in the series

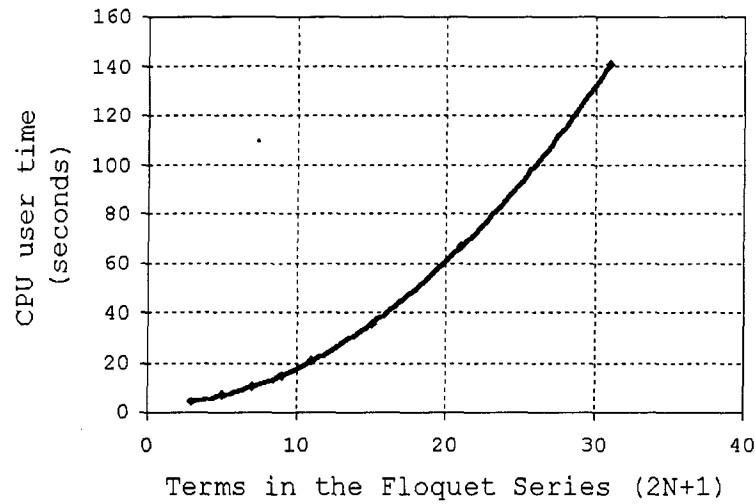


Figure 5.4. The required computation time grows exponentially with the number of terms in the Floquet series.

($N = 1$) and that determined using 31 terms ($N = 15$) was much less than one percent, and therefore, the STW mode shape is sufficiently modeled using only three terms in the series. However, as shown in Fig. 5.4, the computational cost of using five terms was not significantly greater than the cost of using three terms, and therefore $N = 2$ was used for the solution of the STW mode shape.

5.2.2 Calculation of Biasing State. The stresses and strains in the resonator resulting from a 1 g acceleration applied in the x_2 direction are calculated using finite element analysis [10, 11]. Initially, a model of the system is created. The model is then broken down into a three dimensional grid. Each point of the grid becomes a node in the finite element model. The connection between the nodes is modeled as being either linear, quadratic, or cubic. For the analysis performed by the author, all connections are quadratic. Each node is given material properties for either quartz or silicon. It is assumed that the STW resonator is rigidly mounted to the silicon isolation platform. The resulting model is symmetric about two axes. Utilizing this symmetry, it is possible to calculate all deflections with a one quarter model of the system. The one quarter model is shown in Fig. 5.5. The model uses an isolation platform that is the same length as the STW resonator, and therefore there is no overhang in the x_3 axis.

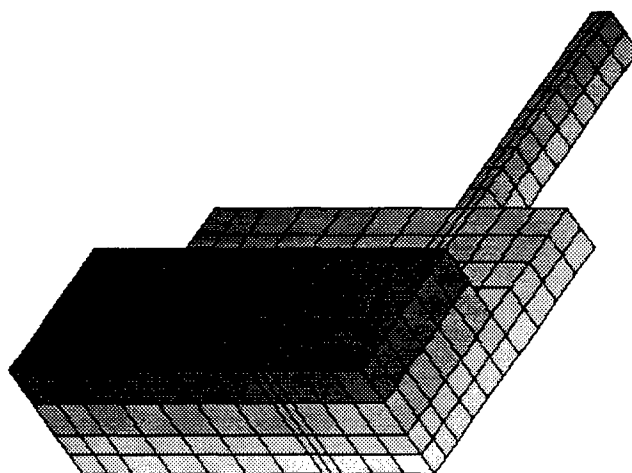


Figure 5.5. One quarter model finite element mesh.

After the one quarter model is generated, a 1 g acceleration is applied in the x_2 direction to all nodes in the mesh. The resulting stresses and strains are calculated as described in references [10, 11]. The model is then mirrored around two axes to form a complete model as shown in Fig. 5.6. The deflections are stored and later used as the solution to the static biasing problem.

The accuracy of the solution is dependent upon the type of connectivity elements used and the spacing of the nodes. As mentioned above quadratic elements were used. The small deflections resulting from a 1 g load should not require the more complex cubic connections [10]. Studies of the acceleration sensitivity with respect to both the number and spacing of the nodes were performed to ensure adequate convergence. Previous use of this code with STW resonators showed that the calculated value is not exact [117]. However, the calculated acceleration sensitivity is close enough to allow an analysis of the properties which result in changes of the acceleration sensitivity such as the resonator dimensions, or in this case the parameters of the vibration isolation system.

5.2.3 Calculation of the Acceleration Sensitivity. The frequency shift under a given static biasing state is computed using Tiersten's perturbation integral for small fields superposed on a bias [42]. The change in resonant frequency of the μ^{th} eigen-mode

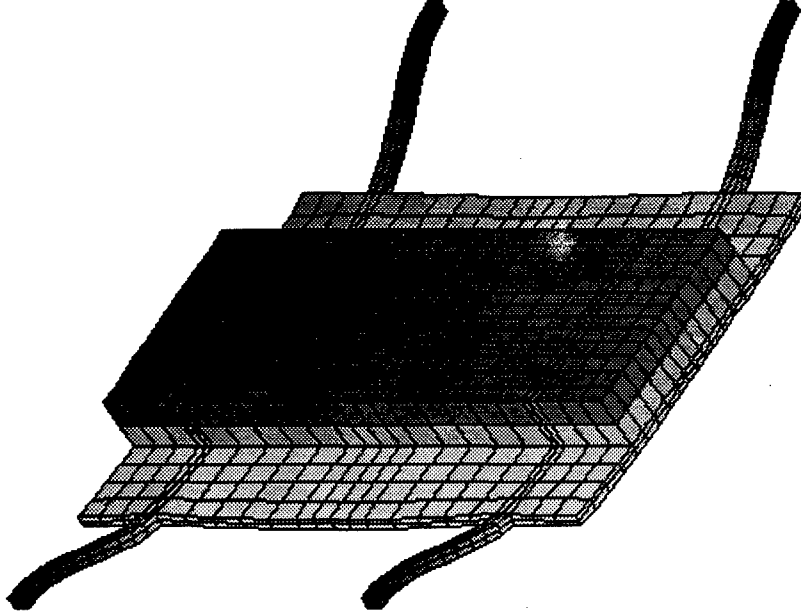


Figure 5.6. A 1 g acceleration is applied in the x_2 direction. After the calculating the deformations, the one quarter model is mirrored about two axes to generate a complete model.

is calculated as [42].

$$\Delta_\mu = \frac{H_\mu}{2\omega_\mu} \quad (5.6)$$

where

$$H_\mu = - \int_V \hat{c}_{L\gamma M\alpha} g_{\alpha,M}^\mu g_{\gamma,L}^\mu dV \quad (5.7)$$

is the integral over the volume, V , of the normalized mode shape g , and the spatially varying effective elastic constants $\hat{c}_{L\gamma M\alpha}$. The spatially varying constants, $\hat{c}_{L\gamma M\alpha}$, are derived from the biasing state solved in the previous section [2, 118].

The calculation of the perturbation integral is described by Stewart [119]. A summary of this is presented here to provide the necessary understanding of the calculation. The perturbation integral, Eq. 5.7, is evaluated as a sum over N elements as

$$H_\mu = - \sum_{i=1}^N \int_{\Omega_i} \hat{c}_{L\gamma M\alpha} g_{\alpha,M}^\mu g_{\gamma,L}^\mu d\Omega_i \quad (5.8)$$

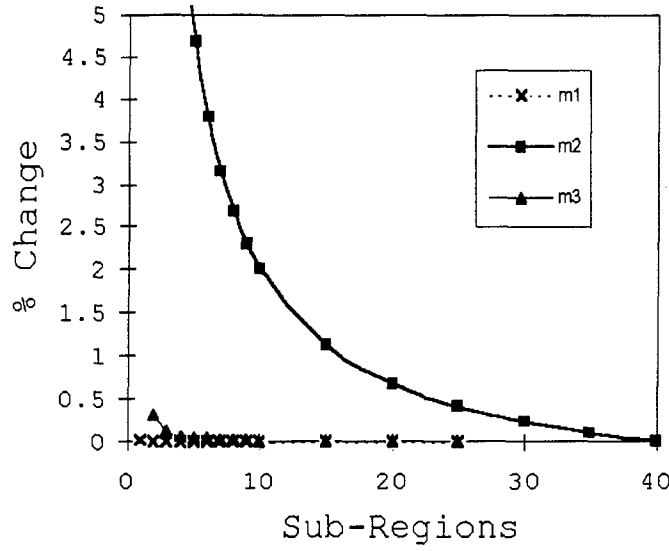


Figure 5.7. Convergence of the calculated acceleration sensitivity with respect to the number of sub-regions, m_1 , m_2 , m_3 . The percentage change is relative to the acceleration sensitivity calculated with the maximum value of sub-regions in the direction that is being evaluated.

where Ω_i denotes the volumetric domain of the i^{th} element. The integral is solved by assuming the spatially varying effective elastic constants remain constant over a sub-region of the domain Ω_i . The integral is then evaluated as

$$\int_{\Omega} \hat{c}_{L\gamma M\alpha} g_{\alpha,M}^{\mu} g_{\gamma,L}^{\mu} d\Omega \approx \sum_{i=1}^{m_1} \sum_{j=1}^{m_2} \sum_{k=1}^{m_3} \hat{c}_{L\gamma M\alpha} \int_{\Omega^{(i,j,k)}} g_{\alpha,M}^{\mu} g_{\gamma,L}^{\mu} d\Omega^{(i,j,k)} \quad (5.9)$$

where $\hat{c}_{L\gamma M\alpha}$ is sampled at the center of the (i, j, k) sub-region of the domain $\Omega^{(i,j,k)}$ under consideration. The integral $\int_{\Omega^{(i,j,k)}} g_{\alpha,M}^{\mu} g_{\gamma,L}^{\mu} d\Omega^{(i,j,k)}$ in Eq. 5.9 is evaluated exactly using the form given by Eq. 5.4. The resulting change in the frequency is then divided by the calculated center frequency resulting in the acceleration sensitivity of the system.

The number of elements, m_1, m_2, m_3 determines the accuracy of the approximation. As with the other values, the appropriate number of terms was determined by studying the convergence of the final results. Convergence of the acceleration sensitivity was determined by multiple runs while varying the number of terms. The results, shown in Fig. 5.7, show that m_2 has a significant effect on the calculated acceleration sensitivity while m_1 and m_3

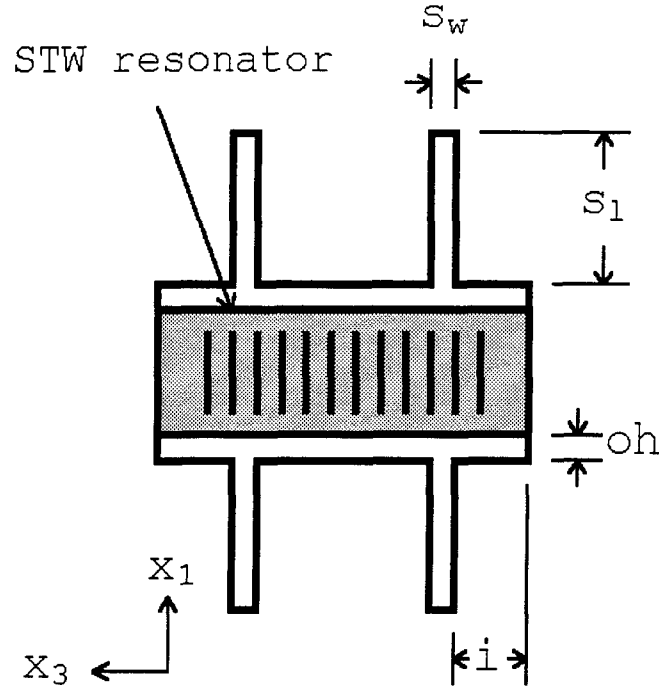


Figure 5.8. Model parameters for the silicon isolation system. Not shown, the system is of a uniform thickness, t .

have almost no effect. For all of the results presented in the next section, values of $m_1 = 2$, $m_2 = 21$, and $m_3 = 3$ were used.

5.2.4 Numerical Results. An analysis using the STW resonator previously described was performed over a range of isolation platform parameters. The parameters support length, s_l , support width, s_w , inset, i , thickness, t , and platform overhang, oh are defined in Fig. 5.8. The resonator is assumed to be rigidly mounted onto the silicon support platform. Unless otherwise specified, the parameters are defined as $i = 1.0$ mm, $t = 0.4$ mm, $oh = 0.573$ mm, $s_l = 2.00$ mm, and $s_w = 0.05$ mm.

The effect of the inset on acceleration sensitivity is shown in Fig. 5.9. Increasing the inset moves the supports closer to the center of the resonator resulting in reduced deflection in the IDT region of the resonator. This results in a decrease in the calculated acceleration sensitivity.

Figure 5.10 shows the effect of thickness on acceleration sensitivity. Increasing the

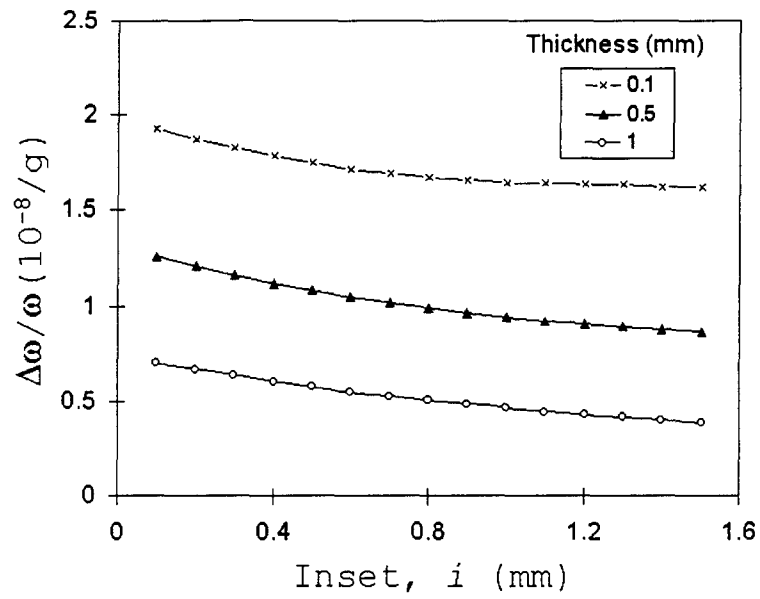


Figure 5.9. The effect of support location on acceleration sensitivity. Data are presented for three different silicon thickness values.

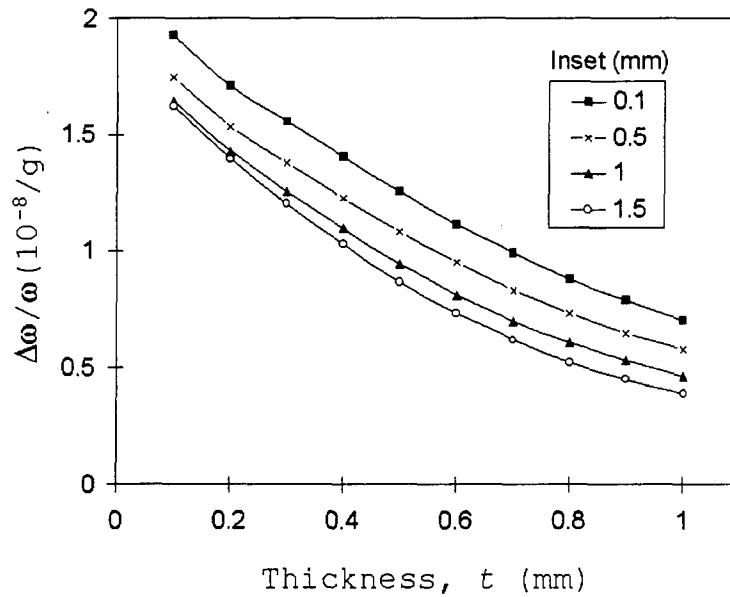


Figure 5.10. The effect of platform and support thickness on acceleration sensitivity.

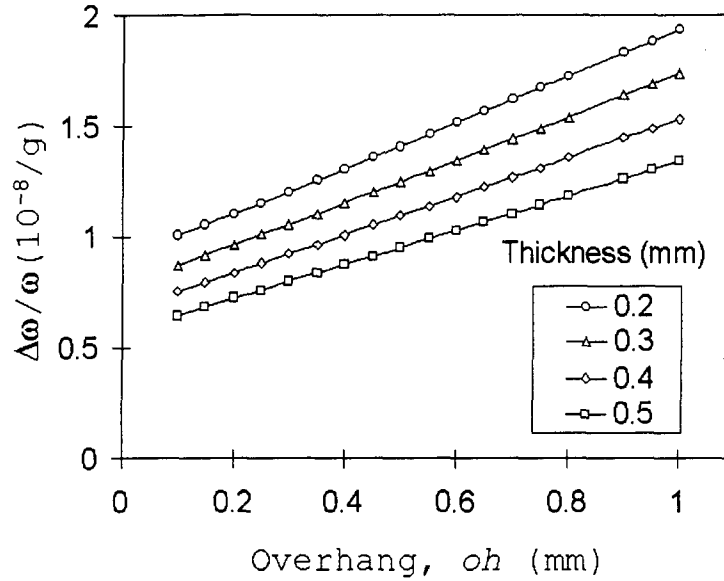


Figure 5.11. The effect of platform overhang on acceleration sensitivity. Note, inset = 0.8 mm.

thickness provides a more rigid support for the resonator and thus decreases the deformation. Again, this directly leads to decreased acceleration sensitivity. Since the resonator and the platform are assumed to be rigidly connected, the acceleration sensitivity should be inversely proportional to thickness as predicted by Kosinski [118].

The effect of platform overhang is shown in Fig. 5.11. As seen, increasing the overhang leads to an increased acceleration sensitivity. The reason for the increasing acceleration sensitivity due to increasing the overhang is not obvious. However, on close evaluation, the reason becomes clear. The deformation of the resonator is proportional to the applied force. Since the resonator is rigidly mounted to the support platform, increasing the area of the platform increases the mass which corresponds to an increase in the force applied to the resonator. It is then not surprising that the deflection would increase, and thus the acceleration sensitivity increases.

The effects of support width and support length are shown in Figs. 5.12 and 5.13, respectively. The support width has minimal effect on acceleration sensitivity, while increasing support length leads to increased acceleration sensitivity. The cause of the

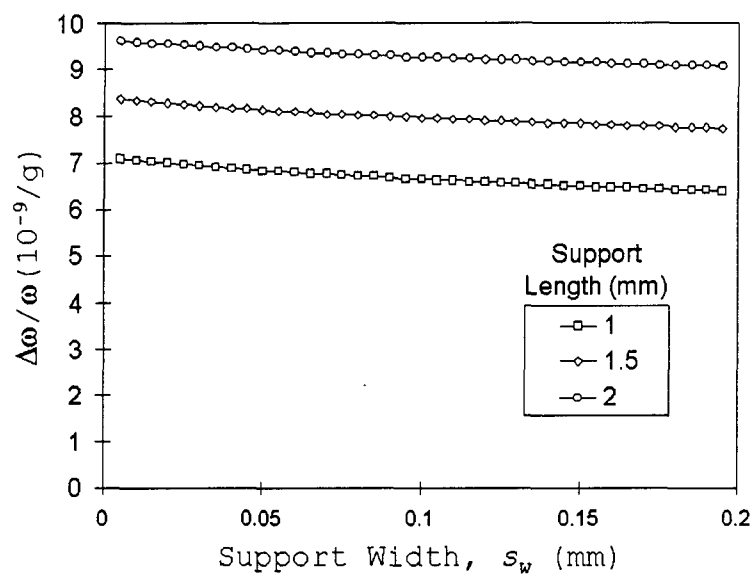


Figure 5.12. The effect of support width on acceleration sensitivity.

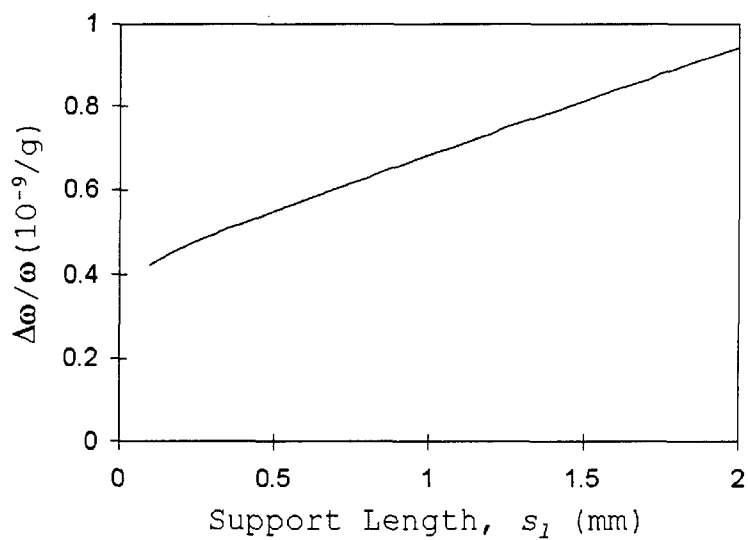


Figure 5.13. The effect of support length on acceleration sensitivity.

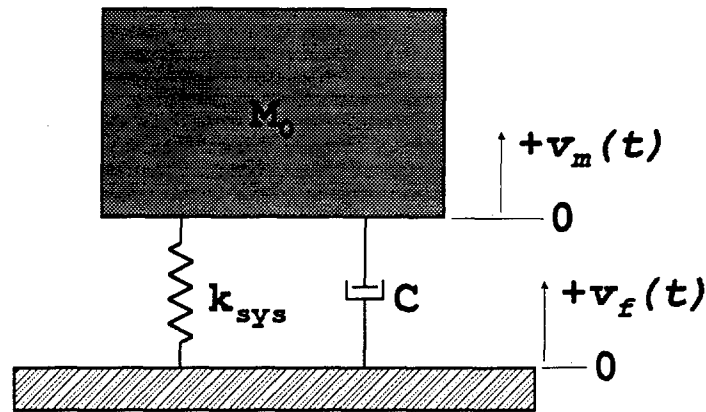


Figure 5.14. Model parameters of the single degree of freedom, damped, mass-spring system. M_0 is the mass of the isolated platform and the resonator, k_{sys} is the spring constant resulting from the support arms, and C is the viscous damping coefficient with two components, C_m and C_r as defined in Chapter III.

increased length is most likely the increased force applied to the edges of the platform due to the increased mass resulting from the elongated arms.

All of the results presented in this section are consistent with the work of Kosinski, *et. al* [118]. In particular, two important conclusions should be considered. First, it is the deformation that results in the change in the frequency. The deformation is caused by the applied force which is proportional to both the acceleration and the mass [3]. And second, the design of the platform will not completely eliminate the acceleration sensitivity, but a bad platform design can result in a larger sensitivity. Therefore, this micromachined platform will primarily serve as a vibration isolation system.

5.3 Mass-Spring Model

Determining the vibration of the isolated platform and resonator is done by modeling the system as a damped mass-spring system with a single degree of freedom as described in Chapter III. The basic model parameters are illustrated in Fig. 5.14. The model parameters are calculated from the parameters of the isolation system described previously in Fig. 5.8. Calculation of the model parameters is described in the following section.

5.3.1 *Calculation of Model Parameters.* The mass is simply computed as

$$M_0 = M_{STW} + M_P \quad (5.10)$$

where M_{STW} is the mass of the STW resonator and M_P is the mass of the silicon isolation platform. The effective mass of the support arms is much less than M_P and is therefore neglected. The masses of the metalizations, epoxy, and wire bonds are also neglected. The mass of the resonator is calculated as

$$M_{STW} = t_{STW} \times w_{STW} \times l_{STW} \times \rho_q \quad (5.11)$$

where ρ_q is the density of quartz, and t_{STW} , w_{STW} , and l_{STW} are the thickness, width, and length of the STW resonator. The mass of the platform is calculated as

$$M_P = t \times p_w \times p_l \times \rho_{si} \quad (5.12)$$

where ρ_{si} is the density of silicon, and t , p_w , and p_l are the thickness, width, and length of the silicon isolation platform respectively.

The spring constant, k_{sys} results from the restoring force of a bent beam. It is calculated as [120]

$$k_{sys} = 4(k_1 + k_2 + k_3) \quad (5.13)$$

where k_1 is the spring constant due to the deflection of the beam, k_2 is the spring constant due to residual stress, and k_3 is the spring constant due to stress induced by bending the beam. Residual stress in single crystal silicon is very low, and therefore, k_2 can be neglected. For a small deflection of the beam relative to the beams length, k_3 can also be neglected. Note that for this design, a deflection less than 50 μm over a 2 mm long beam is expected, and therefore k_3 is neglected. The resulting spring constant is then calculated as [120]

$$k_{sys} = 4k_1 = 4 \times \frac{E_{si}s_w t^3}{s_l^3} \quad (5.14)$$

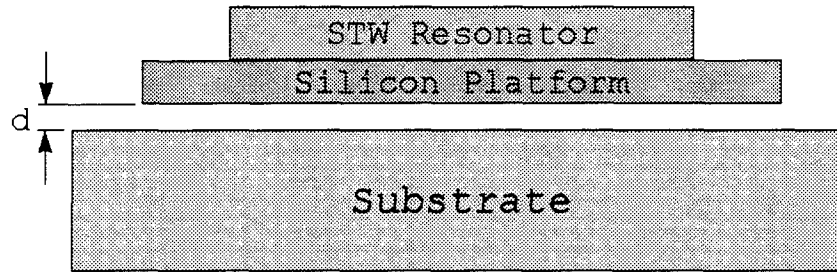


Figure 5.15. The platform is suspended by the springs a distance, d , above the substrate.

Calculation of the damping coefficients, C_r and C_m , is more difficult than that of the mass or the spring constant. The relative motion damping coefficient, C_r , is primarily due to heating of the support arms. For small motions, this loss is negligible. Damping relative to the motion of the mass is dependent upon the cause of the damping. The value of C_m is dependent upon the relationship between the area of the isolation platform and the distance between the platform and the substrate which it is mounted to as shown in Fig. 5.15. When the plates meet the four criteria of Griffin *et. al* [121], summarized as:

- 1) The length and width of the plates are much greater than the plate separation:
 $p_l, p_w \gg d$,
- 2) The gas flow between the plates is laminar and primarily viscous resulting in a low Reynolds number,
- 3) The ratio of the localized gas pressure and the localized gas density is constant,
- 4) The primary motion of the plates is perpendicular to the plate surface, and the relative motion of the plates is much less than the plate separation;

then, the damping coefficient is primarily due to the flow of the gas in and out of the region between the plates. The damping coefficient is then calculated as [122]

$$C = \frac{0.42 A^2 \mu}{d^3} \quad (5.15)$$

where $A = p_l \times p_w$ is the area of the platform, μ is the viscosity of the gas, and d is the distance between the plates as defined in Fig. 5.15.

5.3.2 *Model Results.* The calculation of the mass, spring constant, and resonant frequency are done for a system with $i = 1.0$ mm, $t = 0.4$ mm, $oh = 0.573$ mm, $s_l = 2.00$ mm, and $s_w = 0.05$ mm. The resonator is assumed to be 3.99 mm long, 1.85 mm wide, and 0.51 mm thick. The resonator is assumed to be the same length as the support platform. The mass is calculated as

$$M_0 = 2.1 \times 10^{-5} \text{ kg} \quad (5.16)$$

and the spring constant is calculated as

$$k_{sys} = 3.04 \times 10^5 \text{ N/m} \quad (5.17)$$

The resonant frequency is then calculated

$$f_0 = \frac{1}{2\pi} \sqrt{\frac{k_{sys}}{M_0}} = 19.2 \text{ kHz} \quad (5.18)$$

This frequency is much higher than a desired value less than 200 Hz. To reduce the resonant frequency, two options exist, increasing the mass or reducing the spring constant. Increasing the mass has a detrimental effect on the acceleration sensitivity of the system due to the resulting increase in the applied force, while f_0 decreases only with the square root of the mass. Therefore, reducing the spring constant is a more desirable choice. The spring constant is directly proportional to the support width and the cube of the support thickness, and inversely proportional to the cube of the support length, resulting in the following effect on the resonant frequency

$$f_0 \propto (s_w)^{(1/2)}, \left(\frac{1}{s_l}\right)^{(3/2)}, (t)^{(3/2)} \quad (5.19)$$

It is clear from Eq. 5.19 that either the length of the supports must be significantly increased, or the thickness of the supports must be decreased. Unfortunately, fabrication presents some limitations on both. Further, decreasing the thickness of the support platform results in a less rigid structure and increases the acceleration sensitivity of the system. A system with support arms significantly thinner than the platform, however, can provide

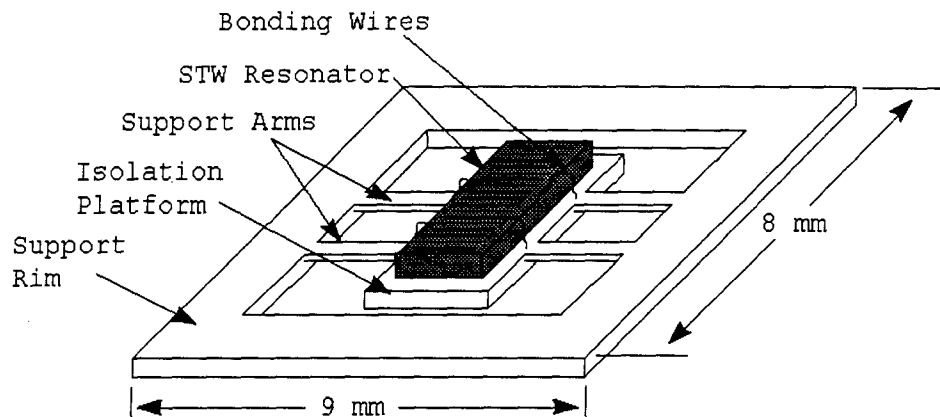


Figure 5.16. Schematic view of the modified resonator design.

both a low resonance frequency, and a rigid platform. This complicates the fabrication process, but provides a solution to the problem at hand.

5.4 Final System Design

The analysis that has been done suggests that the basic system design must be modified so that the support arms are thinner than the support platform. A schematic view of the new design is shown in Fig. 5.16 while the parameters of the platform design are specified in Fig. 5.17. The dimensions of the isolation system are, $p_t = 4.5$ mm, $p_w = 3.0$ mm, $p_t = 0.4$ mm, $s_t = 2.0$ mm, $s_w = 0.1$ mm, $s_t = 0.05$ mm, $sr_1 = 1.0$ mm, and $sr_2 = 1.5$ mm. The total dimensions of the isolation platform are then 8 mm \times 9 mm.

5.4.1 Expected Vibration Sensitivity of the Modified Design. Evaluating the plots from Section 5.2.4, the normal acceleration sensitivity of the mounted resonator, Γ_2 , is expected to be $\Gamma_2 \approx 1.2 \times 10^{-8}/g$. However, the mass of the isolation platform has been increased due to overhang in the x_3 axis. The overhang will result in approximately a 10% increase in the both the mass and the projected acceleration sensitivity. Therefore, an acceleration sensitivity of $\Gamma_2 = 1.3 \times 10^{-8}/g$ is used as the projected acceleration sensitivity of the isolated resonator. The accuracy of the finite element calculation is not sufficient to warrant reevaluating the new design, and therefore values from the original design are

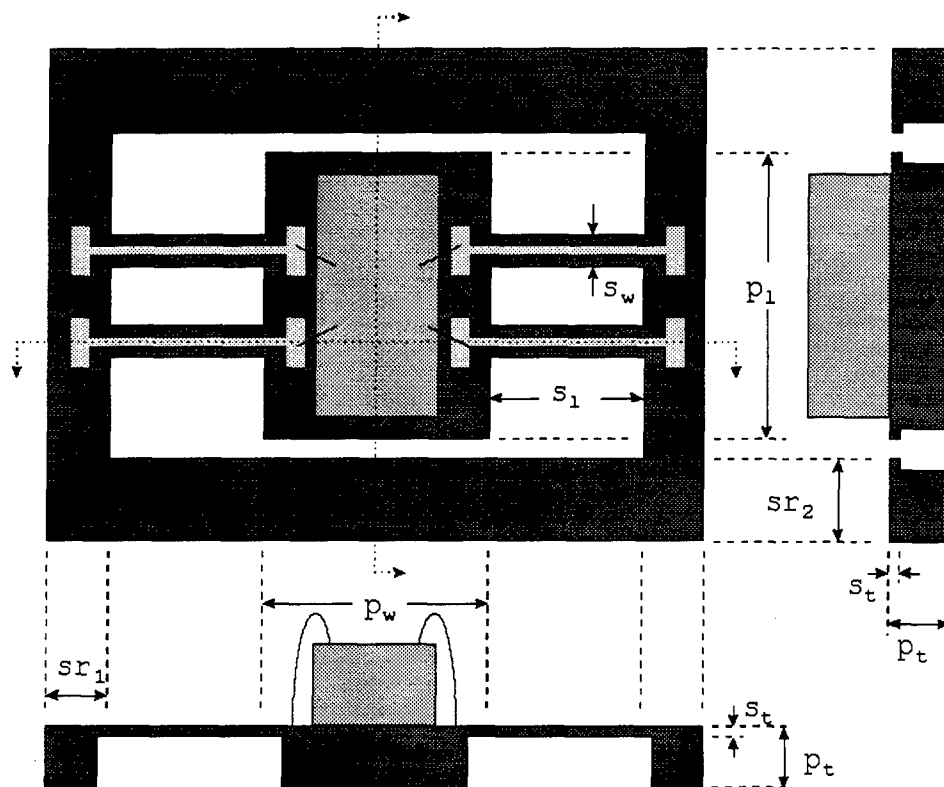


Figure 5.17. The modified design of the isolation system. The cut away views on the right and the bottom run along the dotted lines of the top view.

Table 5.2. Calculated Mass-Spring Model Parameters for the Final Isolation System Design

Parameter	Calculated Value
M_0	2.24×10^{-5} kg
k_{sys}	296.875 N/m
f_0	1159.8 Hz
C_m ($d = 25$ μm)	6.18×10^{-2} kg * s
C_m ($d = 50$ μm)	7.73×10^{-3} kg * s
C_m ($d = 100$ μm)	9.66×10^{-4} kg * s
C_m ($d = 400$ μm)	1.51×10^{-5} kg * s

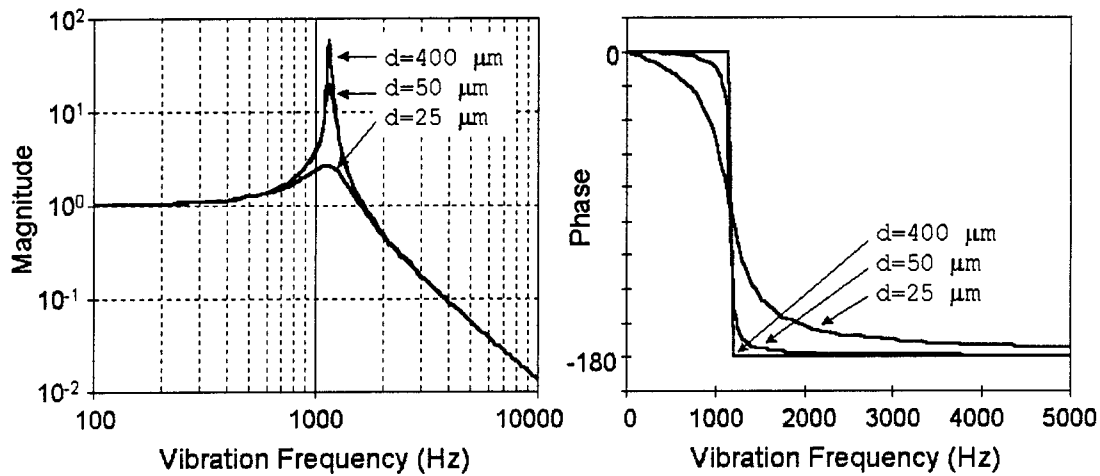


Figure 5.18. Expected absolute transmissability of the micromachined vibration isolation system for several different plate separation values, d .

used. The thickness, t , is set equal to the platform thickness, p_t . The resonator used has dimensions, $l = 3.87$ mm, $w = 1.87$ mm, and $t = 0.51$ mm.

The calculated parameters of the mass spring model are shown in Table 5.2. This includes values of the damping coefficient, C , for several separation values, d . It is clear from the value of f_0 that the resonance frequency has been successfully reduced to around 1 kHz. Further reduction of this frequency is possible by further reducing the mechanical spring constant. Fig. 5.18 shows the expected absolute transmissability of the micromachined vibration isolation system. Multiplying the absolute transmissability by the expected ac-

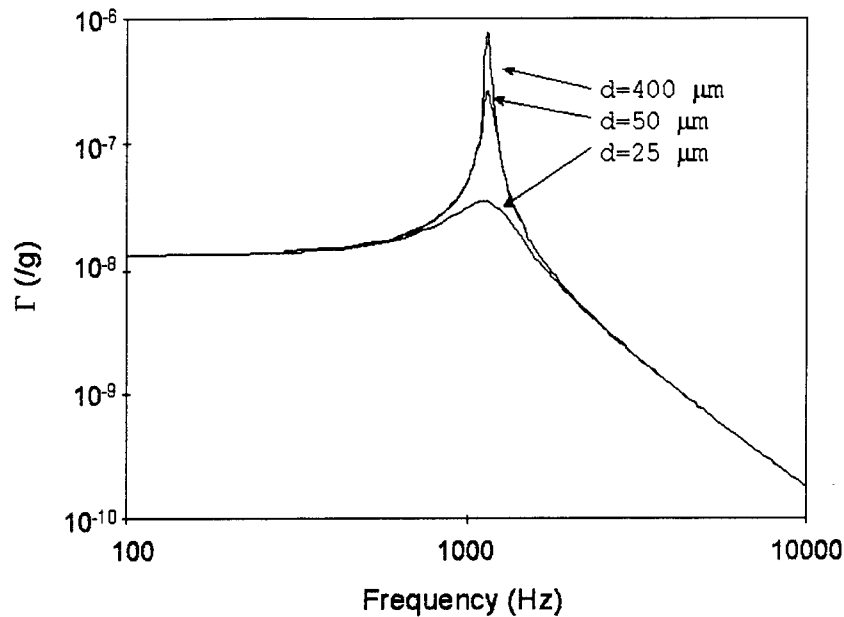


Figure 5.19. Expected vibration sensitivity of the STW resonator mounted on the vibration isolation platform for several values of plate separation, d .

celeration sensitivity results in the expected vibration sensitivity of the isolated resonator. A plot of the expected vibration sensitivity is shown in Fig. 5.19

5.5 Summary

The design of a passive vibration isolation system has been generated. Finite element analysis showed that the design parameters can be modified to reduce but not eliminate the acceleration sensitivity of the isolated resonator. The values give general guidelines for the location of the support arms and the requirement that the platform be reasonably thick. Analyzing the system as a damped mass-spring system with one degree of freedom results in the conclusion that the support arms must be thinner than the platform. Therefore, the design has been modified. Utilizing expected parameters of the new design, the absolute transmissibility from the foundation to the isolated platform was calculated. Multiplying this by the expected acceleration sensitivity from the finite element analysis results in the expected vibration sensitivity of the isolated STW resonator.

VI. Device Fabrication Process

In Chapter V, it was decided that none of the commercially available processes were capable of fabricating the isolation system. Therefore, a process utilizing the facilities available at AFIT was needed. The fabrication process must meet the six criteria listed in Table 6.1. A process meeting all of the listed criteria has been developed and is described in this chapter. The process uses two sided anisotropic etching of {110} silicon wafers. The initial etch removes material from the back side of the wafer resulting in thin and thick regions. The front side etch pattern is aligned to the regions on the back of the wafer allowing the fabrication of devices using both regions. The process utilizes only standard equipment and therefore can be easily repeated. It also allows the batch fabrication of up to 36 isolation systems per wafer. The next section provides an overview of the process. This is followed by discussion of each processing step.

6.1 Process Overview

The fabrication process is illustrated in Fig. 6.1. Schedules for individual processing steps are provided in Appendices E-I, while detailed discussion of the steps is provided in the following sections. The use of two separate silicon etches makes the process more difficult, however, it allows the thickness of the support arms to be different than the thickness of the isolation platform and the support rim. The entire process requires three photolithography masks. Each mask is used to define the specific pattern that is desired

Table 6.1. Fabrication Process Requirements

- | |
|--|
| <ol style="list-style-type: none">1) Fabrication of devices from 200 μm to 1 mm thick.2) Regions with two separate thickness values, one less than 100 μm.3) Batch fabrication allowing large number of devices to be easily produced.4) Limited processing steps.5) Utilize only standard 3 inch wafer processing equipment.6) No damage can occur to the substrate or aluminum metalization of the STW resonator. |
|--|

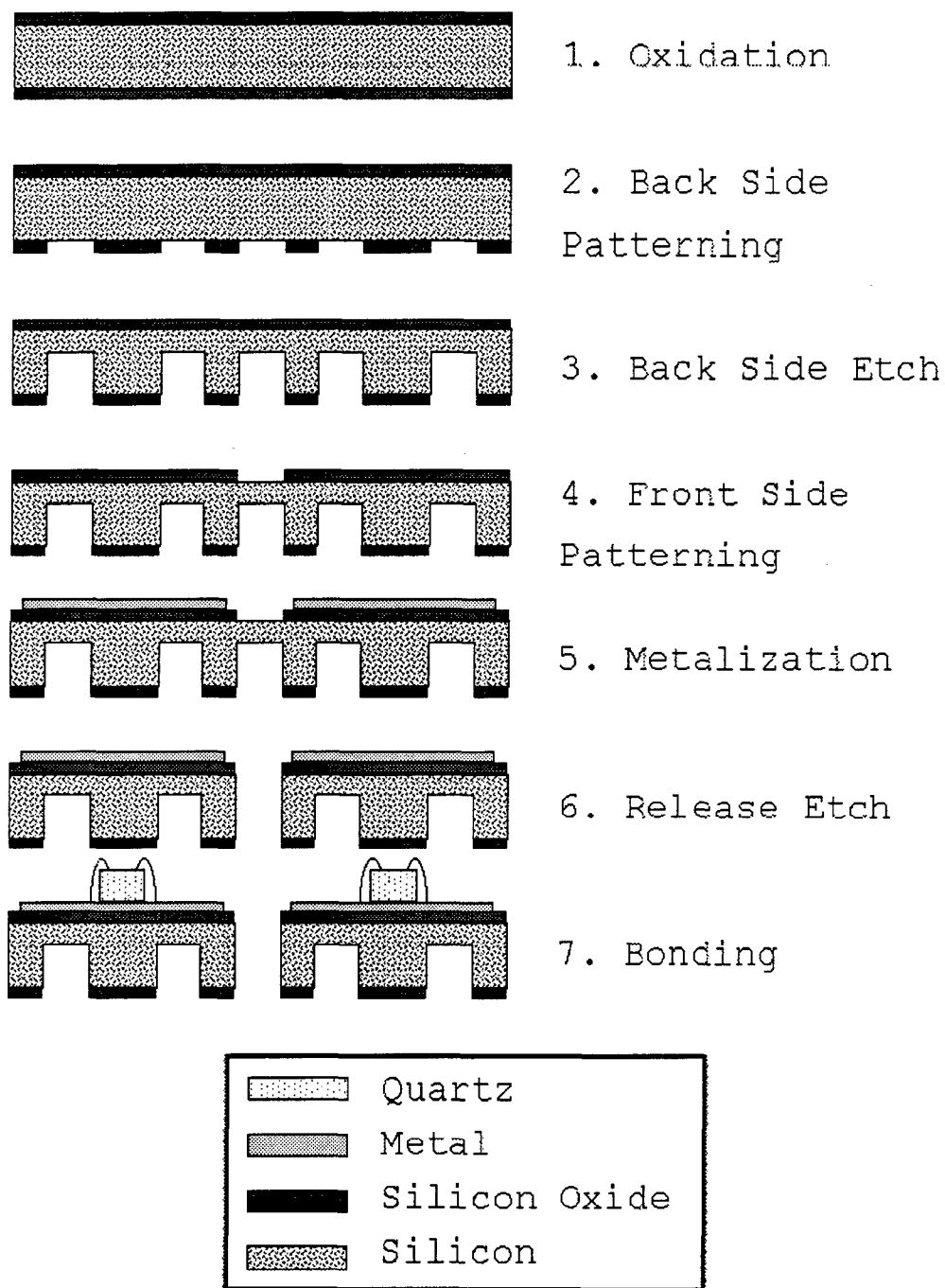


Figure 6.1. Overview of the fabrication process.

during a given step. The masks are designed and fabricated at AFIT using the process described in Appendix C. The mask designs are discussed in the next section.

Fabrication begins with commercially available, 3 inch diameter, 0.4 mm thick, double side polished, {110} silicon wafers with the primary wafer flat aligned to the {111} crystal plane. Several {111} planes are normal to the {110} wafer surface, and it is therefore possible to etch deep vertical structures into the surface of the wafer using a highly selective anisotropic etchant such as potassium hydroxide (KOH) [86, 87, 123, 124], or tetramethyl ammonium hydroxide (TMAH) [83]. For this work, anisotropic etching of the wafers is done using a potassium hydroxide solution. KOH was chosen for its high etch selectivity. Using a KOH and deionized water (DIW) solution, the etch rate in the {110} direction can be over 400 times the etch rate in the {111} direction [123, 124]. Oxide is the preferred masking material due to the availability of both thermal oxidation furnaces and chemical etchants.

6.2 Mask Fabrication

Three photo masks are required by the process; one for patterning the back side oxide, one for patterning the front side oxide, and one for patterning the metalization. The masks are fabricated at AFIT using the process described in Appendix C. For all three masks, the basic pattern is repeated on a 1 cm \times 1 cm square grid to form a 6 \times 6 array of the pattern. Therefore, 36 copies of the pattern are created on each mask. This allows up to 36 platforms to be fabricated from each wafer. The basic pattern of the back side oxide mask is shown in Fig. 6.2. The dark regions of the pattern are protected from the oxide etch, while the light regions are etched. The front side oxide mask determines the size and dimensions of the top of the platform, the support arms, and the support rims. The front side mask pattern is shown in Fig. 6.3. Again, the dark regions remain protected from the etch and form the platform, support arms, and support rim. The small notches where the support arms connect with the support rim were originally designed for corner compensation. However, the area where the support arms and the support rim connect has a fabricated thickness of only 50 μ m and therefore corner compensation is not necessary. Finally, the metalization mask determines where metal is deposited. The basic

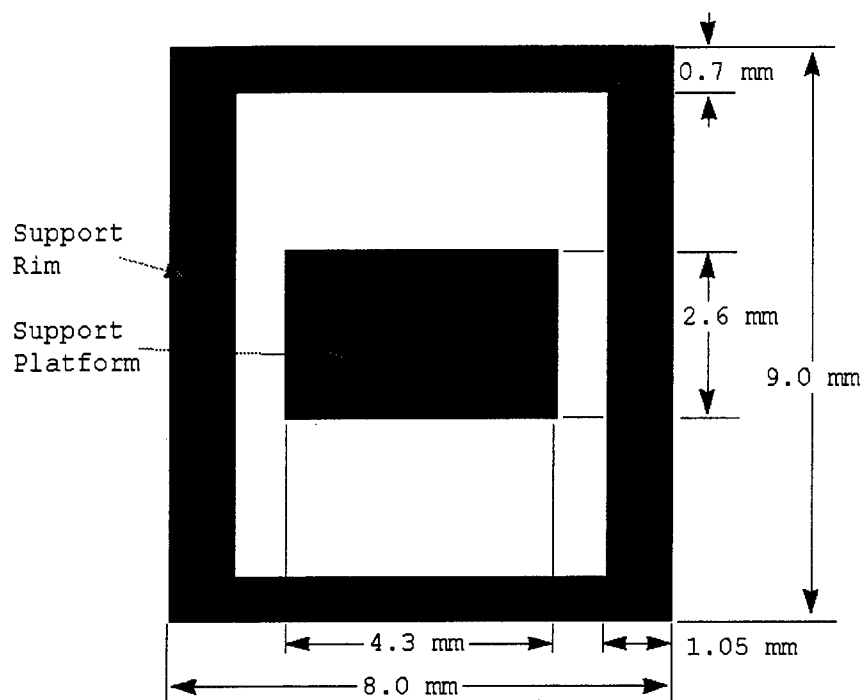


Figure 6.2. The pattern used for the back side oxide mask is shown here.

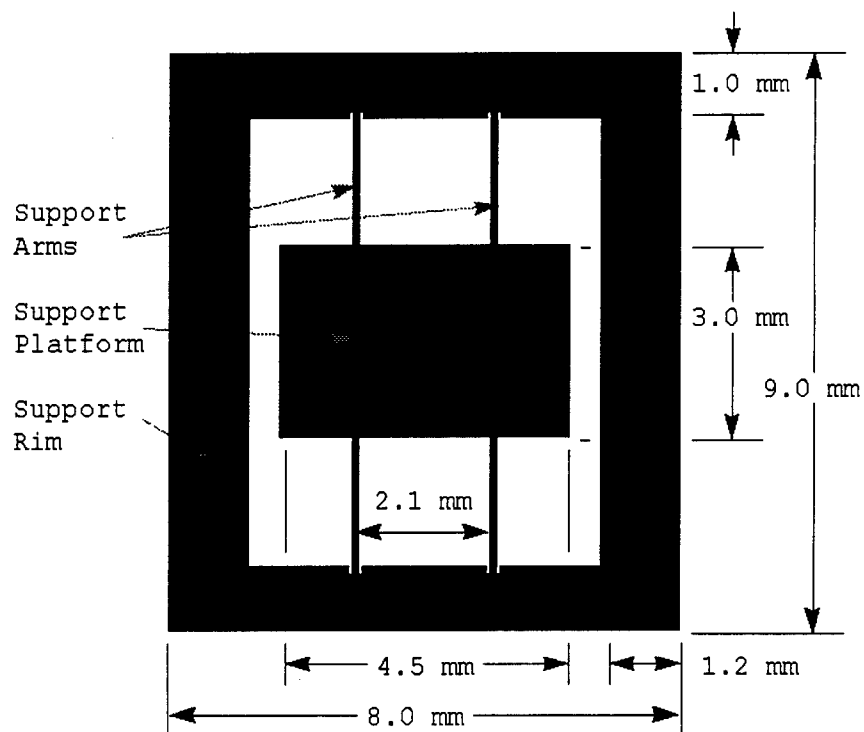


Figure 6.3. The pattern used for the front side oxide mask. Dark regions remain protected while light regions are etched.

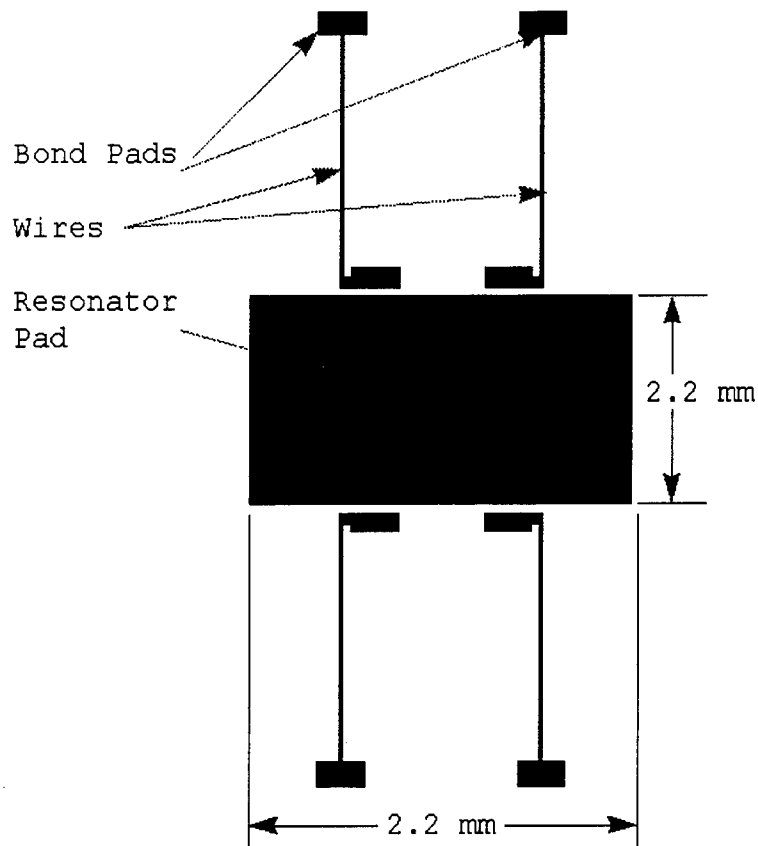


Figure 6.4. The pattern used for the metal mask. The dark areas represent the regions where metal is deposited on the wafers. The bond pads on the support rim are $250\ \mu\text{m}$ by $500\ \mu\text{m}$ while the bond pads on the platform are $200\ \mu\text{m}$ by $500\ \mu\text{m}$. The wires are $30\ \mu\text{m}$ wide.

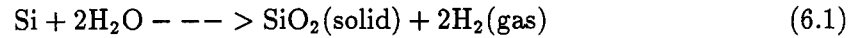
metalization pattern is shown in Fig. 6.4. The dark regions represent the area where the metal is deposited while in the light regions the metal is removed.

6.3 Oxidation

Oxide thickness is determined by the etchant selectivity and wafer thickness. KOH etches silicon 200-250 times faster in the $\langle 110 \rangle$ direction than it etches SiO_2 [124]. The lower bound selectivity (200:1) is used to ensure sufficient oxide thickness. For the $400\ \mu\text{m}$ thick wafers a $2.0\ \mu\text{m}$ thick oxide mask is required. Following the final KOH etch, the released systems should still have sufficient oxide to serve as an isolation layer. Therefore, actual mask oxides were grown $2.4\ \mu\text{m}$ thick.

Thermal oxidation can be done using either a "dry" or a "wet" process. The dry process is a high temperature oxide growth process performed in a gaseous oxygen environment, while the wet process is performed in a steam environment. Typically, dry oxide results in better electrical properties, however the growth rate is significantly slower [82]. For the work here, the oxide serves primarily as an etch mask. Further, the oxide is thick enough that dry oxidation would require several days to complete. Therefore, wet thermal oxidation is used to grow the oxide mask.

The basic thermal oxidation process is well understood since it has been widely used in microelectronic processing. The basic wet thermal oxidation process is described as [82]



where the silicon surface reacts with the steam resulting in the the formation of silicon dioxide on the surface of the wafer. For the growth of a thick oxide, the time required is proportional to the square of the desired thickness as [82]

$$t_{ox}^2 = B(t + \tau) \quad (6.2)$$

where t_{ox} is the desired oxide thickness, B is the parabolic rate coefficient, t is the time in hours, and τ is the initial oxide thickness. For thick wet oxide growths with a clean wafer, $\tau \approx 0$. The value of B is dependent upon the conditions of the oxidation, primarily temperature. Values of B are taken from Fig. 7, page 349 of Sze [82]. All oxidations for this dissertation were done at 1100° C with steam flowing through the furnace at a rate of 1 liter per minute. An initial oxide growth for 13 hours resulted in an oxide that was 2.1 μm thick. The parabolic coefficient is then calculated as $B = 0.336 \mu\text{m}^2/\text{Hr}$. This is a little lower than the expected value of $B = 0.4 \mu\text{m}^2/\text{Hr}$. The required etch time for a 2.4 μm thick oxide is then

$$t = \frac{t_{ox}^2}{B} = \frac{2.4^2}{0.336} = 17.45 \text{ hours} \quad (6.3)$$

An actual growth time of 18 hours was used and the resulting oxide was $2.395\text{ }\mu\text{m}$ thick. Therefore, the coefficient is still a little high, however the resulting oxide is sufficient.

6.4 Back Side Patterning

To etch the back side of the wafers, it is necessary to pattern the back side oxide without damaging the front side oxide. The process begins by patterning photo-resist on the back side of the wafer. Next, a protective coating of photo-resist is applied to the front side of the wafer. The undesired oxide is etched away and the photo-resist is removed in a piranha clean.

Following an initial piranha clean (Appendix D), negative photo-resist, Waycoat HR 200, is spun onto the wafer at 5000 RPM for 20 seconds. The resist is soft baked for 15 minutes at 65°C . The resist is exposed with a contact mask aligner using back side oxide mask shown previously in Fig. 6.2. The mask is aligned so that the short side of the support platform runs parallel with the $\{111\}$ wafer flat, and as a result when the front side mask is aligned, the support arms are parallel with the $\{111\}$ planes as well. The resist is developed by spinning the wafer at 500 RPM and spraying on Xylenes for 30 seconds followed by n-Butyl Acetate for 30 seconds. The spin speed is then increased to 5000 RPM for 15 seconds to dry the wafer. The resist is hard baked at 135°C for 15 minutes. HR 200 is then spun onto the back side of the wafers at 2000 RPM and hard baked at 135°C for 30 minutes.

To etch the oxide, a solution of hydrofluoric acid (HF) buffered with ammonia fluoride (NH_4F) is used. The solution ($\text{NH}_4\text{F}:\text{HF}$ 4:1) typically etches the oxide at a rate of $0.16\text{ }\mu\text{m}$ per minute resulting in an expected etch time of approximately 15 minutes. However, the etch rate is dependent upon several factors including temperature. Therefore, two minutes prior to the expected etch time, the wafers are removed from the solution and observed. The wafers are immersed in the solution for 30 second intervals and re-checked until the wafer surface is hydrophobic. The wafers are then rinsed in deionized water (DIW) followed by a clean in a piranha etch of sulfuric acid and hydrogen peroxide ($\text{H}_2\text{SO}_4:\text{H}_2\text{O}_2$ 3:2) for 20 minutes to remove the photo-resist. Following the clean, the depth of the oxide etch is measured with a profilometer. Figure 6.5 shows a typical profile of the oxide etch.

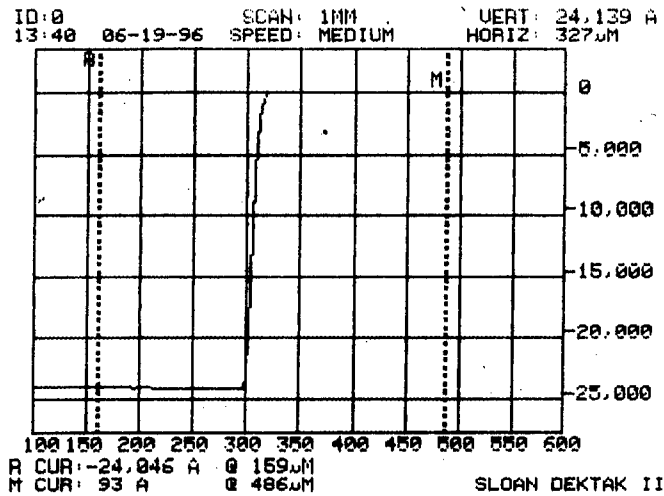


Figure 6.5. Profile of the oxide etch. The etch depth of 2.4 μm corresponds with the oxide thickness as expected.

6.5 Back Side Etch

After patterning the oxide, the wafers are etched in a solution of 500 grams of KOH dissolved in 500 mL of water. KOH is used because of its high $\{110\}/\{111\}$ etch ratio, and because the etch rate in the $\{110\}$ directions is higher than that of TMAH or EDP. The KOH solution is prepared in a sealed one liter container. The container is placed into a Lufran Superbowl which maintains a reservoir of DIW at 85° C. The container is placed in such that the DIW level is 1-2 inches above the level of KOH solution. After the Superbowl has reached 85° C, the solution is allowed at least 2 hours for the temperature of the KOH solution to stabilize. The wafers are initially immersed in the KOH solution for 15 minutes. They are then removed, rinsed in DIW, and dried. The depth of the etch is again measured with a profilometer and the oxide thickness is measured with a Leica MVP-SP thin film measurement system. The depth of the oxide is subtracted from the total etch and the etch rates for both silicon and oxide are calculated. A typical KOH etch profile measured using the Dektak IIa profilometer is shown in Fig. 6.6. As seen, the total etch depth is around 32 μm . The oxide thickness is still close to 2.4 μm so the etch rate is approximately 2.0 μm per minute. The total etch time is then calculated as 122.5 minutes for a 250 μm etch. Finally, the wafers are returned to the KOH solution and etched until the total etch time is 122.5 minutes.

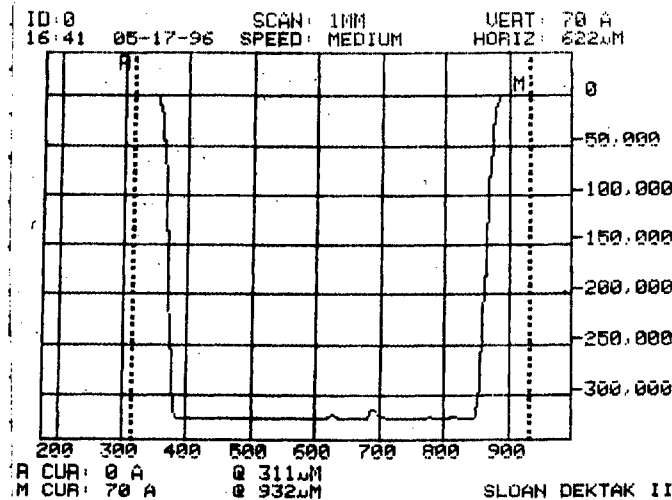


Figure 6.6. Profile of the wafer after a 15 minute etch in KOH. Hillocks that formed during the etch are visible on the bottom of the etched surface. The formation of the hillocks did not noticeably effect the etch.

The KOH solution was used for a period of 2-3 days with no noticeable change in the etch properties. After longer periods, the etch rate of the solution varied, and the silicon/oxide selectivity decreased. Following the etch in KOH the wafers appear as seen in Fig. 6.7. During the etch, 1-1.2 μm of oxide is removed. Therefore, the Leica MVP-SP is again used to measure the thickness of the oxide. The remaining oxide is typically 1.2-1.3 μm thick.

6.6 Front Side Patterning

The back side etch goes through over half the thickness of the wafer. As a result, the wafers are very fragile and the spinner is unable to secure the wafers on the vacuum chuck. Therefore, it is necessary to attach the device wafers to handle wafers for further processing. For this work, the handle wafers are commercially available test grade, 3 inch diameter, {100} silicon wafers, however, any 3 inch wafer can be used. Positive photo-resist, Shipley 1350j, is spun onto a handle wafer at 1000 RPM. The slow spin speed provides a thicker coating and facilitates the later separation of the two wafers. The back side of the device wafer is placed onto the resist such that the wafer flat of the device wafer protrudes 2-3 mm past the edge of the handle wafer as seen in Fig. 6.8. Using wafer tweezers, the

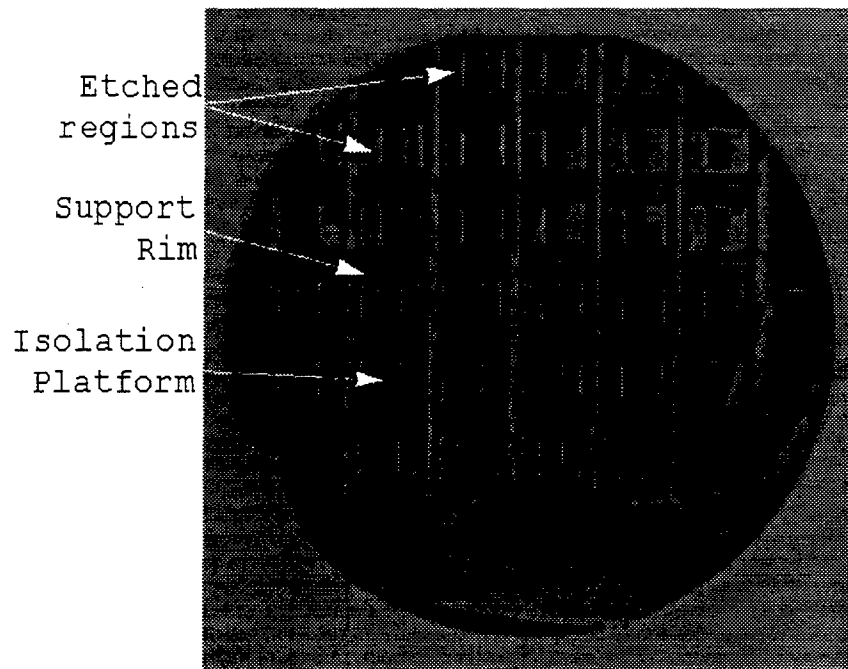


Figure 6.7. Photograph of a wafer following the KOH etch. The rough appearance of the etched regions is due to the formation of hillocks on the etched surface.

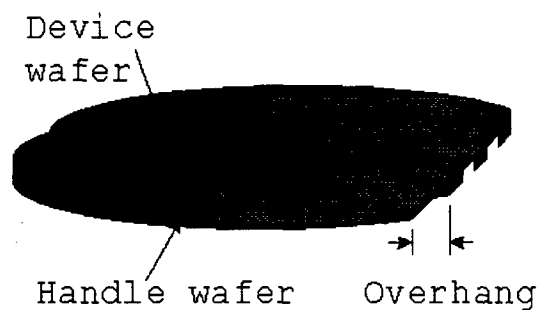


Figure 6.8. The device wafer is attached to the handle wafer using positive photo-resist as an adhesive layer. The device wafer overhangs the edge of the handle wafer by 2-3 mm to facilitate the alignment of the front side oxide mask.

outside rims of the two wafers are pushed together. This improves the adhesion of the resist to the device wafer and is necessary to protect the oxide on the back side of the device wafers. The paired wafers are hard baked for 30 minutes at 100° C. Positive photo-resist dissolves readily in acetone and therefore allows separation of the wafers without damaging the metal that is deposited on the front side of the device wafer. Further, the metalization uses a lift off process to pattern the metal. This process utilizes the same positive photo-resist which is removed with a rinse in acetone. Therefore, the final step of the metalization serves to both pattern the metal and separate the device wafer from the handle wafer.

After the device wafers are attached to handle wafers, they can be processed as normal wafers. HR 200 is spun onto the front side of the device wafers at 5000 RPM. The resist is patterned as before using the second photo-mask previously shown in Fig 6.3. Alignment of the masks is done using a small piece from a second silicon wafer. The marker piece is placed next to the wafer flat of the device wafer, and aligned so that the edge of the marker corresponds to the pattern on the back side of the wafer. The pattern is visible due to the overhang shown in Fig. 6.8. The aligner can then use the marker and the edge of the wafer to align the front side pattern with the back side pattern. Following the exposure, the resist is developed. The oxide is then etched in a buffered HF solution ($\text{NH}_4\text{F}:\text{HF}$ 4:1). Note that the positive photo-resist connecting the two wafers protects the oxide on the back side of the device wafer. For the 1.2-1.3 μm thick oxide, an etch time of approximately 8 minutes is required. Again, two minutes prior to the expected etch time, the wafers are removed and observed. The wafers are repeatedly etched for 30 second intervals and checked until the wafer surface is hydrophobic. The wafers are again cleaned in a piranha etch ($\text{H}_2\text{SO}_4:\text{H}_2\text{O}_2$ 3:2) for 20 minutes to remove the negative photo-resist. The cleaning etch dissolves some of the positive resist connecting the handle wafer to the device wafer but does not release the two wafers.

6.7 Metalization

The wafers are now ready to be metalized. The metal is patterned using a lift off process. The first step is to deposit and pattern a photo-resist layer. First, an adhesion

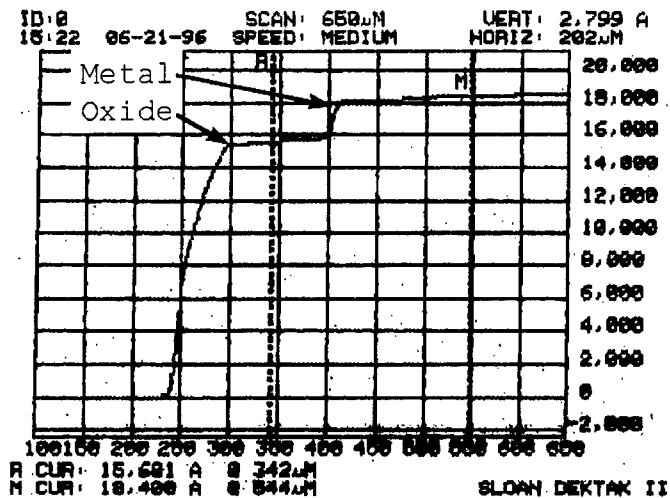


Figure 6.9. Profile of the wafers following the metalization. The metal layer is approximately 2700 Å while the oxide is approximately 9000 Å.

promoter, HMDS, is spun onto the wafer at 4000 RPM. This is immediately followed by spinning Shipley 1350j positive photo-resist onto the wafer at 5000 RPM for 20 seconds. The resist is soft baked for 20 minutes at 70° C. The wafers are exposed with the metal mask shown in Fig. 6.4 and then soaked in chlorobenzene for 10 minutes to swell the photo-resist. Next, the wafers are dried for 15 minutes at 70° C. Finally, the wafers are developed by spinning the wafers at 500 RPM and spraying them with a developer solution (AZ351:DIW 1:3) for 30 seconds followed by spraying on DIW for 20 seconds. The spin rate is accelerated to 5000 RPM for 15 seconds to dry the wafers.

The wafers are placed into a Denton DV-602 thin film deposition system. Under vacuum, 300 Å of chromium followed by 2200 Å of platinum are deposited onto the wafers using RF sputtering. Finally, the wafers are removed from the vacuum and immersed in acetone to lift off the undesired metal. If necessary, the undesired metal is lightly brushed off with a cotton swab. The wafers remain in the acetone until the handle and device wafers are completely separated. Typically, this occurs after 15-20 minutes, but it can take as long as 2 hours. The wafers are cleaned with a 10 minute rinse in methyl alcohol and blown dry with nitrogen. A profilometer is then used to measure the thickness of the metal and depth of the oxide etch. Fig. 6.9 shows the measured profile of the metal and etched oxide.

6.8 Release Etch

To release the devices, a KOH solution is prepared as described in Section 6.5. Again, a 15 minute etch is performed and the total depth of the etch is measured with a profilometer. The {110} silicon etch rate is calculated and the wafers are returned to the KOH solution. The wafers are etched until the devices have been completely released and the support beams are of the desired thickness. During this final etch, the wafers are etched from both the front and back sides. Therefore, the etch rate of $2.0\ \mu\text{m}$ per minute is doubled. Releasing the devices requires etching through the final $150\ \mu\text{m}$ of silicon. This requires an etch time of only 37.5 minutes. Typically, the etch is allowed to proceed for 60 minutes to thin the support arms. Following a 55 minute etch, the support arms are approximately $50\ \mu\text{m}$ thick. During the etch, the individual devices are separated from each other. Therefore, they must be filtered out of the KOH solution. This is done by pouring the KOH solution into another container without pouring the isolation systems out. With tweezers, the platforms are then lifted individually into a container of DIW. Following a 10 minute rinse, the isolation systems are rinsed in methyl alcohol for 15 minutes. They are finally dried by lightly blowing them with nitrogen.

6.9 Bonding

As the released devices are very fragile, they are secured before mounting the resonators. This is done by again using the handle wafers. Shipley 1350j positive photo-resist is spun onto the handle wafers at 1000 RPM. The released devices are placed onto the wafer with the metalized side facing upward. The photo-resist is hard baked for 20 minutes at 100°C . The STW resonators are mounted to the center of the platform using Ablebond 84-1LMI conductive epoxy. The epoxy is cured at 160°C for 30 minutes. The resonators are wire bonded using an ultrasonic ball bonder. The completed devices are then released by a 5-10 minute etch in acetone. This is the only exposure the STW resonators have to chemicals during the fabrication process and therefore, the aluminum metalization on the resonators is not damaged. The fabricated devices are 9 mm long by 8 mm wide by 1 mm thick. Figure 6.10 shows an isolator with a mounted resonator. The devices are now ready to be connected to an oscillator circuit.

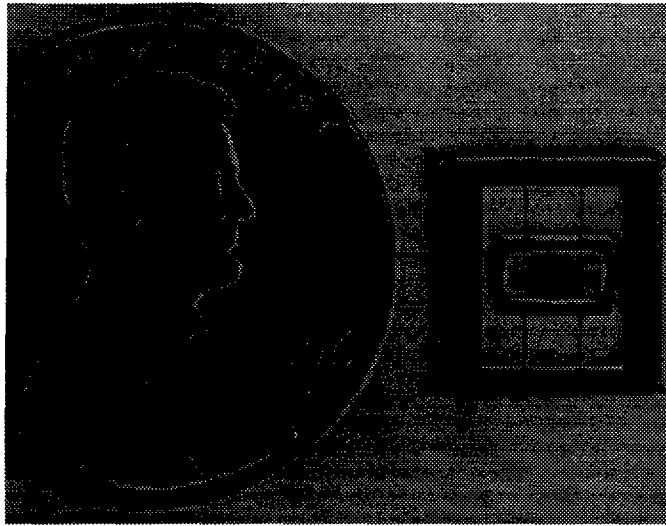


Figure 6.10. A photograph of the fabricated isolation system with a STW resonator bonded on the platform.

6.10 Summary

A fabrication process capable of meeting all of the specified requirements has been developed. The developed process offers several advantages over other techniques that were available to the author. First, the entire process can be performed with standard 3 inch wafer, integrated circuit fabrication equipment. Even the fabrication of the photo masks was done by the author at AFIT. This keeps the cost of the fabrication low. Second, the process results in the batch fabrication of up to 36 devices per wafer. This allows the fabrication costs to be shared over a large number of devices. Third, the process utilizes limited steps, including three photolithography steps. Fourth, the process only exposes the STW resonators to acetone. Acetone is an organic etchant that does not damage the quartz resonators or their aluminum metalization. Finally, the process uses only commonly available chemicals. All of the chemicals are commonly used in the fabrication of integration circuits except for KOH, and KOH is readily available for a number of other processes. Utilizing the new process, the author fabricated several hundred isolation systems and STW resonators were bonded to over 20 of the platforms. In the current form, the process can be used to fabricate a wide variety of mechanical systems.

VII. Experimental Results

Using the process described in Chapter VI, over 100 isolation platforms were fabricated. 1 GHz STW resonators provided by SAWTEK, Inc. were mounted and bonded onto over 20 of the isolation platforms. The equipment required for measuring the vibration sensitivity is not available at AFIT, and therefore testing was conducted by the author at SAWTEK's facilities in Orlando, Florida. The resonators were attached to a proprietary oscillator circuit designed for the 1 GHz STW resonator. Four oscillator circuits were available, and resonators were connected to all four. However, time permitted measurement of the vibration sensitivity of only three of the resonators. During testing, the mechanical resonance of the oscillator was observed. Further, the measured vibration sensitivity was approximately that predicted in Chapter V. However, several differences between the predicted vibration sensitivity and the measured values are apparent. These are discussed in the following sections.

7.1 Mounting the Oscillator

The resonators were tested using oscillators originally designed for the 1 GHz STW resonators mounted in surface mount packages (SMPs) [22, 35]. The isolation system is significantly larger than the SMP, but there is enough space on the oscillator substrate to fit the isolators as seen in Fig. 7.1. Unfortunately, one edge of the isolation platform hangs off the end of the oscillator substrate by approximately 1 mm. The overhanging end was

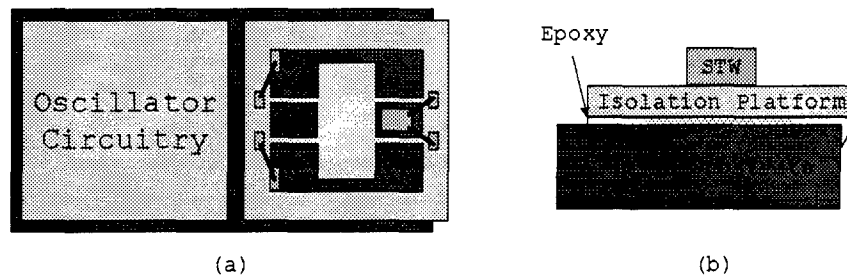


Figure 7.1. The isolated resonator is mounted on the end of the oscillator. One side of the isolator overhangs the edge of the oscillator substrate by approximately 1 mm. (a) The top view shows the position of the isolator, and the bonding, while (b) a side view shows how the overhang was secured with epoxy.

supported by additional epoxy to ensure a rigid mount of the isolation system. Using the proprietary oscillator circuits eliminates the need to design a custom oscillator. Further, the performance of the oscillator circuit is better optimized than a custom built circuit is likely to be. The measured vibration sensitivity of the oscillators with SMP mounted STW resonators was on the order of $2-3 \times 10^{-10}/g$ and therefore the sensitivity of the oscillator circuitry should be well below that of the isolated resonators [22]. Four oscillator circuits were available for testing. Isolated STW resonators were mounted on all four oscillators. Testing was performed at SAWTEK's facilities in Orlando, Florida, over a period of three days. Testing time was thus limited. Isolators were successfully mounted and operated on all four oscillator circuits, however, time permitted testing of only three of the units.

Initially, a single isolated resonator was mounted onto one oscillator using the configuration shown in Fig. 7.1. Ablebond 84-1-LMI, non-conductive epoxy, was placed onto the oscillator substrate in the region where the support rim would be located. The isolation system was then placed onto the oscillator substrate so that the support rim was on the epoxy. The support rim was then pushed down towards the oscillator substrate to spread the epoxy resulting in uniform coating that is approximately $25 \mu m$ thick. The isolation platform is left suspended approximately $25 \mu m$ above the oscillator substrate and is thus free to move. Additional epoxy was used under the overhanging edge of the isolator to provide a rigid support. Finally, the epoxy was cured.

Wire bonds were connected from the support rim to the oscillator bonding pads as illustrated in Fig. 7.1. With this initial setup, it was very difficult to achieve a proper impedance match between the isolated STW resonator and the oscillator circuit. When a relatively close match was achieved, the oscillator loop resulted in a signal loss over 10 dB. It was determined that the wires running across the isolator support arms were the source of the large signal loss. This was confirmed using a test fixture. Two of the wires were shorted together as shown in Fig. 7.2, and a loss of 36.7 dB was measured between the bond pads on the support rim for a 1 GHz signal. This loss is too large for the amplifier in the oscillator circuit to overcome, and therefore it is necessary to bypass these wires. This problem results from the thin wire across the arm acting as a poorly designed microstrip

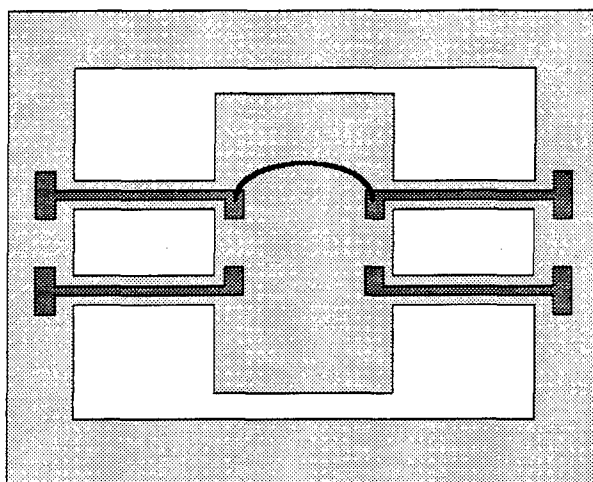


Figure 7.2. The signal loss across two support arms shorted together with a bonding wire showed 36.7 dB of loss.

transmission line. It should be possible to redesign the wires, however this has not yet been explored.

The initial wire bonds were removed and new bonds were made directly from the STW resonator to the oscillator bonding pads as illustrated in Fig.7.3. The 25 μm motion of the platform does not result in damage to the support arms, and therefore with care the resonator can be bonded without fixing its position. Due to their length, size, and relatively low Young's modulus, the wires directly connecting the resonator to the platform should not have a significant effect on the spring constant of the system. Further, their mass should have only a minor effect on the system and therefore both effects are considered negligible.

The oscillator was successfully impedance matched to the resonator with the new wire bonding configuration. The matching is shown in Fig. 7.4, while Fig. 7.5 shows the magnitude and phase of the oscillator loop. A 2.29 dB gain is measured at zero phase shift. As described in Chapter II, 2-4 dB net gain is desired for the oscillator to operate over a range of environmental conditions. Therefore, the oscillator loop was closed, and the output of the oscillator was measured. Figure 7.6 shows the output of the oscillator after it has been turned on. The oscillator has the expected center frequency of 1 GHz and the oscillator peak is over 70 dB above the noise near the carrier.

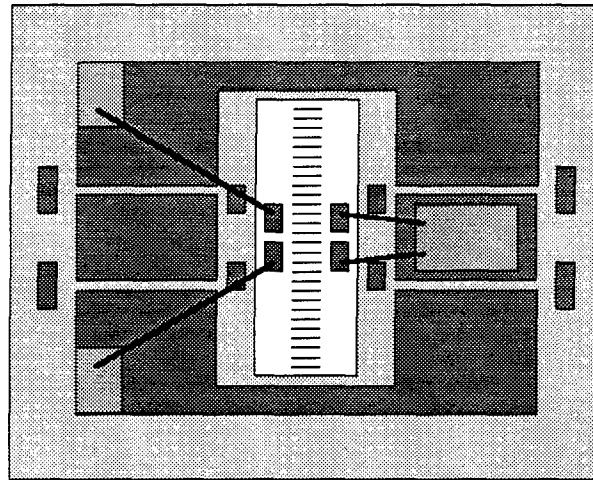


Figure 7.3. The wires on the support arms were bypassed by directly bonding from the oscillator circuit to the STW resonator.

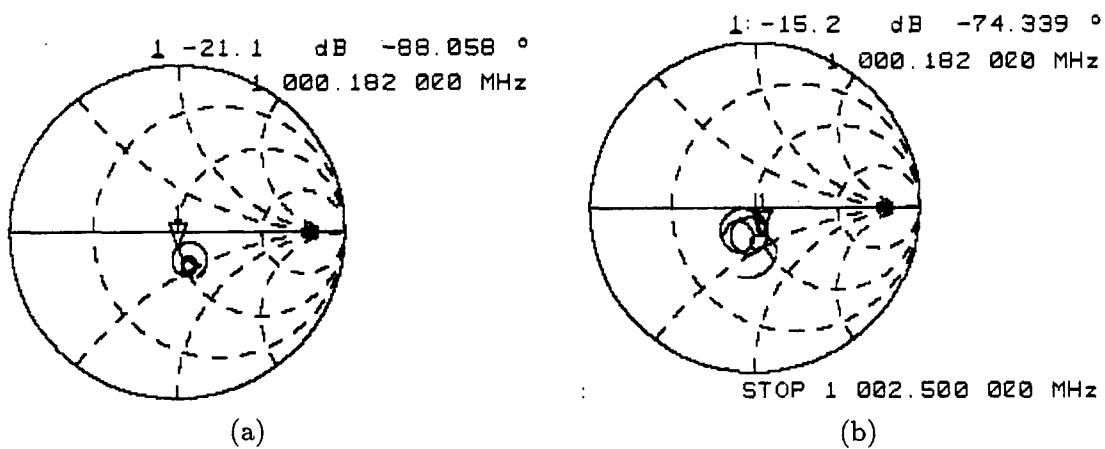


Figure 7.4. Impedance matching of the STW resonator to the oscillator circuit. (a) Looking into the STW resonator. (b) Looking into the oscillator circuit.

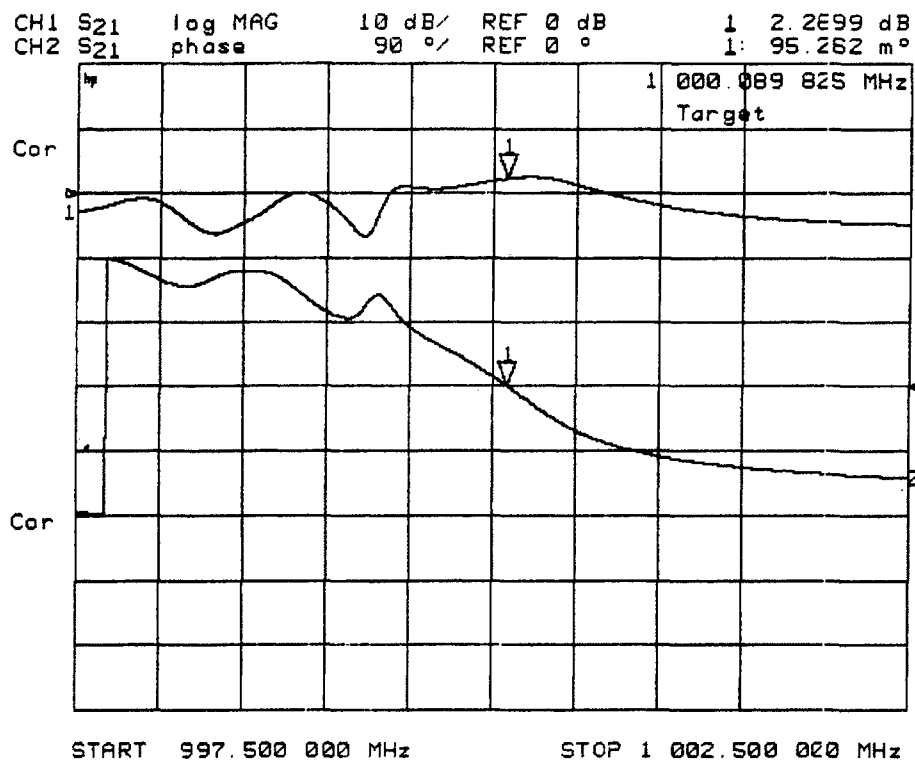


Figure 7.5. Magnitude and phase of the oscillator loop.

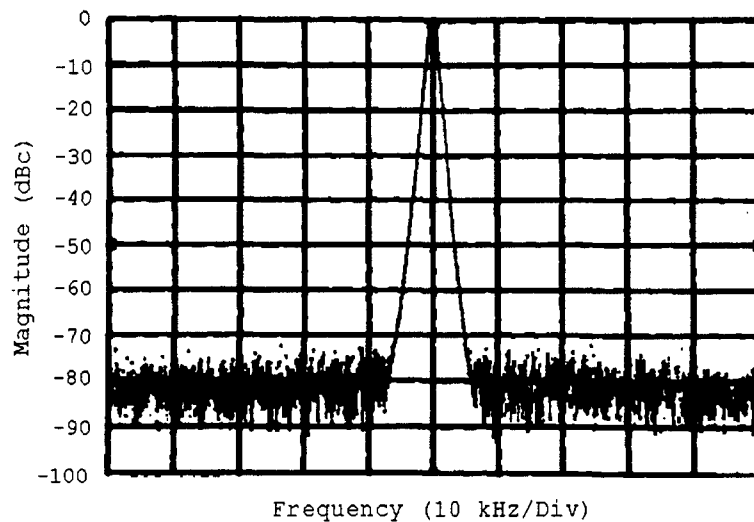


Figure 7.6. The output spectrum of the oscillator. The center frequency is at 1.0001042 GHz, and the noise close to the carrier is over 70 dB below the peak at the center frequency. The plot has a frequency span of 100 kHz.

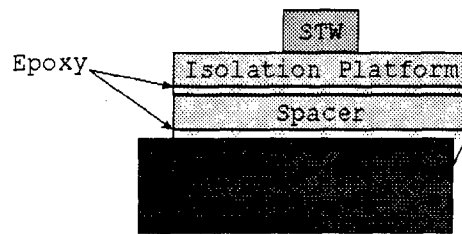


Figure 7.7. To provide a larger gap and decrease the damping, a spacer was placed in between the isolation platform and the substrate. The spacer is simply the support rim of an isolation platform with the isolation platform removed.

Finally, the other three oscillator circuits were modified, and isolated resonators were mounted on them. The second resonator was mounted in the same manner as the first. The third and fourth oscillators were mounted with a spacer rim as shown in Fig. 7.7. The spacer increases the separation between the oscillator substrate and the isolation platform resulting in lower damping. Bonding the third and fourth oscillators required bonding to the STW resonator before mounting the isolation platform and leaving flying leads at the other end of the bond. Once the isolation system was secured and the epoxy cured, the flying leads were bonded to the oscillator bonding pads. During this process, one arm of the second resonator, and two arms of the fourth resonator were broken. Since time was limited, conductive epoxy was applied to the cracks and cured. The epoxy should provide a rigid connection, but may have had some effect on the resonant frequency of the isolation systems.

All four oscillators were powered up and successfully operated at a 1.00 GHz operating frequency. However, limited time allowed the testing of only three oscillators. The oscillators are referred to by number corresponding to their fabrication order (1-4). Therefore, oscillator 1 was the first oscillator used for testing. Oscillators 1 and 2 have a separation between the isolation platform and the oscillator substrate of approximately 25 μm , while oscillators 3 and 4 have a separation of approximately 450 μm . After testing of oscillator 1 was complete, non-conductive epoxy was placed under the isolation platform, connecting it to the oscillator substrate. The epoxy was then cured. This rigidly mounts the isolation platform to the substrate, and eliminates the isolation provided by

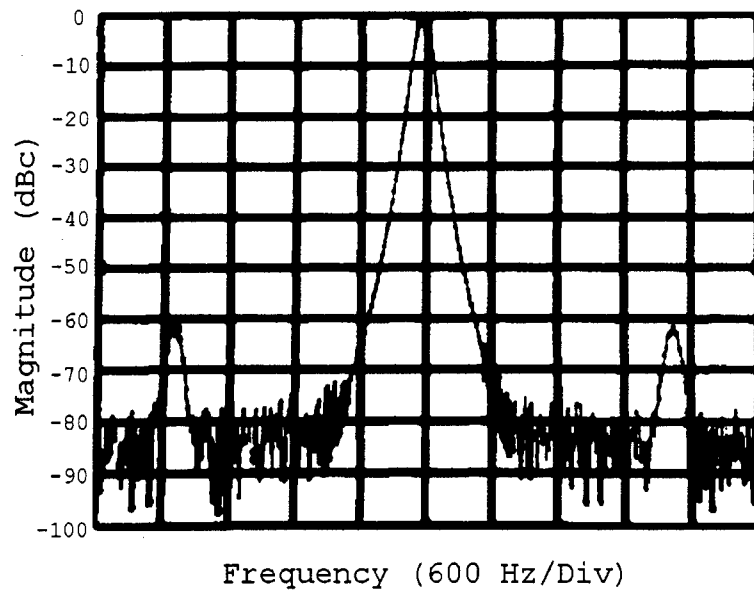


Figure 7.8. Vibration of the oscillator results in vibration induced sidebands in the frequency spectrum. Here a 1 g vibration at a frequency, $f_v = 2250$ Hz is applied to the oscillator. The vibration is normal to the surface of the resonator. The plot has a span of 6 kHz.

the support arms, however, nothing else with the circuit is modified. This oscillator is referred to as the baseline oscillator.

7.2 Test Set Up

All vibration testing was done with the standard setup used by SAWTEK [22, 35]. The vibration sensitivity is measured by mounting the oscillator on a vibration table. The table is vibrated with a vibration having a magnitude, A_v , and a frequency, f_v . The magnitude of the vibration is measured with an accelerometer on the table. The output spectrum of the oscillator is recorded with a spectrum analyzer. Applying a vibration results in sidelobes in the output spectrum as detailed in Chapter II. Figure 7.8 shows sidebands in the power spectrum resulting from a vibration with $A_v = 1$ g, and $f_v = 2.25$ kHz, applied to oscillator 1. All vibrations are applied normal the surface of the resonator (the x_2 axis).

7.3 Vibration Sensitivity Measurements

Testing was performed on three oscillators. Initially, the oscillator being tested was turned on and allowed 5-10 minutes to warm up so that the center frequency could stabilize. Using a constant magnitude, the vibration frequency was varied from 100 Hz up to 5 kHz. Generally, from 100 Hz to 2 kHz, measurements were taken at intervals of 100 Hz. Above 2 kHz, the step size was increase to 250 Hz until 3 kHz was reached. Finally, the step size was increased to 500 Hz until the final measurement at 5 kHz. Measurements were taken and the power in the side lobes was recorded. The vibration sensitivity was then calculated using Eq. 2.19. Time permitted the testing of oscillators 1, 2, and 3, and the testing of the baseline oscillator. The magnitudes used during testing and the calculated vibration sensitivity of the devices are presented in the following sections.

7.3.1 Baseline Measurement. Measurements of the baseline oscillator were taken for both $A_v = 1$ g and $A_v = 3$ g. At $A_v = 1$ g measurements were taken from 100 Hz up to 4 kHz while at $A_v = 3$ g measurements were taken up to 5 kHz. The measured vibration sensitivity of the baseline oscillator is shown in Fig. 7.9. Figure 7.9 shows that the normal vibration sensitivity of the oscillator remains relatively constant at a value of 2×10^{-9} /g over the entire frequency range. Recall that the baseline oscillator is just oscillator 1 with the isolation platform secured to the substrate, and therefore, the flat vibration sensitivity curve is expected. Also as expected, the vibration sensitivity of the oscillator under both 1 g and 3 g vibrations is very close. The measured values are lower than the acceleration sensitivity predicted by finite element analysis for the isolated resonator. This implies that the isolation platform is not rigid enough, resulting in additional deformation of the platform and a higher acceleration sensitivity. Again, this is not a surprising result as the alumina oscillator substrate is very rigid compared to the isolation system.

7.3.2 Oscillator 1. Four separate measurements were made for the first oscillator. An initial test was done with a 0.5 g vibration over the entire frequency range. The second test was also done at 0.5 g, but measurements were taken only up to 3 kHz. Measurements were then taken at 1 g up to 3 kHz and 3 g up to 5 kHz. The measured vibration sensitivity of oscillator 1 is shown in Fig. 7.10. As seen, the vibration sensitivity at low frequencies

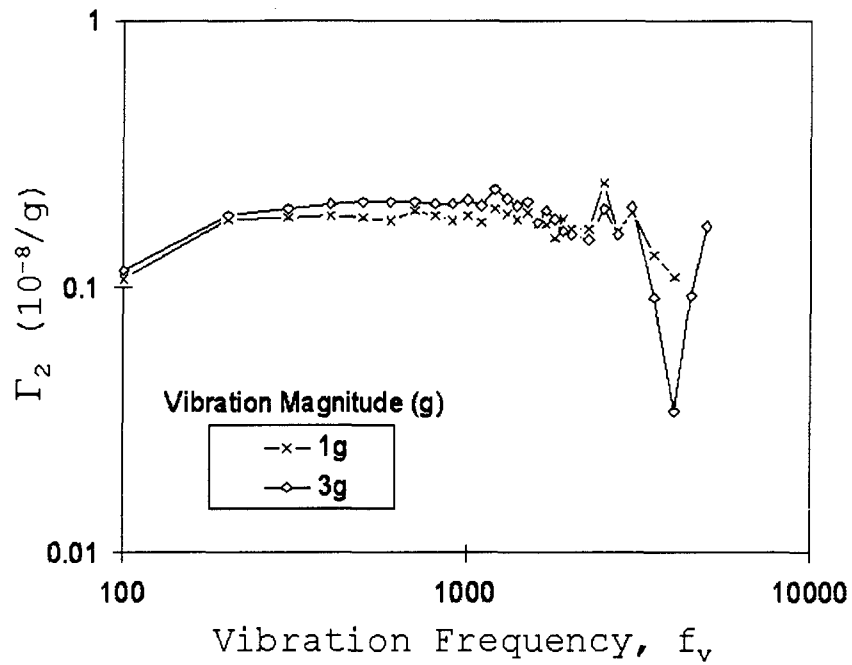


Figure 7.9. Measured vibration sensitivity of the baseline oscillator.

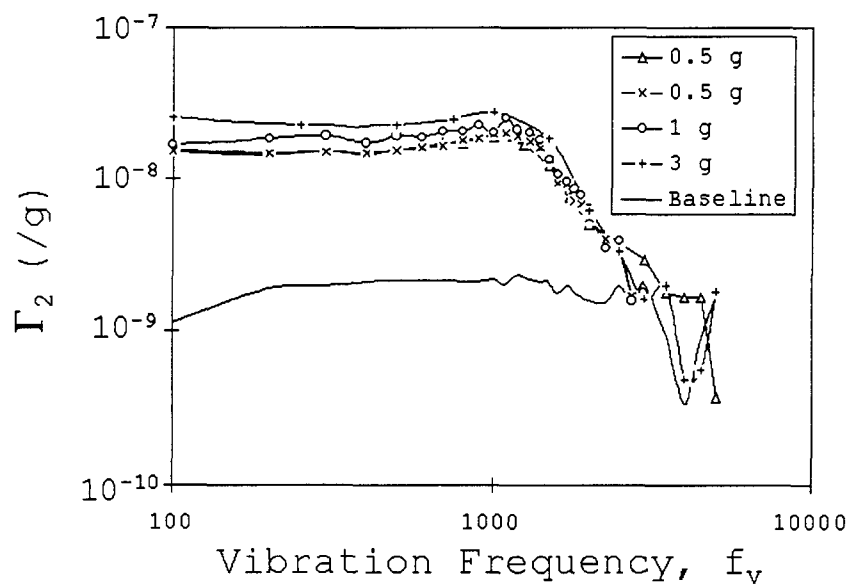


Figure 7.10. Measured vibration sensitivity of oscillator 1. The vibration sensitivity of the baseline oscillator is shown for comparison.

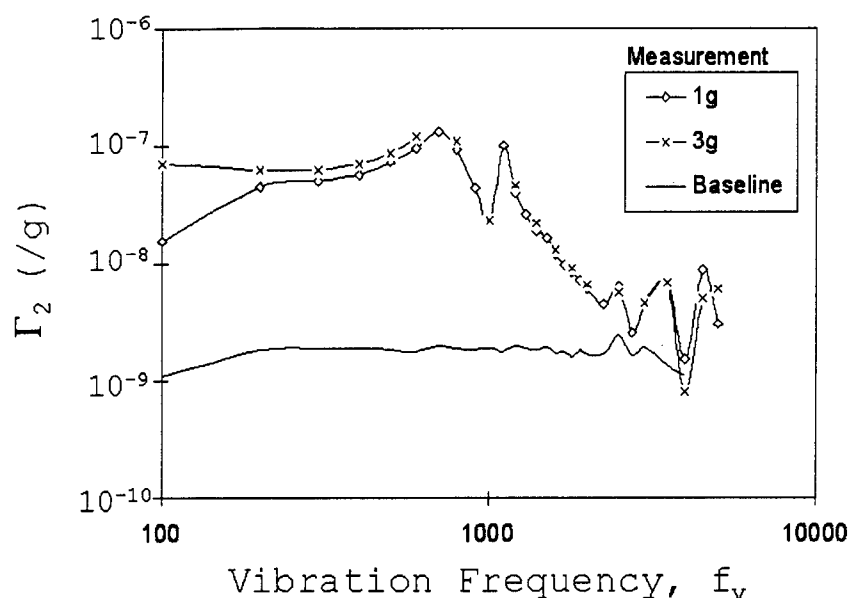


Figure 7.11. Measured vibration sensitivity of oscillator 2.

(<500 Hz) is well above that of the baseline oscillator. As the vibration frequency rises above 1 kHz, the vibration sensitivity increases, peaking around 1.1 kHz. After reaching a peak, the vibration sensitivity falls off rapidly. This follows the general pattern expected from a resonant system. Note that the same pattern is not observed in the baseline measurement. Since the only difference between the baseline and the current system is the epoxy fixing the isolation platform in place, and the expected resonance frequency of the isolation system is 1159 Hz, it is reasonable to conclude that this is the mechanical resonance of the isolation system. Looking at the data also makes one other point clear; the vibration sensitivity for vibrations with frequencies below the resonance frequency increases with the vibration magnitude. However, at frequencies above the resonance, the vibration sensitivity is independent of vibration magnitude as it should be. Further discussion of this and comparison with the expected curves is provided in Section 7.4.

7.3.3 Oscillator 2. Measurements of the second oscillator were taken for vibrations having magnitudes of $A_v = 1$ g and $A_v = 3$ g. For both magnitudes the measurements were taken up to 5 kHz. The measured vibration sensitivity of oscillator 2 is shown in Fig. 7.11. In this plot, there appear to be two resonance peaks with the first centered be-

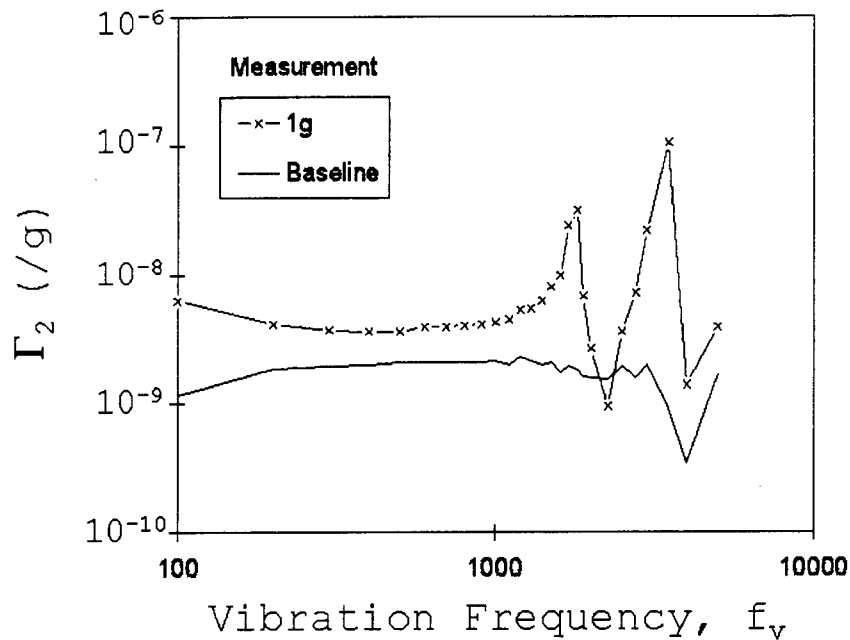


Figure 7.12. Measured vibration sensitivity of oscillator 3.

low 1 kHz and the second centered around 1.1 kHz. Again, at frequencies below resonance, a dependence between vibration magnitude and vibration sensitivity is apparent.

7.3.4 Oscillator 3. For the third oscillator, time only permitted taking data at $A_v = 1$ g. The vibration sensitivity was measured up to 5 kHz. The measured vibration sensitivity of oscillator 3 is shown in Fig. 7.12. Note that the third oscillator has a separation between the isolation platform and the oscillator substrate of approximately 450 μm while the first two oscillators had a separation of only 25 μm . Again, a clear resonance curve appears. The peak however is located around 1.8 kHz. Further, a second peak appears at approximately 3.6 kHz, and the sensitivity at this peak is higher than that observed at the original 1.8 kHz peak. Note also that the sensitivity in the range below resonance is significantly lower than that of oscillators 1 or 2, but is still above the baseline value.

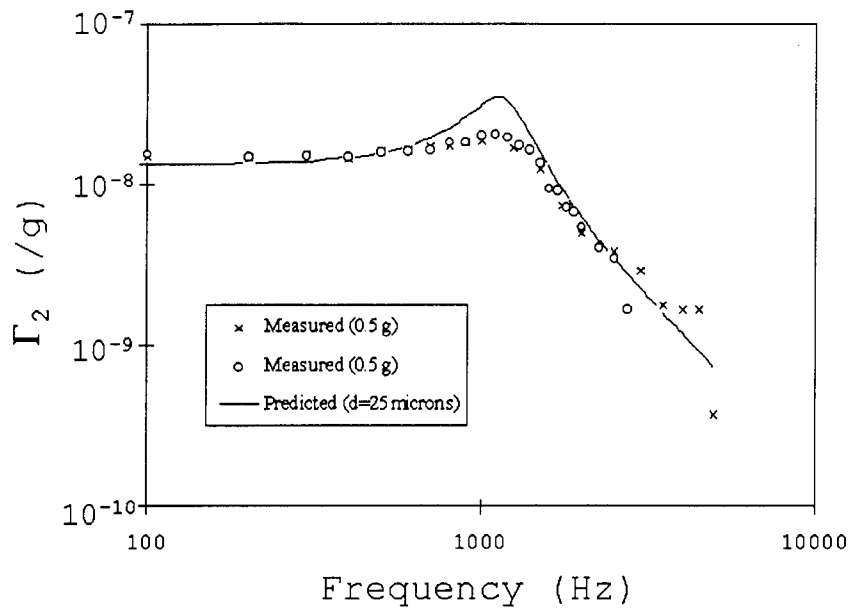


Figure 7.13. Predicted vibration sensitivity for an isolated resonator with the isolation platform separated from the oscillator substrate by 25 μm compared with the measured vibration sensitivity of oscillator 1. The measured values, x's and o's, were measured with a vibration with a 0.5 g magnitude.

7.4 Discussion

The measured vibration sensitivity clearly shows that a resonance defined by the mechanical properties of the isolation system exists. The vibration sensitivity curves generally follow the expected pattern of a typical resonance curve. This is particularly true with oscillator 1. Oscillator 2 follows the general pattern of a resonance curve, but two separate peaks occur. Oscillator 3 also shows a second peak. This peak results in a higher measured vibration sensitivity than the lower frequency peak. Both peaks have a characteristic resonant shape to them with a gradual rise, then a jump at resonance and finally a rapid fall off. The cause of the second peak is probably a second vibrational mode or in oscillator 3 a harmonic of the resonant frequency.

Figure 7.13 shows the vibration sensitivity of oscillator 1 as measured with a vibration of 0.5 g and the predicted vibration sensitivity for the isolation platform assuming that the baseline acceleration sensitivity is 1.3×10^{-8} /g and the isolation platform is separated from the oscillator substrate by 25 μm . From the curve, it is clear that the data fits

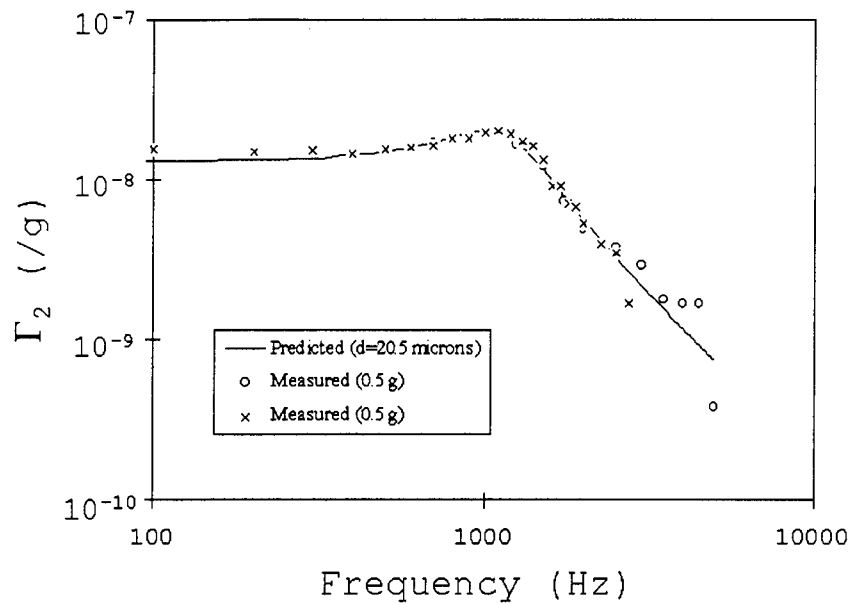


Figure 7.14. Predicted vibration sensitivity for an isolated resonator with the isolation platform separated from the oscillator substrate by 20.5 μm compared with the measured vibration sensitivity of oscillator 1. The measured values, x's and o's, were measured using vibrations of 0.5 g magnitude.

very well with the predicted value. It appears however, that the system is damped more than expected. However, the separation between the isolation platform was not measured, and could easily be more or less than the expected value of 25 μm . Figure 7.14 shows the measured values versus a curve predicted with a separation of 20.5 μm . Note that the fit is extremely good. Two minor discrepancies can be apparent, however. First, the vibration sensitivity of the oscillator at frequencies below 500 Hz is significantly above that of the predicted curve, and second the resonance frequency of the measured curve appears to be slightly higher. However, both discrepancies are small enough that minor variations in the platform design parameters can account for them. From the curves, however, it is clear that the basic model is valid. In order to improve the model and remove discrepancies, a better characterization of the isolation systems fabricated dimensions is needed.

As mentioned previously, measured values of the vibration sensitivity in the region below resonance depended upon the magnitude of the vibration. Figure 7.15 provides a comparison of the predicted vibration sensitivity of the isolated resonators with the vibration sensitivity measured using 1 g and 3 g vibrations. The most likely explanation of

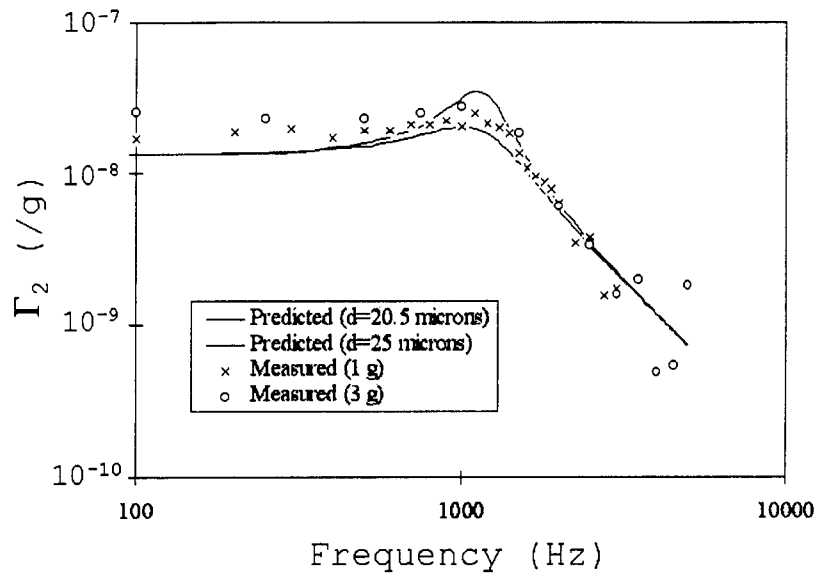


Figure 7.15. Predicted vibration sensitivity compared with measured vibration sensitivity. The two solid curves are the predicted sensitivity for isolation platforms separated from the oscillator substrate by 20.5 μm and 25 μ . The o's show the vibration sensitivity of the oscillator to a 3 g vibration, while the x's show the measured sensitivity to a 1 g vibration.

the increasing vibration sensitivity is that the deformation of the oscillator is large enough to result in a non-linear shift in the center frequency of the oscillator. This hypothesis is also consistent with the fact that the vibration sensitivities of all measured curves converge as the vibration increases above resonance. In the region above resonance, the motion resulting from the vibration is reduced, and therefore the deformation is reduced.

Figure 7.16 shows the measured vibration sensitivity of oscillator 2 compared with the predicted vibration sensitivity. In the region above resonance, the data fits well with the predicted values. Again, the values at and below resonance show significant variation from the predicted values. This is consistent with the data from oscillator 1. The cause of the large variation in the low frequency range can be due to a number of factors including the mounting of the resonator on the platform. It is also possible the resonant frequency and damping of this resonator are lower resulting in more deflection in the low frequency range.

Figure 7.17 shows the measured data of oscillator 3 compared to the predicted vi-

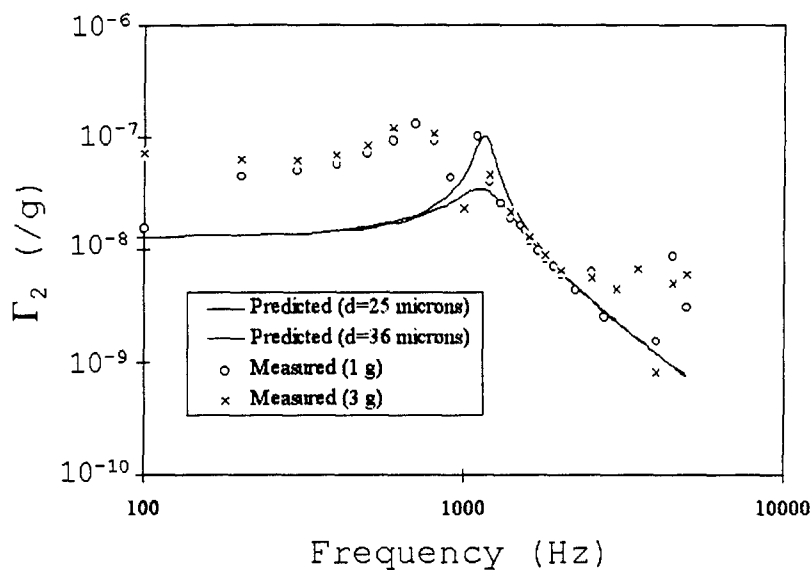


Figure 7.16. Measured vibration sensitivity of oscillator 2 compared with the predicted vibration sensitivity. Predicted curves for 25 μm and 36 μm separations are presented. Measured values were taken with 1 g, o's, and 3 g, x's, vibrations.

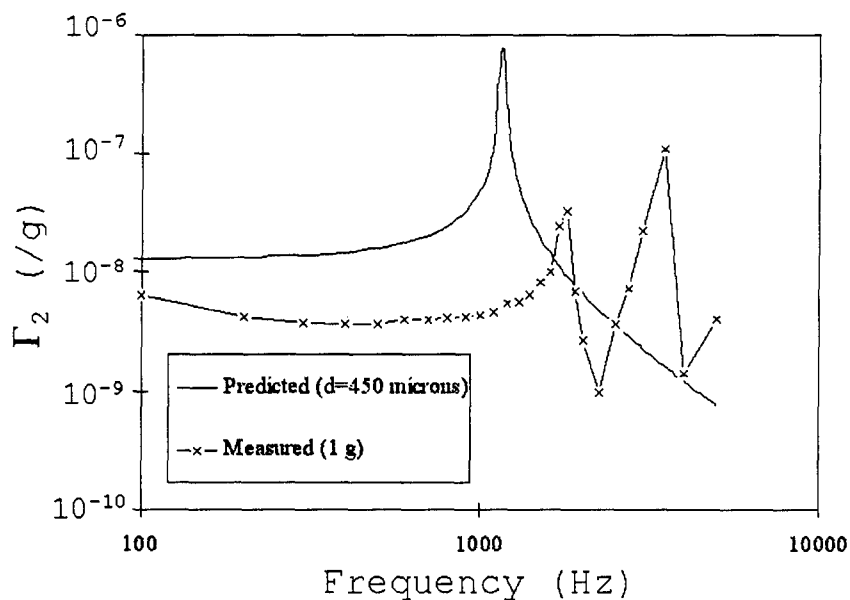


Figure 7.17. Measured vibration sensitivity of oscillator 3 compared with the predicted vibration sensitivity. The predicted curve is for an isolator with 450 μm between the oscillator substrate and the isolation platform. Measured data was taken using vibrations of 1 g magnitude.

bration sensitivity. Note that the predicted curve does not fit well with the measured data. This is most likely due to the parameters of the isolation platform. Variation in the thickness of the support arms was not measured, and could account for the large increase in the resonant frequency seen here. However, the damping of in the measured curves, while significantly less than that in the early curves is greater than that predicted. This is most likely a result of the large separation between the plate and the oscillator substrate. The current calculation of the damping coefficient only considers squeeze film damping. However, as the resonator is moved further away, the viscous flow of air around the resonator becomes more significant. The second peak is most likely due to a second vibration mode. Note that noise appears in both the oscillator 1 and oscillator 2 measured curves. It appears that in the first two oscillators, the damping reduced the magnitude of the motion and therefore the resulting variation is lower. For oscillator 3, the damping is much lower, and therefore the vibration magnitude is larger resulting in the large second peak.

7.5 Summary

The vibration sensitivity of 3 oscillators has been measured. The measured vibration sensitivity curves clearly show that the mechanical isolation platforms function generally as expected. However, the appearance of a number of variations from expectation exist. In particular, the appearance of a second resonance peak in the measured vibration sensitivity of oscillator 3. For the first two oscillators, the calculated damping coefficient appears valid. However, for oscillator 3, the damping is higher than predicted. Better characterization of the isolator dimensions should result in improved prediction of the vibration sensitivity curves. However, the data collected in this chapter is sufficient to answer the primary questions of this dissertation. Clearly, a micromechanical vibration isolation system can be fabricated. The performance of the system can be modeled and predicted. Further work is needed to optimize the design, particularly the mounting of the resonators, however, this data serves as a starting point for further research.

VIII. Conclusions and Recommendations

8.1 Summary

This research has led to the design and fabrication of a large variety of MEMS with the goal of demonstrating that MEMS can be used for reducing the vibration sensitivity of SAW/STW resonator based oscillators. Parallel research into the types of MEMS that can be fabricated led to the development of several systems including scanning and rotating micromirrors. Table 8.1 lists several of the devices that were fabricated as a part of this research and shows potential applications for these devices. These devices demonstrate that large scale MEMS can be built, however, research using the MUMPs process also shows that surface micromachining technology is still limited by the planar nature of the devices. In particular, it is difficult to fabricate large, millimeter scale devices.

A vibration isolation system was designed for a 2 mm \times 4 mm STW resonator. The design utilizes a platform suspended by four support arms to provide vibration isolation for the resonator. This type of design can be generically applied to any resonator. An approximation of the acceleration sensitivity of the STW resonator rigidly mounted on the isolation platform was obtained using finite element analysis. The platform was then modeled as a damped mass-spring system to predict the vibration sensitivity of the resonator.

A bulk micromachining process was developed to allow the fabrication of millimeter scale devices. The process utilizes only common microelectronic fabrication equipment and can therefore be repeated with only modest fabrication facilities. It allows the batch fabrication of systems utilizing {110} silicon wafers. Further, the process does not expose the resonators to any chemical etchants that could result in damage to the resonator. In order to fabricate systems having regions of two separate thickness values, the process utilizes two sided patterning and etching of the wafers. A large number of isolation platforms were fabricated using the new process. STW resonators were mounted onto several of the isolation platforms, and the vibration sensitivity was measured. The fabricated devices are the first devices fabricated with the intended goal of isolating the resonator, which

Table 8.1. Additional MEMS Devices Fabricated During This Research.

Device	Application
Scanning micromirror	Beam steering, optical couplers, system alignment optical bar code scanner
Lateral Scanning Micromirror	Beam steering, optical couplers, system alignment
Force Tester	Measure the force delivered by microactuators
Optimized Lateral Thermal Actuators	The new design provides more force from an actuator of approximately the same size
Elevated Platforms	Suspended optical components for coupling external optical sources to the chip, beam steering, compensation for topology
Rotating Micromirror	Beam steering

potentially offers size and weight advantages over more traditional methods which tend to isolate the entire oscillator.

This research has demonstrated that micromachining can be used to cheaply fabricate a vibration isolation system for SAW/STW resonators. This is the first time such a system has been fabricated, and this type of isolation has potential applications in a number of areas. The fabricated isolation system is less than $1\text{ cm} \times 1\text{ cm} \times 1\text{ mm}$ and can be mounted on a standard oscillator circuit. The isolation system adds less than 2 grams to the oscillator due to the low density of silicon. The small size and weight of the isolation system allow it to be easily incorporated in current systems. This was illustrated by utilizing and testing the isolated STW resonators using a previously designed oscillator circuit. Micromechanical vibration isolation can be applied to reduce the vibration applied to any milli-scale resonator.

8.2 Conclusions and Significance

This research was intended to answer several questions:

- 1) Can a micromachined system be built around SAW/STW resonators?
- 2) Can a micromachined system be reliably manufactured in large quantities at low cost?

- 3) Can a micromachined isolation system successfully reduce the vibration sensitivity of SAW/STW resonators?
- 4) Can a micromachined system be incorporated with existing oscillators without significantly increasing the size or weight of the oscillator?
- 5) What areas should future research focus on in the design of a micromachined vibration isolation system?

The fabrication and testing of a micromachined vibration isolation system around currently available resonators and oscillator circuits clearly demonstrates that a micromachined isolation system can be successfully fabricated. The process developed utilizes only commonly available equipment and chemicals and provides batch fabrication of the isolation platforms, thus allowing costs to be spread over a large number of units. Testing of the devices shows that an effective vibration isolation system has been fabricated. Above the mechanical resonance of the isolation system, the vibration magnitude is decreased at a rate of 12 dB/octave. Therefore, questions 1-4 have been successfully answered. The next section answers question 5.

The small size and weight of the micromachined isolation system is ideal for applications where size and weight are important constraints in the design of the system. In particular, missile seeker systems and space based platforms require that isolation systems meet very strict space and weight requirements. These requirements combined with the strict vibration sensitivity levels required for many military radar applications result in the need for a small, light, low cost system capable of providing oscillators with low vibration sensitivity. The devices fabricated for this research demonstrate for the first time that MEMS can be used to provide a small, light, vibration isolation system that can be built in conjunction with existing oscillator technology. Utilizing a MEM vibration isolation system, it should be possible to meet the size, weight, and performance requirements for low vibration sensitivity oscillators.

8.3 Further Research

This research was aimed at evaluating a new application for MEMS. Many of the fundamental questions about using MEMS for reducing vibration sensitivity have been answered. A system can be fabricated at low cost in large volumes. The system can be designed into current oscillators without significantly increasing the oscillator size or weight. For high frequency vibrations (above 1 kHz) the system can provide vibration isolation while improvements in the current design can potentially provide isolation at lower frequencies. The answers generated by this research now lead to a new set of questions. This section provides recommendations for future research.

Future research needs to address three questions: how can the acceleration sensitivity of isolated resonators be reduced, how can the MEM vibration isolation system be improved, and how can a micromachined system be hardened so that it can withstand the high shock and acceleration experienced in an operational environment. All three questions can be answered using MEMS. The following sections provide specific recommendations for future research into reducing vibration sensitivity using MEMS. A section on modifications to the current fabrication process is also included.

8.3.1 Design of the Isolation System. The basic design of a support platform with four support arms can be significantly improved. The primary problem with the current design is the strength of the support arms. Because of the high Young's modulus of silicon, the support arms must be long and thin. Further, the crystalline nature of silicon results in a system that shatters when too much force is applied. Therefore, one of the first areas of future research should be the evaluation of other materials for fabricating the support arms. One potential solution is the use of a polymer thin film such as a photosensitive polyimide. These films are widely available and can be used with standard integrated circuit fabrication equipment. The polymers are not as rigid as silicon, and therefore should allow the use of shorter and wider arms while still allowing the resonant frequency of the vibration isolation system to be decreased. Further, the failure mechanism of polymers is not as catastrophic as it is for silicon.

8.3.2 Low Mass Rigid Structures. The acceleration sensitivity, and thus vibration sensitivity, of the resonators can be reduced by decreasing the magnitude of the deformation caused by an acceleration. Reducing the magnitude of the deformation is done by making the platform more rigid and reducing its mass. The basic question is one often faced by mechanical engineers in designing bridges or other structures: how to make a structure more rigid while decreasing its mass. With MEMS the process is complicated by the limitations of the fabrication process. However, as demonstrated in this research, a large variety of structures can be fabricated with currently available processes. It should be possible to design a platform with lower mass that deflects less under a given force. However, the primary advantage is increasing the rigidity of the platform. The current design isolates a platform and a resonator that has only 2-3 times the mass of the resonator. Therefore, further reduction in the mass will have a limited effect. Increasing the rigidity of the platform, however, should result in a significantly lower vibration sensitivity.

One solution that should be explored is the fabrication of the isolation system and the resonator out of the same material. This allows the designer to control both the resonator dimensions, and the types and locations of forces applied to the resonator. Further, the resonator will be isolated without any associated structure so it will have the lowest possible mass. The primary difficulty with this type of system will be the design of the fabrication process.

8.3.3 Isolation of Packaged Resonators and Oscillators. The oscillator circuit provided by SAWTEK uses an alumina substrate to provide a rigid mount. Further, the STW resonator is typically mounted in a surface mount package (SMP) that provides a rigid, hermetically sealed package for the resonator. The entire oscillator is approximately a 1 cm by 2 cm rectangle. A micromachined isolation system based on the design used in this dissertation can be fabricated to provide isolation of this entire oscillator circuit. The isolation system would rest between the alumina substrate and the microwave header package. This type of system has several advantages. First, the resonator has a rigid support system that has been optimized for low vibration sensitivity. Second, the oscillator has significantly more mass than the isolation platform and the resonator alone. Therefore,

the designer is allowed more flexibility in the design of the isolation support system. The additional mass makes it easier to fabricate a system with a lower resonance. It should be possible to fabricate such a system with thicker and shorter support arms while still decreasing the resonance below 200 Hz. Therefore, the system will not be as fragile as it currently is. Not all oscillator circuits are this small, and therefore it may not always be possible to isolate the entire oscillator. However, isolating a resonator packaged in a rigid mount such as the SMP should provide the same advantages as isolating the entire oscillator. Either of these options may be the best near term solution available.

8.3.4 Active Mounting. The acceleration sensitivity is decreased in two ways: controlling the shape of the deformation, and decreasing the deformation. In general, controlling the shape of the deformation can be done with the design of the mounting system. However, this method requires that the resonator and the mounting system be connected precisely as designed. In reality, achieving the required precision is difficult and expensive. However, a MEMS that basically appears as a bed of nails can be used to create a dynamic mount. The MEMS would be fabricated as an array of piston-type parallel actuators. Each actuator would be on the order of $50\text{ }\mu\text{m}$ square with a center to center spacing between actuators on the order of $100\text{ }\mu\text{m}$. The resonator would then be rigidly attached to the actuators using a technique similar to direct wafer bonding. An active control system would then be used to determine the shape of the forces applied to the resonator. This solution is clearly complicated both in the fabrication of the MEMS and the design of the control system, and therefore should be considered only after further evaluation of passive isolation systems.

8.3.5 Modifications to the Fabrication Process. The fabrication process as it currently exists is capable of the batch fabrication of devices with regions of two separate silicon thickness values. Currently, both the first and second silicon etches utilize KOH as the etching solution. KOH is used in the first etch due to both its high $\{110\}/\{111\}$ selectivity and its high etch rate in the $\langle 110 \rangle$ directions. The second etch, however, does not require as deep an etch and therefore neither etch selectivity or etch rate is as critical. Therefore the second etch can be performed with another etchant such as TMAH.

TMAH exhibits extremely high selectivity to oxide, and the etch rate of aluminum can be significantly reduced utilizing dissolved silicon, and thus it is often used in conjunction with CMOS circuits. Utilizing an etchant such as TMAH, additional processing can be done after the first etch. In particular, CMOS type devices can be fabricated on the front side of the wafer. It also enables the use of different metals for the fabrication of the isolation systems.

Appendix A. CMOS-MEMS Release Process

After the CMOS die are delivered to AFIT, they are released by etching in EDP. Figure A.1 shows the setup for the EDP etch. The length of the EDP etch varies with a number of factors. It is therefore necessary to monitor the process to determine when the etching is complete. The progress of the etch can be observed optically by removing the die and viewing it under a microscope. The dice are checked in 10-15 minute intervals following an initial 30 minute etch. After etching, the dice are submerged in deionized water to remove any etchant. This is followed by a short dip in methyl alcohol. The methyl dip is necessary to prevent stiction. The release process is listed below.

Step	Process	Time	Comments
1)	Etch in 10:1 HF:DIW	10 sec.	Remove any native oxide that has grown on the exposed silicon
2)	Rinse in DIW	1 min.	Remove any HF
3)	Etch in EDP at 100°C.	> 30 min.	Time depends on the size of the structures being undercut
4)	Rinse in DIW	10 min.	Remove any EDP
5)	Rinse in methyl	60 secs.	Methyl has lower surface tension than water
6)	Dry on a hot plate	≈ 1 min.	Increase the evaporation rate to decrease stiction

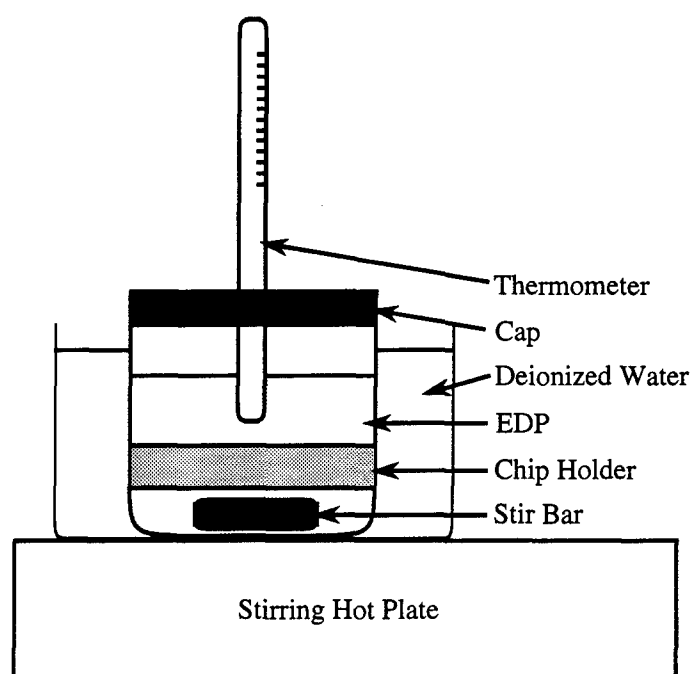


Figure A.1. EDP etching setup.

Appendix B. MUMPs Release Process

The MUMPs release process requires very little preparation. Acetone, methanol, isopropyl alcohol, and HF (49% by wt.) are used directly out of their containers.

Step	Process	Time (min.)	Comments
1)	Acetone Rinse	15	Remove the protective photoresist
2)	Methanol Rinse	5	Rinse off the acetone
3)	DIW Rinse	5	Rinse off the methanol
4)	HF (49% by wt.)	2.5	Etch the sacrificial layer
5)	DIW Rinse	10	Rinse off the HF
6)	Isopropyl Rinse	5	Rinse off the DIW
7)	Methanol Rinse	10	Final rinse and clean. The methanol also serves to reduce stiction.
8)	Dry on a hot plate	≈ 1	Increasing evaporation rate decreases stiction.

Appendix C. Mask Fabrication

Masks are fabricated at the cooperative materials and processes laboratory currently located in building 125. The masks are fabricated on 4 inch square photographic glass plates by exposing them with images created on transparencies. The masks can be designed using any of the available CAD layout packages available in the VLSI laboratory, including MAGIC and Cadence.

Step	Process
1)	Lay out the design in MAGIC or Cadence.
2)	Generate a CIF file of the design. Note that with MAGIC, lambda must be set to the desired value before the CIF file is generated.
3)	Chose the desired reduction factor. A limited set of lenses are available for the reducing camera, and therefore arbitrary reduction values are not possible. Generally, a reduction of 20 or 50 times is used.
4)	Generate a black and white postscript image of the design using: <div style="padding-left: 40px;"><code>cif2mask -m MAG <ciffile> > <outfile.ps></code></div> where MAG is the reduction factor from step 3, <ciffile> is the file generated in step 2, and <outfile.ps> is the postscript output file.
5)	Print the file on a transparency using a high quality (> 600 dpi resolution) laser printer.
6)	Set up the reduction camera in Bldg. 125 with the correct lenses. See the lab technician for assistance if needed.
7)	Expose the plates for 1-5 minutes.
8)	Develop the plates in <div style="padding-left: 40px;">Developer for 4 minutes</div> <div style="padding-left: 40px;">Stop for 1 minute</div> <div style="padding-left: 40px;">Fixer for 5 minutes</div> <p>Note that the times will vary so appropriate fab times should be determined when the masks are fabricated.</p>

If desired, multiple images can be fabricated using the step and repeater. Multiple images are printed onto a mask and then the mask is developed as before. Masks can also be duplicated and inverted as needed.

Appendix D. Standard Pirranha Clean

The standard pirranha clean removes any contaminants from the wafer. This process using sulfuric acid will also remove metals such as aluminum, and therefore must be used with care. It does not, however, dissolve silicon oxide. The pirranha clean is listed below.

Step	Process	Time	Comments
1)	Etch in $\text{H}_2\text{SO}_4:\text{H}_2\text{O}_2$ 3:2	20 min.	Remove any contaminants
2)	Rinse in DIW	≈ 10 min.	Rinse until the resistivity of the DIW reaches 5 $\text{M}\Omega$.
3)	Blow dry with N_2		Remove DIW from the surface of the wafers
4)	Bake at 200° C	1 hour	Remove all moisture from the wafers

Appendix E. Oxidation

The wafers are oxidized using the wet thermal oxidation process listed below. Wet oxidation has a significantly higher growth rate which is necessary for the thick oxides grown on the wafers. The oxidation furnace must be turned on several hours before being used to allow the temperature to stabilize. It is also necessary to ensure that sufficient amount of DIW:HCL 19:1 solution is prepared and that sufficient oxygen is available. Finally, the heater must be turned on to bring the DIW:HCL solution up to 95° C.

Step	Process
1)	Immerse the wafers in a solution of 10:1 DIW:HF for 1 minute to remove any native oxide.
2)	Rinse the wafers in deionized water until the resistivity reaches 5 M Ω .
3)	Blow the wafers dry with N ₂ .
4)	Bake the wafers at 200° C for 1 hour. Note that any water remaining on the wafer surface can result in the wafer cracking when it is placed into the diffusion oven.
5)	Place the wafers in the quartz boat for the oxidation furnace.
6)	Slide the wafers into the furnace at a rate of 1 inch per minute until they reach the center of the furnace tube.
7)	Turn on the oxygen flow at a rate of 1 liter per minute
8)	After the specified time, turn the oxygen flow off and turn the N ₂ flow back on. Note this occurs automatically when the oxygen flow is turned off.
9)	Pull the wafers out of the furnace at a rate of 1 inch per minute.
10)	Allow the wafers 10 minutes to cool.

Appendix F. Back Side Patterning

The back side patterning process etches away the undesired oxide on the back side of the wafers. The oxide etch uses a solution of $\text{NH}_4\text{F}:\text{HF}$ 4:1. This solution must be prepared at least 2 hours in advance to allow it to settle before being used. The solution should not be used more than 6 hours after it was prepared. The patterning process is listed below.

Step	Process
1)	Pirranha clean, see Appendix D for details.
2)	Spin negative photoresist (Waycoat HR-200) onto the back side of the wafers at 5000 RPM for 20 seconds.
3)	Soft bake the wafers for 15 minutes at 65° C.
4)	Align the primary wafer flat to the back side oxide mask and expose for 45-55 seconds.
5)	Develop the wafers by spinning them at 500 RPM and spraying them with <ul style="list-style-type: none">- Xylenes for 30 sec- n-Butyl Acetate for 30 sec then increase the spin speed to 5000 RPM for 15 seconds to dry the wafers
6)	Hard bake the photoresist at 135° C for 20 minutes.
7)	Spin on negative photoresist (Waycoat HR-200) to the front side of the wafers at 4000 RPM for 15 seconds.
8)	Hard bake the wafers at 135° C for 20 minutes.
9)	Etch the oxide in a solution of $\text{NH}_4\text{F}:\text{HF}$ 4:1. The etch time is dependent upon the oxide thickness, but an approximate rate of 1500 Å per minute is a good estimate. Two minutes before the expected etch time is complete, remove the wafers from the solution and observe them to see if the wafer surface is hydrophobic. If it is not, etch the wafers for another 30 seconds and check them again. Repeat this until the surface is hydrophobic.
10)	Rinse the wafers in DIW until the resistivity reaches 1 MΩ.
11)	Clean the wafers with the pirranha clean.

Appendix G. KOH Etch Process

The (110) silicon wafers are etched in a solution of KOH dissolved in deionized water (50% by wt.). The solution must be prepared in advance. 500 grams of KOH is poured into a 1 liter container. 500 ml of deionized water is then poured in, and the solution is stirred until all of the KOH is dissolved. The container is sealed by placing plastic wrap over the top and placing on the container lid. This prevents evaporation of the water allowing the KOH solution to remain at the specified balance. The container is placed into a Lufran II Superbowl. The Superbowl maintains a reservoir of deionized water at 85° C. The solution is allowed at least one hour to settle. Typically, the solution can be used over a period of 2-3 days. After that, the etch rate of the solution begins to vary. The KOH etch process is listed below.

Step	Process
1)	Pirranha clean as described in Appendix D
2)	Immerse the wafers in the KOH solution for 15 minutes
3)	Rinse the wafers in DIW for 5 minutes
4)	Blow the wafers dry with N ₂
5)	Measure the etch profile with the Dektak IIa profilometer
6)	Calculate the (110) etch rate
7)	Immerse the wafers in the KOH solution and etch until the desired depth is reached
8)	Rinse the wafers in DIW until the resistivity reaches 5 MΩ
8a)	If these are the released isolation platforms, rinse in methyl alcohol for 5 minutes
9)	Gently blow the wafers, or released devices with N ₂

Appendix H. Front Side Patterning

The front side patterning, is very similar to the back side patterning process. However, the wafers now have etch holes in the back side of the wafer that project over half of the wafers width. Therefore, the wafers are very fragile, and handle wafers must be attached before the oxide can be patterned. Again, a solution of $\text{NH}_4\text{F}:\text{HF}$ 4:1 must be prepared 2-6 hours before it is used. The process is listed on the next page.

Step	Process
1)	Pirranha clean of both the handle and device wafers.
2)	Spin on positive photoresist (Shipley 1350j) to the back side of the handle wafers. Spin at 1000 RPM for 20 seconds.
3)	Place the front side of the device wafer onto the resist leaving the wafer flat of the device wafer overhanging the handle wafer by 2-3 mm. Press the wafers together using tweezers.
4)	Hard bake the wafers at 100° C for 30 minutes.
5)	Spin negative photoresist (Waycoat HR-200) at 5000 RPM for 20 seconds onto the front side of the device wafers.
6)	Soft Bake the wafers for 15 minutes at 65° C.
7)	Align the primary wafer flat to the front side oxide mask and expose for 45-55 seconds.
8)	Develop the wafers by spinning them at 500 RPM and spraying them with <ul style="list-style-type: none">- Xylenes for 30 sec- n-Butyl Acetate for 30 sec then increase the spin speed to 5000 RPM for 15 seconds to dry the wafers
9)	Hard bake the photoresist at 135° C for 20 minutes.

Step	Process
------	---------

-
- | | |
|-----|---|
| 10) | Etch the oxide in a solution of $\text{NH}_4\text{F}:\text{HF}$ 4:1. The etch time is dependent upon the oxide thickness, but an approximate rate of 1500 Å per minute is a good estimate. Two minutes before the expected etch time is complete, remove the wafers from the solution and observe them to see if the wafer surface is hydrophobic. If it is not, etch the wafers for another 30 seconds and check them again. Repeat this until the surface is hydrophobic. |
| 11) | Rinse the wafers in DIW until it reaches a resistivity of 1 MΩ. |
| 12) | Clean the wafers with the piranha clean. |

Appendix I. Metalization

The metalization processes follows the front side patterning process. Generally, the two process should be performed on the same day, but this is not necessary. The metalization is patterned using a lift off process as described below. It is assumed that the wafers are clean after the front side patterning process.

Step	Process
1)	Spin HMDS onto the front side of the device wafers at 4000 RPM for 10 seconds.
2)	Spin positive photoresist (Shipley 1350j) onto the front side of the wafers at 5000 RPM for 20 seconds.
3)	Soft bake at 70° C for 20 minutes.
4)	Expose for 50-60 seconds.
5)	Soak in chlorobenzene for 10 minutes.
6)	Bake at 70° C for 15 minutes.
7)	Develop by spinning at 500 RPM and spraying with: <ul style="list-style-type: none">- AZ351:DIW 1:3 for 30 seconds- DIW for 20 seconds then increase the spin speed to 5000 RPM for 15 seconds to dry the wafers.
8)	Place the wafers in the Denton DV-602.
9)	Sputter 300 Å of chromium followed by 2200 Å of platinum.
10)	Remove the wafers from the vacuum.
11)	Soak in acetone until the metal has been lifted off, and the device and handle wafers have separated.
12)	Soak in methyl alcohol for 10 minutes.
13)	Blow the wafers dry with N ₂ .

Appendix J. Commonly Used Acronyms

Acronym	Definition
AFIT	Air Force Institute of Technology
APCVD	Atmospheric Pressure Chemical Vapor Deposition
ARL	Army Research Laboratory
CMOS	Complementary Metal Oxide Semiconductor
DIW	Deionized water
EDP	Ethylene Diamine Pyrocatechol
HCL	Hydrochloric Acid
HF	Hydrofluoric Acid
LIGA	A German acronym for lithography, electroplating, and molding
LPCVD	Low Pressure Chemical Vapor Deposition
MCNC	Microelectronics Corporation of North Carolina
MEM	MicroElectroMechanical
MEMS	MicroElectroMechanical Systems
MITE	Micromachining by Ion Track Etching
MOSIS	Metal oxide semiconductor implementation service
MUMPs	Multi-User MEMS Processes
PMMA	Polymethylacrylate
PSG	PhosphoSilicate Glass
RIE	Reactive Ion Etching
RPM	Revolutions Per Minute
SAW	Surface Acoustic Wave
SEM	Scanning Electron Microscope
STW	Surface Transverse Wave
TMAH	TetraMethyl Ammonium Hydroxide

Appendix K. Submitted and Published Papers Related to This Research

- 1) J.R. Reid and V.M. Bright, "A process for the fabrication of micromechanical vibration isolation systems for reducing the vibration sensitivity of acoustic wave resonators," submitted for publication in *Sensors and Actuators A*.
- 2) J.R. Reid, V.M. Bright, and J.H. Comtois, "Force measurements of polysilicon thermal micro-actuators," *Proc. SPIE: Micromachined Devices and Components II*, vol. 2882, pp. 296-306, Oct. 1996.
- 3) J.R. Reid, V.M. Bright, and J.H. Comtois, "A surface micromachined rotating micro-mirror normal to the substrate," in *Digest IEEE/LEOS 1996 Summer Topical Meetings*, Aug. 1996.
- 4) J.R. Reid, V.M. Bright, and J.H. Comtois, "Arrays of thermal micro-actuators coupled to micro-optical components," to be published *Proc. SPIE: International Symposium on Optical Science, Engineering, and Instrumentation*, August 1996.
- 5) J.R. Reid, V.M. Bright, J.T. Stewart, J.A. Kosinski, "Reducing the normal acceleration sensitivity of surface transverse wave resonators using micromachined isolation systems," in *Proc. of the 50th Annual IEEE International Frequency Control Symposium*, pp. 464-472, June 1996.
- 6) V.M. Bright, J.H. Comtois, J.R. Reid, and D.E. Sene, "Surface micromachined micro-opto-electro-mechanical systems," to be published *Special Issue of IEICE transactions on Electronics: Micromachine technology*.
- 7) V.M. Bright, J.H. Comtois, D.E. Sene, J.R. Reid, S.C. Gustafson, and E.A. Watson, "Realizing micro-opto-electromechanical devices through a commercial surface micromachining process," in *Proc. SPIE*, vol. 2687, pp. 34-46.

Bibliography

1. J. R. Vig, C. Audoin, L. S. Culter, M. M. Driscoll, E. P. EerNisse, R. L. Filler, R. M. Garvey, W. J. Riley, R. C. Smythe, and R. D. Weglein, "The effects of acceleration on precision frequency sources," Tech. Rep. SLCET-TR-91-3 (Rev. 1), Army Research Laboratory, Jul. 1992.
2. J. A. Kosinski and A. Ballato, "Designing for low acceleration sensitivity," *IEEE Transactions on Ultrasonics, Ferroelectrics, and Frequency Control*, vol. 40, pp. 532-537, Sept. 1993.
3. J. A. Kosinski, "The fundamental nature of acceleration sensitivity," in *Proc. of the 50th Annual IEEE International Frequency Control Symposium*, pp. 439-448, 1996.
4. J. H. Comtois, *Structures and techniques for implementing and packaging complex, large scale microelectromechanical systems using foundry fabrication processes*. PhD thesis, Air Force Institute of Technology, May 1996.
5. J. Reid, V. M. Bright, and J. H. Comtois, "Force measurments of polysilicon thermal microactuators," in *Proc. SPIE: Micromachined Devices and Components II*, vol. 2882, pp. 296-306, 1996.
6. J. Reid, V. M. Bright, and J. H. Comtois, "Arrays of thermal micro-actuators coupled to micro-optical components," in *To be published, Proc. SPIE: International Symposium on Optical Science, Engineering and Instrumentation*, vol. 2865, 1996.
7. J. R. Reid, V. M. Bright, and J. H. Comtois, "A surface micromachined rotating micro-mirror normal to the substrate," in *Digest IEEE/LEOS 1996 Summer Topical Meetings*, August 1996.
8. V. M. Bright, J. H. Comtois, J. R. Reid, and D. E. Sene, "Surface micromachined micro-opto-electro-mechanical systems," *Special Issue of IEICE Transactions on Electronics: Micromachine Technology*, p. to be published.
9. V. M. Bright, J. H. Comtois, D. E. Sene, J. R. Reid, S. C. Gustafson, and E. A. Watson, "Realizing micro-opto-electro-mechanical devices through a commercial surface-micromachining process," *Proc. SPIE*, vol. 2687, pp. 34-46, 1996.
10. J. T. Stewart, 1995-1996. Personal Correspondence.
11. J. R. Reid, V. M. Bright, J. T. Stewart, and J. A. Kosinski, "Reducing the normal acceleration sensitivity of surface transverse wave resonators using micromachined isolation systems," in *Proc. of the 50th Annual IEEE International Frequency Control Symposium*, pp. 464-472, 1996.
12. J. R. Reid and V. M. Bright, "A process for the fabrication of micromechanical vibration isolation systems for reducing the vibration sensitivity of acoustic wave resonators," *Submitted to Sensors and Actuators A*, 1996.
13. L. Rayleigh, "On waves propagating along the plane surface of an elastic solid," in *Proc. of the London Mathematical Society*, pp. 4-11, 1885.
14. R. M. White and F. W. Voltmer, "Direct piezoelectric coupling to surface elastic waves," *Applied Physics Letters*, vol. 7, pp. 314-316, Dec. 1965.

15. J. Himmel, R. McGowan, J. A. Kosinski, and T. Lukaszek, "Market survey of acceleration-insensitive SAW oscillators," in *Proc. of the 1992 IEEE Frequency Control Symposium*, pp. 849-859, 1992.
16. J. Browne, "SAW devices set long-term stability marks," *Microwaves and RF*, pp. 136-138, May 1994.
17. C. C. W. Ruppel, R. Dill, A. Fischerauer, G. Fischerauer, W. Gawlik, J. Machui, F. Müller, L. Reindl, W. Ruile, G. Scholl, I. Schropp, and K. C. Wagner, "SAW devices for consumer communication applications," *IEEE Transactions on Ultrasonics, Ferroelectrics, and Frequency Control*, vol. 40, pp. 438-451, Sept. 1993.
18. B. A. Auld, J. J. Gagnepain, and M. Tan, "Horizontal shear waves on corrugated surfaces," *Electronics Letters*, vol. 12, pp. 650-651, Nov. 1976.
19. T. L. Bagwell and R. C. Bray, "Novel surface transverse wave resonators with low loss and high Q," in *Proc. of the 1987 Ultrasonics Symposium*, pp. 319-324, 1987.
20. I. D. Avramov, "Gigahertz range resonant devices for oscillator application using shear horizontal acoustic waves," *IEEE Transactions on Ultrasonics, Ferroelectrics, and Frequency Control*, vol. 40, pp. 459-468, Sept. 1993.
21. T. E. Parker and G. K. Montress, "Precision surface-acoustic-wave (SAW) oscillators," *IEEE Transactions on Ultrasonics, Ferroelectrics, and Frequency Control*, vol. 35, pp. 342-364, May 1988.
22. R. C. Almar and M. S. Cavin, "Low g-sensitivity fixed-frequency oscillators," *Microwave Journal*, pp. 88-98, Feb. 1995.
23. D. Andres and T. E. Parker, "Designing smaller SAW oscillators for low vibration sensitivity," in *Proc. of the 48th Annual IEEE International Frequency Control Symposium*, pp. 352-358, 1994.
24. C. Campbell, *Surface Acoustic Wave Devices and Their Signal Processing Applications*. Boston, MA: Academic Press, Inc., 1989.
25. S. Datta, *Surface Acoustic Wave Devices*. Englewood Cliffs, NJ: Prentice-Hall, 1986.
26. P. S. Cross and S. S. Elliott, "Surface-acoustic-wave resonators," *Hewlett-Packard Journal*, pp. 9-17, Dec. 1981.
27. R. J. Kansy, "Introducing the quartz surface acoustic wave resonator," in *SAW Resonator Application Handbook*, RF Monolithics, Inc., 1983.
28. K. H. Yen, K. L. Wang, and R. S. Kagiwada, "Efficient bulk wave excitation on ST quartz," *Electronics Letters*, vol. 13, pp. 37-38, Jan. 1977.
29. K. H. Yen, K. F. Lau, and R. S. Kagiwada, "Energy-trapped shallow bulk acoustic waves," *Electronics Letters*, vol. 15, p. 206, 1979.
30. D. F. Thompson and B. A. Auld, "Surface transverse wave propagation under metal strip gratings," in *Proc. of the 1986 Ultrasonics Symposium*, pp. 261-266, 1986.
31. C. A. Flory and R. L. Baer, "Surface transverse wave mode analysis and coupling to interdigital transducers," in *Proc. of the 1987 Ultrasonics Symposium*, pp. 313-318, 1987.

32. I. D. Avramov, "Design and applications of surface transverse wave resonant devices in stable microwave oscillators and communication systems," in *Tutorial Notes from the 50th Annual IEEE International Frequency Control Symposium*, 1996.
33. I. D. Avramov, V. S. Aliev, S. Denissenko, and A. S. Kozlov, "2 GHz surface transverse wave oscillators. design performance and limitations," in *Proc. of the 49th Annual IEEE International Frequency Control Symposium*, pp. 459-468, 1995.
34. T. I. Browning and M. F. Lewis, "New family of bulk-acoustic-wave devices employing interdigital transducers," *Electronics Letters*, vol. 13, pp. 128-130, Mar. 1977.
35. M. S. Cavin and R. C. Almar, "An oscillator design using low g-sensitivity, low phase noise STW devices," in *Proc. of the 49th Annual IEEE International Frequency Control Symposium*, pp. 476-485, 1995.
36. S. Denissenko, E. Gavignet, S. Ballandras, E. Bigler, and E. Cambril, "Design and test of 3 GHz, fundamental mode STW resonators on quartz," in *Proc. of the 49th Annual IEEE International Frequency Control Symposium*, pp. 469-475, 1995.
37. H. G. Vollers, "General-purpose SAW resonator oscillator for 300 MHz to 1000 MHz," in *SAW Resonator Application Handbook*, RF Monolithics, Inc., 1983.
38. J. R. Vig, "Introduction to quartz frequency standards," Tech. Rep. SLCET-TR-92-1 (Rev. 1), Army Research Laboratory, Oct. 1992.
39. R. L. Filler, "The acceleration sensitivity of quartz crystal oscillators: a review," *IEEE Transactions on Ultrasonics, Ferroelectrics, and Frequency Control*, vol. 35, pp. 297-305, May 1988.
40. A. Ballato, J. A. Kosinski, T. J. Lukaszek, M. Mizan, R. McGowan, and K. Klohn, "Acceleration sensitivity reduction in SAW and BAW resonators by electronic means," in *Proc. of the 1990 Ultrasonics Symposium*, pp. 573-576, 1990.
41. J. C. Baumhauer and H. F. Tiersten, "Nonlinear electroelastic equations for small fields superposed on a bias," *Journal of the Acoustical Society of America*, vol. 54, no. 4, pp. 1017-1034, 1973.
42. H. F. Tiersten, "Perturbation theory for linear electroelastic equations for small fields superposed on a bias," *Journal of the Acoustical Society of America*, vol. 64, pp. 832-837, Sept. 1978.
43. D. V. Shick and H. F. Tiersten, "An analysis of the acceleration sensitivity of ST-cut quartz surface wave resonators supported along the edges," in *Proc. of the 40th Annual IEEE International Frequency Control Symposium*, pp. 262-268, 1986.
44. H. F. Tiersten and D. V. Shick, "An analysis of the normal acceleration sensitivity of ST-cut quartz surface wave resonators rigidly supported along the edges," in *Proc. of the 41st Annual IEEE International Frequency Control Symposium*, pp. 282-288, 1987.
45. D. V. Shick and H. F. Tiersten, "An analysis of the in-plane acceleration sensitivity of ST-cut quartz surface wave resonators with the substrate extending beyond the supports," in *Proc. of the 42nd Annual IEEE International Frequency Control Symposium*, pp. 230-238, 1988.

46. H. F. Tiersten and D. V. Shick, "An analysis of the in-plane acceleration sensitivity of ST-cut quartz surface wave resonators with interior rectangular supports," in *Proc. of the 43rd Annual IEEE International Frequency Control Symposium*, pp. 396-404, 1989.
47. J. A. Kosinski, A. Ballato, and T. J. Lukaszek, "A new approach to modeling quartz resonator and oscillator acceleration sensitivity," in *Proc. of the 5th European Frequency and Time Forum BESANCON*, pp. 25-29, Mar. 1991.
48. J. A. Kosinski and A. Ballato, "Advances in acceleration sensitivity measurement and modeling," in *Proc. of the 46th Annual IEEE International Frequency Control Symposium*, pp. 838-848, 1992.
49. M. Valdois, J. Besson, and J. J. Gagnepain, "Influence of environment conditions on a quartz resonator," in *Proc. of the 28th Annual IEEE International Frequency Control Symposium*, pp. 244-248, 1974.
50. J. M. Przyjemski, "Improvement in system performance using a crystal oscillator compensated for acceleration sensitivity," in *Proc. of the 32nd Annual IEEE International Frequency Control Symposium*, pp. 426-431, 1978.
51. R. L. Filler, "The effect of vibration on frequency standards and clocks," in *Proc. of the 35th Annual IEEE International Frequency Control Symposium*, pp. 31-39, 1981.
52. R. L. Filler, J. A. Kosinski, and J. R. Vig, "Further studies on the acceleration sensitivity of quartz resonators," in *Proc. of the 37th Annual IEEE International Frequency Control Symposium*, pp. 265-271, 1983.
53. T. E. Parker, J. A. Greer, and G. K. Montress, "SAW oscillators with low vibration sensitivity," in *Proc. of the 45th Annual IEEE International Frequency Control Symposium*, pp. 321-329, 1991.
54. A. Ballato, J. A. Kosinski, T. J. Lukaszek, M. Mizan, and R. McGowan, "Electronic desensitization of resonators to accelerations," in *Proc. of the 44th Annual IEEE International Frequency Control Symposium*, pp. 444-451, 1990.
55. J. A. Kosinski, 1995. Personal Correspondence.
56. T. E. Parker, J. Callerame, and G. K. Montress, "A new all quartz package for SAW devices," in *Proc. of the 39th Annual IEEE International Frequency Control Symposium*, pp. 519-525, 1985.
57. W. K. Wilson, *Vibration Engineering*. London: Charles Griffin & Company Lmt., 1959.
58. J. E. Ruzicka and T. F. Derby, *Influence of Damping in Vibration Isolation*. Washington, DC: The Shock and Vibration Information Center, 1971.
59. M. L. D. Gaudreault, *Simultaneous design of active vibration control and passive damping*. PhD thesis, Air Force Institute of Technology, 1993.
60. R. P. Feynman, "There's plenty of room at the bottom," *Journal of Microelectromechanical Systems*, vol. 1, pp. 60-66, Mar. 1992.

61. R. P. Feynman, "Infinitesimal machinery," *Journal of Microelectromechanical Systems*, vol. 2, pp. 4-14, Mar. 1993.
62. F. Goodenough, "Airbags boom when ic accelerometer sees 50 g," *Electronic Design*, Aug. 8 1991.
63. J. M. Younse, "Projection display systems based on the Digital Micromirror DeviceTM (DMDTM)," *Proc. SPIE Microelectronic Structures and Microelectromechanical Devices for Optical Processing and Multimedia Applications*, vol. 2641, pp. 64-75, Oct. 1995.
64. Y. Konaka and M. G. Allen, "Single- and multi-layer electroplated microaccelerometers," in *The 9th Annual International Workshop on Microelectromechanical Systems*, pp. 168-173, 1996.
65. C. Hierold, A. Hildebrandt, U. Näher, T. Scheiter, B. Mensching, M. Steger, and R. Tielert, "A pure CMOS surface micromachined integrated accelerometer," in *The 9th Annual International Workshop on Microelectromechanical Systems*, pp. 174-179, 1996.
66. R. M. Kuhns, "Design and fabrication of a micromechanical gyroscope," Master's thesis, Air Force Institute of Technology, December 1995.
67. R. A. Buser and N. F. de Rooij, "Silicon pressure sensor based on a resonating element," *Sensors and Actuators A*, vol. 25-27, pp. 717-722, 1991.
68. R. Schörner, M. Poppinger, and J. Eibl, "Silicon pressure sensor with frequency output," *Sensors and Actuators A*, vol. 21-23, pp. 73-78, 1990.
69. M. A. Michalicek, "Design, fabrication, modelling and testing of surface-micromachined micromirror devices," Master's thesis, Air Force Institute of Technology, June 1995.
70. G. T. A. Kovacs, C. W. Storment, M. Halks-Miller, C. R. Belczynski, C. C. D. Santana, E. R. Lewis, and N. I. Maluf, "Silicon-substrate microelectrode arrays for parallel recording of neural activity in peripheral and cranial nerves," *IEEE Transactions on Biomedical Engineering*, vol. 41, pp. 567-577, June 1994.
71. T. Akin, K. Najafi, R. H. Smoke, and R. M. Bradley, "A micromachined silicon sieve electrode for nerve regeneration applications," *IEEE Transactions on Biomedical Engineering*, vol. 41, pp. 305-313, Apr. 1994.
72. A. Rogner, J. Eicher, D. Münchmeyer, R.-P. Peters, and J. Mohr, "The LIGA technique-what are the new opportunities," *Journal of Micromechanics and Microengineering*, vol. 2, pp. 133-140, 1992.
73. A. B. Frazier, C. H. Allen, and M. G. Allen, "Development of micromachined device using polyimide-based process," *Sensors and Actuators A*, vol. 45, pp. 47-55, 1994.
74. W. H. Brünger and K. Kohlmann, "E-beam induced fabrication of microstructures," *Journal of Microelectromechanical Systems*, vol. 2, pp. 30-32, March 1993.
75. B. C. Read, "Silicon based microactuators for telerobotic tactile stimulation," Master's thesis, Air Force Institute of Technology, December 1994.

76. K. E. Petersen, "Silicon as a mechanical material," *Proc. of the IEEE*, vol. 70, pp. 420-457, May 1982.
77. W. Benecke, L. Csepregi, A. Heuberger, K. Kühn, and H. Seidel, "A frequency-selective, piezoresistive silicon vibration sensor," in *Record of the 3rd International Conference on Solid-State Sensors and Actuators*, pp. 105-108, 1985.
78. J. B. Angell, S. C. Terry, and P. W. Barth, "Silicon micromechanical devices," *Scientific American*, pp. 44-55, October 1987.
79. H. Seidel and L. Csepregi, "Three-dimensional structuring of silicon for sensor applications," *Sensors and Actuators*, vol. 4, pp. 455-463, 1983.
80. S.-C. Chang and D. B. Hicks, "The formation of microbridges on (100)-oriented silicon," *Journal of Micromechanics and Microengineering*, pp. 25-29, 1990.
81. D. A. Neamen, *Semiconductor Physics and Devices*. Boston, MA: Irwin, 1992.
82. S. M. Sze, *Semiconductor Devices*. New York, NY: John Wiley and Sons, 1985.
83. O. Tabata, R. Asahi, H. Funabashi, K. Shimaoka, and S. Sugiyama, "Anisotropic etching of silicon in TMAH solutions," *Sensors and Actuators A*, vol. 34, pp. 51-57, 1992.
84. O. Tabata, "pH-controlled TMAH etchants for silicon micromachining," *Sensors and Actuators A*, vol. 53, pp. 335-339, 1996.
85. R. J. Reay, E. H. Klaassen, and G. T. A. Kovacs, "Thermally and electrically isolated single crystal silicon structures in CMOS technology," *IEEE Electron Device Letters*, vol. 15, pp. 399-401, Oct. 1994.
86. P. Cook, "Silicon micromachining applied to the management of the thermal environment in wafer scale integration technology," Master's thesis, Air Force Institute of Technology, December 1992.
87. D. M. Sowders, "Low observables technology facilitated by the silicon micromachining process and the use of anti-reflective thin films," Master's thesis, Air Force Institute of Technology, December 1993.
88. K. Hjort, G. Thornell, R. Spohr, and J.-A. Schweitz, "Heavy ion induced etch anisotropy in single crystalline quartz," in *The 9th Annual International Workshop on Microelectromechanical Systems*, pp. 267-271, 1996.
89. G. Thornell, K. Hjort, B. Studer, and J.-A. Schweitz, "Cut-independent deep structuring of quartz for frequency control applications," in *Proc. of the 50th Annual IEEE International Frequency Control Symposium*, pp. 615-622, 1996.
90. L. Ristic, ed., *Sensor Technology and Devices*. Norwood, MA: Artech House, 1994.
91. J. Marshall, M. Gaitan, M. Zaghloul, D. Novotny, V. Tyree, J. Pi, C. Pina, and W. Hansford, "Realizing suspended structures on chips fabricated by CMOS foundry processes through the MOSIS service." U. S. Department of Commerce, National Institute of Standards and Technology, NISTIR, 5402, June 1994.

92. D. J. Anderson, K. Najafi, S. J. Tanghe, D. A. Evans, K. L. Levy, J. F. Hetke, X. Xue, J. Zappia, and K. D. Wise, "Batch-fabricated thin-film electrodes for stimulation of the central auditory system," *IEEE Transactions on Biomedical Engineering*, vol. 36, pp. 693-703, July 1989.
93. T. Akin and K. Najafi, "A micromachined silicon sieve electrode for nerve regeneration applications," in *Proceedings of the 6th. International Conference on Solid-State Sensors and Actuators*, pp. 128-131, 1991.
94. G. T. A. Kovacs, C. W. Storment, and J. M. Rosen, "Regeneration microelectrode array for peripheral nerve recording and stimulation," *IEEE Transactions on Biomedical Engineering*, vol. 39, pp. 893-902, Sept. 1992.
95. F. I. Chang, R. Yeah, G. Lin, P. B. Chu, E. Hoffman, E. J. J. Kruglick, and K. S. J. Pister, "Gas-phase silicon micromachining with xenon difluoride," *Proc. SPIE Microelectronic Structures and Microelectromechanical Devices for Optical Processing and Multimedia Applications*, vol. 2641, pp. 117-128, Oct. 1995.
96. F. I.-J. Chang, "Xenon difluoride etching of silicon for mems," Master's thesis, University of California, Los Angeles, June 1995.
97. W. Kühnel, "Silicon condenser microphone with integrated field-effect transistor," *Sensors and Actuators A*, vol. 25-27, pp. 521-525, 1991.
98. D. A. Koester, R. Mahadevan, and K. W. Markus, "Multi-user mems processes (MUMPSs) introduction and design rules," tech. rep., MCNC MEMS Technology Applications Center, 3021 Cornwallis Road, Research Triangle Park, NC, 27709, October 1994.
99. G. Delapierre, "Micro-machining: a survey of the most commonly used processes," *Sensors and Actuators*, vol. 17, pp. 123-138, 1989.
100. Information available from the MCNC World Wide Web home page, WWW url: <http://www.mcnc.org>.
101. J. Mohr, B. Bley, M. Strohrmann, and U. Wallrabe, "Microactuators fabricated by the LIGA process," *Journal of Micromechanics and Microengineering*, vol. 2, pp. 234-241, December 1992.
102. A. B. Frazier and M. G. Allen, "Metallic microstructures fabricated using photosensitive polyimide electroplating molds," *Journal of Microelectromechanical Systems*, vol. 2, pp. 87-94, June 1993.
103. A. B. Frazier and M. G. Allen, "Uses of electroplated aluminum in micromachining applications," *Solid State Actuator Workshop*, pp. 90-94, June 1994.
104. DuPont Electronics, Barley Mill Plaza, P.O. Box 80019, Wilmington, DE 19880-0019, *Pyralin PD Polyimide Coatings: PI-2700 Processing Guidelines*, March 1991.
105. K. S. J. Pister, M. W. Judy, S. R. Burgett, and R. S. Fearing, "Microfabricated hinges," *Sensors and Actuators A*, vol. 33, pp. 249-256, 1992.
106. S. R. Burgett, K. S. J. Pister, and R. S. Fearing, "Three dimensional structures made with microfabricated hinges," *Micromechanical Systems, ASME 1992*, pp. 1-11, 1992.

107. D. Sene, "Design, fabrication, and characterization of micro-opto-electro-mechanical systems," Master's thesis, Air Force Institute of Technology, December 1995.
108. J. D. Kraus, *Electromagnetics*. New York: McGraw-Hill, fourth ed., 1992.
109. J. H. Comtois, V. M. Bright, S. C. Gustafson, and M. A. Michalick, "Implementation of hexagonal micromirror arrays as phase-mostly spatial light modulators," *Proc. SPIE Microelectronic Structures and Microelectromechanical Devices for Optical Processing and Multimedia Applications*, vol. 2641, pp. 76-87, Oct. 1995.
110. J. M. Younse, "Mirrors on a chip," *IEEE Spectrum*, Nov. 1993.
111. P. Osterberg, R. Gupta, and S. Senturia, "Quantitative models for the measurement of residual stress, poisson ration, and young's modulus using electrostatic pull-in of beams and diaphragms," in *Technical Digest, Solid State Sensor and Actuator Workshop*, pp. 38-42, 1994.
112. J. H. Comtois, V. M. Bright, and M. Phipps, "Thermal microactuators for surface micromachining processes," *Proc. SPIE: Micromachined Devices and Components*, vol. 2642, pp. 23-24, Oct. 1995.
113. M. W. Phipps, "Design and development of microswitches for micro-electro-mechanical relay matrices," Master's thesis, Air Force Institute of Technology, June 1995.
114. A. L. Simon and D. A. Ross, *Principles of Statics and Strength of Materials*. Dubuque, Iowa: Wm. C. Brown Co., Publishers, 1983.
115. D. S. Gunawan, L.-Y. Lin, and K. S. J. Pister, "Micromachined corner cube reflectors as a communication link," *Sensors and Actuators A*, vol. 46-47, pp. 580-583, 1995.
116. J. T. Stewart, J. A. Kosinski, and A. Ballato, "An analysis of the dynamic behavior and acceleration sensitivity of a SAW resonator supported by flexible beams," in *Proc. of the 49th Annual IEEE International Frequency Control Symposium*, pp. 507-513, 1995.
117. D. Huynh, R. McGowan, J. A. Kosinski, J. T. Stewart, R. Piekarz, and C. D. Mulford, "Experimental studies of SAW and STW acceleration sensitivity," in *Proc. of the 49th Annual IEEE International Frequency Control Symposium*, pp. 494-498, 1995.
118. J. A. Kosinski, J. T. Stewart, A. Ballato, and R. Almar, "An analysis of the normal acceleration sensitivity of rotated Y-cut quartz surface transverse wave resonators simply supported along rectangular edges," in *Proc. of the 49th Annual IEEE International Frequency Control Symposium*, pp. 486-493, 1995.
119. J. T. Stewart, R. McGowan, J. A. Kosinski, and A. Ballato, "Semi-analytical finite element analysis of acceleration-induced frequency change in SAW resonators," in *Proc. of the 49th Annual IEEE International Frequency Control Symposium*, pp. 499-506, 1995.
120. B. E. Boser, R. T. Howe, and A. P. Pisano, "Course notes: monolithic surface-micromachined inertial sensors, university of california, berkeley," 1995.
121. W. S. Griffin, H. H. Richardson, and S. Yamanami, "A study of fluid squeeze-film damping," *Journal of Basic Engineering*, pp. 451-456, June 1966.

122. M. Andrews, I. Harris, and G. Turner, "A comparison of squeeze-film theory with measurements on a microstructure," *Sensors and Actuators, A*, vol. 36, pp. 70-87, 1993.
123. D. L. Kendall, "On etching very narrow grooves in silicon," *Applied Physics Letters*, vol. 26, pp. 195-198, 15 Feb. 1975.
124. K. E. Bean, "Anisotropic etching of silicon," *IEEE Trans. on Electron Devices*, vol. ED-25, pp. 1185-1192, October 1978.

Vita

Captain James R. Reid, Jr. was born 17 April 1970 in Columbus, Ohio. He graduated from Duke University in May 1992 with a Bachelor of Science degree in Electrical Engineering and accepted a commission as a Second Lieutenant in the United States Air Force. He was immediately assigned to the Air Force Institute of Technology, Wright-Patterson, Air Force Base, Ohio, to pursue a Masters of Science degree in Electrical Engineering. He graduated as a distinguished graduate in December 1993 and stayed at AFIT to pursue his PhD degree in Electrical Engineering. He is a member of Tau Beta Pi and a student member of IEEE.

REPORT DOCUMENTATION PAGE			Form Approved OMB No. 0704-0188	
Public reporting burden for this collection of information is estimated to average 1 hour per response, including the time for reviewing instructions, searching existing data sources, gathering and maintaining the data needed, and completing and reviewing the collection of information. Send comments regarding this burden estimate or any other aspect of this collection of information, including suggestions for reducing this burden, to Washington Headquarters Services, Directorate for Information Operations and Reports, 1215 Jefferson Davis Highway, Suite 1204, Arlington, VA 22202-4302, and to the Office of Management and Budget, Paperwork Reduction Project (0704-0188), Washington, DC 20503.				
1. AGENCY USE ONLY (Leave blank)	2. REPORT DATE Dec 96	3. REPORT TYPE AND DATES COVERED Dissertation, 1996		
4. TITLE AND SUBTITLE Microelectromechanical Isolation Of Acoustic Wave Resonators			5. FUNDING NUMBERS	
6. AUTHOR(S) James R. Reid				
7. PERFORMING ORGANIZATION NAME(S) AND ADDRESS(ES) Air Force Institute of Technology Wright-Patterson AFB, OH 45433			8. PERFORMING ORGANIZATION REPORT NUMBER	
9. SPONSORING/MONITORING AGENCY NAME(S) AND ADDRESS(ES) John A. Kosinski, Ph.D. U.S. Army Communications-Electronics Command AMSEL-RD-IE-TI Fort Monmouth, NJ 07703-5211			10. SPONSORING/MONITORING AGENCY REPORT NUMBER	
11. SUPPLEMENTARY NOTES				
12a. DISTRIBUTION/AVAILABILITY STATEMENT Distribution Unlimited			12b. DISTRIBUTION CODE	
13. ABSTRACT (Maximum 200 words) Microelectromechanical systems (MEMS) is a rapidly expanding field of research into the design and fabrication of actuated mechanical systems on the order of a few micrometers to a few millimeters. MEMS potentially offers new methods to solve a variety of engineering problems. A large variety of MEMS systems including flip-up platforms, scanning micromirrors, and rotating micromirrors are developed to demonstrate the types of MEMS that can be fabricated. The potential of MEMS for reducing the vibration sensitivity of surface acoustic wave and surface transverse wave resonators is then evaluated. A micromachined vibration isolation system is designed and modeled. A fabrication process utilizing two sided anisotropic etching of {110} silicon wafers is developed. The process utilizes standard microelectronic fabrication equipment to batch fabricate the isolation systems. The fabricated systems are only 1 cm by 1 cm by 1 mm. Several oscillators are fabricated using commercially fabricated STW resonators mounted on the isolation systems. The resonators are driven by their standard oscillator circuit. Incorporating the isolation system into the oscillator does not result in an appreciable increase the size or the weight of the oscillator. Testing of the oscillators shows that the isolators successfully function as passive vibration isolation systems.				
14. SUBJECT TERMS Acceleration Sensitivity, Micromachining, KOH, Vibration Isolation			15. NUMBER OF PAGES 197	
			16. PRICE CODE	
17. SECURITY CLASSIFICATION OF REPORT Unclassified	18. SECURITY CLASSIFICATION OF THIS PAGE Unclassified	19. SECURITY CLASSIFICATION OF ABSTRACT Unclassified	20. LIMITATION OF ABSTRACT UL	